Wind Tunnel Investigation of the Effect of Duct and Cross-flow on Small Propellers for Unmanned Aerial Vehicles

by

David Serrano

A thesis submitted in partial fulfillment of the requirements for the degree of

Master of Science

Department of Mechanical Engineering
University of Alberta

Abstract

The expanding field of unmanned aerial vehicles (UAV) has introduced a variety of flight operating conditions and thus, performance requirements. As a method to improve performance in the propulsion systems of UAVs, two topics of interest are emphasized in this thesis: the potential improvements offered by ducted propellers, and the relatively uninvestigated performance of small-scale rotors at non-zero angle-of-attack. The growing capabilities of UAVs equipped with propellers imply that rotor disks operate at a much higher angle-of-attack than in the case of helicopters or propeller powered airplanes. These two topics are the focus of this thesis, namely: the aerodynamic performance of a small ducted propeller with in axial flow condition; and the performance of small propellers at angles-of-attack ranging from 0° to 90°.

The experiments were performed inside a close-loop wind tunnel facility. Load cell measurements performed at free stream velocities of 0 m/s to 15 m/s demonstrated that the four ducted propeller models tested outperformed the open propellers in thrust generation up to an advance ratio of 0.25~0.35. Inlet flow visualization using planar particle image velocimetry demonstrated that one of the reasons for the drop in performance of the ducted propeller with increasing advance ratio was a reduction in the mass flow rate through the rotor disk plane relative to the open propeller by approximately 2.5%. Flow visualization at the exit of the duct using stereoscopic particle image velocimetry revealed that the ducted propeller mitigated the contraction of the propeller jet by achieving an exit area-to-rotor disk area ratio of 1.04.

In the second investigation, the performance of four 12 inch propellers was investigated at angles-of-attack ranging from 0° to 90° and free-stream advance ratios ranging from 0 to 0.55. The propellers differed in terms of airfoil section, chord length and pitch angle distribution along the

span of the blade. Wind tunnel load measurements revealed that with increasing angle of attack and constant advance ratio, an increase in thrust was achieved, for constant propeller rotational velocity. Aerodynamic moments provided evidence of pitch and yaw moments generated by the non-uniform distribution of the blade angle-of-attack over the rotor disk area. An analytical performance prediction model was developed using blade element theory, where a first harmonic induced velocity model was applied. The model was adjusted using the experimentally obtained data and the Genetic Algorithm from MATLAB. The resultant model successfully predicted distributions of the effective angle-of-attack of the blade elements and of the differential thrust generated that coincided with the experimental wind tunnel data.

Preface

All of the material presented in this thesis including the planning of the experiment, the design of the experimental setup, the carrying out of the experiments and data processing were performed under the supervision of Dr. Sina Ghaemi from the Mechanical Engineering Department at the University of Alberta.

The LabVIEW interface used to operate the propeller system was developed by Rick Conrad from the Mechanical Engineering Department at the University of Alberta.

Prototypes for the 3D printed parts used in this investigation were facilitated by the laboratory of Dr. David Nobes from the Mechanical Engineering Department at the University of Alberta.

The results of section Chapter 5 of this thesis were consulted with Dr. Ahmed Qureshi, also from the Mechanical Engineering Department at the University of Alberta, and a portion of the experiments were conducted with the help of Max Ren.

Acknowledgements

I would like to express my gratitude to my supervisor Dr. Sina Ghaemi, whom without his guidance, knowledge and expertise I could not have accomplished a fruitful learning experience. The completion of this thesis depended heavily on the experimental implications, which could not have been possible without the help from Bernie and Rick.

My achievements in this degree or any other professional endeavours I might take upon fall short to the human experiences that I will gracefully remember I lived in the duration of this degree. To my research friends who made this possible, Wagih, Daren, Desiree, Rafat, Sadek, Drew, Felix, Brad, Elyasi, Mohammad, Masoud, Sen, Farzad. I hope the list of laughs, stories, good memories, football discussions and failed dinner attempts will only keep growing over the years. Special thanks to Wagih and Daren, for being able to transform four office walls into a universe of joyful conversation and friendship.

To my friends apart from the research, Andres, Beatriz, Gabriel, Yishak, Lisa, I want to thank you for providing me with a family apart from home.

To my mom, my dad, my brother, my grandmother and my girlfriend; there are no words to describe my gratitude for your support, guidance and love.

Table of Contents

List of Figures

List of Tables

Nomenclature

Acronyms

BLDC	Brushless Direct Current
CCD	Charge-Coupled Device
CFD	Computational Fluid Dynamics
DA	Diffuser Angle
DAQ	Data Acquisition
ESC	Electronic Speed Controller
FOV	Field of View
IW	Interrogation Window
LE	Leading Edge
MA	Master Airscrew
MAV	Micro Aerial Vehicles
NACA	National Advisory Committee for Aeronautics
NSMB	Netherlands Ship Model Basin
OP	Open Propeller
PIV	Particle Image Velocimetry
PWM	Pulse Width Modulation
RAM	Random Access Memory
RPM	Revolutions per Minute
SF	Slow Flyer
SP	Sport
STOL	Short Take Off and Landing
UAV	Unmanned Aerial Vehicles
VFD	Variable Frequency Drive
VTOL	Vertical Take Off and Landing

Symbols

A	rotor disk area = $\pi D_P^2/4$
a_1, a_2, a_3 and a_4	parameters of the correction factors f_1 and f_2
c_D	chord length of the cross-section of the duct
C_D	drag force coefficient = $F_D/\rho n^2 D^4$
C_L	lift force coefficient = $L/\rho n^2 D^4$
C_M	moment coefficient = $M/\rho n^3 D^5$
C_P	power coefficient = $T\Omega/\rho n^3 D^5$
C_T	thrust force coefficient = $T/\rho n^2 D^4$
$C_{T,h}$	thrust force coefficient in the hover condition
d	separation distance between the rotor disk and the center of the load cell
D	minimum internal diameter of the duct
D_E	external diameter of the duct
D_P	nominal diameter of the propeller or rotor disk
D_h	diameter of the propeller hub
E	energy
f_1, f_2	linear correction factors applied in the induced velocity models
$f_\#$	camera aperture setting
F_x, F_y and F_z	the x, y and z-components of force measured by the load cell
FM	figure of merit = $C_T^{3/2}/\sqrt{2}C_P$
J	free-stream advance ratio = V_∞/nD_P
J_a	inflow advance ratio = $V_\infty\cos(\alpha_P)/nD_P$
J_a'	inflow advance ratio non-dimensionalized by the blade tip speed= $V_\infty\cos(\alpha_P)/\Omega R$
J_t	tangential advance ratio = $V_\infty\sin(\alpha_P)/nD_P$
k_x, k_y	longitudinal and lateral weighing factors in the linear inflow model, respectively
$\dot{m}$	mass flow rate
M	magnification

Ma Mach number

M_x, M_y and M_z x, y and z-components of moment generated by the propeller

n angular velocity of the propeller in revolutions per second

N number of trials considered

P power consumed by the propeller = $Q\Omega$

Q Output torque from the propeller

r radial coordinate

r_i internal diameter of ring element

r_o external diameter of ring element

r_{LE} leading edge radius

R nominal radius of a propeller

R_T nominal radius of the propeller with trimmed ends, used with the duct

R_{eff} effective blade radius

S standard deviation

t thickness of the duct cross-section

$t_{\alpha/2}$ t-distribution value with 95% confidence level

T total thrust force

u x-component of velocity

U instantaneous x-component of velocity

v y-component of velocity

v_h induced velocity in hover (zero free-stream)

v_i induced velocity at the rotor disk plane

V_a axial component of the resultant velocity on the blade element = $v_i + V_\infty \cos(\alpha_P)$

V_j exit jet velocity

V_t tangential component of the resultant velocity on the blade element=$\Omega R + V_\infty \sin(\alpha_P)\sin(\Psi)$

V_R resultant velocity incident on the blade element = $V_a^2 + V_t^2$

V_∞ free-stream velocity, in meters per second

V	instantaneous y-component of velocity
w	z-component of velocity
W	instantaneous z-component of velocity
x	Cartesian coordinate x
y	Cartesian coordinate y
$\bar{y}$	y-coordinate normalised by the duct internal diameter D
z	Cartesian coordinate z
α_P	angle-of-attack of the rotor disk with respect to the free stream, in degrees
α_b	local effective angle-of-attack of the blade elements, in degrees
$\alpha_{L=0}$	zero lift angle-of-attack of a blade element
β	systematic uncertainty
ϵ_{Fz}	percent discrepancy between calculated and measured force F_z
χ	wake skew angle
λ	inflow ratio = $V_a / \Omega R$
λ_i	induced inflow ratio = $v_i / \Omega R$
λ_h	induced inflow ratio in hover = $v_h / \Omega R$
δ_{tip}	blade tip clearance
Δt	time step between camera frames
ϵ	percent discrepancy
η	propulsive efficiency = $C_T J / C_P$
μ	dynamic viscosity of air
φ	blade inflow angle
ψ	azimuthal location along the circumference of the rotor disk
Ω	angular velocity of the propeller in radians per second
Π	random uncertainty
ρ	density of air
σ	exit area-to-rotor area ratio

θ_b blade collective angle of the propeller blades, in degrees

θ_D diffuser angle of the ducts, in degrees

σ_e effective diffusion expansion ratio achieved by the duct

ζ vorticity vector

Chapter 1. Introduction

1.1 Motivation of the Project

Unmanned Aerial Vehicles (UAVs) are being increasingly implemented in a variety of industries such as agriculture, military, transportation, entertainment, and many public services such as emergency response and surveillance [1]. The exponential advances the electronics field has undergone in the past decade have allowed the technological world to downsize their instruments. This has played an important role in the increasing interest for small scale UAVs and Micro Aerial Vehicles (MAVs), since the instrumentation possibilities are continuously growing, and in turn, expanding the potential of UAV applications [2]. Unmanned vehicles propose several advantages over their manned counterparts. Eliminating the requirements of a human-operated device in order to carry out investigative, rescue or military aerial missions which are considered to be of high risk, is the most notable safety feature of UAVs [3]. The ability to navigate in environments with small available aerial space, such as highly developed metropolitan areas, is a challenge that can be overcome by the significantly small size, and the enhanced maneuverability of UAVs.

It is evident that UAVs may be considered as one of the technological milestones of this decade [4], but in conjunction with a growing demand, there comes the necessity to develop their technology in a manner that fulfills the sustainability requirements of today's world. The search for a more efficient and safer design of UAVs is a continuous process, and it is the core of the majority of research subjects in the field of UAV development. As it was previously done with the development of transportation airplanes and combat aircrafts, the performance optimization of UAV's and MAV's is strongly dominated by an understanding of the aerodynamic characteristics of the vehicles at low Reynolds numbers, and the ability to project this knowledge onto an increment of the overall efficiency of these systems. An increase in efficiency will not only decrease the energy consumption, but it will also allow the aircraft to carry a higher payload, better flight endurance, and a widening of the allowable flight regimes. The vast majority of UAVs and MAVs of today achieve flight through the use of electric powered propulsion. The high flight endurance achieved by the combination of electric motors and multi-cell batteries in comparison to gasoline powered systems has made this system a popular choice for commercial users of UAVs.

The most popular mechanism used to generate propulsion in UAVs is propellers. Propeller powered systems allow multi-rotor combination designs that significantly increase the flight capabilities of UAVs, allowing the aircraft to move on multiple directions, or remain static (hover) in a specified spatial location. Quadcopters, helicopters and other types of Vertical/Short Take Off and Landing (V/STOL) UAVs as the ones shown in Figure 1-1 (a) to (c), are some of the designs that are powered through the use of a multi-rotor design.

(a)

(b)

(c)

Figure 1-1: Examples of VTOL Unmanned Aerial Vehicles such as (a) the V BAT model from Martin UAV, capable of transitioning to forward flight, (b) the Draganflyer X6 quadcopter from Draganfly Innovations, and (c) the MQ-8B Fire Scout operated by the United States Navy. The images in (a) – (c) are used here through permissions granted from direct contact with the copyright owners. The images in (a) and (b) have been used with permissions from Martin UAV and Draganfly Innovations Inc., respectively. The image in (c) is publicly available in http://www.navy.mil/view_image.asp?id=108121, and has been shot by Kelly Schindler.

As of today, there is a great variety of UAV manufacturers, with many different designs. However, only a select number of them have attempted to modify the propulsion mechanism to improve flight performance. One technology that has not yet become popular in the construction of UAVs

is the ducted propeller. For the purpose of propulsion, ducted propellers make their appearance in the beginning of the 1930's: in 1930 German fluid dynamicist Ludwig Kort designed the "Kort Nozzle", shown in Figure 1-2(a), used with screw propellers for boats; and in 1931 Italian aeronautical engineer Luigi Stipa obtained the first experimental data on "Intubed Propellers" intended for aerial purposes, later used on his aircraft the *Stipa Caprioni*, shown in Figure 1-2(b). In 1936, Kort's patent for a "Combined Device of a Ship's Propeller Enclosed by a Nozzle", was accepted by the United States Patent Office. Kort mentioned why previous attempts to implement ducts around propellers failed to provide any significant improvement, and stressed the fact that this was due to an improper design of the duct shapes: "All of these combinations having as their aim to increase the propulsive efficiency of the propeller, and yet they all failed in practical use, as none of them were uniting the proper shape of the nozzle with the proper relation between the propeller, its revolutions, the areas at the narrowest cross section and at the mouth of the nozzle and the form, speed and resistance of the ship. ([5])".

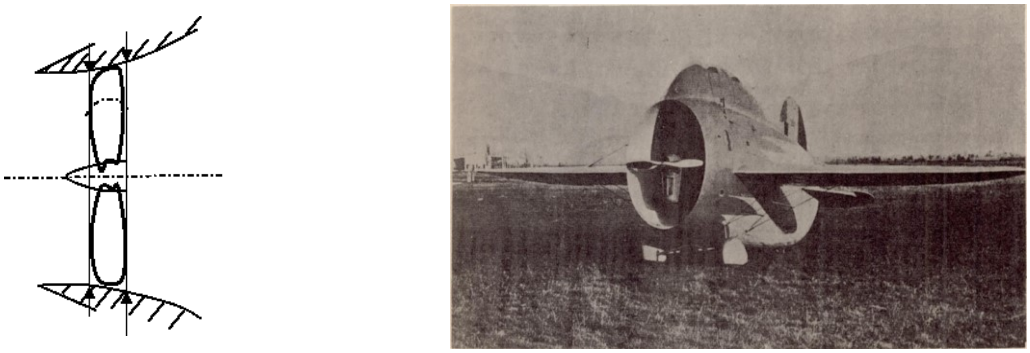

(a) **(b)**

Figure 1-2: In (a), a schematic of the "Kort" Nozzle, recreated from Kort [5]**, US Patent # 2,030,375. The design is also referred to as a flow accelerating nozzle. In (b), A photograph of the Stipa Caprioni, designed and built by Luigi Stipa in 1933. The image in (b) has been obtained from Stipa** [6]**, publicly available through the NASA Technical Reports Server: https://ntrs.nasa.gov/search.jsp?R=19930094761**

In both Kort's and Stipa's investigations, it was proven that the use of a duct around the propeller increased the thrust-to-input power ratio, as well as the propulsive efficiency of the system, for selected operating ranges. These findings have inspired engineers across the decades to introduce ducted propellers on full-scale vehicles, in both the marine and aerospace fields, seeking to achieve a more efficient operation. An example of the use of ducted propellers in the aerospace industry is

the tail rotor of helicopters, also known by their trademark name Fenestron™. The Fenestron™ was first implemented in 1968 on the helicopter SA340 Gazelle, fabricated by Aerospitale in France, shown in Figure 1-3(a); its main purpose being the same as open tail rotors: to counteract the torque produce by the main rotor. Since its creation, it has being widely used in other helicopters, such as the Eurocopter EC135. With the ducted propeller system, the anti-torque effect was enhanced, the safety of the operations crew was improved, and the noise and vibrations produced by the system was significantly reduced ([7]).

Figure 1-3: Examples of ducted propellers used in helicopters through the popularly known Fenestron™ in a SA340 Gazelle model helicopter. The image has been captured by the online user Aerofossile2012 on www.flickriver.com, and made publicly available through the Creative Commons License: https://creativecommons.org/licenses/by-nc-sa/2.0/legalcode.

Nonetheless, helicopter tail rotors are not the only example of ducted propellers in the aeronautical field. In the time period of 1950-1970 the booming interest of military industry for VTOL aircrafts led them to invest in research and development of these vehicles. The aerodynamic properties of ducted propeller were already known by then, and this resulted in a variety of full-scale models and prototypes using this technology. Some examples of these designs are the Doak VZ04, the Bell X-22, and the Avro Canada VZ-9 Avrocar, shown in Figure 1-4 (a) to (c), respectively. The development of aircrafts with ducted propellers was not exclusive to the military industry; one example is the Nord Aviation Nord-500 built by Nord Aviation in 1967.

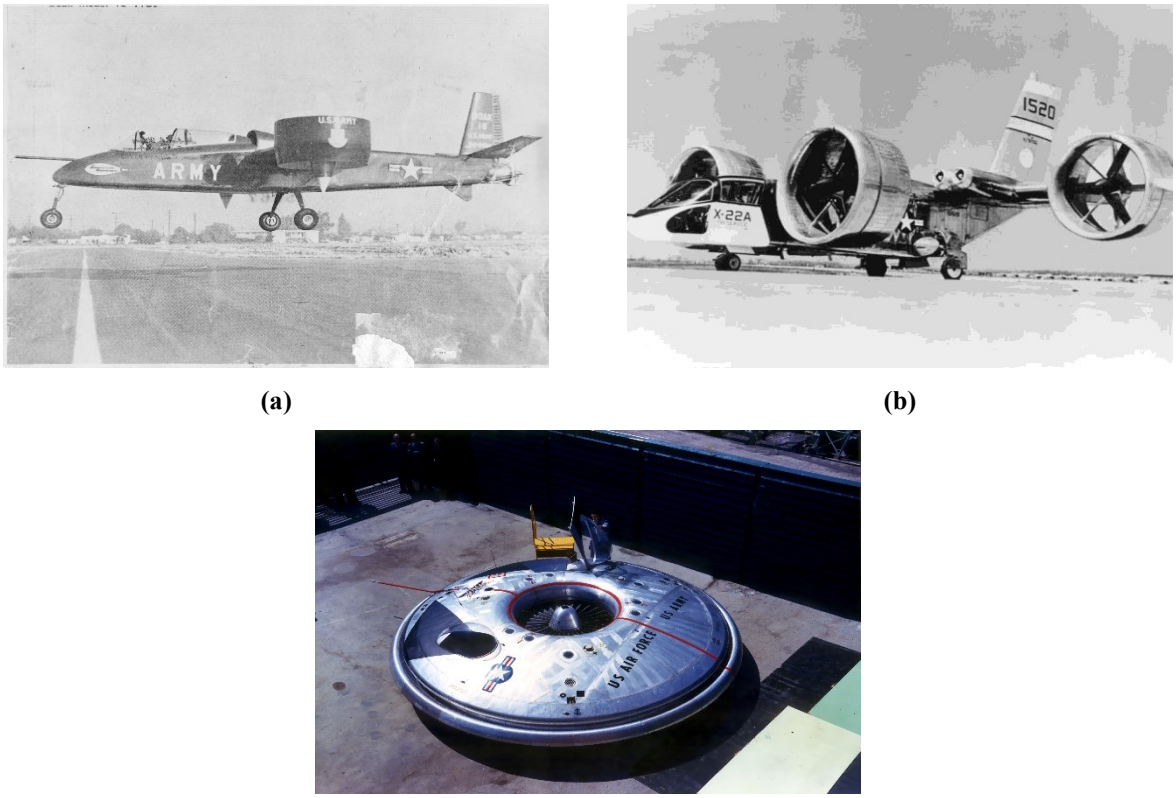

(a) **(b)**

(c)

Figure 1-4: Example of large scale aircrafts that implemented ducted propellers as their principal means of propulsion. The vehicles shown are (a) the Doak VZ04 model from the Doak Aircraft Company (Image is a work of the United States federal government, available in the public domain through https://www.flickr.com/photos/sdasmarchives/4564654232/) (b) the Bell X-22 from Bell Aircraft (Image is a work of the United States federal government, available on the public domain) and (c) the Avrocar VZ-9 from Avro Canada (Image from the book "Avrocar: Canada's Flying Saucer, 2001," available on the public domain).

There are examples of ducted propellers used in UAVs, as is the case of the V BAT from Martin UAV shown in Figure 1-1(a); however, as it was previously mentioned, it is not a common design. One of the main reasons why the ducted propeller has not been a popular choice in the design of multi-rotor UAVs is its performance hindering effects when the aircraft is travelling at high flight speeds. At high flight velocities, the drag generated by the duct itself overcomes the thrust benefits provided by it.

To achieve meaningful improvements in performance and efficiency of UAVs, a deeper understanding of the aerodynamics concerning these devices is needed. Much of the technology

involved in the development of UAVs, such as ducted propellers, is of common knowledge to aerodynamicists of today; however, its implementation at such a small scale is relatively new, and thus, requires special attention.

The use of propellers in UAVs has also amplified the operating regime of propellers themselves. More specifically, with the extensive flight maneuvers and pirouettes achieved by UAVs, the propellers or rotors in a multi-rotor UAV are subject to a rotor angle-of-attack, α_P, range of $0° \leq \alpha_P \leq 90°$, which in comparison to the operation of rotors in helicopters or propeller powered airplanes (approximately $80° \leq \alpha_P \leq 90°$ and $0° \leq \alpha_P \leq 10°$, respectively) is a substantially wider range. Changes in the angle-of-attack of a rotor has sever effects, on the performance of the rotor, depending on the magnitude of the angle and operating condition.

The majority of small unmanned aerial vehicles (UAVs) implement a multi-rotor configuration to carry out maneuvers such as hover and vertical take-off and landing. The multi-rotor propulsion simplifies the control system and increases the maneuverability of the vehicle. However, the multi-rotor propulsion is not as efficient as a fixed-wing vehicle for forward flight. This has limited the range and endurance of small multi-rotor UAVs.

The forward flight of a multi-rotor vehicle is typically achieved by tilting the rotor disk (and the vehicle) to project a component of the propeller thrust in the direction of motion. The rotor will operate with its disk at a non-zero angle-of-attack, α_P, with respect to the free-stream velocity. The projection of the free-stream velocity perpendicular and parallel to the rotor disk results in variation of the effective angle-of-attack, α_b, and the generated force of the blade elements. As a result, the aerodynamic performance of the rotor deviates from a conventional propeller operating with its rotor disk perpendicular to the free-stream velocity. In extreme conditions, the variation of α_b can cause flow separation over the propeller disk and reduce the net thrust. The load non-uniformity over the propeller disk can also result in yaw, pitch or rolling moments on the vehicle, affecting its stability. An understanding of the aerodynamic performance of small propellers at a wide range of disk angles is required for the design of efficient and stable UAVs. A UAV performs a variety of maneuvers in a single flight mission, which requires operation of its rotor at wide range of angle-of-attack covering $90° \leq \alpha_P \leq 0°$.

1.2 Project Objective

The focus of this dissertation is on the two aforementioned concerns regarding the operation of propellers namely, the aerodynamic performance of ducted propellers and the effect of operating a propeller at non-zero angles-of-attack will be studied. The objective of this investigation is to provide insight into these systems from a fluid dynamics point of view.

Chapter 2 presents a summary of the relevant investigations carried out in the past, regarding large and small-scale ducted propellers, as well as large and small-scale experiments with propellers at non-zero angle-of-attack.

The experimental setup used for the purposes of this thesis is described in Chapter 3. This chapter includes details such as the design, manufacturing and assembly of the duct and propeller systems used for the investigation.

Section Chapter 4 of this thesis presents the results of the experimental investigation on the aerodynamic performance of a 10 in (254 mm) diameter ducted propeller system. The purpose of this study is to investigate the behavior of ducted propellers and provide insight on the performance differences when compared to an open propeller system. Four duct models are tested, and their performance is compared to an open propeller system. Load cell measurements are performed at an advance ratio range of 0 to 0.65 to acquire readings of thrust, torque and to calculate propulsive efficiency curves. Flow visualization through Particle Image Velocimetry (PIV) are implemented to regions upstream and downstream of the rotor disk to visualize the structure of the flow, and make inferences about the rotor disk loading, contraction of the slipstream and mitigation of tip vortices.

Chapter 5 entails the results of the investigation on small-scale rotors, with a nominal diameter of 12 inches, operating at non-zero angles of attack. The purpose of this study is to investigate the aerodynamic performance of propellers designed for small UAVs in operating conditions with non-zero α_P. The results provide a database for UAV design and enhances the understanding of propeller operation at non-zero α_P. Two propeller models, namely the Slow Flyer and Sport models from APC Propellers, with nominal diameter of 12 inches are tested in a range of $0° \leq \alpha_P \leq 90°$ and a free-stream advance ratio range of $0 \leq J \leq 0.55$. Measurements of thrust, power, resultant moments and propulsive efficiency are provided. In addition to the experimental work, an

analytical model of the propeller performance based on the blade element theory for $0° \leq \alpha_P \leq 90°$, which implements different methods of calculating the induced velocity, is investigated. The model is validated and improved using the experimental data and is applied to provide distributions of the local effective angle-of-attack α_b and the differential thrust over the rotor disk for non-zero α_P.

The conclusion of this thesis is provided in Chapter 6, following by recommendations for future research in Chapter 7.

Chapter 2. Literature Review

2.1 Classical Momentum Theory

Newton's second law of motion states that the force exerted on a body, or fluid, is equal to the product between its mass, m, and the acceleration of the body, $\vec{a}$, such that

$$\vec{F} = m \cdot \vec{a} \qquad \textbf{2-1}$$

The right-hand side of 2-1 may be expressed more generally as the time rate of change of momentum, written as

$$\vec{F} = \frac{d}{dt}(m \cdot \vec{V}) \qquad \textbf{2-2}$$

where $\vec{V}$ is the velocity of the body or fluid. The left-hand side of 2-2 represents the forces exerted on the fluid. The surfaces forces in $\vec{F}$ are pressure, p, and shear stress acting on the differential control surface dS of the fluid. The body forces, F_{body}, in $\vec{F}$ are forces such as gravity and electromagnetic forces, which act upon the mass enclosed by the differential volume $d\vartheta$; and viscous forces F_{vis}. Substituting these into equation 2-2 the following result is obtained

$$-\oiint p \cdot dS + \iiint \rho \vec{F}_{body} \cdot d\vartheta + \vec{F}_{vis} = \frac{d}{dt}(m \cdot \vec{V}), \qquad \textbf{2-3}$$

where ρ is the density of the fluid. The right-hand side of equation 2-3 is composed of two terms, one of which represents the net flux of momentum across the control surface dS expressed as

$$\oiint (\rho \vec{V} \cdot dS)\, \vec{V} \qquad \textbf{2-4}$$

and a second one which represents the time rate of change of momentum due to fluctuations of the properties of the flow within the volume $d\vartheta$, expressed as

$$\frac{\partial}{\partial t} \iiint \rho \vec{V} d\vartheta. \qquad \textbf{2-5}$$

Therefore, substituting these two expressions into equation2-3, the momentum equation is written in its integral form as

$$-\oiint p \cdot dS + \iiint \rho \vec{F}_{body} \cdot d\vartheta + \vec{F}_{vis} = \frac{\partial}{\partial t} \iiint \rho \vec{V} d\vartheta + \oiint (\rho \vec{V} \cdot dS) \vec{V} \qquad \textbf{2-6}$$

For a propulsion unit such as a propeller, the net contribution of the terms in the left hand side of equation 2-6 can be conglomerated as a single resulting value of thrust, T, which may be positive or negative depending on the operating state of the propeller; thus, simplifying equation 2-6 to

$$T = \frac{\partial}{\partial t} \iiint \rho \vec{V} d\vartheta + \oiint (\rho \vec{V} \cdot dS) \vec{V}. \qquad \textbf{2-7}$$

The application of the momentum theorem to the performance of propellers assumes steady state operation, rather than the periodicity experienced by the individual blades. Therefore, the time derivative term in equation 2-7 vanishes, and equation 2-6 reduces to

$$T = \oiint (\rho \vec{V} \cdot dS) \vec{V} \qquad \textbf{2-8}$$

A generalized schematic of the flow across an open propeller is shown in Figure 2-1. The stage denoted by the subscript ∞ corresponds to a location far upstream from the rotor disk plane, where the pressure p_∞ is equal to the atmospheric pressure, and the velocity V_∞ is the free stream velocity (velocity at which the rotor disk is travelling at). Stages 1 and 2 are immediately upstream and downstream of the propeller plane, respectively. Stage 3 is located far downstream of the rotor disk.

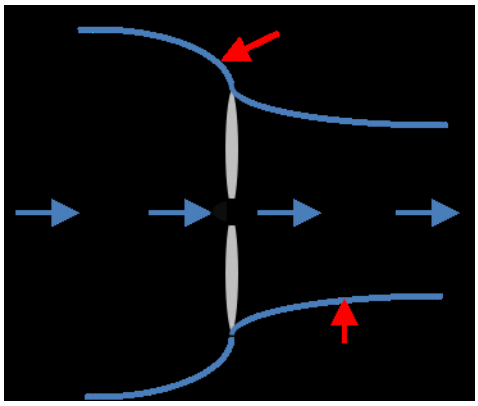

Figure 2-1: Generic flow across an open propeller.

The velocity at the rotor disk, V_1, is equal to the free stream velocity increased by the induced velocity v_i, and is discussed with further detail in section 2.3.2 of this thesis. Since stage 2 is immediately downstream, $V_2 = V_1$. Similarly, the flow velocity experiences a change in magnitude once more in stage 3, as the stream tube of the exit jet undergoes contraction. In summary:

$$V_0 = V_\infty \tag{2-9}$$

$$V_1 = V_2 = V_\infty + v_i \tag{2-10}$$

$$V_3 = V_\infty + v_j \tag{2-11}$$

The principle of conservation of mass indicates that the mass flow rate must be constant at stages 0, 1, 2 and 3. Therefore, the following equality applies

$$\dot{m} = \rho V_0 A_0 = \rho V_1 A_1 = \rho V_3 A_3 \tag{2-12}$$

Integrating 2-8 between stages 3 and 0, the following is obtained

$$T = \iint_0^3 (\rho \vec{V} \cdot dS)\, \vec{V} = \dot{m}(V_\infty + v_j) - \dot{m} V_\infty = \dot{m} v_j \tag{2-13}$$

where now the only variable required to compute the thrust generated is the fluid velocity increment at the exit jet. Evaluating the change of kinetic energy between stages 0 and 3, the ideal power P_i transmitted to the fluid is equal to the change in kinetic energy per unit time of the fluid, such that

$$P_i = \Delta KE = \frac{1}{2}\dot{m}(V_\infty + v_j)^2 - \frac{1}{2}\dot{m} V_\infty^2 = \frac{1}{2}\dot{m} v_j (2V_\infty + v_j) \tag{2-14}$$

From a disk actuator model of the propeller, the same ideal power is expressed as the product of the inlet velocity and the thrust produced as

$$P_i = T(V_\infty + v_i) \tag{2-15}$$

Then, by equating both expressions for the ideal power, namely equations 2-14 and 2-15,

$$\frac{1}{2}\dot{m} v_j (2V_\infty + v_j) = T(V_\infty + v_i) \tag{2-16}$$

thus, substituting equation 2-13 into equation 2-16, a relationship between the induced velocity at the rotor disk and the velocity increment at the exit jet is established as

$$v_j = 2v_i \quad \textbf{2-17}$$

Using equation 2-17 along with the mass conservation, the mass flow rates at stages 3 and 1 are equated, such that

$$\rho(V_\infty + v_i)A_1 = \rho(V_\infty + v_j)A_3. \quad \textbf{2-18}$$

An expression for the exit area-to-rotor disk area ratio is defined as

$$\sigma = \frac{A_3}{A_1} = \frac{(V_\infty + v_i)}{(V_\infty + v_j)}, \quad \textbf{2-19}$$

and substituting equation 2-17 into equation 2-19

$$\sigma = \frac{(V_\infty + v_i)}{(V_\infty + 2v_i)}. \quad \textbf{2-20}$$

w

For an open propeller in axial (or climb) flight, the value of σ from equation 2-20 is between 0.5 and 1, according to Pereira [4].

2.1.1 Hover Flight

For an open propeller in hovering flight, the free stream velocity is zero (V_∞ = 0 m/s) and therefore from equation 2-20, the value of the area ratio is σ = 0.5, and the ideal power becomes

$$P_{i_{OP}} = T_{OP} v_{i,h} \quad \textbf{2-21}$$

where subscript *OP* indicates the thrust of the open propeller, and $v_{i,h}$ is the induced velocity in hover. Combining the results from equations 2-13, 2-15 and 2-17 the value of the induced velocity at the rotor plane in hover is obtained as

$$v_{i,h} = \sqrt{\frac{T_{OP}}{2\rho A_1}} \quad \textbf{2-22}$$

Substituting this result into equation 2-21, the ideal power of an open propeller in hover may be calculated as

$$P_{i_{OP}} = \frac{T_{OP}^{3/2}}{\sqrt{2\rho A_1}} \quad \textbf{2-23}$$

In the case of a ducted propeller, the underlying assumption that is applied in the momentum analysis is that the exit cross sectional area of the stream tube is defined by the exit area of the duct. In theory, if the flow remains attached to the internal walls of the duct, the shape of the duct may cause the exit area to decrease, remain the same or even increase with respect to the rotors disk area, according to Pereira [4]. Therefore, for a ducted propeller in hover, mass conservation dictates that the relationship between the induced velocity at the rotor disk and the increase of velocity at the exit stream jet is

$$v_j = \frac{v_{i,h}}{\sigma} \quad \textbf{2-24}$$

thus, the thrust of the ducted system, as calculated from equation 2-13, becomes

$$T_{DP} = \rho A_1 \frac{v_{i,h}^2}{\sigma} \quad \textbf{2-25}$$

where T_{DP} is the thrust generated by the ducted propeller. From equation 2-22 an expression for the induced velocity at the rotor disk may be obtained as

$$v_{i,h} = \sqrt{\frac{\sigma T_{DP}}{\rho A_1}} \quad \textbf{2-26}$$

Applying the condition that $V_\infty = 0$ m/s in hover to equation 2-23, the ideal power becomes

$$P_{i_{DP}} = \frac{1}{2}\dot{m}v_j^2 = \frac{1}{2}\rho A_1 \frac{v_{i,h}^3}{\sigma^2} \quad \textbf{2-27}$$

2.1.2 Axial Flight

In axial (or climb) flight, the analysis is parallel to that of the hover condition. The velocities across stages 0-3 remain as defined by equations 2-9 to 2-11. From conservation of momentum the thrust generated by an open propeller is

$$T_{OP} = \dot{m} v_j \quad \textbf{2-28}$$

and from conservation of energy, the ideal power consumed by an open propeller is

$$P_{i,OP} = \frac{1}{2} \dot{m} v_j \left(2V_\infty + v_j\right) \quad \textbf{2-29}$$

Considering equations 2-28, 2-29 and 2-15, it is trivial to conclude that the results from equation 2-17 remains valid for an open propeller in axial flight. Thus, after algebraic operations, a relationship between the induced velocity in hover and the induced velocity in axial flight is obtained as

$$\frac{v_i}{v_{i,h}} = -\frac{V_\infty}{2v_{i,h}} + \sqrt{\left(\frac{V_\infty}{2v_{i,h}}\right)^2 + 1} \quad \textbf{2-30}$$

where $v_{i,h}$ can be calculated using equation 2-26.

In the case of a ducted propeller system, the value of σ is determined by the geometry of the duct, and may also be calculated using equation 2-20. Therefore, using the principle of mass conservation, the exit jet velocity from a ducted propeller is

$$v_j = \frac{V_\infty + v_i}{\sigma} - V_\infty \quad \textbf{2-31}$$

The expression for the total thrust generated remains unchanged from equation 2-13:

$$T_{DP} = \dot{m} v_j \quad \textbf{2-32}$$

By solving equations 2-31 and 2-32 alongside equation 2-26 a relationship between the induced velocity in hover and the induced velocity in axial flight is obtained as

$$\frac{v_i}{v_{i,h}} = \frac{V_\infty}{2v_{i,h}} (\sigma - 2) + \sqrt{\left(\frac{\sigma V_\infty}{2v_{i,h}}\right)^2 + 1} \quad \textbf{2-33}$$

To isolate the thrust generated by the rotor and duct individually, the disk actuator model is used. The thrust generated by the rotor only may be considered to be the action of the pressure difference onto the rotor disk plane as

$$T_{DP} = \Delta p \cdot A_1 \quad \textbf{2-34}$$

Applying Bernoulli's equation between locations 0 and 1, and locations 2 and 3 yields

$$p_0 + \frac{1}{2}\rho V_\infty^2 = p_1 + \frac{1}{2}\rho(V_\infty + v_i)^2 \quad \textbf{2-35}$$

$$p_2 + \frac{1}{2}\rho(V_\infty + v_i)^2 = p_3 + \frac{1}{2}\rho\left(V_\infty + v_j\right)^2 \quad \textbf{2-36}$$

Thus, the pressure difference across the rotor disk is calculated as the difference between p_2 and p_1 as

$$\Delta p = p_2 - p_1 = \frac{1}{2}\rho\left(V_\infty + v_j\right)^2 - \frac{1}{2}\rho V_\infty^2$$
$$\Delta p = \rho v_j\left(\frac{v_j}{2} + V_\infty\right) \quad \textbf{2-37}$$

Substituting equation 2-37 into equation 2-34, and using equation 2-13, the ratio of the thrust generated by the rotor only to the total thrust generated by the ducted propeller is expressed as

$$\frac{T_{rotor}}{T_{DP}} = \frac{\Delta p A_1}{\dot{m} v_j} = \frac{v_i + V_\infty(\sigma + 1)}{2\sigma(v_i + V_\infty)} \quad \textbf{2-38}$$

2.1.3 Propulsive Efficiency

The propulsive efficiency of a propeller is, as defined by Glauert [8], is the ratio of the energy spent towards propulsion to the total energy input to the system. The power consumption from a propeller can be experimentally determined if the torque, Q, of the propeller, and the angular velocity, Ω, are measured, thus, the input power may be calculated as

$$P = Q \cdot \Omega \quad \textbf{2-39}$$

where Q is in Newton-meters, and Ω is in rad/s.

The propulsive efficiency of a propeller η, is defined as the ratio of the work that is spent toward the propulsion of the aircraft, to the work output from the propeller shaft as

$$\eta = \frac{T \cdot V_\infty}{Q \cdot \Omega} \quad \textbf{2-40}$$

2.2 Propeller Performance Coefficients

The thrust produced and power consumption of a propeller may be represented through the non-dimensional coefficients

$$C_T = \frac{T}{\rho n^2 D_P^4} \quad \textbf{2-41}$$

and

$$C_P = \frac{P}{\rho n^3 D_P^5} = \frac{Q \cdot \Omega}{\rho n^3 D_P^5} \quad \textbf{2-42}$$

respectively, where n is the angular velocity of the propeller in revolutions per second, ρ is the air density and D_P is the propeller or rotor disk diameter. The operating condition of a propeller is determined through the advance ratio J, defined as

$$J = \frac{V_\infty}{nD_P} \quad \textbf{2-43}$$

Thus, using equations 2-39 to 2-43, the propulsive efficiency can be expressed as

$$\eta = \frac{C_T J}{C_P} \quad \textbf{2-44}$$

Evidently, for a vehicle that is hovering $V_\infty = 0$ m/s and $\eta = 0$, therefore the efficiency of a propeller in hover is measured through the Figure of Merit, FM, often referred to as the static efficiency, defined as

$$FM = \frac{C_T^{3/2}}{2\sqrt{\sigma} C_P} \quad \textbf{2-45}$$

where σ is the ratio of the cross-sectional area of the exit jet streamtube A_j (also known as wake or *slipstream*) to the rotor disk area A, expressed as

$$\sigma = \frac{A_j}{A} \quad \textbf{2-46}$$

2.3 Blade Element Theory

In order to provide a theoretical analysis for interpretation of the experimental results, an analytical prediction of the performance of the propeller is developed. The analytical model is based on the blade element momentum theory (BET) applied to the forward flight of a helicopter rotor, adapted from Leishman [9]. The blade element momentum theory indicates that the differential lift dL and drag dD generated by each blade element (blade elements is shown in Figure 2-2(a)) depends on the inflow angle φ shown in Figure 2-2(b), and thus, the differential thrust dT as well, such that

$$dT = dL \cdot \cos(\varphi) - dD \cdot \sin(\varphi) \quad \textbf{2-47}$$

where the differential lift is defined as

$$dL = \frac{1}{2}\rho V_R^2 C_l c \cdot dr \quad \textbf{2-48}$$

and the differential drag as

$$dD = \frac{1}{2}\rho V_R^2 C_d c \cdot dr \quad \textbf{2-49}$$

where V_R is the resultant relative wind vector, incident on the blade element in m/s, and C_l and C_d are the lift and drag coefficients of the airfoil, respectively. The chord length distribution over the blade is calculated using the fourth order polynomial equation obtained from Figure 3-8(b).

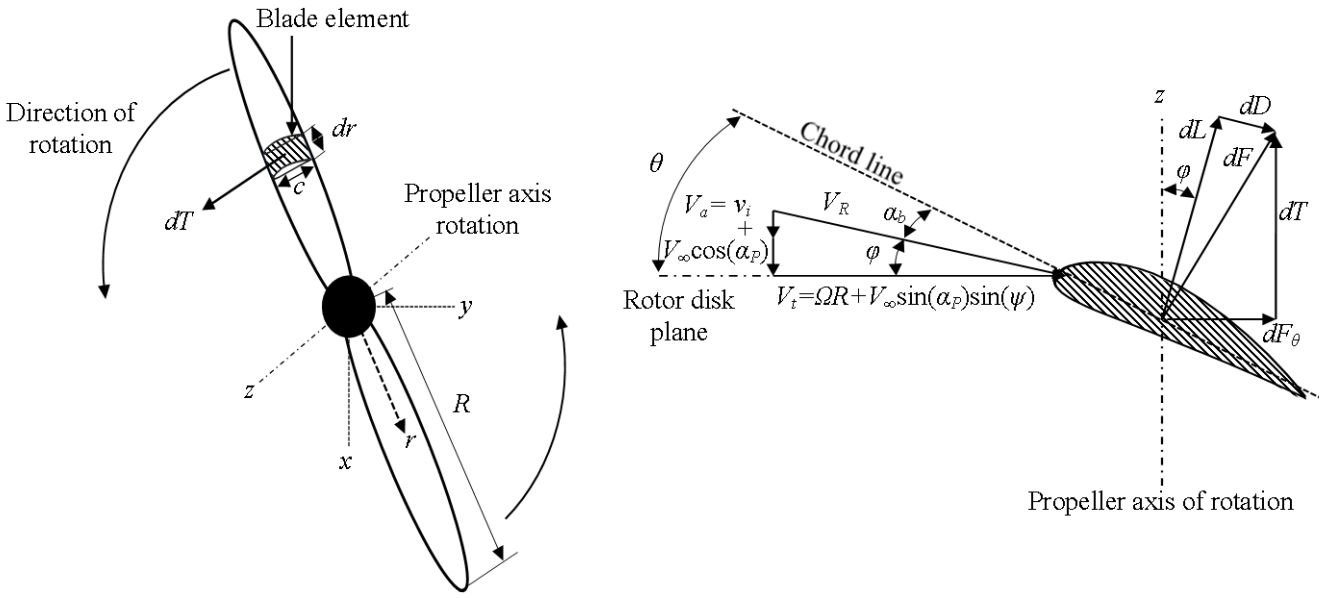

Figure 2-2: (a) Diagram defining the blade element within the propeller. (b) The velocity vector diagram that is incident to the blade element. The diagram also includes the differential forces acting upon the blade element.

2.3.1 Local Effective Angle-of-Attack

As shown in Figure 2-2(b), the effective angle-of-attack of a blade element, α_b, is defined as the angle formed between the relative wind vector, V_R, and the chord line. For a rotor operating at a non-zero α_P and constant Ω, the free stream velocity can be decomposed into an axial and tangential

component relative to the rotor disk, as shown in Figure 3-10(c). The resultant velocity incident on the blade elements, V_R can also be decomposed into a component that is perpendicular to the rotor disk (V_a) and one that is tangential to the rotor disk (V_t) as shown in Figure 2-2(b). These components are functions of V_∞, α_P, the induced axial velocity v_i, the distance r of the blade element from the center of the rotor, and the azimuthal location of the blade element in the rotor disk, ψ, such that

$$V_a = V_\infty \cos(\alpha_P) + v_i \quad \textbf{2-50}$$

and

$$V_t = \Omega r + V_\infty \sin(\alpha_P) \sin(\psi) \quad \textbf{2-51}$$

Equations 2-50 and 2-51 are simplified versions of the helicopter rotor performance equations presented by Leishman [9] for forward flight since the effects of blade flapping and blade flapping displacement (coning) are neglected due to the small diameter of the propellers. Using equations 2-50 and 2-51, α_b is computed as the difference between the pitch angle of the blade element and the inflow angle as follows:

$$\alpha_b = \theta - \varphi \quad \textbf{2-52}$$

where the inflow angle can be calculated using the following expression:

$$\varphi = \text{atan}\left(\frac{V_a}{V_t}\right) = \text{atan}\left(\frac{V_\infty \cos(\alpha_P) + v_i}{\Omega r + V_\infty \sin(\alpha_P)\sin(\psi)}\right) \quad \textbf{2-53}$$

The pitch angle at a particular radial location r is calculated using the fourth order polynomial equation obtained from Figure 3-8(a).

2.3.2 Induced Velocity Calculation

The non-uniform distribution of the induced velocity v_i, over the rotor disk area during forward flight of a helicopter has been addressed in the past through the use of "inflow models", which have been used to approximate the performance of helicopter rotors during forward flight, operating in a rotor angle-of-attack range of approximately $75° \leq \alpha_P < 90°$ during forward flight. An early model developed by Glauert [10] implements a longitudinal distribution of the induced inflow, λ_i, defined as

$$\lambda_i = \frac{v_i}{\Omega R} \tag{2-54}$$

across the rotor disk area, through a weighing factor k_x, such that

$$\lambda_i = \lambda_0 \left(1 + k_x \frac{x_l}{R}\right) \tag{2-55}$$

where λ_0 is the induced inflow ratio in forward flight, as derived by the momentum theory by numerically solving

$$\lambda_0 = \frac{v_i}{\Omega R} = J_t \cot(\alpha_P) + \frac{C_{T,h}}{2\sqrt{J_t^2 + {\lambda_0}^2}} \tag{2-56}$$

where J_t is the tangential advance ratio, based on component of the free stream velocity that flows tangentially to the rotor disk, defined as

$$J_t = \frac{V_\infty \sin(\alpha_P)}{\Omega R} \tag{2-57}$$

It must be noted that in equation 2-57, the value of J_t is calculated using the blade tip speed, complying with the American format used by Leishman [9]. A simple, fixed-point iteration method in MATLAB was used to numerically solve for λ_0 in equation 2-56 with a residual error of 0.05%. A modification of Glauert's model includes an additional variation in the lateral direction (y axis), as presented by Leishman [9], which is shown in equation 2-58 below

$$\lambda_i = \lambda_0 \left(1 + k_x \frac{x_l}{R} + k_y \frac{y_l}{R}\right) = \lambda_0 \left(1 + k_x\, r \cos(\psi) + k_y r \sin(\psi)\right) \tag{2-58}$$

Glauert [10] suggested the values for the weighing factors to be k_x=1.2 and k_y=0. Other studies such as the ones performed by Coleman *et al.* [11], Drees [12], and Pitt and Peters [13] suggest methods of calculating the weighing coefficients k_x and k_y as functions of the wake skew angle, χ, which is the angle between the axis of the ideal helical streamtube of the wake and the rotor's axis of rotation, calculated as

$$\chi = \tan^{-1}\left(\frac{J_t}{J_a{}' + \lambda_i}\right) \tag{2-59}$$

Where J_a' is the inflow advance ratio, based on the component of the free-stream velocity that flows perpendicular to the rotor disk, and it is non-dimensionalized by the tip speed as

$$J_a' = \frac{V_\infty \cos(\alpha_P)}{\Omega R} \quad \textbf{2-60}$$

The k_x and k_y coefficients of the mentioned methods based on the wake skew angle are summarized in Table 2-1, and will be used for comparison in this section. In the case of Drees [12], at $\alpha_P = 0°$ a value of $k_x = 0$ is prescribed. An intensive summary of the inflow models used can be found in a literature survey compiled by Chen [14]. Coleman *et al.* [11] wanted to characterize the longitudinal distribution of the induced velocity, and used vortex theory along with a uniformly loaded disk to develop his model, in which the weighing factor is a function of χ; thus, becoming the first attempt to analytically calculate the weighing coefficients proposed by Glauert [10]. Using a modification of the wake geometry defined by Coleman *et al*. [11], Drees [12] developed a model which aimed to include the azimuthal changes in the bound circulation of the blade elements. Pitt and Peters [13] modified a model previously developed for hovering flight to account for forward flight conditions. Chen [14] claims that Pitt and Peters' model performs relatively well in comparison with the other models mentioned above. The models hereby mentioned are first harmonic models, and their analyses are based on the assumption of a time-averaged behavior of the rotor disk. Chen [14] provides comparisons of Drees' and Pitt and Peters' models with experimental data from a wind tunnel investigation of the downwash of a helicopter by Cheeseman and Haddow [15], where the tests were performed at $\alpha_P \approx 88.25°$ and the rotor radius was 0.675 m. They report that Drees' model deviates from the experimental data by 10% to 16%, while Pitt and Peters' model by 2% to 7%, depending on the operating condition.

Table 2-1: The weighing coefficients for the linear distribution of the induced inflow.

Author(s)	k_x	k_y
Coleman *et al.* [11]	$\tan(\chi/2)$	0
Drees [12]	$(4/3)(1-\cos(\chi)-1.8J_t^2)/\sin(\chi)$	$-2J_t$
Pitt and Peters [13]	$(15\pi/23)\tan(\chi/2)$	0

2.3.3 The influence of tip vortices

Consider the flow over a three-dimensional wing composed of airfoil cross-sections as shown on Figure 2-2(b). The acceleration of the flow on the suction surface of the wing creates the pressure imbalance that generates lift. As a by-product of this pressure imbalance, the flow at the tip of the wing tends to "leak" from the high pressure side to the low pressure side, generating downwash and what is known as the trailing or tip vortices on a wing. This effect is the same for a propeller blade, and has the same results as it does on conventional wings, with the addition of the effects caused by the rotational motion of the propeller. The system of trailing vortices generated by a propeller can be regarded as a confinement of the flow downstream of the propeller, which creates the cylindrical stream tube known as the slipstream. In reality, this slipstream is "contracted" as the vortices travel downstream, however, to take into account the changing size of the trailing vortices is a complex task, and for the purposes of blade element analysis it is neglected [16]. The trailing vortices generated from the tip of a propeller's blade travel in a helical path rather than the rectilinear travel path, found in the vortices generated from an airplane's wings. This helical motion of the vortices induces a change in the axial velocity of the flow field, as well as a rotational velocity component about the axis of rotation of the propeller, and in the same direction as the propeller's rotation.

Within the slipstream cylinder, the velocity at any point is subject to the influence from the entirety of the helical vortex system. Considering the helical path of the vortex system to be a vortex filament of the same shape, the filament sections closer to a certain location within the slipstream will have a stronger influence on the velocity at that particular location. Now consider a location inside of the slipstream, and far downstream from the propeller plane. The velocity at this location will be influenced by the sections of the helical vortex system upstream from the location, as well as downstream of the location. In the other hand, if we consider a point located at the propeller plane, were the helical vortex system is bounded, any point located at the propeller plane will only be influenced by the downstream section of the helical vortex system. For this reason, the induced velocity downstream from the propeller is approximately twice as much as it is on the propeller plane [64].

Ultimately the complex vortex system that is emanated from the blade tips carries a significant amount of kinetic energy relative to the free-stream flow, that represents an energy expenditure

not dedicated to propulsion, and thus the vortex system is a substantial source of energy loses in propeller propulsion systems. By this understanding, one way to approximate the propulsive efficiency of propellers is to consider the ratio of the energy output from the system to the sum of the energy input and the energy of the wake ([17]) as

$$\eta = \frac{E_{input}}{E_{input} + E_{wake}} \qquad \textbf{2-61}$$

2.3.4 Tip Loss Factor

To estimate the effect of the energy losses from flow leakage at the blade tips many approximations have been developed in the past. One of the most renowned methods is the one developed by Prandtl [18]. The effects of tip loss based on the approximation formulated by Prandtl [18] was applied to the analytical results from Glauert [10], Coleman et. al. [11] Dress [12] and Pitt and Peters [13]. The idea behind the formulation from Prandtl [18] is that the tip losses can be accounted for by the introduction of a factor which reduces the effective rotor disk area of the propeller, and thus Prandtl [18] provided that an effective blade radius, R_{eff}, may be calculated as

$$\frac{R_{eff}}{R} = 1 - \left(\frac{1.386}{N}\right) \cdot \frac{\lambda_i}{\sqrt{1 + \lambda_i^2}} \qquad \textbf{2-62}$$

2.3.5 Slipstream Diffusion in the Far Wake

As air passes through the rotor disk plane of a propeller, the slipstream (exit jet flow) is accelerated with respect to the free-stream ambient. An increase in the velocity of the flow yields a drop in static pressure and thus, the effect of the higher free-stream pressure forces the exit jet stream tube to contract. This effect occurs immediately downstream of the propeller ([19]). In the region downstream of the rotor disk plane, viscous effects within the slipstream along with turbulent eddies cause the stream tube of expand again ([19]). This expansion is referred to as the diffusion of the slipstream. Khan *et. al*. [19] illustrates this phenomena in the image shown in Figure 2-3. The wake regions defined in Figure 2-3 have been determined by Stewart *et. al.* [20], in which the region immediately downstream of the rotor disk plane experiences a contraction, followed by a region in the stream-wise direction of length $3.25D_P$ where diffusion begins.

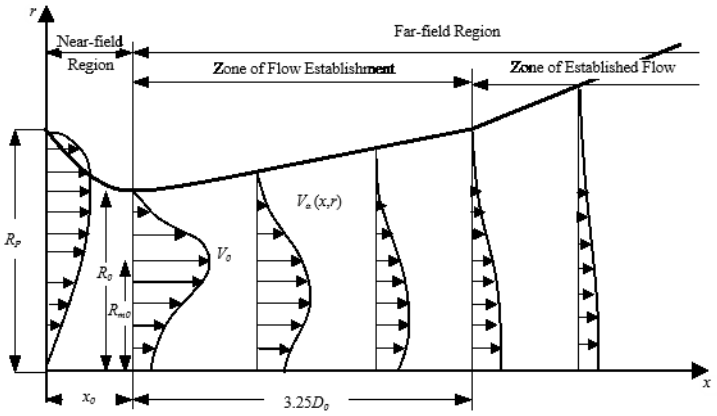

Figure 2-3: Exit jet velocity profile at various downstream locations generated by an open propeller, as illustrated by Khan *et. al.* [19]. The image has been recreated from Khan *et. al.* [19].

2.4 Theoretical Background on Ducted Propellers

Ducted propellers as a mean of propulsion present an alternative to the conventional open propellers and have been considered in many designs in the aeronautical and marine fields in the past. A ducted propeller can potentially increase the thrust output, T, when compared to an open propeller of the same rotor disk area and with the same power input, P. The performance benefits achieved by using a duct around the propeller are due to the manner in which the presence of the duct influences and changes the flow field generated by the propeller's rotational motion, or as stated by McMahon [21]: "the function of the duct is to set the operating point of the rotor". Placing a duct around the propeller decreases the pressure at the leading edge of the duct and consequently allows the rotor disk to draw in more air ([22]) and increase the flow rate through the rotor disk plane. This in turn decreases the effective angle-of-attack of the propeller blades α_b ([22], [23], [24]) as shown in Figure 2-4; thus, offloading the rotor disk, which means reducing the contribution from the propeller to the total thrust of the ducted propeller system. Decreasing the effective angle-of-attack of the blades also increases the advance ratio limit at which the blade would begin to stall. The increased mass flow rate over the leading edge of the duct generates a section of the duct where low pressure suction forces are present, providing the propulsion system with an increment in thrust ([4], [22]).

One of the primary mechanisms through which ducted propellers become advantageous is their potential to reduce the contraction of the exit jet flow observed in open propellers ([4], [22], [23]), caused by the increase in the kinetic energy of the flow when it crosses the rotor disk plane. Momentum theory along with the disk actuator model predict that the increase in the wake velocity of an open propeller v_j is twice the induced velocity of the flow at the rotor disk plane v_i;

$$v_j = 2v_i \tag{2-63}$$

thus, due to the principle of mass conservation, the cross-sectional area of the exit jet A_j, must be ½ of that at the rotor disk. In the case of the ducted propeller, the exit jet area is dictated by the geometry of the duct ([4], [24]), and if the flow is able to remain attached to the internal surface of the duct, the exit jet area may even increase with respect to the rotor disk area, resulting in a decrease in the exit jet velocity and thus, a decrease in the energy expenditure required to produce thrust ([4], [25]). This concept is illustrated in Figure 2-4. Momentum theory predicts that the ratio σ in axial (or vertical climb) is obtained through the following expression

$$\sigma = \frac{(V_\infty + v_i)}{(V_\infty + v_j)}\,. \tag{2-64}$$

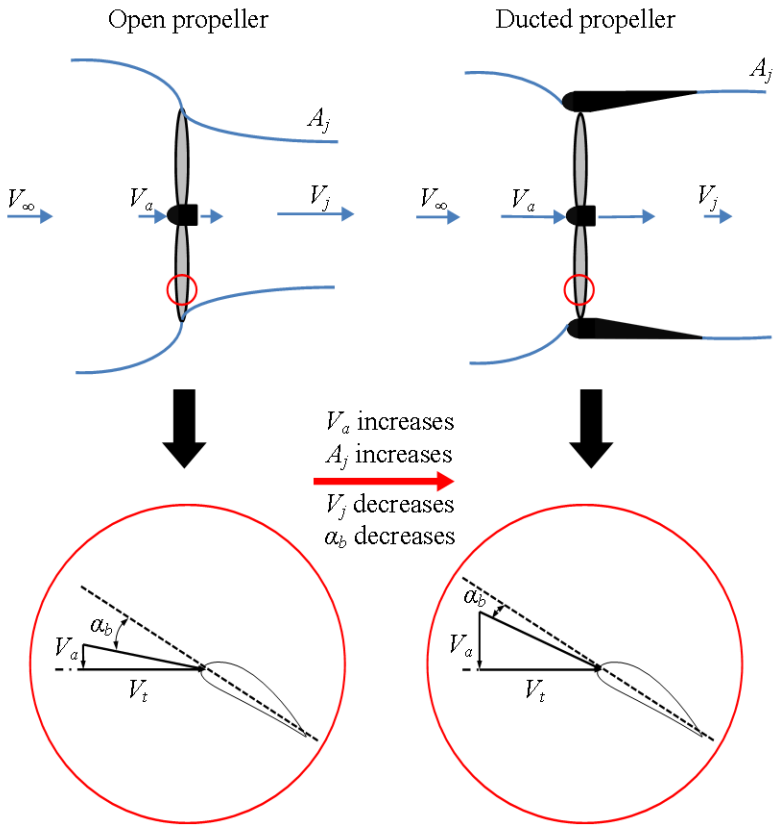

Figure 2-4: The schematic provides an explanation of the effects of using a duct around a propeller. The left case indicates the open propeller, and the right case is the ducted propeller. The figure illustrates that the implementation of the duct accelerates the inlet flow V_a at the rotor disk plane resulting in a reduction of α_b, and reduces the exit jet velocity V_j by increasing A_j.

The placement of a duct around the propeller imposes a physical barrier that helps in the mitigation of the effects from the three-dimensional tip vortices emanated from the flow leaking at the blade tips as it was previously discussed ([21], [26], [27]). Therefore, reducing the amount of energy that is wasted through the generation of these vortices, and permitting the propeller blades to be loaded even more towards the blade tips, improving the efficiency of the propeller. In addition to the performance benefits, using a ducted propeller can attenuate the noise emanated from the open rotor ([4], [28]), and serves as a safety feature by protecting personnel operating near the vicinity of the rotor, as well as the equipment itself ([4]).

The benefits of ducted propellers are well known when the system is operating at the hover condition where theoretically, momentum theory predicts that a ducted propeller with $\sigma = 1$ in hover can potentially increase the thrust output by 26% when compared to an open propeller of

the same size and same power consumption. However, in axial and forward flight, the benefits of the duct may diminish as the free stream velocity increases. One reason for this loss in performance is due to the decreased ability of the duct to reduce the slipstream contraction. As the free stream velocity increases the contraction of the slipstream from open propellers diminishes, and the ducted propellers lose their ability to accelerate the flow and decrease the contraction of the slipstream.

In addition to this loss in performance, the benefits achieved by using a duct come with the complication of the weight addition by the duct which reduces the payload of the aircraft, the drag created by the duct, and the increment in structural complexity of the aircraft. Therefore, the majority of the applications that use ducted propellers have been dedicated to improve the hovering flight conditions, but scarce efforts have been made to enhance the performance of ducted propellers in axial or climbing flight.

2.5 Previous Investigations on the Performance of Ducted Propellers

In this section, a review of the most relevant studies on ducted propellers is presented, beginning by the earliest studies corresponding to large scale ducted propeller applications, and finishing with the latest studies on ducted propellers for UAVs and MAVs. Several investigations performed parametric studies on the geometry of the duct, for which some common variables were used such as duct chord length c_D, leading edge radius r_{LE}, internal duct diameter or throat diameter D, diffuser angle θ_D and duct thickness t, and are defined in Figure 2-5 below.

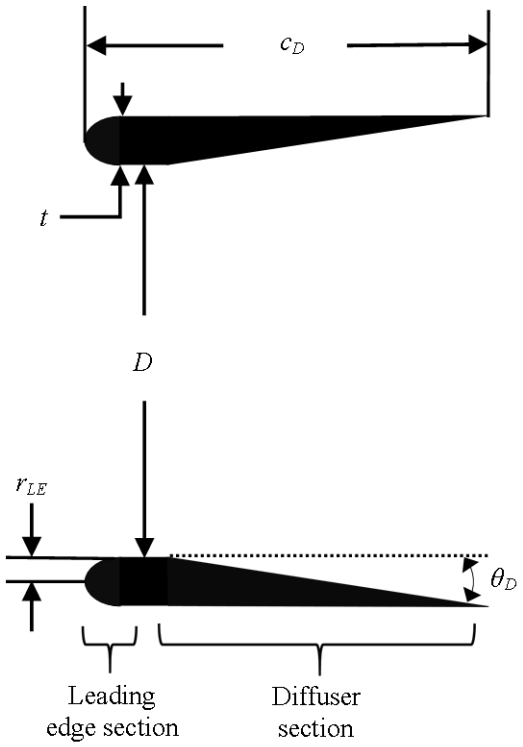

Figure 2-5: Definition of the most common geometric parameters used in the design of ducts, these include the leading edge radius r_{LE}, the diffuser angle θ_D, the duct chord length c_D, internal duct diameter D and duct thickness t.

The earliest account for experimental work on ducted propellers for aeronautical purposes was done by Stipa [6] in the early 1930's. Stipa [6] referred to the duct-propeller combination as the "intubed propeller". In his investigation, Stipa [6] studied three duct models, shown in Figure 2-6, in which he varied the cross-sectional geometry of the ducts. The first model was shaped as a Venturi-type nozzle, the second model maintained the same external profile, but changed the internal shape to have a straight contraction section rather than curved, and the third model altered the internal and external shapes of the duct. The three ducts had a constant duct chord length of c_D = 1.5 m. The internal diameter at the section of maximum contraction was not reported, however, it is indicated in Figure 2-6 that the distance between the chordlines of the top and bottom cross-section of the ducts was 520 mm. Stipa [6] used two types of propellers for his investigation, a CR-20 propeller and an S-59 propeller. The CR-20 propeller had a pitch of 0.472 m/rev and nominal diameter of 0.48 m, and the S-59 propeller had a pitch of 0.41 m/rev and a nominal diameter of 0.5205 m.

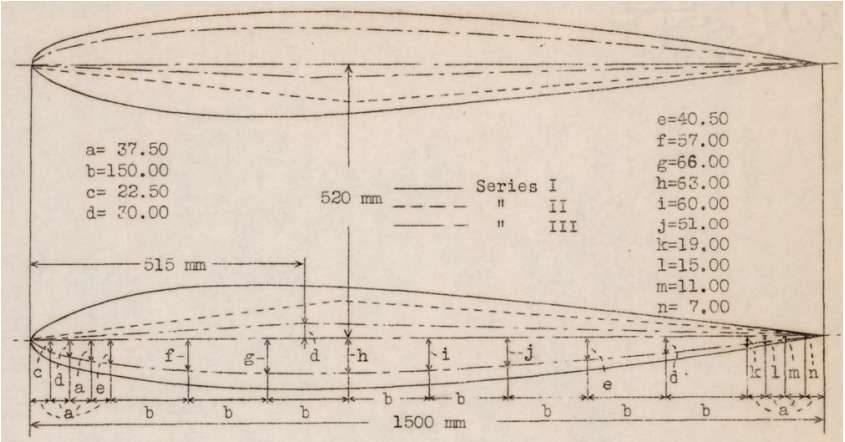

Figure 2-6: Duct models tested by Stipa [6]**. Series I features a Venturi-type cross section, Series II maintains the same external surface geometry, but has a straight contraction internally. Series III changes the contraction slope, as well as the external surface. Image obtained from Stipa** [6]**, publicly available through the NASA Technical Reports Server: https://ntrs.nasa.gov/search.jsp?R=19930094761**

Stipa's experiments were carried out in a wind tunnel with a circular cross section, equipped with an external balance. Static tests were carried out at propeller rotational speeds of 1800 to 5000 RPM. Axial flow tests were performed at free stream velocities of V_∞ =15 m/s and 20 m/s, with propeller rotational speeds ranging from 3000 RPM to 5200 RPM, which corresponds to a J range of 0.46 to 0.78. For all the configurations tested, Stipa [6] compared the values of thrust, power consumption, thrust-to-power ratio, and drag force. In Stipa's tests, the propeller was not located inside the duct, or at the location of highest contraction, rather, it was positioned upstream from the duct. In this manner, Stipa [6] performed three types of test, one in which the propeller was isolated, a second in which the duct was placed downstream of the propeller so as to have the propeller "in presence" of a duct, and a third one in which the duct and propeller were rigidly attached, so as to have the propeller and duct "integrated". For all tests, the propeller "in presence" of the duct tests exhibited higher propulsive efficiencies than the propeller alone at all advance ratios tested. However, for the free stream tests, the propeller "in presence" of a duct generated high coefficients of thrust than the propeller alone, but only for the lower advance ratios tested. Stipa's experiments were the cornerstone of ducted propeller investigations for large scale

applications, and provided the earliest accounts of experimental data suggesting the performance benefits of ducted propellers.

Another work on large scale ducted propellers was performed by Platt Jr [23], who carried out static tests (V_∞ = 0 m/s) on three 1.2 m diameter ducted propeller systems, as well as on an isolated propeller. The three ducts tested were named "Short Cruise" (c_D =0.82 m, σ =1.1, θ_D =7°), "Short Take Off" (c_D =0.82 m, σ =1.3, θ_D =22.4°) and "Long Take Off" (c_D =1.02 m, σ =1.3, θ_D =14.4°), due to their respective intended purposes. Platt [23] used an elliptical geometry to manufacture the leading edge of the ducts. The blade tip clearance, δ_{tip}, which is the clearance between the propeller blade tips and the internal surface of the duct was 1.59 mm. Two high-solidity, dual rotating propellers were used for all the tests. The tests were performed at blade collective angles ranging from 35° to 45° for the ducted configurations, and from 15° to 40° for the isolated propeller test. With the use of a dynamometer, electrical strain gauges, and a multiple tube manometer, Platt [23] obtained readings of torque, thrust, and pressure measurements on the internal and external surfaces of the duct. Figure 2-7 shows a schematic of the test setup used by Platt [23] in his experiments.

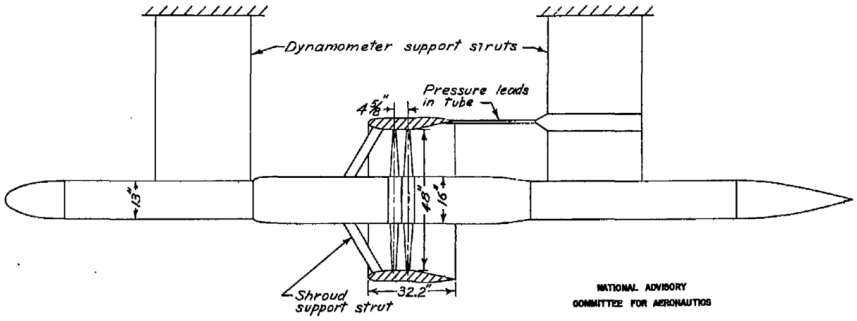

Figure 2-7: Schematic of Robert J. Platt's (1948) experimental setup. Image obtained from Platt [23], **publicly available through the NASA Technical Reports Server: https://ntrs.nasa.gov/search.jsp?R=19930085700**

Tests were performed up to a maximum blade tip Mach number of 0.7. Platt's experiments showed that for the same power consumption value, the ducted propeller produced approximately two times as much static thrust in comparison with the open propeller, as shown in Figure 2-8. Platt

[23] attributed this behavior to the fact that with an increase in the mass flow rate through the propeller plane, for the case of the ducted propeller, the local effective angle-of-attack of the propeller blades, α_b, was reduced and therefore, it could operate at a higher blade tip Mach numbers without stalling. He also concluded that part of the duct's contribution to the thrust generation is due to a low pressure and high velocity region created at the leading edge of the duct. Platt [23] determined that the effect of changing the duct's c_D as well as θ_D had negligible effects on the performance of the system; however, he noted that these conclusions would not be valid for shorter duct chords.

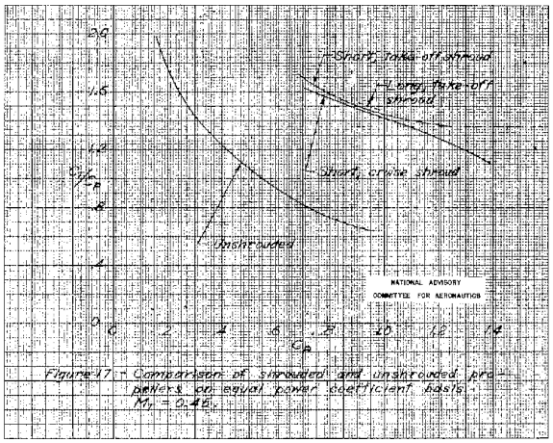

Figure 2-8: The C_T/C_P ratio comparison between the ducted an open propeller done by Platt [23]**, as a function of C_P. In the graph it can be observed that for all C_P values, the ducted propeller performs at a higher C_T/C_P value than the open propeller. Image obtained from Platt** [23]**, publicly available through the NASA Technical Reports Server: https://ntrs.nasa.gov/search.jsp?R=19930085700**

Prior to the implementation of ducted propellers for aeronautical purposes, this technology was most commonly used for marine applications. A significant contribution to the development of ducted propellers was done in the Netherlands Ship Model Basin (NSMB) by Van Manen and Oosterveld [29]. One of the works by Van Manen and Oosterveld [29] investigated the performance of five diverging ducts (diverging ducts slow down the flow incident to the rotor disk plane, rather than accelerating it), to investigate their ability to mitigate cavitation effects on the propeller blades. The investigation consisted of an analytical portion, in which momentum theory and vortex theory were implemented in a computer software, to numerically determine the geometry of the duct; and an experimental portion, in which the performance of three of the ducts was investigated in a 90 cm × 90 cm cavitation water channel. The main difference between the

five ducts investigated was the shape of the camber line. The method presented by Van Manen and Oosterveld [29] provided a design methodology for the cross-sectional area or the ducts, in which the camber line was a function of the strength of the vortices along the duct surface, the ratio between the vortex strength at the rotor disk plane and the advance ratio, and the geometry of the system. All of the five ducts investigated had a thickness distribution along the chord direction based on the NACA 0015 airfoil, a clearance of δ_{tip} = 1 mm, and used Kaplan type propellers. The ducts chosen for the experiments were designed to operate at the same C_T for similar flow rates, but at different propeller thrust-to-total thrust ratios. Each of the three ducts was tested with 5 different propellers, which varied only in the nominal pitch value, and had a diameter of D_P = 240 mm. The experiments were carried out at advance ratios ranging from 0 to 2. Torque and thrust readings on the duct were obtained using strain gauges. The results from the investigation showed that with an increasing ratio of propeller thrust-to-total thrust, the propulsive efficiency of the system decreased, and that this effect was less severe for lightly loaded systems (low T/A). The experiment also confirmed that for diverging ducts, the thrust component generated by the duct itself is negative (opposite to the direction of travel).

On a later publication, Van Manen and Oosterveld [24] presented a summary of the experimental work done regarding ducted propellers at the NSMB, as well as a summarized theoretical analysis of the performance of ducted propellers. In this work, Van Manen and Oosterveld [24] mention several important claims regarding the design and operation of ducts. They highlighted the fact that a duct surrounding a propeller will provide a negative or positive contribution of thrust, depending on the operating condition defined by J. They also convey that a converging or flow accelerating duct is beneficial in cases where the propeller is subject to high loading (T/A), and that in comparison to the case of an open propeller, the forces acting on the duct are strongly dependent on the slipstream contraction of the flow in the wake region of the propeller, as well as on the geometry of the duct. Regarding the design of the ducts, Van Manen and Oosterveld [24] highlight that the selection of a specific duct geometry and length depends on the requirements of efficiency, concerns regarding flow separation, cavitation, and structural support; and that in the perspective of efficiency, a maximum contraction of the duct at the location of the propeller is desired for optimal operation. The experimental results presented in this paper include tests performed on ducts which varied in c_D/D ratios from 0.3 to 0.83, θ_D from 10.2° to 15.2°, and had cross-sectional areas which consisted of NACA airfoils 4415, 5415, and 3415. The main

conclusion from the experiments performed on these ducted propeller systems was that the optimal propeller diameter (in regards to propulsive efficiency) was significantly smaller in the ducted systems when compared to the open propeller cases. In addition to the ducts previously mentioned, three improved duct models shown in Figure 2-9 were tested, which featured a straight cylindrical internal surface at the location of the propeller, a diffuser portion downstream of the propeller location, and a maximum t/c_D ratio of 0.15. A diffuser angle of 10° was used for these designs. It was noted that the cross-sectional geometry of these ducts had close resemblance to a NACA 25015 profile. The c_D/D ratio used in these ducts was 0.5.

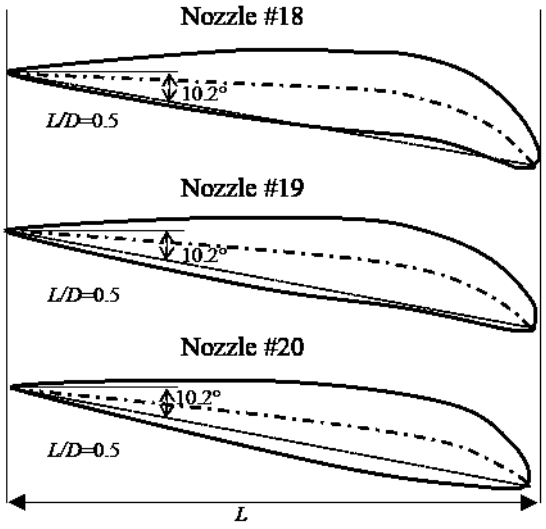

Figure 2-9: The cross-sections of the improved duct models designed and tested by Van Manen and Oosterveld [24]**, recreated from Fig. 18 in Van Manen and Oosterveld** [24]**.**

In addition to varying the duct shapes, Van Manen and Oosterveld [24] also investigated the influence of varying the propeller type. From the theoretical investigation of the improved ducts with a Kaplan propeller, it was determined that a propeller thrust-to-total thrust ratio of 0.7 is recommended for ducts with a c_D/D ratio of 0.5. Through the experimental tests, it was concluded that the c_D/D ratio of 0.5 provided good efficiency results, and was not significantly underwhelmed by ducts with c_D/D>0.5.

The rising interest for VTOL vehicles in the 1950's inspired multiple investigations in the topic of ducted propellers for this particular application. These vehicles offer several attractive characteristics such as transportability, the ability to hover at a specific location, greater thrust

generation for a smaller aircraft size (downsizing), and protection from impact with the rotating blades. With the implementation of ducted propellers on these vehicles, the energy expenditure was meant to be reduced and the operational safety increased. This led to multiple investigations on the performance of ducted propeller for their application in small scale aircrafts.

One of the earliest accounted works on small scale ducted propellers was done by Kruger [30], who performed an experimental investigation on such systems to determine the range of applicability of ducted propellers. For this purpose Kruger [30] tested 15 different duct models shown in Figure 2-10(a), which differed in chord length, thickness, angle of incidence of the leading edge and camber. Included in the 15 duct models Kruger [30] investigated the use of flow accelerating and decelerating ducts, where the location of the propeller was not always positioned at the location of maximum contraction, as shown in Figure 2-10(a). Two propeller types were used which differed mostly in angular twist and cross-sectional blade geometry. The propellers had a nominal diameter of $D_P = 240$ mm, 8 blades, and a hub-to-propeller diameter ratio of $D_h/D_P = 0.35$. Kruger's experimental setup shown in Figure 2-10(b), featured an elliptical nacelle (or propeller hub), and exit stator vanes which were attached to the duct itself. In the investigation Kruger [30] obtained measurements of the propeller thrust and torque, duct thrust and drag forces, pressure distributions over the nacelle and the duct's external and internal surfaces, as well as the distribution of the axial velocity passing through the rotor disk along the radial direction of the blades.

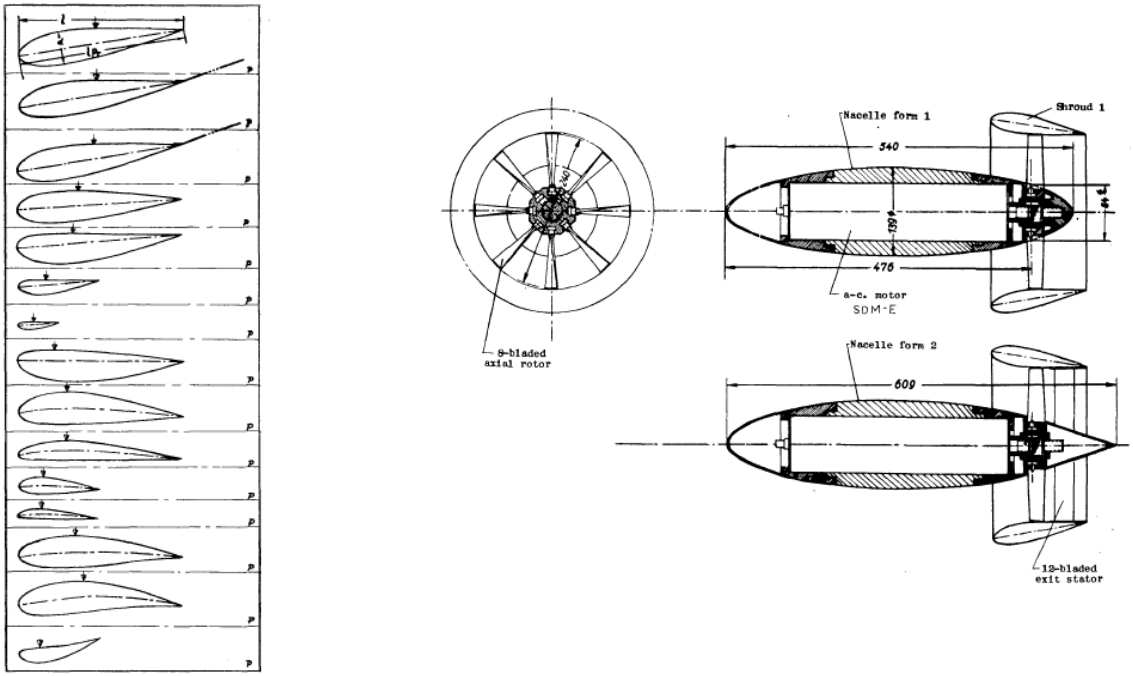

(a) (b)

Figure 2-10: In (a), diagram of the various duct shapes tested by Kruger [30]**. In the diagrams, the down oriented arrow indicates the location of the propeller, and the relative sizes of each model are drawn to scale. In (b), the experimental setup of Kruger** [30]**, in which the nacelle, duct, rotor disk and stator vanes can be observed. Images obtained from Kruger** [30]**, publicly available through the NASA Technical Reports Server: https://ntrs.nasa.gov/search.jsp?R=20050241797**

Kruger [30] noted that the use of the nacelle resulted in an increase of the net propulsive force when using a flow decelerating duct, and a decrease of propulsion when using a flow accelerating duct. Measurements of the inlet axial velocity along the radial distance from the hub *r* were performed with and without the propeller operating, as well as with the propeller alone, and in all cases, the results showed that an increase in the axial velocity was observed with increasing *r*. An example of these results is shown in Figure 2-11(a). Kruger [30] also concluded that changes in the propeller loading did not affect the distribution of the axial velocity distribution over the rotor disk plane. For brevity, Kruger [30] presents in his work the ducted propeller results for two of the configurations tested only. Kruger's findings show that in the ducted propeller system, the duct takes on a significant portion of the thrust, especially at the low free-stream advance ratio regime and static conditions, as shown in Figure 2-11(b). Kruger [30] also performed measurements of the ducted propeller's performance using propellers of various nominal pitch values as well, which were characterized by the blade angle at the tip of the blade. Blades with a blade tip angle ranging

from 15° to 55° were used. From these tests, Kruger [30] was able to determine that the use of the duct around the propeller allowed the blades to offer a "still sound" performance at blade angles that without the presence of the duct would have otherwise stalled.

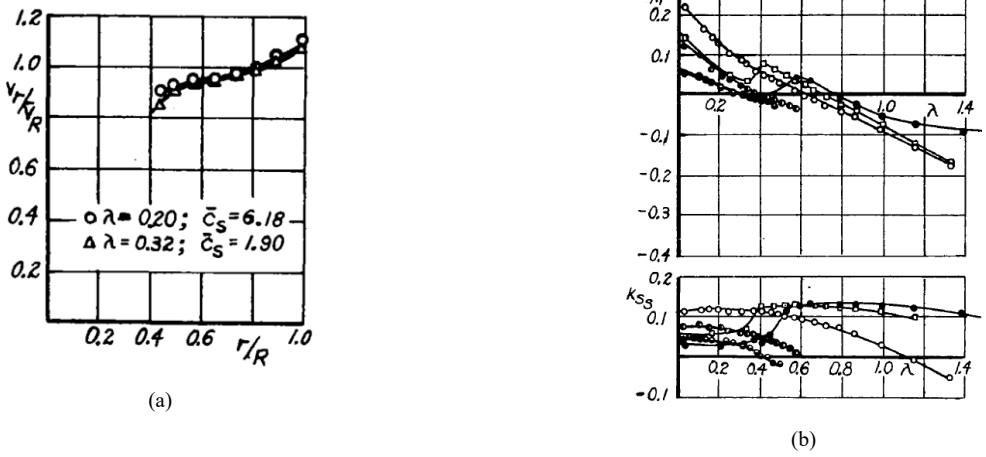

(a) (b)

Figure 2-11: In (a), the axial velocity distribution at the rotor disk plane, as a function of the radial distance from the hub, as measured by Kruger [30]**. In (b), the coefficient of duct thrust K_{SM} and the coefficient of propeller thrust K_{SS} as a function of the free-stream advance ratio measured by Kruger** [30]**. The figure shows that the duct provides a portion of the total thrust up to an advance ratio of approximately 0.8. Images obtained from Kruger** [30]**, publicly available through the NASA Technical Reports Server: https://ntrs.nasa.gov/search.jsp?R=20050241797**

Gamse & Mort [31] performed a study on a 2.13 m internal diameter ducted propeller system shown in Figure 2-12(a), which is based on the system used in the Bell Aerosystems Co. X-22A aircraft shown in Figure 1-1(b). The objective of the investigation was to characterize the aerodynamic performance of the system by evaluating measurements of thrust and propulsive efficiency, examine the effects of implementing an exit vane, and determine the flow separation limits for the upstream and downstream regions of the duct when it becomes subject to a rotor disk angle-of-attack α_P, greater than 0°. The maximum external diameter of the duct was 2.58 m, and the chord length was c_D = 1.2 m. The duct had an area ratio of σ = 1.1. A 3 bladed propeller was used, and was located at the 0.29c_D location, with δ_{tip} = 10.16 mm. The exit vane used shown in Figure 2-12(b), had a thickness of 134.6 mm, and was hinged at the 0.85c_D location. Pressure orifices were available along the internal and external surfaces of the duct. To measure the aerodynamic loads on the system, a six-component force balance was used.

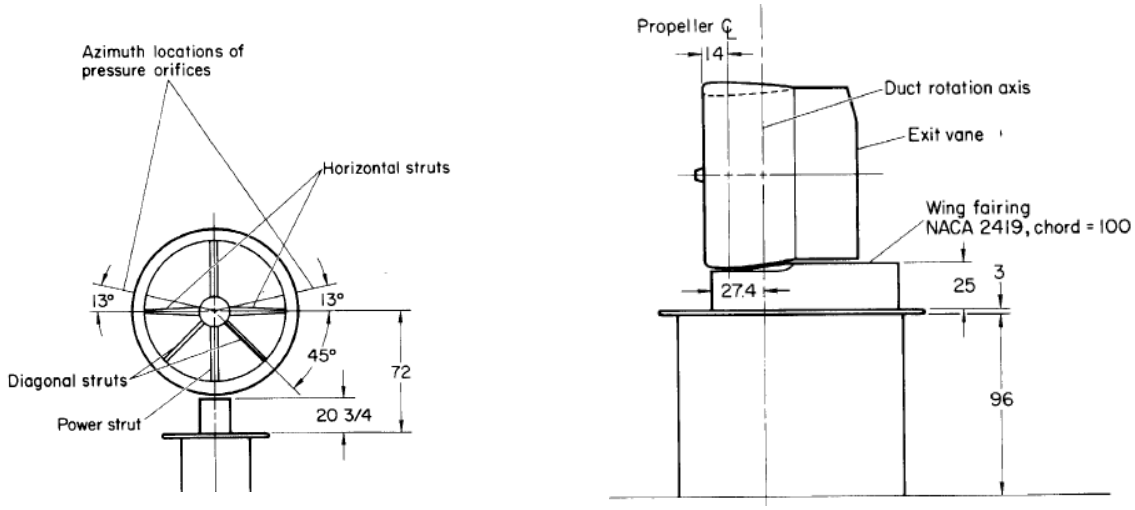

(a) (b)

Figure 2-12: In (a), front view of the experimental setup used by Gamse and Mort [31]**. The ducted propeller system is mounted on an airfoil-shaped support structure. In (b). side view of the ducted propeller system, revealing the exit vane used by Gamse and Mort** [31]**. Images obtained from Gamse and Mort** [31]**, publicly available through the NASA Technical Reports Server: https://ntrs.nasa.gov/search.jsp?R=19670025554**

The results obtained by Gamse and Mort [31] showed that the use of the exit vane resulted in improvements of the static and propulsive efficiency, while C_P remained constant with the use of the vane, and C_T decreased without the presence of the vane. Results for the propulsive efficiency are presented up to a free stream advance ratio of $J = 1.8$, and it was concluded that with increasing blade pitch angle, the advance ratio corresponding to the maximum propulsive efficiency increases. The maximum *FM* achieved in the static condition was 81%, and the maximum propulsive efficiency was $\eta = 74\%$. Gamse and Mort [31] indicated that the propulsive efficiency of the system had room for improvement, given that the support structure for the duct and the central hub of the propeller were not designed for flight at high advance ratios. A comparison between the experimental thrust results and the theoretical prediction showed that significant deviation between the two methods were observable at free stream velocities higher than 50 m/s. The theoretical model used to compare the experimental data obtained for thrust was based on the simple momentum theory, shown in equation 2-65, with the assumption of zero duct drag, and that 90% of the input power was delivered to the airstream.

$$T = \rho A_j \left(V_j^2 - V_\infty V_j \right) \qquad \textbf{2-65}$$

Using the pressure ports located in the internal and external surfaces of the duct, Gamse and Mort [31] obtained the location of the onset of separation within the duct, when the ducted propeller system was positioned at a non-zero α_P. Flow separation over the internal surface of the duct was monitored on both the upstream and downstream inlet sections, as defined in Figure 2-13(a). These tests were performed on the 2.13 m internal diameter model and a 1/5 scaled down model. The performance data shown in Figure 2-13(b) demonstrated that at the onset of flow separation, the performance of the system is not significantly affected; however, when separation occurs in 100% of the internal surface of the upstream leading edge, the performance becomes significantly affected. A comparison between the results obtained with the 2.13 m and the 1/5 scaled down model showed that for the same C_T, the α_P value at which 100% of the upstream leading edge was subject to flow separation was approximately 38% lower for the 1/5 scaled-down model. Gamse and Mort [31] concluded that there is a strong scaling effect, and that there is a critical r_{LE} above which the delay of separation is no longer evident, and below which the flow will separate at a lower α_P value.

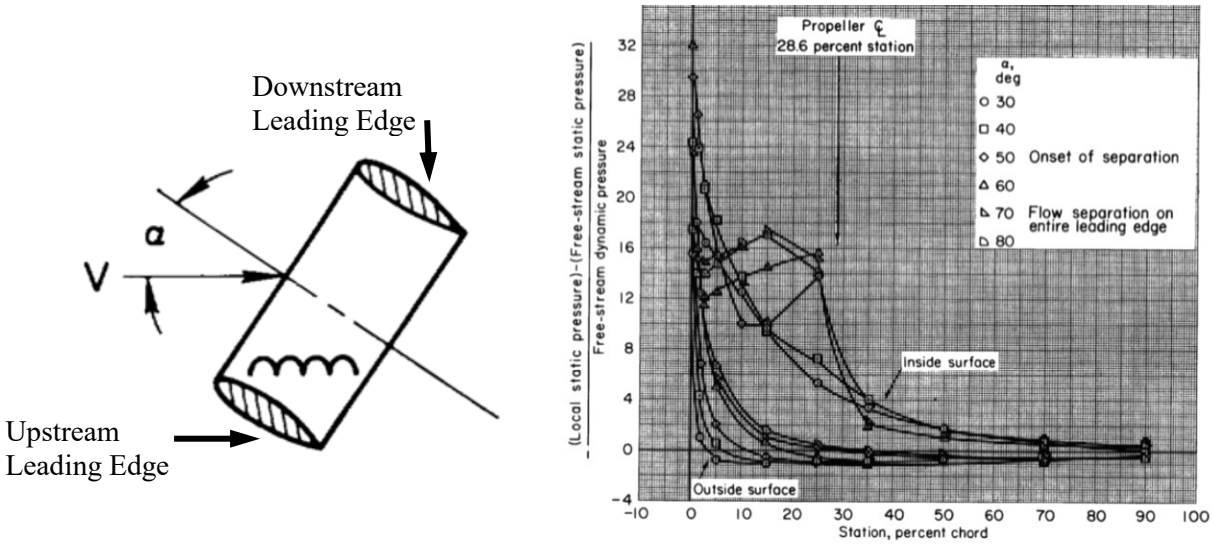

(a) (b)

Figure 2-13: In (a), schematic of a ducted propeller operating at a non-zero α used by Gamse and Mort [31] **to define the upstream and downstream leading edges. In (b), pressure distribution over the internal surface of the upstream leading edge of the 2.13 m diameter duct, with n=1806 RPM, β=19° and 1/C_T=5. Images obtained from Gamse and Mort** [31]**, publicly available through the NASA Technical Reports Server: https://ntrs.nasa.gov/search.jsp?R=19670025554**

Parlett [32] investigated the performance of a ducted propeller at static and non-uniform inlet flow conditions. The ducted propeller model used by Parlett [32] had an internal diameter of $D = 457.2$ mm, a duct length of $c_D = 311.15$ mm, a two-bladed propeller located at the $0.5c_D$ location, and $\delta_{tip} = 1.52$ mm. A straight cylindrical internal surface was used, with a wall thickness of $t = 12.7$ mm. In the static condition, the effect of changing the leading edge radius of the duct was investigated, by varying r_{LE} between 12.7 mm to 76.2 mm. The static tests were performed by varying the rotational velocity of the propeller from 6000 RPM to 10,500 RPM. The thickness of the duct was maintained constant through the changes in r_{LE}, and thus, the duct models were shaped as shown in Figure 2-14.

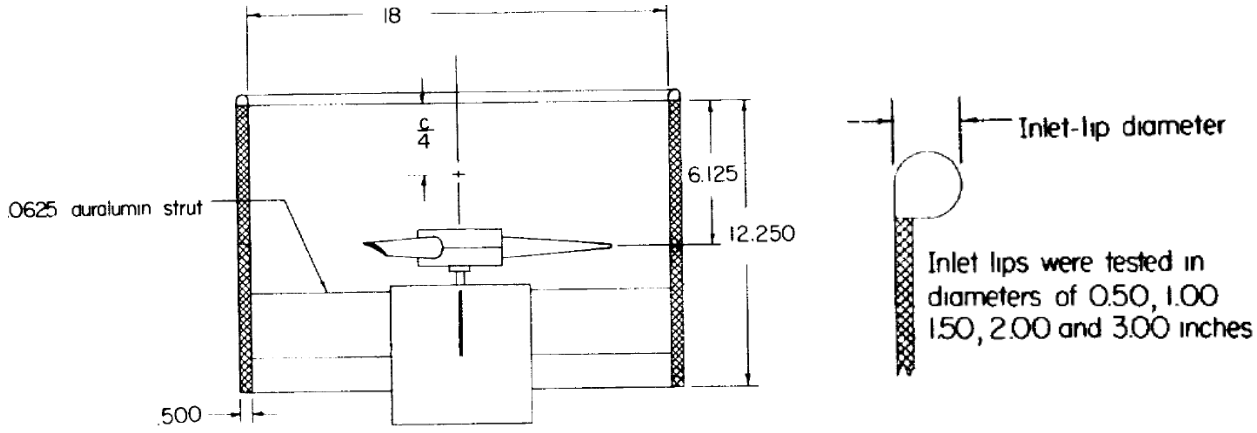

(a) (b)

Figure 2-14: In (a), the cross-sectional model of the ducted propeller used by Parlett [32] **for the investigation. The duct featured a straight cylinder structure (no diffuser). In (b), the definition of the leading edge radius variations used by Parlett** [32] **is shown. With a constant duct thickness, increments in r_{LE} resulted in the leading edge extruding outwards. Images obtained from Parlett** [32]**, publicly available through the NASA Technical Reports Server: https://ntrs.nasa.gov/search.jsp?R=19930084303**

Parlett [32] concluded from his static tests that the static efficiency of the ducted propeller system increased with increasing r_{LE}, as shown in Figure 2-15. To investigate the effect of non-uniform inlet flow, Parlett [32] performed tests at angles-of-attack ranging from 0° to 90°. For the tests with $\alpha_P > 0°$, a leading edge radius of 12.7 mm was used. This experiments provided the conclusion that with increasing α_P, both the drag and thrust generation of the ducted propeller

system increased, for all the advance ratios investigated. Pitching moment results demonstrated a similar trend, but exhibited a maximum value at an advance ratio of approximately J=0.13.

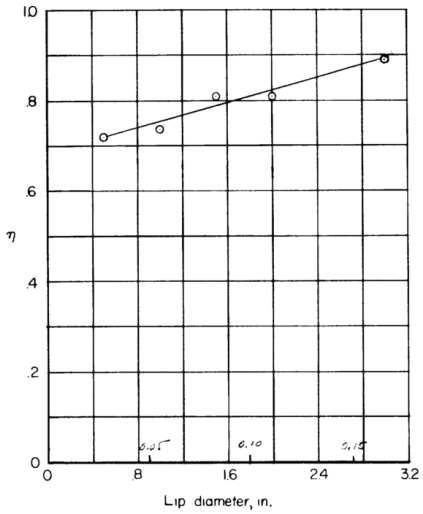

Figure 2-15: Variation of static efficiency as a function of the leading edge radius obtained by Parlett [32]**. The results indicate that the static efficiency of the ducted propeller system increased with increasing r_{LE}. Image obtained from Parlett** [32]**, publicly available through the NASA Technical Reports Server: https://ntrs.nasa.gov/search.jsp?R=19930084303**

An interesting study was conducted by Fletcher [33], in which the aerodynamic properties of five annular airfoils (ducts) without any propellers, at various angles-of-attack were investigated. The five duct models studied differed in aspect ratio, which Fletcher [33] defined as the ratio of the diameter of the duct to the cord length of the duct (c_D/D). The aspect ratios investigated were 1/3, 2/3, 1, 3, and 3.2. All five duct models were manufactured from mahogany laminates, and had the cross sectional geometry of a Clark Y airfoil, with a maximum t/c_D = 0.117. A schematic of the 5 ducts used by Fletcher [33] is shown in Figure 2-16. The investigation was conducted in a 1.8 m × 1.8 m wind tunnel, in which a six-component electromechanical balance was used to measure aerodynamic forces and moments. As a mean of flow visualization, tufts were used to obtain images of the flow field. The tests were performed at a Mach number of Ma = 0.13, which corresponds to a Reynold's number range, based on the chord length of the ducts, of $70.4\times10^4 < Re < 211\times10^4$. The α_P value was varied from -4° to 90°.

Fletcher [33] presented his results in the form of plots of C_L, C_D and C_M as a function of α_P. Pitching moment data showed that for all the ducts tested, except for the duct with an aspect ratio of 1/3, the center of pressure remained at a constant location through the tests performed at angles-of-attack for which the duct was unstalled. Fletcher [33] showed that by increasing aspect ratio of the ducts, the aerodynamic center shifted towards the trailing edge.

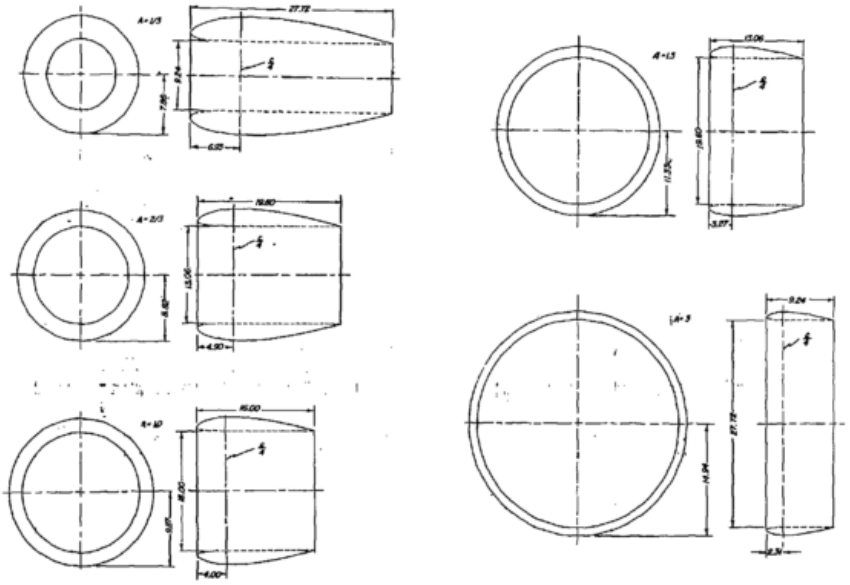

Figure 2-16: Drawings of the duct models tested by Fletcher [33]**. Image obtained from Fletcher** [33]**, publicly available through the NASA Technical Reports Server: https://ntrs.nasa.gov/search.jsp?R=19930084906**

Curves of C_L as a function of α_P showed that the results were similar to those of fixed wings at angle-of-attack values of α >35°. Form the C_D results obtained, Fletcher [33] concluded that the induced drag coefficient of the ducts was one-half of the induced drag coefficient of an elliptical airfoil. Through the use of tufts, the flow field in the wake region of the ducts was visualized, and it was observed that such a flow field shared similarities with the wake of a low aspect ratio or highly swept airfoil.

A parametric study on the design parameters of ducts for ducted propeller systems was performed by Taylor [34], where the effects of changing the duct's r_{LE}, c_D and θ_D on the static performance of the system was investigated. These tests were done using a 406.4 mm internal diameter duct. Taylor's test matrix is summarized in Table 2-2. Taylor [34] was able to test each design variable by manufacturing a laminated mahogany ducts with interchangeable parts, which could be

assembled in multiple combinations. By changing r_{LE}, Taylor [34] found that significant deficiencies in the static efficiency of the system were obtained when a leading edge radius lower than $0.06D$ was used. This was attributed to the enhancement of flow separation in the internal surface of the duct by the small r_{LE}.

Table 2-2: Experimental parameters used by Taylor [34] **in his investigation.**

Parameter	Value
r_{LE}	0 to $0.125D_P$
Duct length ahead of propeller	0 and $0.25D_P$
Duct length behind propeller	0.03D to $1.03D_P$
δ_{tip}	1/16 in
θ_D	0°, 7°, 14°
Blade collective angle	12°-32°
Blade Airfoil	Clark-Y

Taylor [34] also noted from his experiments that even when using a blunt leading edge (r_{LE}/D=0), the duct still generated approximately 30% of the total thrust produced by the system. To characterize the effect of changing the diffuser angle, Taylor [34] presents some of the data as a function of σ. Through this experiment, it was concluded that with increasing σ, the static efficiency of the ducted propeller decreased, as shown in Figure 2-17(a), while the total thrust achieved showed significant increase over open propellers as shown in Figure 2-17(b). In addition to an increase in static thrust, Taylor [34] also found that the contribution to the total thrust from the propeller decreased with increasing σ (offloading). Taylor's results showed the ducted propellers exhibited an increase in maximum static thrust efficiency of approximately 10% when compared to open propellers. The investigation also determined that variations in the blade's relative location within the duct, and the duct's chord length have negligible effects on the performance of the system.

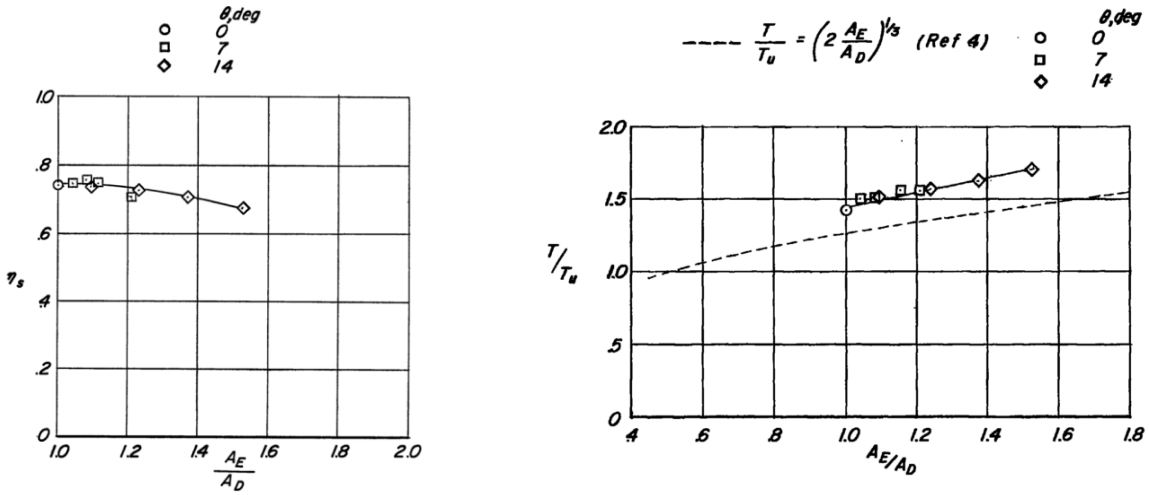

(a) (b)

Figure 2-17: In (a), the static efficiency as a function the area ratio σ, for ducts with diffuser angles 0°, 7° and 14° found by Taylor [34]**. In (b), the ratio of ducted propeller to open propeller thrust as a function of σ, for ducts with diffuser angles 0°, 7° and 14° found by Taylor** [34]**. Images obtained from Taylor** [34]**, publicly available through the NASA Technical Reports Server: https://ntrs.nasa.gov/search.jsp?R=19930084866**

A report compiled by the Hiller Aircraft Corporation [35] presented the results of an extensive study on the performance of ducted propellers, in which 84 different configurations were investigated, where the nominal internal diameter of the ducts ranged between 183 mm to 1.68 m. In the investigation, performance charts were developed for the ducted propeller systems in hover (static), axial flow, and forward flight operating regimes. The duct design parameters tested in the investigation were c_D/D ratio, t/c_D ratio, profile camber, leading edge radius, θ_D, δ_{tip}, chordwise location of maximum thickness, and angular chordline orientation relative to the axis of rotation. In regards to the propeller, the study investigated the effects of propeller solidity, average pitch setting, blade form, blade twist, and cross sectional geometry. Other parameters tested were the hub diameter-to-propeller diameter ratio, hub shape, and the propeller location within the duct. The report also includes a two-dimensional theoretical analysis of the duct performance. The results from the static condition tests revealed that the maximum figure of merit recorded was 1.4 and was achieved by a duct with a diffuser section of unspecified θ_D, and an external duct diameter-to-propeller diameter of 1.6. Also from the static tests, it was concluded that the ducts with higher external diameter-to-propeller diameter ratios resulted in higher *FM*; and ducts with low ratios would sometimes yield lower *FM* values than the open propellers. The axial flow tests were conducted up to a maximum advance ratio of $J = 0.8$. Propulsive efficiency results in this condition

demonstrated that ducted propellers showed superior performance with respect to open propellers up to an advance ratio of $J = 0.4$. The efficiency loss for higher advance ratios was attributed to the increased drag force generated by the duct. By comparing the results between ducts with a straight cylindrical internal surface, and ducts with a diffuser section at the exit, it was found that an increase in the propulsive efficiency of approximately 17% was achieved through the use of a diffuser section. It was also determined that the maximum propulsive efficiency was obtained at the advance ratio range $0.4 < J < 0.5$, where the duct was providing negative thrust to the system. By changing the angle-of-attack of the duct, the condition of non-uniform inlet flow was also investigated. In addition to the performance measurements obtained, wake visualization experiments were also conducted, with the difference that these were carried out in a water tank. With the use of food color dye and a Polaroid camera, photographs of the wake structure in the exit jet of the duct were acquired, for models with common leading edge geometry, but varying the exit diffuser angle from 0° to 18°. Form the flow visualization experiments, it was concluded that the cross section of the exit jet in the wake region expands with increasing diffuser angle.

Abrego & Bulaga [36] performed wind tunnel tests on a ducted propeller system shown in Figure 2-18(a), which was based on the SoloTrek XFV model, a manned single-passenger VTOL aircraft, shown in Figure 2-18(b). The experiments were carried out in a 2.13 m × 3.05 m wind tunnel facility, where the ducted propeller was tested in hover, axial flow, and non-zero α_P operating conditions. The study investigated the effect of changing α_P, c_D, implementation of an exit vane flap, and exit vane deflection angle on the performance of the system. Abrego and Bulaga [36] measured the aerodynamic forces and moments experienced by the ducted propeller system using a wind tunnel balance. The base model duct used by Abrego & Bulaga [36] had an internal diameter of $D = 965.2$ mm, a duct chord length of $c_D = 254$ mm, and a diffuser section with $\theta_D = 6°$. To study the effects of duct chord length, a duct model with $c_D = 381$ mm was also tested. The propeller used had 5 fixed-pitch blades, with a nominal diameter of 960.12 mm and a 0.211 D_h/D ratio. Due to manufacturing imperfections, Abrego & Bulaga [36] reported that their system did not have a constant δ_{tip} along the circumference of the duct, rather, that it ranged between δ_{tip}/D ratios of 0.07% to 2.4%.

(a) (b)

Figure 2-18: In (a), ducted propeller and motor used by Abrego and Bulaga [36]**. Image in (a) obtained from Abrego and Bulaga** [36]**, publicly available through the NASA Technical Reports Server: https://ntrs.nasa.gov/search.jsp?R=20020052231. In (b), the SoloTrek VXF single-person VTOL aircraft, powered by ducted propellers, from which Abrego & Bulaga** [36] **based their experimental model on. Image in (b) is available through the CC0 1.0 Universal Public Domain Declaration.**

Two exit vanes were tested, both with a total chord length of 76.2 mm, but with different flap chords of 25.4 mm and 57.15 mm were tested. Axial flow tests were conducted at free stream velocities ranging from 0 m/s to 42 m/s, and at seven rotor angular velocities ranging from 1800 RPM to 3400 RPM. As a part of the axial flow condition investigation, the system was also tested at the descent flight condition (thrust vector in the same direction as the free stream velocity vector), and therefore, a free stream advance ratio range of $-0.11 \leq J \leq 0.25$, where the negative J values correspond to the latter mentioned operating condition. Forward flight tests in the range of $5° < \alpha_P < -25°$ were performed at free stream velocities ranging from 1.5 m/s to 41.1 m/s ($0 \leq J \leq 1.14$), and four rotor angular velocities between 1800 RPM and 3000 RPM. For both the axial and forward flight tests, the exit vane flap angle was varied between -40° to 40°. The results from the axial flow tests showed that for the same J value, variations in the propeller's rotational velocity did not result in significant changes in C_T, C_P, or the FM. These results also revealed that with increasing J, C_T and the FM decreased, but changes in C_P were negligible. The tests at various α_P values exhibited that as α_P increased, the propulsive force (thrust in the direction of the free stream) decreased, and the power consumption increased, for all J values investigated. Increasing

the chord length of the duct by 50% showed to have no significant effects in the thrust generation of the system, as shown on the graph of Figure 2-19. Abrego & Bulaga [36] also found that the use of an exit vane flap was effective in generating side force, however, they did not notice any evident correlation between the generation of such force and the size of the exit vane flap used.

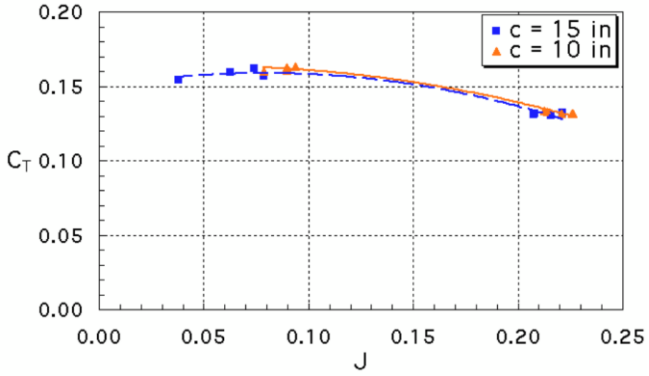

Figure 2-19: The results of C_T as a function of J for the long and short chord duct models tested, in the axial flow condition, obtained by Abrego & Bulaga [36]**. The graph shows no significant changes in performance due to changes in the chord length of the ducts. Image obtained from Abrego and Bulaga** [36]**, publicly available through the NASA Technical Reports Server: https://ntrs.nasa.gov/search.jsp?R=20020052231**

The technological advances of the last decade shifted the focus of ducted propeller research towards their implementation in UAVs. The significant reduction in size that UAVs possess over manned aircrafts result in a proportional reduction of the thrust required; thus, for the case of propeller powered UAVs, this translates to a reduction in the nominal diameter of the propellers used. This fact enabled experimentalists to perform full scale experiments, and obtain results that resemble more accurately real life flight operating conditions.

In an attempt to improve the aerodynamic performance of an MAV prototype developed by Honeywell, shown in Figure 2-20(a), Graf *et. al.* [37] investigated the performance of ducted propellers at non-zero α_P, where the performance of a small scale ducted fan model was tested under static, axial and forward flight conditions. Graf *et. al.* [37] emphasized the necessity to reduce the pitching moment experienced by ducted propellers during forward flight, in order to achieve maneuverability improvements for UAVs. The investigation focused on the effects of changing the duct's leading edge geometry; for this purpose, Graf *et. al.* [37] tested 5 different leading edge models, four of which are shown in Figure 2-20(b). The geometrical parameters varied

between each model were the leading edge radius and the thickness, which were tested in the ranges of $0.0157 < r_{LE}/c_D < 0.0625$ and $0.125 < t/c_D < 0.158$, respectively. Load cell measurements in the static tests allowed to separate the duct thrust and propeller thrust. For the wind tunnel tests, a six axis load cell was used to capture all forces and moments experienced by the ducted propeller, the free stream was varied between 3 m/s to 26 m/s, and the α_P was changed from 0° to 90°.

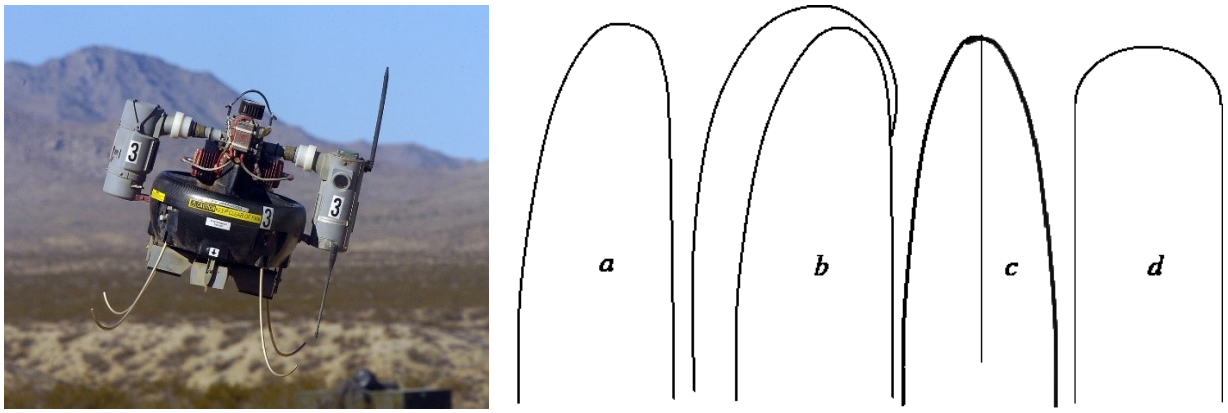

(a) (b)

Figure 2-20: In (a), the Honeywell MAV used by Graf *et. al.* [37] for their experiments. In the image, the MAV can be seen with instrumentation additional to the duct and rotor, such as the engine, exit vanes, and landing gear. This image is available in the public domain. In (b), recreated figures of four of the five leading edge models tested by Graf *et. al.* [37]. In this image, models *a*, *b*, *c* and *d*, namely the Baseline, Enlarged, Elliptic and Circular models are shown. A fifth model, the Revised leading edge was also included in the experiments.

The static test results showed that the Revised leading edge model, with t/c_D=0.125 and r_{LE}/c=0.0375 outperformed all other configurations at all of the propeller rotational speeds tested, and therefore, Graf *et. al.* [37] concluded that the leading edge radius is more influential on the static efficiency of the system than the thickness of the duct. Using the data obtained from the wind tunnel tests, Graf *et. al.* [37] calculated the drag on the model at the various α_P values tested, as well as the contribution of momentum drag, D_m, to the total drag. Momentum drag, as defined by Graf *et. al.* [37], is caused by the act of a force on the center of pressure of the flow that is displaced, required to conserve momentum in the direction of the free stream, and it is calculated through the expression

$$D_m = V_\infty \sqrt{T \rho V_j} \qquad \textbf{2-66}$$

From the wind tunnel tests carried at complete edgewise flow ($\alpha_P = 90°$) Graf *et. al*. [37] notes that D_m constitutes approximately 80% of the total drag experienced by the ducted propeller, and that as the free stream velocity is increased, the profile drag begins to overtake. The wind tunnel tests also revealed that while the Revised leading edge model performed the best in static conditions, it demonstrated to generate higher pitching moments during edgewise flight. Graf *et. al*. [37] explains that the generation of a pitching moment at the edgewise flow condition is due to the asymmetry of thrust generation over the rotor disk, created by the difference in performance between the advancing and retreating blades of the rotor disk. To mitigate the generation of pitch moments at the $\alpha_P > 0°$ condition, Graf *et. al*. [37] investigated the inclusion of two passive control methods denominated "Lip-Mounted Control Effectors". These effectors aimed to decrease or augment the performance of certain sections of the ducted propeller, in order to "balance-out" the effects of a pitching moment. Graf *et. al*. [37] notes that the use of the effectors successfully reduced the magnitude of the pitch moment generated; however, the effectors did compromise the thrust generation of the system.

Martin and Tung [38] carried out a wind tunnel investigation on a ducted propeller system shown in Figure 2-21(a), in order to obtain reference experimental results for validation of a Computational Fluid Dynamics (CFD) model, intended to predict the performance of a VTOL UAV. They tested two ducted propeller models, with leading edge radius-to-chord ratios of 0.05 and 0.03, and *t/c* ratios of 0.2 and 0.19 respectively. Both ducts had an internal diameter of 254 mm, and a chord length of 146.56 mm, with no diffuser at the trailing section of the duct. A propeller with two blades was used, and the radius of the blades was varied from 121.92 mm to 125.73 mm, in order to investigate the effect of varying δ_{tip}. The investigation studied the performance of the system at the hover condition, cross-wind condition, and forward flight at high angles-of-attack. Martin and Tung [38] defined the condition of $\alpha_p = 0°$ to be representative of axial flow, and performed tests at an α_p range of 0° to 110°, while varying the free stream velocity from 0 m/s to 36.6 m/s. For the tests in hover, the angular velocity of the propeller was varied from 2000 RPM to 9500 RPM. It was concluded from the hover experiments that for the low RPM tests (high *J*), a negative thrust contribution from the duct was generated, and this phenomenon was attributed to a loss in the suction pressure at the inlet of the duct, as well as to viscous losses in the internal surface of the duct.

Martin & Tung [38] found that as δ_{tip} was increased, the hover efficiency of the ducted propeller approached the value of $FM = 0.44$, which corresponded to the open rotor hover efficiency. Another conclusion from the hovering tests was that the duct thrust also experienced a drop with decreased leading edge radius. The crosswind tests ($\alpha_p = 90°$) were carried out at 900 RPM, and revealed an increase in the pitching moment about the quarter-chord of the duct with increasing free stream advance ratio. It was also determined that although the leading edge with small radius resulted in a decrease of the hover efficiency, it simultaneously reduced the asymmetric velocity distribution over the propeller plane that is characteristic of cross-wind flow conditions. Additionally, hotwire flow visualization experiments were carried out at the internal and external surfaces of the duct, as well as on the wake region. The results demonstrated that the boundary layer thickness measured along the internal surface of the duct was much greater than the external boundary layer, and that the presence of the duct had an evident momentum deficit at the wake region. An example of the hotwire visualization results from Martin and Tung is shown in Figure 2-21(b).

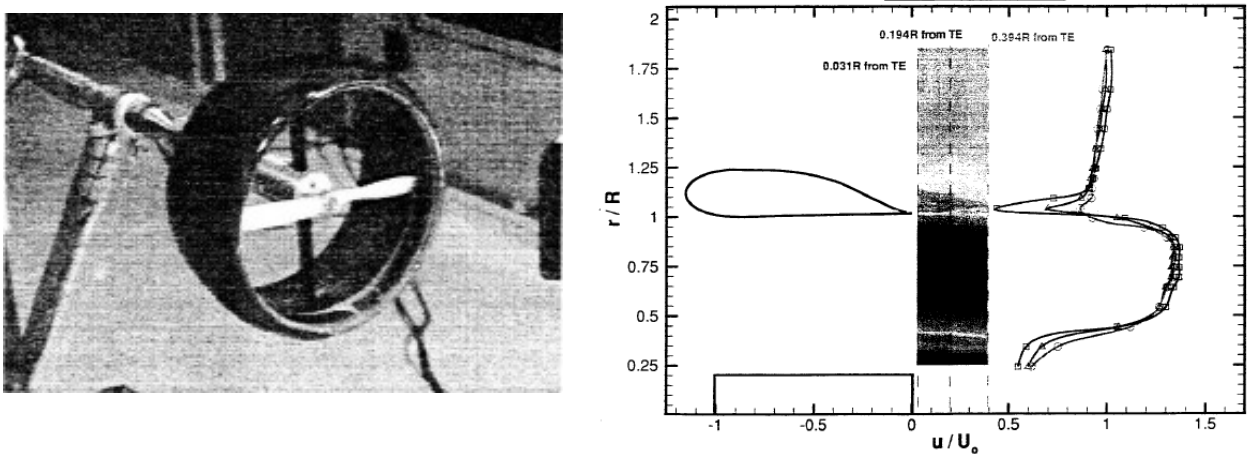

(a) (b)

Figure 2-21: (a) Ducted propeller used by Martin & Tung [38] **for their wind tunnel experiments. (b) Example hot-wire anemometry flow visualization result obtained by Martin and Tung** [38]**, in this case, for the ducted propeller in axial flow at 9000 RPM and 21 m/s. Images obtained from Martin and Tung** [38]**, publicly available through the NASA Technical Reports Server: https://ntrs.nasa.gov/search.jsp?R=20050009943**

As the first part of a two-part study, Akturk and Camci [26] investigated aerodynamic performance of a 558.8 mm internal diameter ducted propeller system, where the study was focused on the effect of δ_{tip} on the hover performance of a ducted propeller UAV. The model studied by Akturk and Camci [26] consisted of a duct with a round leading edge that extruded outwards from the external surface of the duct, a straight cylindrical middle section, and a diffuser section with a diffuser angle of 6°, as seen in Figure 2-22. Akturk and Camci [26] characterized the leading edge of their model by two parameters, its wall thickness and radius of curvature, both normalized with respect to the duct's total chord length. The values for these parameters used by Akturk and Camci [26] were 11% and 3.61%, respectively. The experimental portion of the study involved the acquisition of aerodynamic loads using a six-component load cell, as well as pressure measurements upstream and downstream of the rotor disk using a Kiel total pressure probe. The tests were all conducted at $V_\infty = 0$ m/s, and the rotating speed of the propeller was varied from 1000 RPM to 3000 RPM. The experimental results were compared to a CFD simulation, which was done using the Ansys-CFX solver. In the CFD model, the Reynold's Averaged Navier-Stokes equations were solved using an element based finite volume method, and implementing the k-ω shear stress transport model. The computational domain used in the simulations was divided into three sections, a stationary inlet and outlet regions and a rotating fan region. To connect the domains, a "stage" type interface was used. Akturk and Camci [26] tested the performance of the system using three values of δ_{tip}/R, namely 1.71%, 3.04% and 5.17%, as well as the fan rotor with no duct.

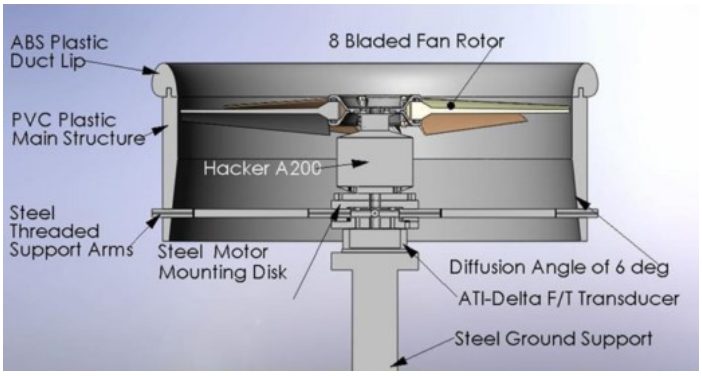

Figure 2-22: Schematic of the ducted fan model used by Akturk and Camci [26]**. The leading edge of the duct extrudes past the external diameter of the duct's cylindrical section. Image obtained from Akturk and Camci** [26] **through requested permissions.**

As can be observed in Figure 2-23 (a) and (b), the results from the load measurements revealed that decreasing δ_{tip} provided significant enhancements to the thrust generation of the system, as well as a maximum increment of 38% of the hover efficiency (quantified using the Figure of Merit) at the higher RPM values tested, relative to the open rotor performance. An interesting result obtained by Akturk and Camci [26] is that the ducted propeller system with δ_{tip}/R = 5.17% resulted in detrimental effects in both the thrust generation as well as the hover efficiency. Akturk and Camci [26] attribute this behavior to increases in the viscous losses related to tip leakage. The pressure measurements revealed that the changes in blade tip clearance have negligible effects in the flow field near the hub of the rotor, however, the effects amplify towards the tip of the blades. The computational results from the study achieved good agreement with the experimental results, although with some discrepancies at the regions near the rotor hub, which the authors attribute to difficulties in modelling low-Reynolds number flows.

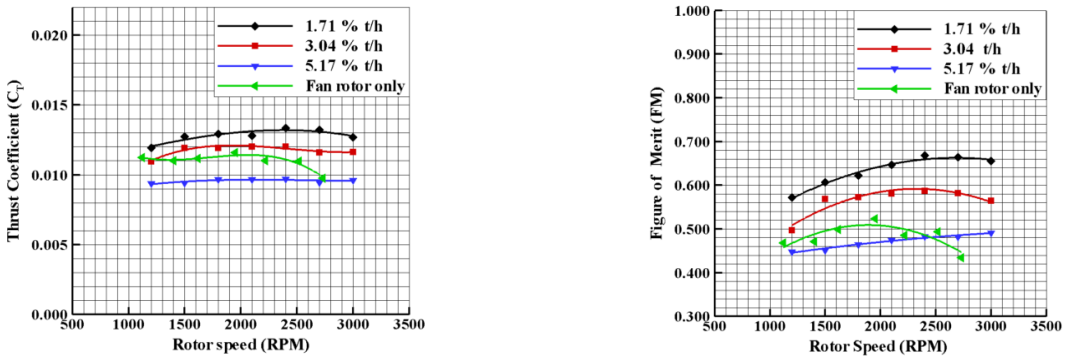

Figure 2-23: The experimental results obtained by Akturk and Camci [26] **which show (a) the thrust coefficient and (b) the figure of merit as a function of propeller rotational speed. Images obtained from Akturk and Camci** [26] **through requested permissions.**

Flow field analysis results from the computational study provided evidence of the existence of tip vortices, and their interaction with the trailing blades in the propeller. Akturk and Camci [26] quantified the tip leakage by calculating the axial tip mass flow rate, as shown in Figure 2-24. These results revealed that as δ_{tip} was increased, a region of momentum deficit increased near the blade tips, as can be observed in Figure 2-24.

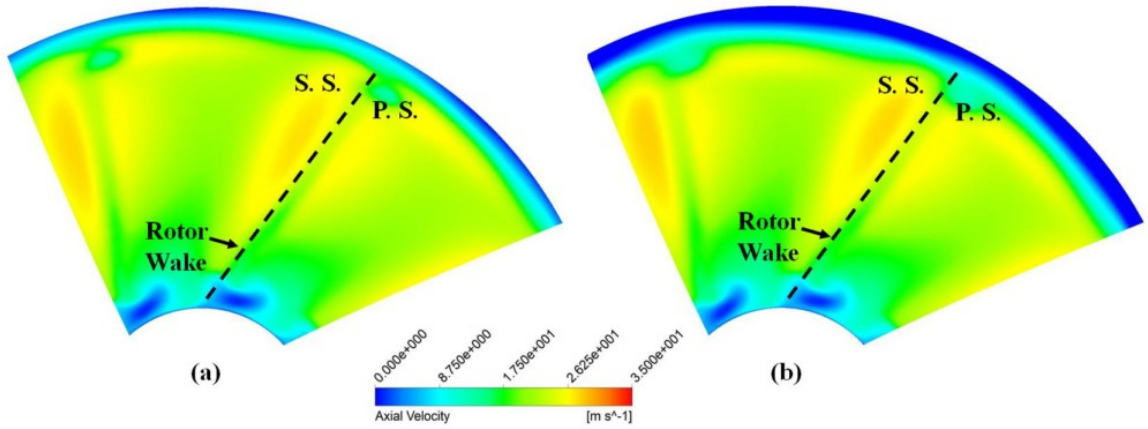

Figure 2-24: The axial velocity map downstream of the rotor disk, obtained from CFD simulation by Akturk and Camci [26] **for a blade tip clearance of (a) 1.71% and (b) 3.04% of the duct's chord length. The image shows how a region of momentum deficiency increases in area near the blade tips when the blade tip clearance is increased from 1.71% to 3.04% of the duct's chord length. Images obtained from Akturk and Camci** [26] **through requested permissions.**

In the second part of the study, Akturk and Camci [27] evaluated the effectiveness of blade tip treatments to mitigate tip leakage and its effects on the performance of ducted propellers. The blade tip treatments applied by Akturk and Camci [27] consisted on five geometric modifications to the blade tips, shown in Figure 2-25(a), which aimed to reduce the flow of air moving from the high pressure side of the blade to the low pressure side. The top two models in Figure 2-25(a) were denominated as "platform extensions" of the tip, and the bottom two models use "squealers", an extrusion in the radial direction of the blade. The third model in Figure 2-25(a) uses a combination of these two designs. The methodology used by Akturk and Camci [27] consisted in evaluating the performance of each treatment using a CFD model to choose the treatments that performed the best, and proceeded to test these experimentally. An example of a blade extension with tip treatment manufactured by Akturk and Camci [27] is shown in Figure 2-25(b). Solutions to the RANS equations were obtained using Ansys-CFX, and simulating the hover performance of the ducted propeller with a constant rotational speed of 2400 RPM, and having a blade tip clearance of δ_{tip}/R = 3.04%. The CFD model followed the same specifications as described in the first part of the study by Akturk and Camci [26].

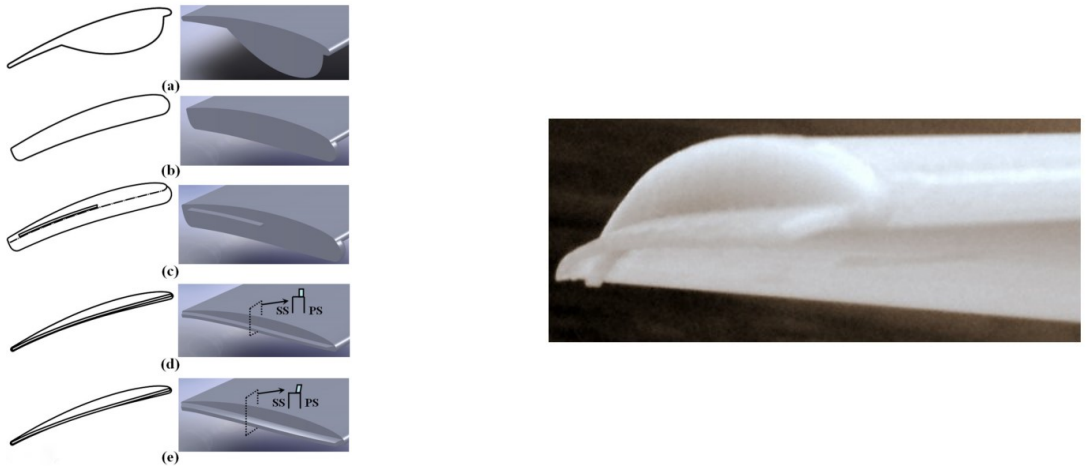

(a) (b)

Figure 2-25: (a) The tip treatments designed and tested by Akturk and Camci [27] **which are named, from top to bottom: Partial Bump Tip Platform Extension, Full Bump Tip Platform Extension, Full Bump and Partial Squealer Tip Platform Extension, Full Squealer Tip Platform Extension and Inclined Full Squealer Tip Platform Extension (b) A sample of a rapid prototyped blade extension with the Inclined Squealer Tip Platform Extension from Akturk and Camci** [27]**. Images obtained from Akturk and Camci** [26] **through requested permissions.**

Flow field visualization obtained through the computational results showed that the models with "platform extensions" did not provide significant improvements to the performance of the system; however, the "squealer" blade treatment achieved relative to the untreated blade. In the results shown in Figure 2-26 (a) and (b), Akturk and Camci [27] illustrated contours of the swirling strength at 9 different planes separated azimuthally, and showed how the squealer blade treatment delayed the formation of the tip vortices to a location further downstream in the chordwise direction, and pushed the tip vortex outwards (toward the internal surface of the duct). Akturk and Camci [27] explain that this is beneficial to the performance of the system, since it reduces the interference of tip vortices with oncoming blades, and thus, energy losses. Computationally, the full inclined squealer treatment achieved a thrust increment of 10.73% with respect to the untreated blade, at δ_{tip}/R = 3.04%. The computational results were validated through experimental tests, in which the blade with inclined squealer tip improved thrust generation by 9.6% at 2700 RPM and δ_{tip}/R = 3.04%. For the same value of δ_{tip}/R, both "squealer" models also showed improvements in the FM.

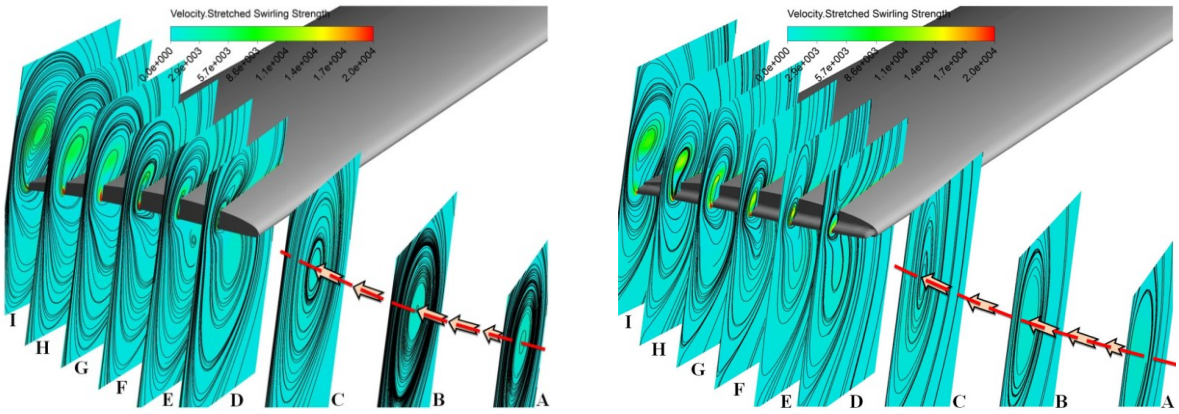

(a) (b)

Figure 2-26: The results obtained by Akturk and Camci [27] **from the CFD simulation at 2400 RPM and δ_{tip}/R = 3.04% for the (a) untreated blade tip and (b) full inclined squealer blade tip. Comparison between the two figures show how the treated blade delays the formation of the tip vortex to a location further downstream in the chordwise direction, and reduces the swirling strength of the vortex core. Images obtained from Akturk and Camci** [26] **through requested permissions.**

On a later publication, Akturk and Camci [39] studied the flow field around a 127 mm diameter ducted fan in hover and edgewise flow condition. The duct used in their study had a blunt leading edge and did not include a tapered diffuser section, as shown in Figure 2-27. The objective of the study was to characterize the flow field near the ducted propeller system in the edgewise and hover condition, in order to apply improvements to the maneuverability of UAVs in such flight regimes.

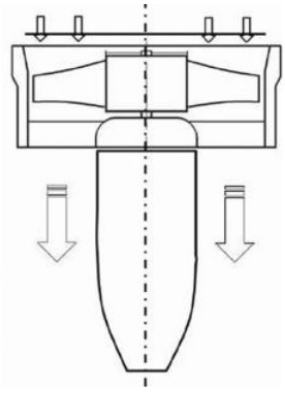

Figure 2-27: Figure of the duct used by Akturk and Camci [39] **in their second investigation showing the blunt leading edge and the cylindrical diffuser section. Images obtained from Akturk and Camci** [26] **through requested permissions.**

The investigation contained CFD analyses as well as PIV experimental data. For the CFD computation, Akturk and Camci [39] developed a rotor disk flow model based on the radial equilibrium equation, the energy equation and the conservation of angular momentum. They introduced a method to calculate the static pressure at each radial location of the blade as a function of the exit jet velocity. PIV images were obtained in regions of the inlet and exit jet of the ducted propeller with fields of view of 156 × 96 mm. Image processing was performed with a 32 × 32 pixel interrogation window size. Propeller rotational speeds of 9,000 and 15,000 RPM were tested, and for the edgewise flow tests, cross-wind speeds of 6 m/s were tested. The experimental results revealed that an increase in the rotational speed of the propeller decreased the size of the separation region near the leading edge of the duct. In the edgewise flow condition, a region of strong recirculation was observed at the leading edge of the duct. The PIV images showed that edgewise flow results in the displacement of the axial velocity peak from the windward side to the hub of the propeller.

Yilmaz *et. al.*[25] investigated the effectivity of using NACA profiles as the cross section of ducts in ducted propellers for UAVs. Two symmetrical profiles, namely NACA 0012 and NACA 0018, and a cambered profile, NACA 4312, were used. Two additional duct models were obtained by making a composite duct in which the leading edge was based on the NACA 4312 profile, and the diffuser section was varied between the NACA 7312 and the NACA M21 profiles. Yilmaz *et. al.* [25] performed load measurements to obtain thrust and torque data, measured the inlet and exit axial velocity profiles using hot wire anemometry, and obtained pressure measurements at the internal and external surfaces of the duct using pressure transducers. The experiments were carried out at a constant propeller rotational speed of 7000 RPM and 0° angle-of-attack. The free stream velocity was varied from 0 m/s to 20 m/s, achieving a maximum advance ratio of J =0.43. The load cell measurements revealed that the ducts contributed a positive thrust addition to the ducted propeller systems; however, at high J, this contribution became negative, in other words the ducts were producing drag. The torque measurements revealed that for the range of J tested, the ducted propeller models operated at a lower C_P than the open propeller, as shown in Figure 2-28(b).

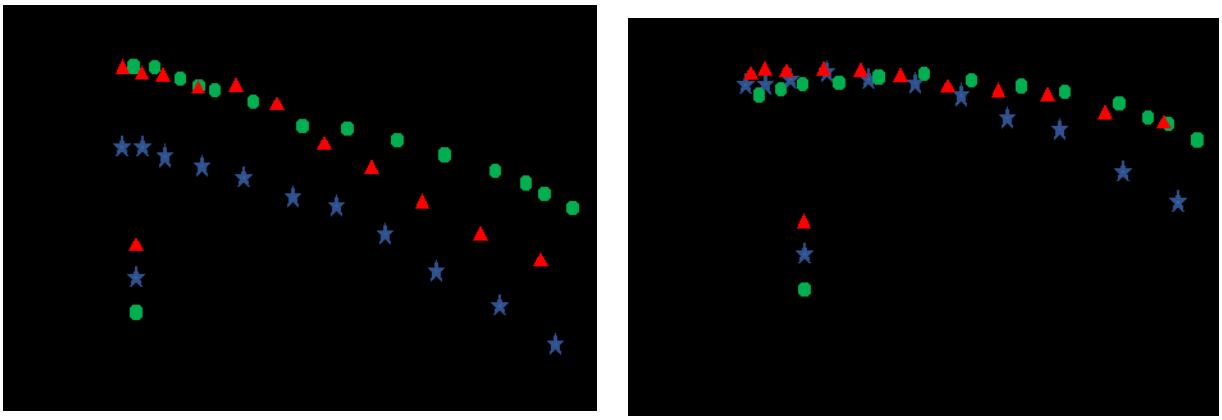

(a) (b)

Figure 2-28: Recreated plots of the load cell measurement results obtained by Yilmaz *et. al.* [25] showing the (a) C_T as a function of J and (b) C_P as a function of J, for the two duct models investigated, and the open propeller. The original graphs from Yilmaz *et. al.* [25] show results for five different ducted propeller configurations.

Inlet and exit axial velocity profiles were obtained at free stream velocities of $V_\infty = 10$ m/s and $V_\infty = 20$ m/s ($J = 0.2$ and $J = 0.4$, respectively). The results demonstrated that for both the ducted and open propellers the inlet axial flow is accelerated with respect to the free stream velocity, where the ducted propeller provided the higher acceleration of the flow. The highest flow acceleration was achieved by the duct model with a leading edge profile based on the NACA 7312 profile. Increasing the free stream velocity resulted in a decrease of the flow acceleration. The measurement of the exit jet velocity profile is shown in Figure 2-29, where Yilmaz *et. al.*[25] indicates that the ducted propellers, with the exception of the model that combines the NACA M21 and the NACA 4312 profiles, successfully reduced the slipstream contraction of the flow.

The majority of the works on ducted propellers for small scale applications have been aimed towards UAVs; however, there is scarce work on applications to MAVs. One of the most detailed investigations on ducted propeller applications to MAVs was performed by Pereira [4], where he performed a parametric study on the duct geometry of a 160 mm internal diameter ducted propeller system, as the main subject of his doctoral thesis. The parameters investigated by Pereira [4] were the blade tip clearance δ_{tip}, the leading edge radius r_{LE} of the duct (a circular leading edge was tested), the diffuser angle θ_D, diffuser length and the exit area-to-rotor disk area ratio σ. The objective in Pereira's investigation was to study the influence each of the aforementioned

parameters held on the performance of the system, and to obtain an understanding on how these parameters interacted with each other.

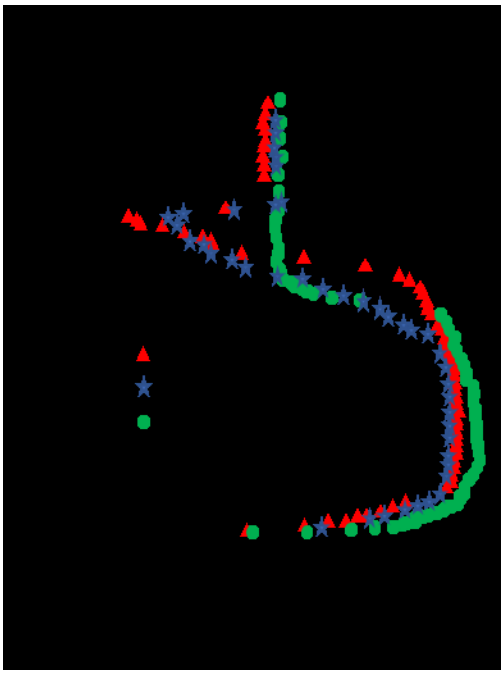

Figure 2-29: A recreated plot of the exit jet axial velocity profile obtained by Yilmaz *et. al.* [25] for the various ducted propeller configurations tested, as well as the open propeller, at $J = 0.2$.

A photograph of the system used by Pereira [4] is shown in Figure 2-30. Similar to the system used by Akturk and Camci [39], the interface between the leading edge and the diffuser section of the duct manufactured by Pereira [4] featured a step. Pereira [4] performed measurements of thrust and torque, pressure measurements along the internal surface of the duct as well as velocity readings of the exit jet flow using a pitot-static probe. The duct models varied in leading edge radiuses of 0.06D-0.13D, diffuser angles of 0°-20°, diffuser lengths of 0.31D-0.72D, blade tip clearances of 0.001D-0.016D and a 3 bladed propeller were investigated. A total of seventeen ducted propeller configurations were tested by Pereira [4]. The models were tested at free stream speeds ranging from 0 m/s to 6.1 m/s, while the rotation of the propeller was varied from 2000 RPM to 4000 RPM. The rotor disk angle-of-attack was varied from -45° (free stream incident to the trailing edge of the duct) to 90° (edgewise flow).

Figure 2-30: The ducted propeller model used by Pereira [4] **in his investigation the leading edge and diffuser sections were printed separately and could be interchanged to test different duct models. The duct models featured a circular leading edge that did not connect in flush with the diffuser section, and twenty four internal pressure transducer ports. The images have been extracted from Jason L. Pereira's Doctoral thesis, publicly available in the Digital Repository at the University of Maryland http://hdl.handle.net/1903/8752.**

Pereira [4] obtained values for the duct thrust independently by integrating the pressure distribution along the internal surface of the duct. The parametric investigation was only carried out in the hover condition. For the tests in hover, Pereira [4] drew the following conclusions:

- Increments in δ_{tip} decreased the static efficiency and the $C_{T,ducted}/C_{T,open}$ ratio for the same C_P, increases $C_{P,ducted}/C_{P,open}$ for the same C_T.
- Increments to the leading edge radius increases the static efficiency and the $C_{T,ducted}/C_{T,open}$ ratio for the same C_P, decreases $C_{P,ducted}/C_{P,open}$ for the same C_T, and decreased T_{rotor}/T_{total}
- A diffuser angle of 10° resulted in the highest static efficiency. Decreasing θ_D to 0° or increasing to 20° resulted in detrimental effects to the static efficiency.
- Variations in the diffuser length had less effect on performance. An increase in the diffuser length showed slight decrease in T_{rotor}/T_{total}.
- Changes to σ, which were applied by changing the diffuser angle and length independently, demonstrated that decreasing σ resulted in detrimental effects on the static efficiency, were changes to the diffuser length had the most significant effects.

Pereira [4] highlights the fact that the effect of a single parameter cannot be classified as having a greater effect than the other by stating that "the amount of influence of any parameter depends on the values of the other parameters", with the exception of the leading edge radius. For the wind

tunnel tests, only the duct model that demonstrated the best performance in hover was tested. The axial flow tests revealed that although the ducted propeller exhibited greater thrust generation than the open propeller in hover, its performance with increasing free stream speeds drops off rapidly after $J = 0.24$ below the achievements of the open propeller, as shown in Figure 2-31(a). Pereira [4] attributed this loss of thrust from the ducted propeller to the collapse of suction pressure at the leading edge that comes with increasing free stream velocity, as well as to the drag created by the duct itself. However, Pereira [4] also found that for the range of advance ratios tested, the ducted propeller always performed at a lower power consumption, as seen in Figure 2-31(b).

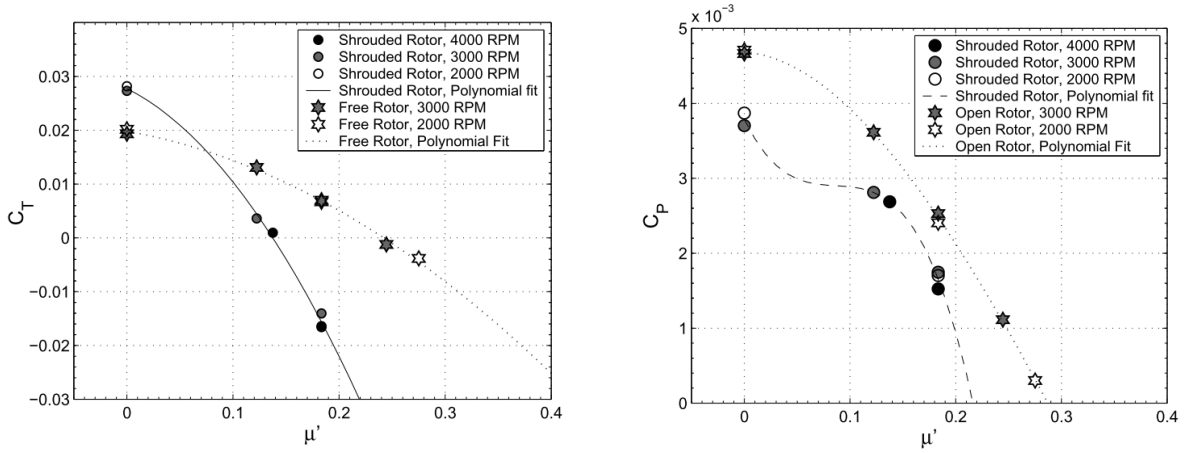

(a) **(b)**

Figure 2-31: The wind tunnel test results obtained by Pereira [4] **showing (a) C_T as a function of the advance ratio and (b) C_P as a function of the advance ratio, for propeller rotational speeds ranging from 2000 RPM to 4000 RPM. The wind tunnel tests were performed on the duct model with the best hover performance, namely the duct with $r_{LE} = 0.13D$, $\theta_D = 10°$, $\delta_{tip}/D = 0.001$, diffuser length of $0.31D$. The images have been extracted from Jason L. Pereira's Doctoral thesis, publicly available in the Digital Repository at the University of Maryland http://hdl.handle.net/1903/8752.**

2.5.1 Lessons Learned from the Literature

The past works on ducted propellers discussed in the preceding section provides insight on design guidelines for ducted propellers and the behaviour of ducted propellers in various operating conditions. A clear consensus among the authors is found upon the fact that the performance benefits of choosing a ducted propeller over an open propeller depend heavily on the advance ratio. A number of authors ([6], [24], [29], [4], [30], [38], [25], [36]) concur in that the ducted propeller only generates a higher thrust output than the open propeller only for low J values; however, there

is no clear finite margin of J at which the performance of the duct begins to decay. For example, Pereira [4] reports that the thrust generated by the ducted propeller underperforms that of the open propeller for $J > 0.24$, while the investigation from the Hiller Aircraft Corporation [35] supports that ducted propellers achieve a higher η than open propellers at $J < 0.4$. Martin and Tung [38] and Yilmaz [25] specify that at high J flight regimes the thrust contribution from the duct is negative. The potential of the duct to reduce the slipstream contraction has not been widely researched; however, the investigations by Yilmaz [25] confirmed this behaviour through flow visualization. Taylor [34] found that for a duct that successfully achieves $\sigma > 1$ the total thrust is augmented while the rotor disk is offloaded. Platt [23] and Kruger [30] determined that one of the reasons why the ducted propeller can produce more static thrust for the same power input than the open propeller, is due to the increase in the mass flow rate through the propeller plane from the duct, which reduces the effective angle-of-attack of the propeller blades, α_b, and thus allows operation at higher blade tip Mach numbers without stalling.

In regard to the design geometry of the duct, the leading edge radius r_{LE} figures as the most influential parameter that directly affects performance. Parlett [32] suggested that an increase in r_{LE} results in increases in FM during hover, Taylor [34] suggested that the FM would experience a drop if the $r_{LE} < 0.06D$, and Martin and Tung [38] observed that C_T in hover of the ducted propeller decreased with decreasing r_{LE}. Graf *et. al.* [37] concluded from his investigation that r_{LE} was a more influential parameter than the thickness of the duct. Another point of convergence in the literature is the insignificance of the duct chord c_D ([23], [24], [34], [36]).

2.6 Previous Investigations on Propellers at Non-Zero Angle-of-Attack

Experimental evaluations and performance data for propellers of small UAVs operating in $50{,}000 < Re < 100{,}000$ (based on the chord length, c, of propeller blade elements) have been developed in the past with most of the experiments conducted for the axial flow condition with $\alpha_P = 0°$. Brandt and Selig [40] measured the performance of 79 propellers from a variety of manufacturers (e.g., APC, Master Airscrew, Graupner, and GWS) ranging in diameter from 9 to 11 inches in the axial flow condition. The tests were conducted at a fixed rotational speed of 1,500 and 7,500 revolutions per minute (RPM) and a maximum free-stream velocity of 24.38 m/s. They observed a maximum efficiency of 65%, and that increasing the rotational speed of the propeller

improved the performance of the system. The extensive database developed by Brandt and Selig [40] provides UAV designers with readily available data for zero α_P; however, it did not include any experiments on propellers operating at non-zero α_P for modern multi-rotor vehicles.

There have been a number of earlier investigations of the performance of large propellers at non-zero values of α_P for large vertical takeoff and landing (VTOL) aircrafts. Kuhn and Draper [41] tested the performance of multiple propellers and a wing-propeller combination for a VTOL vehicle in a range of $0° < \alpha_P < 90°$. The propellers used by Kuhn and Draper [41] were 2 feet in diameter, had three blades, a Clark Y cross-sectional airfoil and operated at collective angles of 8° and 20°. A maximum propulsive efficiency of ~77% was achieved at collective angle of 20°. The experiments were carried out at constant thrust by adjusting the rotational speed of the propeller, which showed an increase of C_T (normalized by RPM) with increase of α_P. McLemore and Cannon [42] investigated the aerodynamic performance of a two-propeller tandem system in $0° < \alpha_P < 180°$ range. The propellers were 5.33 feet in diameter, two-bladed, and the collective blade angle was varied from 0° to 67.5°. They presented their results as a function of the free-stream advance ratio and the inflow advance ratio, which is based on the component of the free-stream velocity that is perpendicular to the rotor disk, defined as

$$J_a = \frac{V_\infty \cos(\alpha_P)}{nD_p} \qquad \textbf{2-67}$$

In the experiment of McLemore and Cannon [42], the inflow advance ratio was varied within $0 < J_a < 6.2$.Their results demonstrated that thrust and power increases with increase of α_P and also J_a when there is no flow separation over the blades. McLemore and Cannon [42] also showed that the J_a value that corresponds to $C_T = 0$ increased with increase of α_P. Yaggy and Rogallo [43] performed wind tunnel experiments on three different propellers operating within $0° < \alpha_P < 85°$, to investigate their operation for a VTOL aircraft. Propeller blades with NACA 16-series, NACA 64-series and a NACA 0009 airfoils and rotor diameter of 12, 10, and 9.5 feet were investigated, respectively. They observed that increase of α_P resulted in increase of the rate of change of C_T, C_P, C_{Fx}, C_{Mx} and C_{My} as a function of J_a. Yaggy and Rogallo [43] also found that for the experiments conducted at $\alpha_P < 45°$ only a moderate change in the rate of change was observed.

There is a limited number of investigations available regarding the performance of small propellers for multi-rotor UAVs operating at non-zero α_P. Hughes and Gazzaniga [44] evaluated the effect of α_P ranging from -16° to 16° on two counter-rotating propellers (~21 to 24 inch in diameter), arranged in a tandem (coaxial) configuration, to simulate takeoff and landing flight regimes. They concluded that the variations in the efficiency and power coefficient were invariant with respect to α_P, within the relatively small range of -16° to 16°. Hughes and Gazzaniga [44] highlighted that when η and C_P data for non-zero α_P are presented as a function of the inflow advance ratio (J_a) the performance curves collapse. More recently, Pereira [4] investigated a rotor with 16 cm diameter for $0 \leq J_a \leq 0.4$ and $0° \leq \alpha_P \leq 90°$. They observed that the thrust generated as well as the power consumed by the propeller increased for increasing J_a and α_P. In a recent investigation, Carrol [45] tested a two-bladed propeller (T-Motor) with 18 inch diameter, 6.1 in/rev pitch, at α_P range of -30° $\leq \alpha_P \leq 90°$, and up to a maximum J value of ~0.35. The tests were performed at three rotating speed of 3,000, 4,000, and 5,000 RPM. They demonstrated that for increasing α_P and increasing J values, the thrust generation of the propeller increases. However, the power consumption at $\alpha_P < 30°$ increased with increase of α_P and also increase of J, while for $\alpha_P \geq 30°$, the power consumption reduces with a parabolic trend. Carrol [45] used the experimental results to validate an analytical model for prediction of propeller performance at the operating regime experimentally tested, as well as in the presence of neighboring rotors. This analytical model was developed using blade element momentum theory (BEMT), in which hover, axial and edgewise flow implemented a uniform λ. For small angle forward flight a radial distribution of λ was used, and for large forward flight angles a wake-interaction model based on vortex theory was used to determine the distribution of λ over the rotor disk.

Aerodynamic performance prediction softwares for UAV propellers are available on the internet, as is the case of QPROP, a prediction software developed by Drela [46], where the blade element momentum theory is used, along with a tip loss model formulated by Goldstein [47], which does not account for the complex wake-rotor interaction present during operation at $\alpha_p > 0°$.

Chapter 3. Experimental Setup

In this section the experimental setup utilized to perform the investigation with the ducted propeller is described. All of the experiments were carried out in the high-speed section of the wind tunnel, located in the Mechanical Engineering Building at the University of Alberta.

3.1 Wind Tunnel Facility

The experiments were performed in the closed-loop wind tunnel facility at the University of Alberta that is vertically arranged in the building, the test section is at the ground floor, and the driving fan and motor are located in the second floor. The test section has a rectangular cross-sectional area of 1.22 m × 2.44 m, and a contraction ratio from the low speed section to the test section of 6.3:1. The tunnel is internally equipped with sets of veins and screens at the elbows that ensure the uniformity of the flow at the test section. The maximum achievable flow velocity at the test section is approximately 30 m/s; however, the tests were only conducted up to a maximum wind speed of 20 m/s suitable for smalls-scale UAVs. An investigation by Kostiuk *et. al.* [48] on the same wind tunnel showed that the maximum turbulent intensity at the test section, with a flow speed of 8 m/s is less than 0.4%. The test section is equipped with a Pitot tube and thermocouple to measure instantaneous wind speed and temperature. The precision of these two instruments are ±0.01 m/s and ±0.01°C, respectively.

Figure 3-1: A photograph of the test section of at the 1.2 m×2.4 m cross-section of the wind tunnel, taken upstream from the experimental setup.

3.2 Duct Design

It was desired to maintain the duct designs as simple as possible; however, without compromising the desired distinctions between each of the duct sections (leading edge, diffuser). As mentioned by Pereira [4], parametric studies on the geometry of ducts for ducted propellers are particularly difficult because of the coupled geometry between all of the design parameters of the duct. These parameters are not exclusive to: leading edge radius, diffuser angle, geometry of the duct's cross-section (airfoil shaped, etc.), chord length of the duct's cross-section, camber of the cross-section, thickness-to-chord ratio of the cross-section. In the current investigation, only three parameters were considered in the design of the duct, namely, the leading edge geometry, the diffuser angle, and the thickness-to-chord ratio of the duct's cross section. In the current investigation, an internal duct diameter of 240 mm was chosen as a suitable size for UAV applications.

The ducts were manufactured using an ABS 3D printer (Stratasys UPrint). The leading edge and diffuser sections were designed to be interchangeable, in order to allow combinations of leading edges and diffusers. Due to the allowable volume of the printer, the leading edges and diffusers were printed in 3 pieces, each spanning 120° of the duct's circumference. Thus, a complete duct was assembled by joining 3 leading edge pieces and 3 diffuser pieces, as shown in Figure 3-2(b). The individual pieces of the leading edge and diffuser were designed with connecting tabs that work as a locking mechanism to secure the pieces together, and allow a quick-release mechanism between the leading edge and the diffuser section. Following the printing of the pieces, the parts were coated with drywall filling, left to solidify, and lastly sanded in order to achieve a smooth finish on the duct surface.

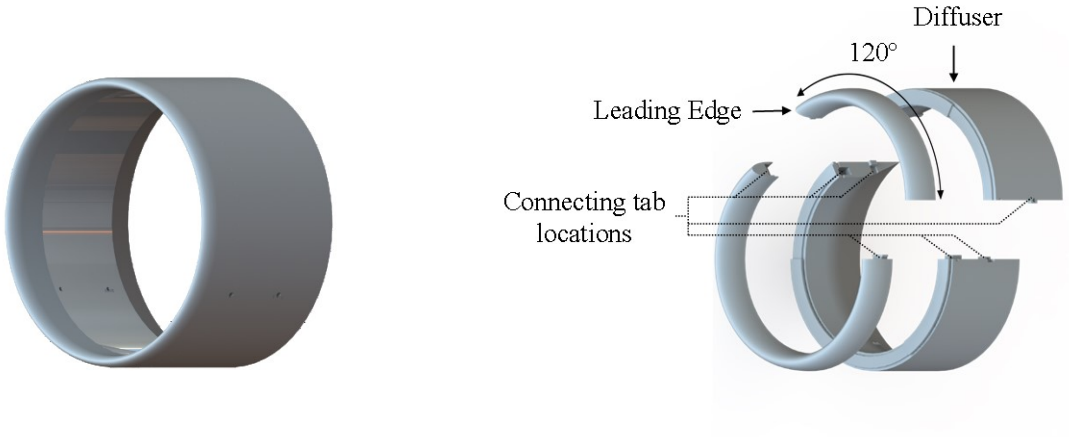

(a) **(b)**

Figure 3-2: 3D Model of the duct. The assembled duct is shown in (a), while (b) shows the disassembled duct. In (b), it is shown that each leading edge and diffuser piece covers 120° of the duct's circumference.

3.2.1 Leading Edge

The leading edge geometry was chosen to be a half ellipse as shown in Figure 3-3. An elliptical leading edge was chosen in order to achieve improvements in the axial flight operating regime by reducing the projected area, and thus, the pressure drag generated by the duct, as suggested by Pereira [4]. The ellipse of the leading edge is characterized by its aspect ratio, which is the ratio between the axial elongation of the ellipse A, to its radial thickness B defined in Figure 3-3, such that

$$Leading\ edge\ aspect\ ratio = \frac{B}{A} \qquad \textbf{3-1}$$

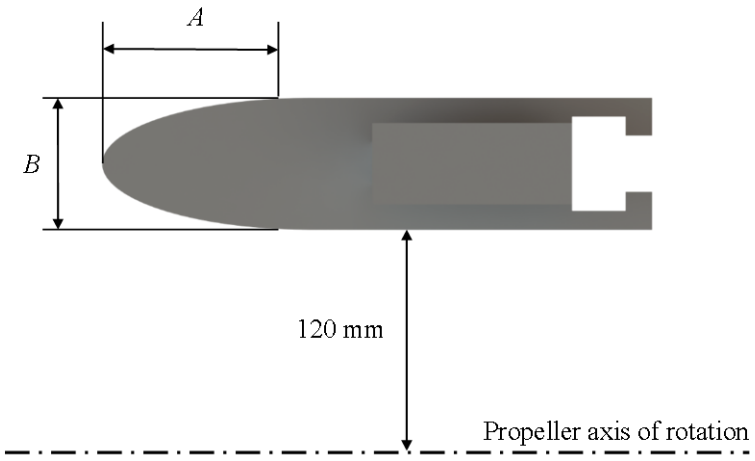

Figure 3-3: Schematic of the leading edge section of the ducts. The image provides the definition of the the axial and radial elongations *A* and *B* used to characterize the leading edge ellipse.

Experiments were performed with leading edge ellipse aspect ratios of 1.5:1 and 1:1. The reason to change from 1.5:1 to 1:1 was due to visualization constrains during the Particle Image Velocimetry (PIV) experiments, in order to shine the laser sheet closer to the rotor disk plane, which will be discussed in further detail in section 3.6. The change to a lower leading edge ellipse aspect ratio resulted in a decrease of the c_D defined in Figure 2-5, from $c_D = 160.26$ mm to $c_D = 148.99$ mm, representing a reduction of 7% , which according to the evidence from literature should not have a significant impact on performance.

3.2.2 Diffuser Section

The cross-section of the diffuser piece is shown in Figure 3-4. The diffuser angle, θ_D, is defined as the angle between the flat internal surface of the duct, and the tapered section of the diffuser. Diffuser angles of 9° and 18° were investigated. To maintain a constant duct chord between the models with equal leading edge aspect ratios but different diffuser angles, the length of the diffuser section was varied. The region between the leading edge-diffuser interface and the beginning of the diffuser's cone is cylindrical, and its thickness defines the thickness of the ducts. Two thickness-to-chord ratios of $t/c_D = 0.06$ and 0.14 were used. The diffuser section accommodates the connection to the support shafts that hold the duct in place, as shown in Figure 3-4.

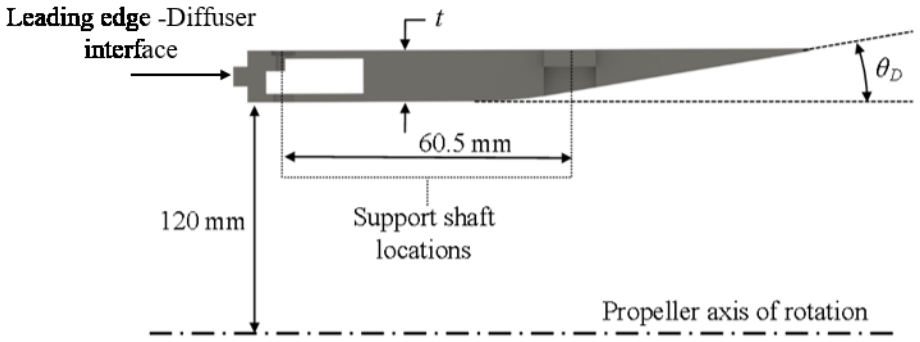

Figure 3-4: Schematic of the diffuser section of the duct. The diffuser angle θ_D and the duct thickness t are defined in the image.

The leading edge and diffuser sections are joined manually by matching the groves located in the interface surface of both sections. Since the duct was assembled by joining multiple parts, it was difficult to obtain a constant δ_{tip} at all azimuthal locations of the duct. An average blade tip clearance of δ_{tip} = 2 mm (4% of the duct internal radius) was achieved after manufacturing and assembly. A summary of all the parameters and their respective values tested in this study is provided in Table 3-1.

Table 3-1: The geometrical specifications of the duct models used in this investigation.

Parameter	Value
D	240 mm
c_D	148.99 mm,160.26 mm
t/c_D	0.06, 0.14
B/A	1:1, 1:1.5
θ_D	9°, -18°
δ_{tip}	~4%
Trailing edge thickness	0.5 mm

A total of four ducts were manufactured for this investigation. For convenience, a nomenclature system has been developed to identify each of the duct models as follows: Each duct is named as LE[Leading edge aspect ratio]-DA[Diffuser angle]-[duct thickness-to-duct chord ratio], such that the duct with a 1.5:1 leading edge aspect ratio, 9° diffuser angle and $t/c_D = 0.06$ would be named LE1.5-DA18-0.06. For the cases where the open propeller is used, the abbreviation OP will be used. The four duct models are shown in Figure 3-5, where the c_D of the models is indicated, as well as the relative location of the propeller within each duct.

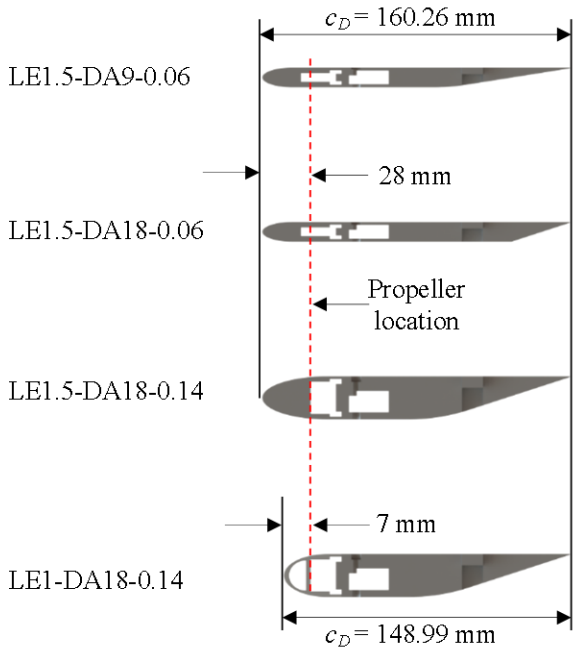

Figure 3-5: A summary schematic of the four duct models used in the investigation. From top to bottom: LE1.5-DA9-0.06, LE1.5DA18-0.06, LE1.5-DA18-0.14, LE1-DA18-0.014. The dotted red line indicates the propeller location in the models, and it can be observed that for the LE1-DA18-0.14 model the propeller sits closer to the leading edge than the rest of the models. The empty (white) spaces within the models are hollow sections designed to reduce the material consumption and weight.

3.3 Propeller System

Two propeller models were used in the ducted propeller investigation. For preliminary tests, a Scimitar model propeller from Master Airscrew with a nominal diameter of 11 in (279.4 mm), 8 in/rev pitch and 2 blades was used. To fit inside the ducts, the propeller was trimmed to a

diameter of 230.7 mm. Using photographs of the blades, images of the two-dimensional projections of the propeller were used to obtain the chord and pitch angle distribution along the radial direction *r*, and are shown on Figure 3-6.

For the performance and PIV experiments, a Sport model propeller from APC Propellers with a nominal diameter of 11 in, 7 in/rev pitch and 2 blades was used. In the same manner of the preliminary tests, the propeller was trimmed to a diameter of 230.7 mm; however, a second identical propeller was kept untrimmed in order to perform a comparison between the two. The exact airfoil cross-section of the propeller blade is proprietary information of the manufacturer, however, as per information provided by APC Propellers, the airfoil can be estimated to be a NACA 4412 airfoil, shown in Figure 3-7(b). This airfoil has a stall angle-of-attack of $\alpha_b = 14°$, and a zero-lift angle-of-attack of $\alpha_{L=0} = -4°$.

The nomenclature used in this thesis to identify each propeller consists of an abbreviation of the propeller model, followed by the nominal diameter × nominal pitch, such that the Sport model with a 12 in diameter and 6 inches/revolution would be SF12×6. Since there is only one Master Airscrew propeller, the model abbreviation used in this case will be MA. The open propeller tests performed with trimmed propellers will be referred to as trimmed OP, and open propeller tests with the untrimmed propeller as untrimmed OP.

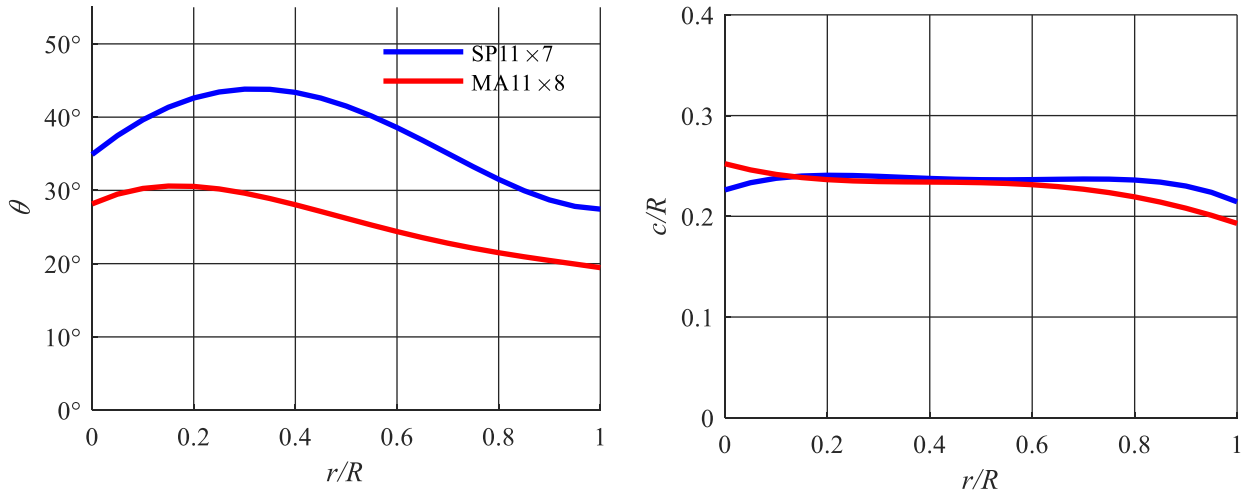

Figure 3-6: The geometric characteristis of the propellers used in this investigation. In (a) the pitch angle distribution along the radial direction is shown, while (b) shows the chord length distribution along the radial direction.

To power the propeller, a 450 W brushless DC (BLDC) motor with 1,000 K_V (Himaxx Outrunner 3528) and an electronic speed controller (ESC) (Phoenix Edge 75) were used in all the experiments. The motor is capable of rotating at a maximum unloaded (no blade rotation or free stream) angular speed of 12,000 RPM using a 12 V power supply. The motor was controlled from a lab computer with LabVIEW, where a Pulse Width Modulation (PWM) signal was sent via the ESC.

For the investigation of propellers at non-zero angle-of-attack two propeller models commercially known as the Slow Flyer (SF) and Sport (SP) models from APC Propellers were used. The two models have several geometrical differences, mainly in the geometry of their airfoils, and the chord distribution along the blade. The exact airfoil geometries of the propellers are proprietary information of APC Propellers; however, as per information provided by the manufacturer, the SF model may be approximated using an Eppler 63 airfoil, and the SP model using a NACA 4412 airfoil, as shown in Figure 3-7 (a) and (b), respectively. These two airfoils have stall angle-of-attack of α_b=9° and α_b=14°, and zero-lift angle-of-attack of $\alpha_{L=0}$=-2° and $\alpha_{L=0}$ = -4°, respectively.

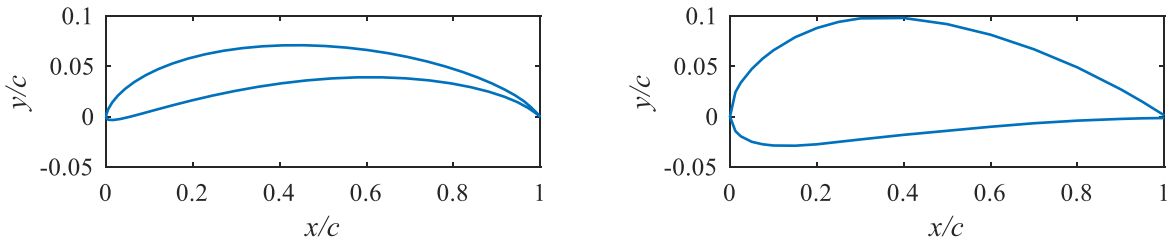

Figure 3-7: The cross section of the SF and the SP propellers resembles an (a) Eppler 63 airfoil, and (b) a NACA 4412 airfoil, respectively, obtained from Selig [49]

Two SF propeller blades with 4.7 and 6 inches / revolution (in/rev) pitch and two SP propellers with 5 and 6 in/rev pitch were used. All of the four propellers tested had a diameter of 12 inches and two blades. The nomenclature used in this paper to identify each propeller consists of an abbreviation of the propeller model, followed by the nominal diameter, multiplication sign, and the nominal pitch. For example, the SF model with 12 inch diameter and 6 inches/revolution would be SF12×6. The distributions of pitch angle and the chord length of the propeller blades in the radial direction were estimated by imaging the blade on two orthogonal planes. The pitch angle distribution is shown in Figure 3-8(a) while the chord length variation is shown in Figure 3-8(b).

The curves in Figure 3-8 (a) and (b) were obtained using 60 discrete measurement points along the radial direction on each propeller blade and fitted with a fourth order polynomial.

As per the manufacturer's recommendation, the structural maximum rotational speed for the SF and SP propeller models are 5,417 RPM and 15,833 RPM, respectively. Therefore, during the experiments the angular speed was maintained at a constant value of 5,000 RPM for the SF model, and 8,000 RPM for the SP model. Angular speed values above 8,000 RPM were achievable; however, for mechanical integrity and reduction of vibration of the system, operation was limited to 8,000 RPM.

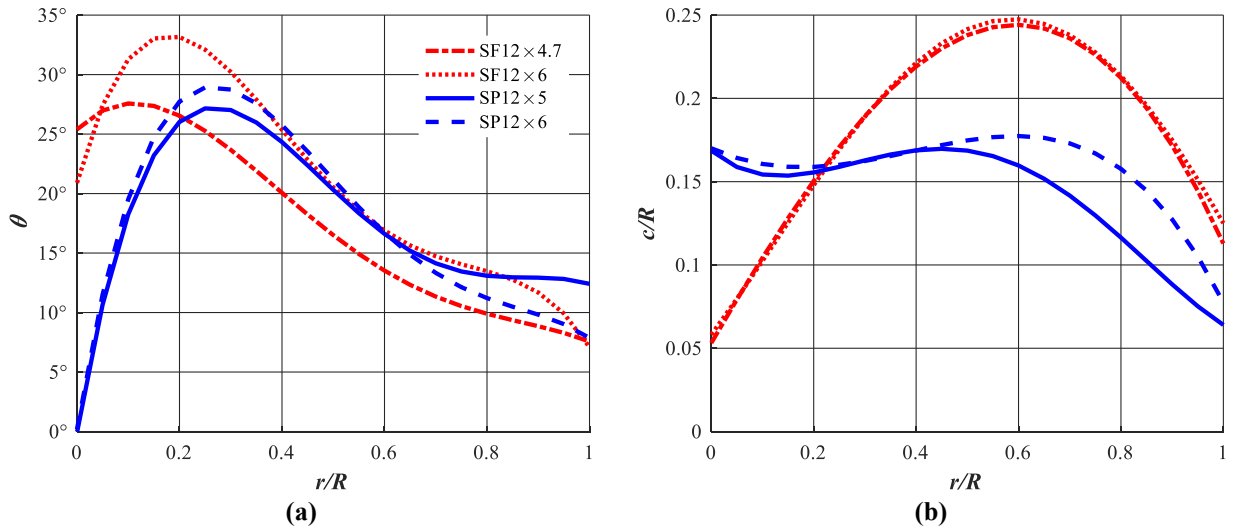

Figure 3-8: The geometric description of the propellers showing (a) the pitch angle distribution, and (b) chord length distribution of the four tested propellers estimated by projection of the blade shape on two orthogonal planes.

3.3.1 Propeller Angular Velocity Data Acquisition

The angular velocity of the propeller, Ω, was obtained as real time data during each experiment from the ESC. A DC voltage signal from an output auxiliary cable of the ESC was configured to provide the revolutions per minute of the motor shaft, and was acquired through a data acquisition card (DAQ) (NI USB-6218, National Instruments) with 16 bit resolution, which was connected to a computer where the data was compiled using LabVIEW. The RPM data was acquired at a rate

of 10 Hz, accounting for 600 data points for each test run. The data logging and the control of the BLDC motor using a pulse width modulation (PWM) signal control are also performed using the NI USB-6218 DAQ card with LabVIEW (National Instruments) interface.

3.4 Support System

The propeller, motor and load cell are connected to a custom made stinger supported by a cylindrical 1.5 inch diameter vertical shaft as shown in Figure 3-9 for the case of the ducted propeller investigation, and in Figure 3-10 for the case of the propeller at non-zero angle-of-attack investigation. The stinger support was designed and manufactured to have minimal interference on the upstream and downstream flow. The vertical shaft is connected to a rotary turntable located below the wind tunnel floor. The stinger support extrudes 1.2 m into the wind tunnel, placing the rotating axis of the ducted propeller model at the center of the test section. The stinger support is shown in Figure 3-11(a), it is made of aluminum and separates the rotor disk plane from the vertical support shaft by 367 mm. Adapting plates were designed to connect the stinger support to the load cell, and the load cell to the propeller system. All connections are fastened through bolted connections. To hold the ducts in place, two sets of three 5 mm diameter support shafts are attached to the adapting plates, separated by 60.5 mm. The turntable is manually operated, and allows the rotor disk to be rotated 360° about the longitudinal axis of the vertical shaft, in increments of $1 \pm 0.5°$. The angle-of-attack α_P is defined as the angle generated between the z-axis of the coordinate system and the free stream velocity, as represented in Figure 3-11(b). In this thesis, $\alpha_P = 0°$ represents the condition of axial flow in which the free stream is perpendicular to the rotor disk. The $\alpha_P = 90°$ represents the condition of complete edgewise flow when the free-stream is parallel to the rotor disk. In addition, a custom made stinger support holds the load cell, propeller system and duct. For the mechanical details of the support system assembly refer to Appendix D.

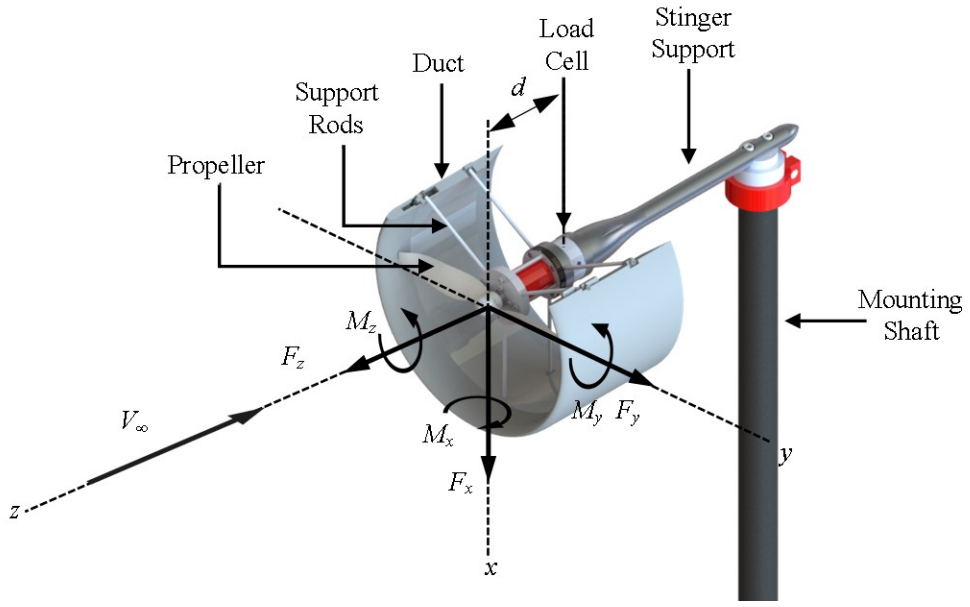

Figure 3-9: Schematic of the ducted propeller setup used in this investigation. The mounting shaft is held upright by a turntable located beneath the wind tunnel floor. The origin of the coordinate system is located at the center of the rotor disk plane.

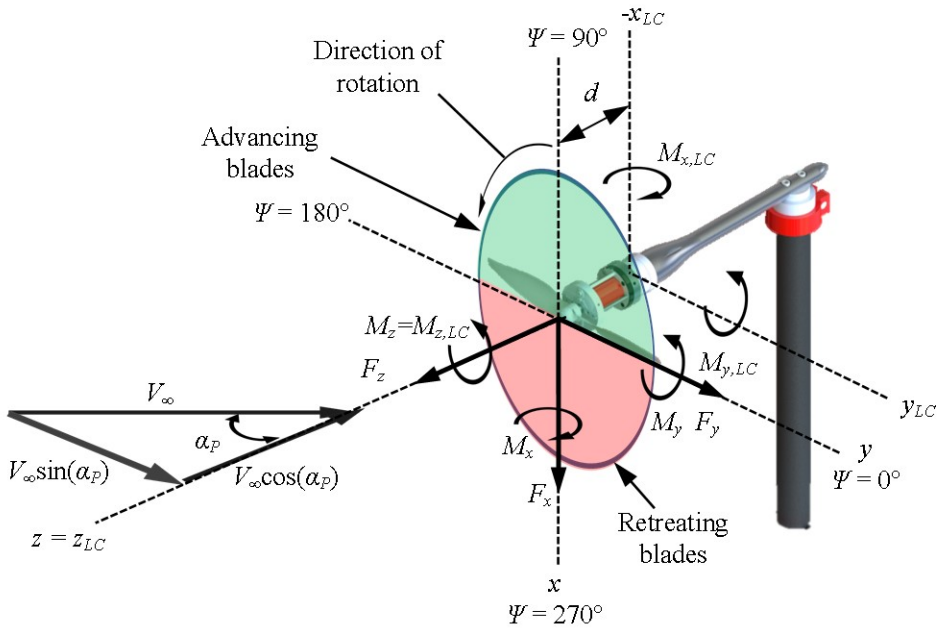

Figure 3-10: A schematic view of the experimental setup when an angle-of-attack of $\alpha_P > 0°$ is applied, showing the main components and the coordinate systems. The trigonometric breakdown of the free-stream velocity is shown.

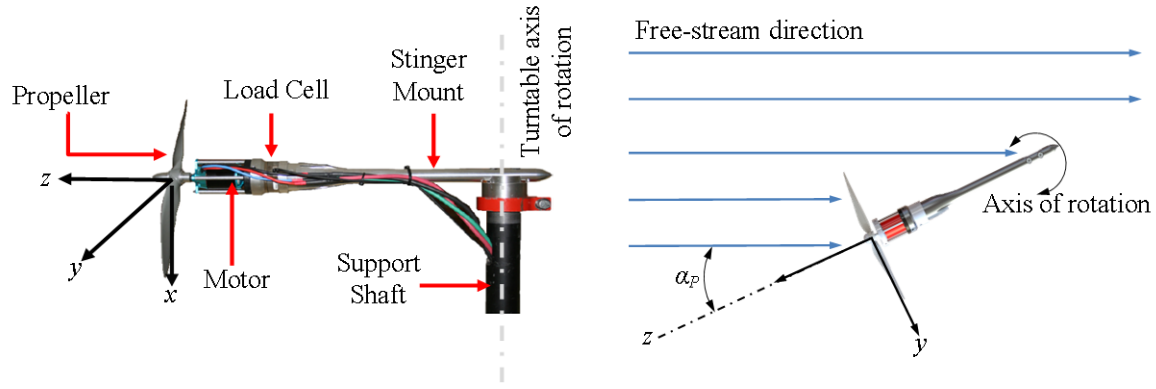

(a) **(b)**

Figure 3-11: A detailed view of the components in the stinger support are shown in (a). In (b), a top view schematic showing the definition of the rotor disk angle-of-attack, α_P, is shown.

3.5 Aerodynamic Load Measurements

Aerodynamic forces and moments acting on the directions x, y and z as defined by the coordinate system of Figure 3-9 is obtained using a six-axis force/torque transducer (Mini45, ATI Industrial Automation). This load cell is capable of measuring the three force components, F_x, F_y, and F_z (thrust), as well as the three components of moments M_x, M_y, and M_z, along the coordinates x, y and z, respectively, shown in Figure 3-9 and Figure 3-10. The origin of the coordinate system is located at the center of the rotor disk plane, at a distance of d = 108 mm upstream of the load cell, as shown in Figure 3-9. The sensitivity and resolution of the load cell (as provided by the manufacturer) in each direction are summarized in Table 3-2. The transducer is capable of measuring forces in the range of ±145 N for the F_x and F_y components, ±290 N for the F_z component, and ±5 Nm for all the moments. The coordinate system of the load cell is specified with x_{LC}, y_{LC} and z_{LC} in Figure 3-10 and has the same orientation as the coordinate system of the propeller. The origin of the load-cell coordinate system is located at x=0, y=0 and z=-108 mm with respect to the propeller coordinate system.

The blade rotating against the free-stream is called the 'advancing' blade, and the blade rotating in the direction of the free stream is indicated as the 'retreating' blade for a propeller operating at a non-zero value of α_P. As a result of variation in the incident velocity vector at the leading edge of the blade, the advancing and retreating blades operate at different effective angle-of-attack, α_b.

The force imbalance between the advancing and retreating blades also results in a moment about the x and y axis of the propeller. To obtain these moments, M_x and M_y, respectively, the moment produced by the product between the side forces F_y, F_x and the moment arm d = 108 mm measured at the load-cell has to be considered. Therefore, M_x and M_y are calculated by subtracting these products from the total moment measured by the load cell, as follows

$$M_x = M_{x,LC} - F_y \cdot d \quad \textbf{3-2}$$

$$M_y = M_{y,LC} - F_x \cdot d \quad \textbf{3-3}$$

Since the propeller's hub and motor are concentric with the load cell, the forces F_x and F_y do not contribute to the moment M_z. Therefore, the torque required to rotate the propeller is equal to the moment M_z and the required power , P, is obtained as:

$$P = M_Z \cdot \Omega \quad \textbf{3-4}$$

where Ω is the angular velocity in rad/s.

Table 3-2: The technical specifications of the Mini45 six-axis load cell used in this investigation

Sensing Ranges				Resolution			
F_x, F_y	F_z	T_x, T_y	T_z	F_x, F_y	F_z	T_x, T_y	T_z
±145 N	±290 N	±5 Nm	±5 Nm	1/16 N	1/16 N	1/752 Nm	1/1504 Nm

3.5.1 Verification of Load Cell Accuracy at Low Loads

The calibration certificate obtained from the manufacturer indicated that the load cell has a measurement uncertainty of 2.175 N in the z-direction. Preliminary tests of the ducted propeller system in hover revealed that the expected F_z was in the range of 0-20 N; thus, an uncertainty of 2.175 N would represent a minimum uncertainty of approximately 11%, and even higher uncertainty at lower loads. Therefore, four trial tests were performed using fixed weights with masses of 10 g, 20 g, 50 g, 100 g, 200 g, 500 g and 1000 g, to further evaluate the accuracy of the load cell in the z direction at low load applications. The force measured by the load cell has been compared to the calculated force in Figure 3-12(a), and the percent discrepancy ϵ_{Fz} between these two values is shown in Figure 3-12(b). It can be observed from these results that the accuracy of the load cell increases with increasing load applied, and that loads above 1 N provide results with under 2% discrepancy with respect to the calculated values.

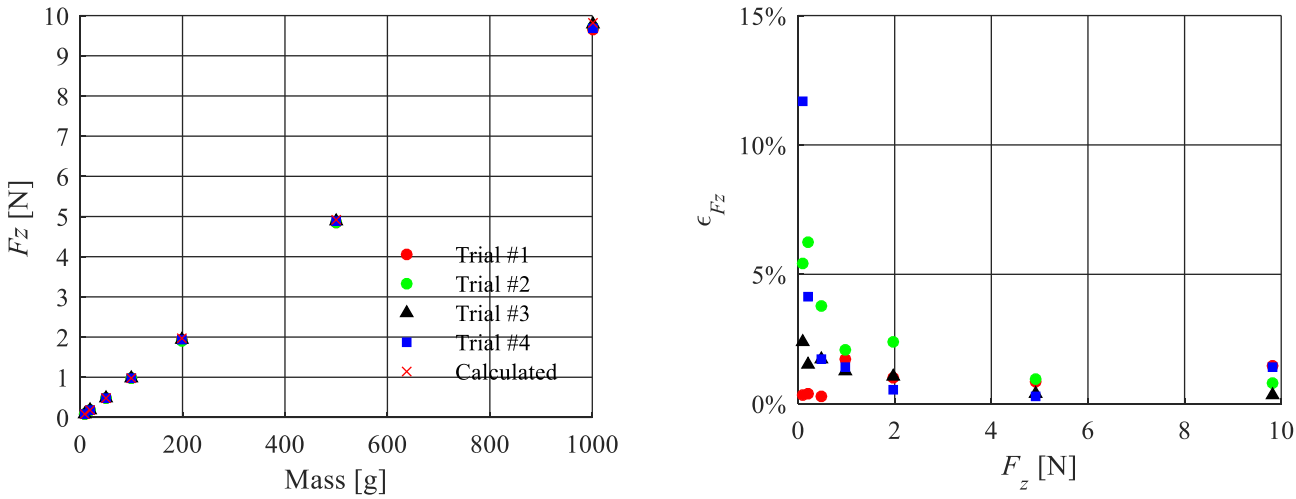

Figure 3-12: The results of the load cell's accuracy at low loads. (a) The F_z response as a function of the test mass applied to the load cell in the z direction. (b) The percent discrepancy between the load cell measurement F_z and the calculated force as a function of the applied load.

3.5.2 Load Cell Repeatability and Measurement Uncertainty

The repeatability of the load measurements was tested using the untrimmed APC 11×7 propeller at four free stream speeds of $V_\infty = 0$ m/s, 5 m/s, 10 m/s and 15 m/s, while maintaining a constant rotational speed of 6000 RPM. Three runs were completed at these conditions for a total of 12 data points, three for each J. The results of the thrust and torque responses are shown in the graphs of Figure 3-13 (a) and (b), respectively. From the thrust force trials in Figure 3-13 (a) the maximum standard deviation in was found to be 0.31 N, and from the torque trials in Figure 3-13 (b) the maximum standard deviation in torque was found to be 0.008 Nm.

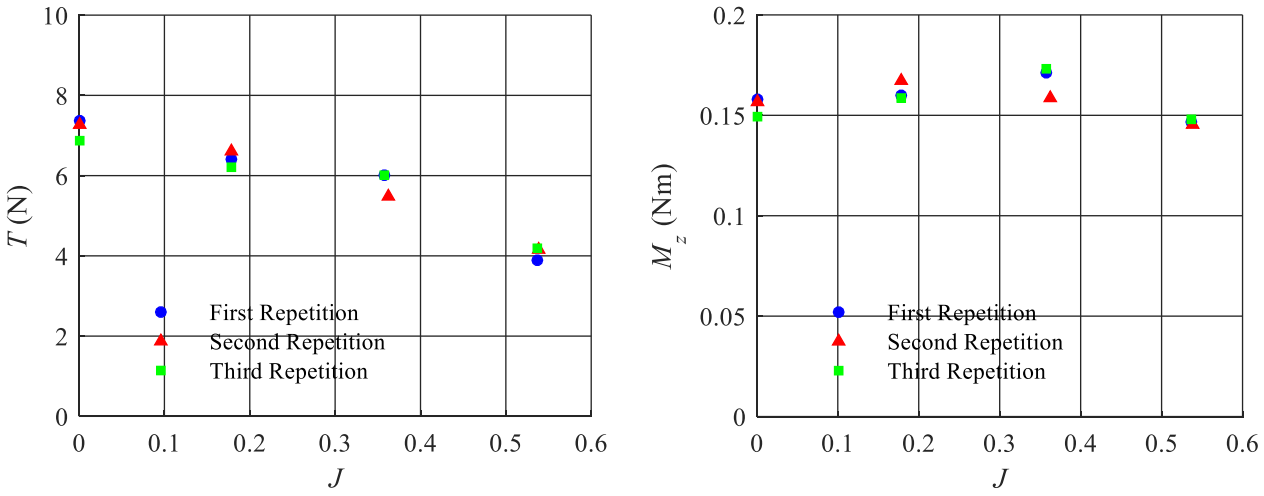

Figure 3-13: Repeatability test results showing the (a) thrust response and (b) torque response, both as a function of the free stream advance ratio *J*.

Uncertainty in the non-dimensional coefficients were calculated using the principle of propagation of uncertainty. As an example, the equation for uncertainty in the non-dimensional coefficient of thrust, δC_T, is shown below

$$\delta C_T = \sqrt{\left(\frac{\partial C_T}{\partial T}\delta T\right)^2 + \left(\frac{\partial C_T}{\partial n}\delta n\right)^2 + \left(\frac{\partial C_T}{\partial \rho}\delta \rho\right)^2 + \left(\frac{\partial C_T}{\partial D_P}\delta D_P\right)^2} \qquad \textbf{3-5}$$

where the partial derivatives in equation 3-5 are calculated as

$$\frac{\partial C_T}{\partial T} = \frac{1}{\rho n^2 D_P^4}$$

$$\frac{\partial C_T}{\partial n} = -\frac{2}{\rho n^3 D_P^4}$$

$$\frac{\partial C_T}{\partial \rho} = -\frac{1}{\rho^2 n^2 D_P^4}$$

$$\frac{\partial C_T}{\partial D_P} = -\frac{4T}{\rho n^2 D_P^5}$$

and where δT, δn, $\delta \rho$, δD_P are the relative uncertainties in thrust, revolutions per second of the propeller, air density and rotor disk diameter, respectively. The aforementioned uncertainties were

calculated considering the systematic or bias uncertainty, β, and the random uncertainty, Π, such that the value of the individual uncertainties is

$$\delta = \sqrt{\beta^2 + \Pi^2} \quad \textbf{3-6}$$

The systematic uncertainty is obtained from the precision of the equipment used to perform the measurements, and the random uncertainty has been calculated from the equation

$$\Pi = t_{\alpha/2} \frac{S}{\sqrt{N}} \quad \textbf{3-7}$$

where $t_{\alpha/2}$ is the are under the *t*-distribution curve with a 95% confidence level ($\alpha = 0.05$), S is the standard deviation of the measurements, an N is the number of trials. The relative uncertainties of C_P and C_T for V_∞ = 0 m/s and 15 m/s are shown in Table 3-3.

Table 3-3: Relative uncertainty in CT and CP at free stream velocities V_∞ = 0 m/s and 15 m/s and n = 6000 RPM.

Coefficient	V_∞ = 0 m/s	V_∞ = 15 m/s
$\delta C_T/C_T$	4.24%	6.32%
$\delta C_P/C_P$	4.32%	4.34%

3.5.3 Data Acquisition Procedure for Aerodynamic Loads

The output voltage from load cell was in the range of ±10 V and was acquired using the same DAQ card used to gather the angular velocity data from the motor. The load measurement tests were conducted for a duration of 60 seconds at an acquisition frequency of 100 Hz, which translated to 6000 data points per test run. The RPM of the propeller and the load measurements were recorded simultaneously. The load measurement acquisition procedure consisted of the following steps:

Step 0. The computer and load cell are turned on, while the propeller remained stationary and the wind tunnel was not running. At this step the load cell readings indicates random noise, which could manifest as positive or negative voltages.

Step 1. The wind tunnel was set to the corresponding test V_∞ value, monitored continuously from the Pitot tube readings. The wind tunnel speed was controlled using a rotating knob to set the frequency for the variable frequency drive (VFD) motor of the wind tunnel fan. The knob position was fixed when the Pitot tube reading reported a velocity within ±0.05 m/s of the desired V_∞. At this step the load cell readings indicate a decrease in F_z with respect to the value at Step 0, corresponding to the drag force experienced by the setup.

Step 2. With the propeller still stationary and the wind tunnel running, the load cell was biased (zeroed), setting the load cell values of F_x, F_y, F_z, M_x, M_y and M_z to zero.

Step 3. The propeller motor was turned on, and the PWM signal was manually controlled until the desired RPM was achieved within ±50 RPM. After the RPM was set, data collection began, and the load as well as RPM were recorded. The F_z value recorded by the load cell was thus the net force in the z direction of the system. The air temperature before and after the tests was recorded.

A graphic representation of this procedure has been summarized in Figure 3-14 below.

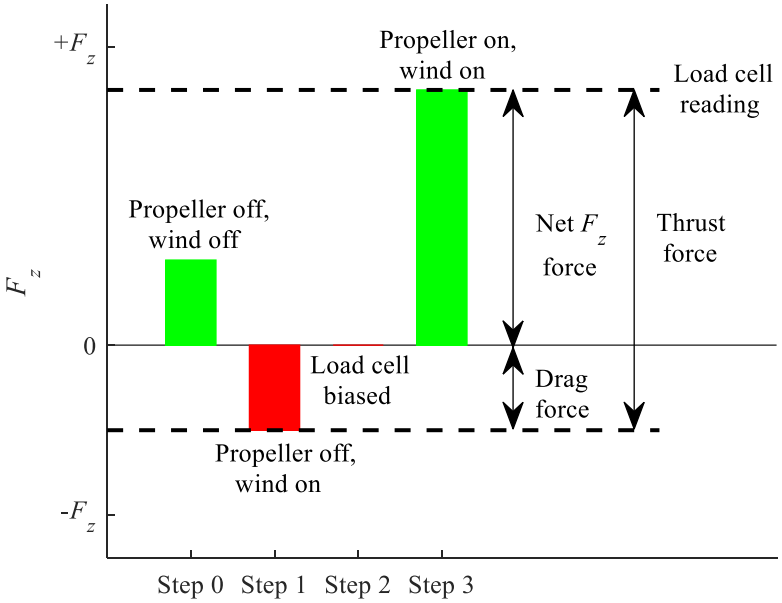

Figure 3-14: Description of the load measurement acquisition procedure. The green bars represent positive F_z reading, while the red bar represents negative readings. The graph summarizes what the load cell response is at each step of the data collection process.

3.6 Flow Measurement with Particle Image Velocimetry

Images of the flow immediately upstream and downstream of the ducted propeller and open propeller were acquired, and velocity vector fields were obtained from these images using Particle Image Velocimetry (PIV). In the following sub-sections a brief introduction to the basic technical background and history on the advancements of this technique will be provided. Lastly, the details of the PIV setup used in the current investigation will be discussed. For both of the PIV experiments the ducted tests were conducted using the LE1-DA18-0.14 with the trimmed SP11X7 propeller, and for the open propeller tests the untrimmed SP11X7.

3.6.1 Introduction to Particle Image Velocimetry (PIV)

Particle Image Velocimetry, or PIV, is a non-intrusive flow visualization technique that uses high sensitivity imaging to obtain quantitative information about the flow field characteristics of a region of interest in the flow. In a basic PIV setup the flow in study is "seeded" with tracer particles and the region of interest in the flow is illuminated by a light source (typically a Laser) at least twice, while a high sensitivity camera captures images of this region. A simplified schematic of this setup is shown in Figure 3-15.

A common laser choice for PIV applications is the Nd-YAG laser (Neodymium-doped Yttrium Aluminum Garnet). According to Adrian [26], the first appearance of Nd-YAG lasers in PIV applications took place in 1986 in the experiments by Kompenhans and Reichmuth [32]. To illuminate an area or volumetric section of the flow the laser beam must be converted to a sheet of a certain thickness through the use of laser optics including mirrors, spherical or cylindrical lenses. The region in the flow that is captured by the cameras is referred to as the field of view (FOV) as indicated in Figure 3-15. The seeding particles can range in size from 1 μm to 30 μm in diameter, and for gaseous flows these particles may be polycrystalline, glass, oil smoke, corn oil, oil, olive oil, TiO_2, Al_2O_3, and others ([50]). Seeding particles flowing through this region of interest reflect the light and scatter it in all directions; however, the intensity of the scattered light will depend on the ratio of the refractive index of the particles to that of the medium, the particle shape, size and orientation. The particles must be small enough to follow the natural motion of the flow, but large enough to reflect enough light for the cameras to capture ([51]). The scattered light is captured by double frame, high sensitivity cameras that digitize the images and send them to a computer for processing. The time step Δt between the two frames must be long enough to detect the motion of

the particles, but short enough to prevent losing particles that move in the out-of-plane direction (Raffel *et. al.* [51]).

In the processing software the image is divided into smaller sub-regions denominated interrogation windows (IW), shown in Figure 3-15, where through the use of statistical operations such as cross-correlation or autocorrelation a particle displacement peak local to the IW is yielded. From this result the velocity vector in that IW can be derived; an consequently a complete velocity field within the FOV is obtained.

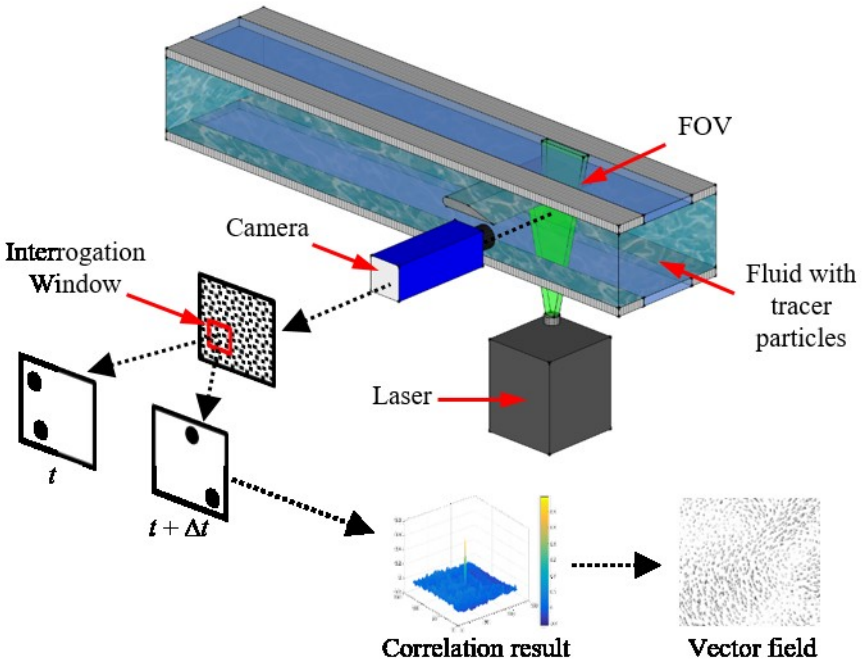

Figure 3-15: A simplified schematic of a PIV experiment showing a planar PIV setup with one camera studying the flow incident on an object immersed in seeded flow. It is shown how the digitized two-frame image is sectioned into smaller interrogation windows, which upon realization of image correlation yields a displacement peak used to recreate the complete vector field.

The conventional PIV setup shown in Figure 3-15 where a single camera is implemented provides two dimensional results which is sometimes referred to as planar PIV or 2D-PIV since only two components of the velocity vector can be retrieved from the images. However, the retrieval of all three components of velocity is possible through three dimensional PIV methods such as

stereoscopic or tomographic PIV. In stereoscopic PIV two cameras are used to obtain the perspective distortion of a displacement vector with respect to one of the cameras and thus allowing the reconstruction of the three components of velocity (Raffel *et. al.* [51]). In stereoscopic PIV the precision of the out-of-plane component of velocity increases as the angle between the two cameras approaches 90°. Raffel *et. al.* [51] suggests that for stereoscopic PIV a camera aperture setting of $f_{\#} < 4$ is required to adequately image small particles, and highlights that this requirement carries the effect of a small depth-of-field which can only be accommodated by the adjustment of the optical planes according to the Scheimpflug criterion, in which the object, lens and image planes are adjusted to coincide as shown in Figure 3-16.

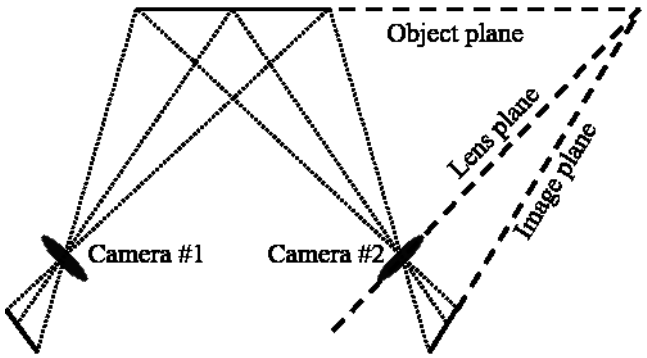

Figure 3-16: The basic configuration used in stereoscopic PIV, showing the Scheimpflug criterion in which the image plane is tilted with respect to the camera plane (adapted from Raffel *et. al.* [51]).

Particle Image Velocimetry formally begun in the 1980's, previous to that date scientists such as Ludwig Prandtl were already using flow visualization techniques similar to tuft and dye visualization to obtain qualitative information from the flow fields ([51]). Adrian [52] describes PIV as "the accurate, quantitative measurement of fluid velocity vectors at a very large number of points simultaneously". The pioneer attempt to visualize fluid flow with optical systems was done by three different groups of contemporary researchers, Barker and Fourney [53], Dudderar and Simpkins [54] and Grousson and Mallick [55]. These three groups utilized the method of laser speckle, used on solids, and demonstrated that it too could be implemented in fluid flows ([52]). The application of this technique on fluid flows was mastered by Meynart at the v. Karman institute in Belgium, and at that time, it was named Laser Speckle Velocimetry ([52]). However, due to findings from Pickering and Halliwell [56] and R. J. Adrian [57] which suggested that speckle patterns would not be generated in fluid particles, the name Particle Image Velocimetry was

adapted, in order to differentiate between the two techniques ([52]). The high demand and interest of investigating turbulent flows motivated the scientists involved in the field to develop a system that would be able to obtain high speed images of small particles, since these characteristics are necessary to study such flow fields.

One of the challenges faced by the scientific community in the development of PIV was the computational power required to process significant amounts of data. In 1985, the common digital computer was a DEC PDP 11/23, with typically 128 KB of RAM and 30 MB of hard drive ([52]), making it extremely difficult to resolve the Fourier transforms required for two-dimensional correlation ([52]). With the advancements of technology, the processing power of computers increased significantly, allowing for larger amounts of data to be processed more rapidly. Another important factor which improved the PIV technique was the transition from photographic image recording to digital image recording ([52]). This change allowed for a greater number of images to be analyzed, and removed the tedious aspects related to manual correlation of images. Digital PIV assumed its current potential with the introduction of interline transfer cameras, also known as double frame cameras, which can hold two frames recorded rapidly one after the other ([52]).

3.6.2 Inlet Flow Visualization using Stereoscopic PIV

To characterize the flow field at the inlet of the ducted propeller system a stereoscopic PIV setup was applied to an area in the *yz*-plane immediately upstream of the rotor disk at the $x = 0$ mm location as shown in Figure 3-17. A stereoscopic setup was chosen not because the third component of velocity was of interest, but because it allowed the acquisition of flow data (to a limited extent) inside of the duct. If a planar PIV setup was used, the visualization of the flow immediately upstream of the rotor disk plane would not have been possible, since the duct would have blocked the F.O.V of the cameras. An Nd-YAG laser (Quanta-Ray PIV 400, Spectra Physics) that operates at a wavelength of 532 nm and 400 MJ/pulse was used. The laser has a maximum operational frequency of 10 Hz and a pulse length of 5-8ns. The CCD double-frame cameras used had an image sensor size of 1376 × 1040 pixels and a 12 bit resolution (ImagerIntense, LaVision), with a pixel size of 6.45 μm×6.45 μm. The FOV captured was 148 mm×112 mm ($0.62D \times 0.47D$) and it covers the area defined by the ranges $0 \leq y \leq 0.62D$ and $0 \leq z \leq 0.47D$. The location and relative size of the FOV are shown in Figure 3-17. Photographs of the Stereoscopic PIV setup may be found for reference in Appendix B. The cameras were located above and below the wind

tunnel's acrylic ceiling and glass floor, positioned at an angle of 105° from each other as shown in Figure 3-18. To achieve coincidence of the sensor, lens and object planes both cameras were equipped with Scheimpflugs, which were adjusted during the calibration process and kept during the data acquisition stages of the investigation. Both cameras were equipped with the same 50 mm focal length lens (Sigma), and were set to the same aperture setting $f_{\#} = 4$. The alignment of the laser beam at the desired location was achieved through the use of mirrors (LaVision), and the transition from a laser beam to a ~2 mm thick laser sheet was achieved with a collimator (LaVision). With these settings, a magnification of $M = 0.06$ and a spatial resolution of 0.108 mm/pixel was achieved. The seeding particles used were generated using a fog generator (Fog Storm 1700 HD) that heated and emanated smoke from a glycerin based solution (Water Base American DJ Fog Juice™), which provided particles of 1-5 μm in diameter. The fog machine was operated remotely and the seeding particles were injected to the flow from the low speed section of the wind tunnel.

A total of 400 images were acquired for each test at a rate of 5 Hz. The time step between the image frames was adjusted on each test run according to the V_∞ and configuration (duct or no duct) corresponding to the test in order to achieve an average pixel displacement at the region of maximum velocity of ~4-12 pixels. Table 3-4 summarizes the corresponding Δt value used in each test. To reduce the amount of glare from the components of the setup the stinger support, ducts, propeller and hub were spray painted with a < 1 mm layer of black paint.

Table 3-4: The Δt values used on each stereoscopic PIV test, adjusted accordingly to achieve an average pixel displacement of 5-12 pixels at the region of maximum velocity.

Test V_∞ (m/s)	Δt (μs)	
	Open Propeller	Ducted Propeller
0	80	80
5	80	80
10	80	80
15	60	60

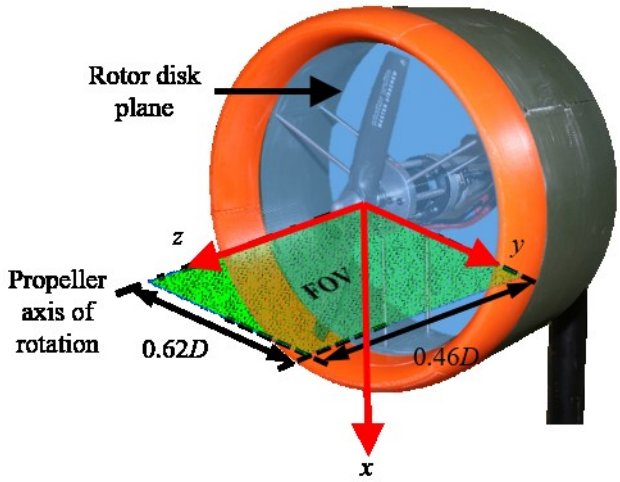

Figure 3-17: The description of the location and relative size of the FOV used in the planar PIV experiment.

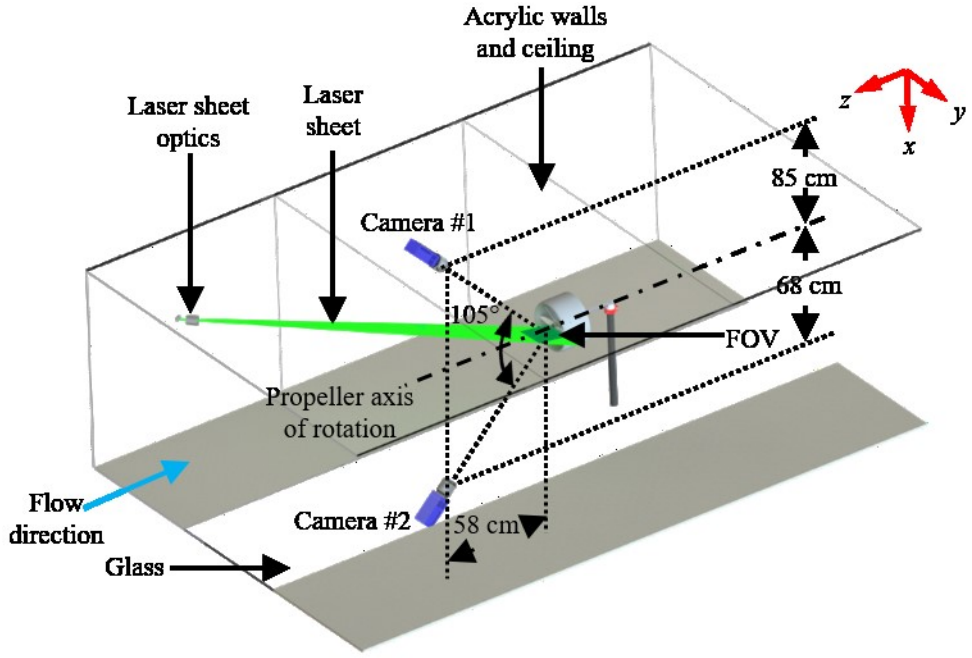

Figure 3-18: Schematic of the stereoscopic PIV setup used to visualize the flow entering the rotor disk of the ducted propeller and open propeller systems.

3.6.3 Exit Jet Visualization Using Planar PIV

The exit jet flow was characterized by applying planar particle image velocimetry to an area 127 mm×96 mm (0.53*D*×0.4*D*) shown in Figure 3-19 that is located at the wake region of the *yz*-

plane, located at $x = 0$ mm, immediately downstream of the trailing edge of the ducts. The FOV obtained covers the area defined by the ranges $0.28D \leq y \leq 0.68D$ and $0.58D \leq z \leq 1.11D$, and it was maintained at the same location for both the open and ducted propeller tests. The camera, lens, laser, optics, seeding particles and fog machine used in this experiment are the same as the ones used in the stereoscopic PIV experiment. A schematic of the arrangement in this experiment is provided in Figure 3-20, showing the location of the camera, laser sheet and ducted propeller setup. In this experiment the camera was also equipped with a UV filter to reduce the glare from the setup. The aperture setting used was $f_{\#} = 4$. The laser sheet used in this experiment was also adjusted to have a thickness of ~2 mm. With this configuration a digital resolution of 0.092 mm/pixel and a magnification of $M = 0.07$ was achieved. For each test 400 images were acquired at a rate of 5 Hz. In the same manner of the stereoscopic PIV experiment, the Δt was adjusted according to the average pixel displacement obtained, and the final Δt choices are summarized in Table 3-5.

Table 3-5: The Δt values used on each planar PIV test, adjusted accordingly to achieve an average pixel displacement of 5-12 pixels at the region of maximum velocity.

Test V_∞ (m/s)	Δt (μs)		
	Open Propeller		Ducted Propeller
	Untrimmed	Trimmed	
0	80	80	80
5	80	80	80
10	60	60	80
15	60	60	60

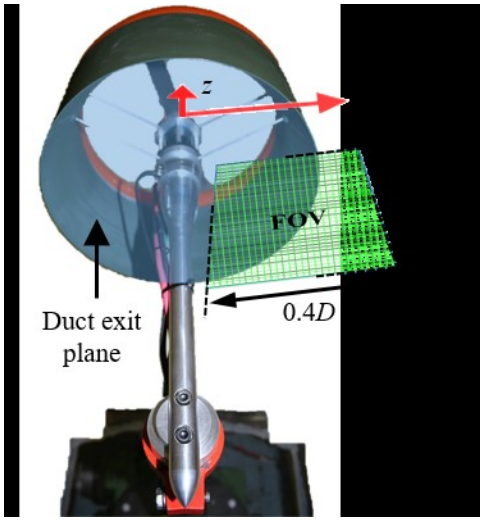

Figure 3-19: The description of the location and relative size of the FOV used to visualize the flow exiting the ducted and open propeller. The location of the FOV was unchanged when switching from the ducted to the open propeller configuration

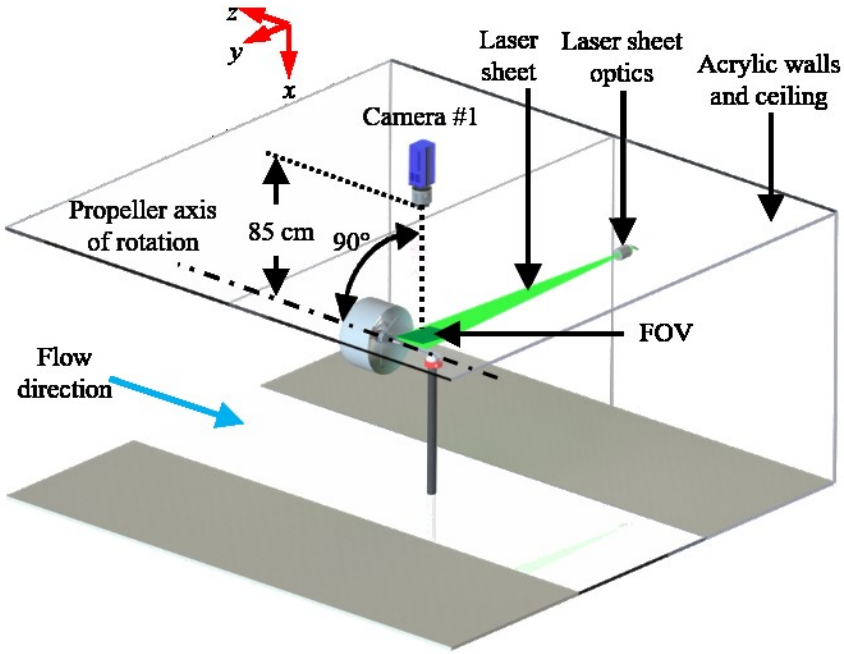

Figure 3-20: Schematic of the planar PIV setup used to visualize the flow in the wake region of the ducted propeller and open propeller systems.

3.6.4 Image Processing

The PIV images were processed using DaVis 8.4.0. Details of the image processing parameters for both the inlet flow and exit jet visualization tests are presented in Table 3-6. Pre-processing was performed on the images to improve the contrast and remove the glare from stationary objects in the FOV such as the duct. This procedure consisted on subtracting the minimum intensity of the ensemble from the individual images, multiplying the difference by a factor which would result in saturation of particles resultant from excessive glare, and lastly normalizing the multiplied images by the average of the difference. For both the stereoscopic and planar PIV images a multi-pass correlation process was used with an initial IW size of 64×64 pixels and a secondary IW size of 32×32 pixels. The set of inlet flow images with the ducted propeller system at V_∞ = 5 m/s, 10 m/s and 15 m/s contained several images with excessive reflection from the duct's leading edge internal surface and the aluminum support rods, which resulted in a large number of missing vectors in the correlation. As previously mentioned, in-situ attempts to reduce this reflection included coating the duct, propeller blades and hub with black paint, as well as covering reflective equipment located within the FOV of the cameras with black covers and black tape.

Table 3-6: The details of the image processing for the stereoscopic and planar PIV experiments.

Visualization region	Inlet (V_∞=0 m/s, 5 m/s)		Exit jet	
Magnification	0.06		0.07	
Digital resolution	0.108 mm pixel^{-1}		0.092 mm pixel^{-1}	
Measurement field	148 mm×112 mm 0.62D×0.47D		127 mm×96 mm 0.53D×0.4D	
Velocity vector	Double-frame, multi-pass stereo correlation		Double-frame, multi-pass correlation	
Interrogation window (IW)	First pass: 64×64 pixels 6.91 mm×6.91 mm	Second pass: 32×32 pixels 3.46 mm×3.46 mm	First pass: 64×64 pixels 5.89 mm×5.89 mm	Second pass: 32×32 pixels 2.94 mm×2.94 mm
IW overlap	50%	75%	50%	75%
Vectors per field	136×133		172×130	

The in-situ solutions proved to be insufficient, and pre-processing steps were applied to the acquired images, in order to reduce the effect of glare. Attempts to correct the images included the application of a geometric mask to the region were the leading edge was located, as well as a low-pass intensity filter; however these were only partially successful.

Ultimately, to improve the quality of the correlation on the ensembles for the ducted propeller tests at V_∞ = 5 m/s, 10 m/s and 15 m/s, the images were pre-processed by subtracting the minimum of the ensemble from all the images as previously done, subtracting the sliding background with a scale length of 5 pixels, and applying an algorithmic mask. For the mask, pixels with an intensity count greater than 90 counts were masked out. The first pass of the processing stage for these ensembles was performed with no overlap between the IW, and the IW size of the second pass was increased to a 48×48 pixel window size. The processing details for these ensembles are provided in Table 3-7 In addition to these actions no additional post-processing operations were applied to the remaining sets. The resultant vector fields, as well as the flow characteristics derived from them, were plotted using MATLAB 2017b.

Table 3-7: The details of the image processing for the stereoscopic PIV inlet visualization experiment at V_∞= 10 m/s and V_∞= 15 m/s.

Visualization region	Inlet (V_∞=10 m/s, 15 m/s)	
Magnification	0.06	
Digital resolution	0.108 mm pixel^{-1}	
Measurement field	148 mm×112 mm 0.62D×0.47D	
Velocity vector	Double-frame, multi-pass stereo correlation	
Interrogation window (IW)	First pass: 64×64 pixels 6.91 mm×6.91 mm	Second pass: 48×48 pixels 5.18 mm×5.18 mm
IW overlap	0%	75%
Vectors per field	91×89	

3.7 Test Matrix

The investigation was completed over three measurement campaigns. Details of the parameters and test conditions of each campaign are summarized in Table 3-8. In the first campaign load measurements of the performance of the LE1.5-DA9-0.06 and LE1.5-DA18-0.06 ducted propeller systems with the trimmed MA11×8 propeller, as well as the OP with the trimmed MA11×8 were conducted to investigate the effect of changing the diffuser angle, and to compare the performance between the ducted and open propeller systems. The tests were conducted at free-stream velocities ranging from 0 m/s to 10 m/s and propeller angular speeds ranging from 6000 RPM to 9000 RPM, corresponding to an advance ratio range of $0 < J < 1.1$. The results of this campaign are presented in section 4.1.

In the second measurement campaign load measurements of the performance of the LE1.5-DA18-0.06 and LE1.5-DA18-0.14 ducted propeller systems with the trimmed SP11×7 propeller, as well as the OP with the trimmed SP11×7 propeller were obtained to test the effect of changing the duct thickness-to-chord ratio. The tests in this campaign were conducted at free stream velocities ranging from 0 m/s to 12 m/s. The results obtained in the first campaign showed that the data at $n < 5000$ RPM was unreliable due to increased fluctuations in n, therefore the n range was restrained to 6000 RPM-9000 RPM, which corresponds to an advance ratio range of $0 < J < 0.63$. The results of this campaign are presented in section 4.2.

In the third measurement campaign load measurements of the performance of the LE1-DA18-0.14 ducted propeller with the trimmed SP11×7 propeller as well as the OP with the untrimmed SP11×7 propeller were obtained in order to investigate the potential of reducing the propeller diameter through the implementation of the duct. The untrimmed OP has a rotor disk diameter that is 21.1% larger than the rotor disk used for the ducted propellers and the trimmed OP. The results are also compared to the performance of the OP with the trimmed SP11×7 propeller. Additional to the performance load measurements PIV images were acquired in this campaign for the inlet and exit jet flow regions for the LE1-DA18-0.14 ducted propeller with the trimmed SP11×7 propeller as well and the OP with the untrimmed SP11×7 propeller. Wake PIV images were also obtained for the OP with the trimmed SP11×7 propeller. The number of data points (J values tested) was reduced to four per configuration, and the n was fixed to 6000 RPM. The propeller's rotation was reduced in this measurement campaign in order to obtain a wider range of J. The load measurement

results of this campaign are presented in sections 5.1 to 5.3, and the inlet and exit jet PIV results are covered in sections 4.4 and 4.5, respectively. All three measurement campaigns covered axial flow tests exclusively ($\alpha_P = 0°$).

Table 3-8: Summarized test matrix of the investigation on the performance of a 240 mm ducted propeller system.

Measurement Campaign	Configurations Tested	V_∞ (m/s)	J	n (RPM)	Propeller Used
1: Preliminary load measurements	Trimmed Open Propeller LE1.5-DA9-0.06 LE1.5-DA18-0.06	0-10	0-1.1	6000-9000	Master Airscrew 11×8
2: Load measurements	Trimmed Open Propeller LE1.5-DA18-0.06 LE1.5-DA18-0.14	0-12	0-0.63	6000-9000	APC Sport 11×7
3: Load measurements + PIV	Trimmed Open Propeller Untrimmed Open Propeller LE1-DA18-0.14	0-15	0-0.65	6000	APC Sport 11×7

The experimental conditions of the propeller at non-zero angle-of-attack investigation are summarized in Table 3-9. The free-stream velocity was varied in increments of 2 m/s, from zero to 14 m/s for the SF models, and from zero to 20 m/s for the SP propellers. The angle-of-attack of the propeller disk was varied in increments of 10° from $\alpha_P = 0°$ to 90° for each velocity, except for $V_\infty = 0$ m/s in which the value of α_P is irrelevant to the performance of the propeller.

Table 3-9: Summarized test matrix of the investigation of the investigation on propellers at non-zero angle-of-attack.

Propeller Model	Propeller pitch, inch/rev	n, RPM	V_∞, m/s with steps of 2 m/s	J	α_P with steps of 10°
Slow Flyer	4.7, 6	5,000	0 – 14	0 – 0.55	0° – 90°
Sport	5, 6	8,000	0 – 20	0 – 0.5	0° – 90°

3.8 Data Reduction

The rotor performance is evaluated by its propulsive efficiency η, which depends on thrust, power consumption, and the advance ratio, as described by the following expression:

$$\eta = \frac{C_T J}{C_P} \cdot 100 \qquad \textbf{3-8}$$

where C_T is the non-dimensional coefficient of thrust defined by Glauert [8] as:

$$C_T = \frac{F_z}{\rho n^2 D^4} \qquad \textbf{3-9}$$

and C_P is the non-dimensional coefficient of power, which using equation (4) for the propeller power, can be expressed as

$$C_P = \frac{M_z \Omega}{\rho n^3 D^5} \qquad \textbf{3-10}$$

In equations 3-9 and 3-10 the symbol ρ denotes the density of air. The density values used in the computation of these coefficients were obtained based on the average temperature recorded during each test. In the results section of this paper, the thrust, power and efficiency data are presented as functions of both J and J_a to evaluate the effect of changing the free-stream and the net inflow into the rotor disk on the performance of the propeller, respectively. In the case where the efficiency is presented as a function of J_a, it is represented by the symbol, η' calculated as

$$\eta' = \frac{C_T J_a}{C_P} \quad \textbf{3-11}$$

Similar to equation 3-10 the moments M_x and M_y are non-dimensionalized using the following expressions:

$$C_{M_x} = \frac{M_x \Omega}{\rho n^3 D^5} \quad \textbf{3-12}$$

$$C_{M_y} = \frac{M_y \Omega}{\rho n^3 D^5} \quad \textbf{3-13}$$

These coefficients will be used for evaluation of the experimental results and development of analytical models. The performance of the ducted and open propeller systems is presented through the non-dimensional performance coefficients C_T and C_P, as well as the propulsive efficiency η, and are presented as a function of the advance ratio J. To compute these coefficients, the n value used is the average of the experimentally obtained angular velocity. Fluctuations in the value of n is manifested in the results of the following sections as misalignment between data points that should fall under the same J. During the tests, the air temperature ranged from 22 °C to 24.5 °C. The air density used to compute C_T and C_P was calculated by interpolating between the properties of air at 20°C and 25°C at 1 atm, such that

$$\rho = -0.004 \frac{kg}{m^3 \cdot ℃} \cdot (Temperature - 20℃) + 1.204 \frac{kg}{m^3} \quad \textbf{3-14}$$

Chapter 4. Experimental Investigation on a Ducted Propeller for UAVs

The evident growth of UAV technology and drones has been in part due to the growing possibility of creating sufficient propulsion at ever smaller scales. For VTOL UAVs designed to perform several flight maneuvers during a single flight mission, the most popular propulsion method has been the implementation of propellers powered by electric motors, due to their potential thrust-to-weight ratio, low cost and versatility. The increase in demand of UAVs has sprouted interest in improving the operating efficiency of UAVs. In regards to propulsion, one method that has been applied to enhance propeller output is the use of ducts around the rotor disk. The first use of ducted propellers is attributed to Kort [5], where a boat "screw" propeller was enclosed by a converging nozzle (or duct). Kort [5] provided that at certain operating conditions, the ducted system offered thrust improvements over that of open screws. Soon after Kort's design, Stipa [6] applied the same principles to ducted propeller powered airplane, resulting in the design of the *Stipa Caprioni* (refer to Figure 1-2). Stipa [6] showed through wind tunnel experiments that his ducted propeller model produced higher thrust-to-power consumption ratios than open propellers with the same rotor disk diameter. This latter mentioned result has been found by all investigators of ducted propellers in the past, where performance measurements show that ducted propellers provide performance benefits in terms of thrust generation and increments in efficiency, only to a certain J value, in both marine ([29]) and aeronautical tests ([4]).

The performance benefits of ducted propellers at low J ranges has drawn the attention of VTOL aircraft designers, for both large scale and UAV applications. In theory, ducted propellers are capable of increasing the mass flow rate across the rotor disk, increasing the load on the blades along the radial direction ([21]). Simultaneously the duct can potentially take over a portion of the total thrust generated by the ducted propeller, thus *offloading* the propeller ([28]), and increasing the propulsive efficiency of the system. Potentially the flow immediately downstream of the propeller can remain attached to the internal walls of the duct, reducing the slipstream contraction of the flow ([23], [4], [22]). Additionally the placement of a duct around the propeller blades serve to mitigate the leak of flow due to downwash from the blades, and in turn, the generation of tip vortices which represent energy loses. However, the aforementioned performance enhancements have been evidenced for hovering and low advance ratios only (Pereira [4]).

A significant portion of the studies on ducted propellers have performed parametric studies on the geometry of the ducts. The duct shape can be defined in three different sections (not exclusively): first, the leading edge of the duct, usually designed with a prominent curvature to "draw in" the air surrounding the rotor disk. Second, a throat, or section of maximum internal area contraction, where the rotor disk is located to maximize the mass flow rate through the rotor disk plane. Lastly, although not always used, a diffuser section where the internal walls of the duct "diverge", intended to increase the cross-sectional area of the exit jet stream tube, and thus preventing the natural contraction of the flow created by the propeller. A major problem encountered by all experimenters who have performed parametric studies on the geometry of ducts for ducted propeller systems is that the majority of the geometric parameters of the duct are coupled with each other, making it difficult for researchers to isolate the effect of one specific design factor ([58]). For this reason there is no universal guideline for the design of ducts in ducted propeller systems. There exists however some common ground in regards to some features, for example, it has been determined that a small as possible δ_{tip} is desired to mitigate tip vortex generation. Experimental and numerical tests such as the ones performed by Akturk and Camci [26] have studied this concept. Akturk and Camci [27] determined that when using a ducted propeller, having a large enough tip clearance may result in a drop in performance even lower than an open rotor of the same diameter. The leading edge shape of the cross section of the duct has also been given particular importance, since it defines the pressure profile at the inlet of the rotor disk ([37]). Martin and Tung [38] determined that a large leading edge radius increases the thrust output of the ducted propeller system in hover conditions. Several studies such as the experiment by Abrego and Bulaga [36] have concluded that the length of the duct has negligible effects on the aerodynamic performance of the system.

Studies on the diffuser section have investigated the length of the diffuser as well as the angle of diffusion, but the majority have procured low θ_D so as to avoid internal flow separation. Sparrow *et. al.* [59] used a Shear Stress Transport turbulence model to study the flow separation on a diverging conical duct (in essence, the same shape as the diffuser on a ducted propeller), and suggested that although flow separation was expected to occur at $\theta_D > 7°$, flow separation was numerically determined to occur at $\theta_D > 7°$ for $Re = 2000$. Similarly, Chandavari and Pelekar [60] determined that the taper angle at which a fluid through a channel of increasing cross-section would separate is $\theta_D > 7°$. Yilmaz *et. al*. [25] performed load measurements and hot-wire

anemometry on the inlet and exit flow of ducted propellers with varied duct cross-section, based on pre-existing airfoil geometries. Yilmaz *et. al.* [25] found through hot-wire anemometry that the duct models were capable of mitigating the contraction of the slipstream. The potential for an even larger expansion has only been proposed in theory, but has not been yet investigated for ducted propellers of the scale proper to UAV applications.

Another parameter that has not been explicitly investigated in the past is the thickness-to-chord ratio, t/c_D of the duct's cross-section. Bontempo and Manna [61] carried out a numerical investigation where a non-linear semi-analytical disk actuator model was used to study the effect of camber and thickness of the duct on the performance of a ducted propeller system. Bontempo and Manna [61] suggest that an increment in both the camber and thickness of the duct's cross section provide improvements on the propulsive efficiency of the system. Zondervan *et. al.* [62] notes that the pressure drop at the leading edge, and consequently the acceleration of the flow towards the rotor disk, increases with higher duct t/c_D ratios. Morgan [63] developed a performance prediction model of ducted propellers based on the vortex theory, in which the effect of the duct on the flow field was represented through ring sources and ring vortices distributed over a cylinder. Morgan [63] determined that the strength of these elementary flow sources was exclusively a function of the thickness of the duct.

In this study, the effect of varying between 9 and 18 degrees, and t/c_D between 0.06 to 0.14 on the thrust, power consumption and propulsive efficiency of ducted propellers will be investigated. Also, the investigation will also explore the potential of reducing the rotor disk area with the use of a duct, by comparing the performance of the ducted propeller system with an untrimmed propeller blade. For these purposes, aerodynamic load measurements in a wind tunnel will be performed using a six axis load cell. In addition to studying the effects of the θ_D and t/c_D parameters, an investigation of the flow field upstream and downstream of the ducted propeller will be conducted using Particle Image Velocimetry (PIV) as a means of non-intrusive flow visualization. Flow visualization through PIV is used in this investigation to study the effect of the duct on the flow field upstream of the rotor disk plane to explore the changes to inlet mass flow rate; as well as downstream of the duct's trailing edge, to characterize the potential reduction of the slipstream contraction. The following sections entail the results of the experiments described in Table 3-8, and they will be presented in the order shown in the table.

4.1 Effect of Diffuser Angle

4.1.1 Thrust

The thrust generation of the LE1.5-DA9-0.06, LE1.5-DA18-0.06 and the trimmed OP for propeller rotational speeds of n = 6000 RPM, 7000 RPM, 8000 RPM and 9000 RPM is presented through C_T as a function of the advance ratio J in Figure 4-1 (a) to (d), respectively, for 0 m/s < V_∞ < 10 m/s. For a fixed free stream velocity, increments in the rotational speed of the propeller result in a decrease of the advance ratio; therefore, the range of J covered in Figure 4-1 (a) to (d) decreases with increasing n. The performance at hover is shown as the data point corresponding to J = 0. The data points of the results for the trimmed OP at n = 6000 RPM shown in Figure 4-1(a) are accompanied by error bars, which have been determined using the maximum and minimum values of C_T obtained between three repetitions of the same J values. The fact that the span of these error bars englobe the data points from the other configurations (LE1.5-DA9-0.06 and LE1.5-DA18-0.14 systems) suggests that there is no significant performance difference between the three systems.

For the axial flow (J > 0), the response for all four n values indicates that with increasing J the thrust generation from all three systems decreases. This behaviour is expected for both ducted and open propellers operating at α_P = 0°. The largest increment in thrust by the ducted propellers with respect to the trimmed OP are 16.57% (n = 9000 RPM, J =0.3) and 11.47% (n = 9000 RPM, J =0.07) by the LE1.5-DA9-0.06 and LE1.5-DA18-0.06, respectively. The results from changing the propeller's rotational speed at various free-stream velocities presented in Figure 4-1 (a) to (d) did not show a clear indication of which system performs at a higher C_T value than the other for J range investigated. Overlapping C_T-J curves at 6000 RPM < n < 9000 RPM for the LE1.5-DA9-0.06, LE.5-DA18-0.06 and the trimmed OP systems are presented in Figure 4-2; where it can be observed that the difference in C_T between the LE1.5-DA9-0.06 and LE1.5-DA18-0.06 ducted propeller systems appears to be marginal.

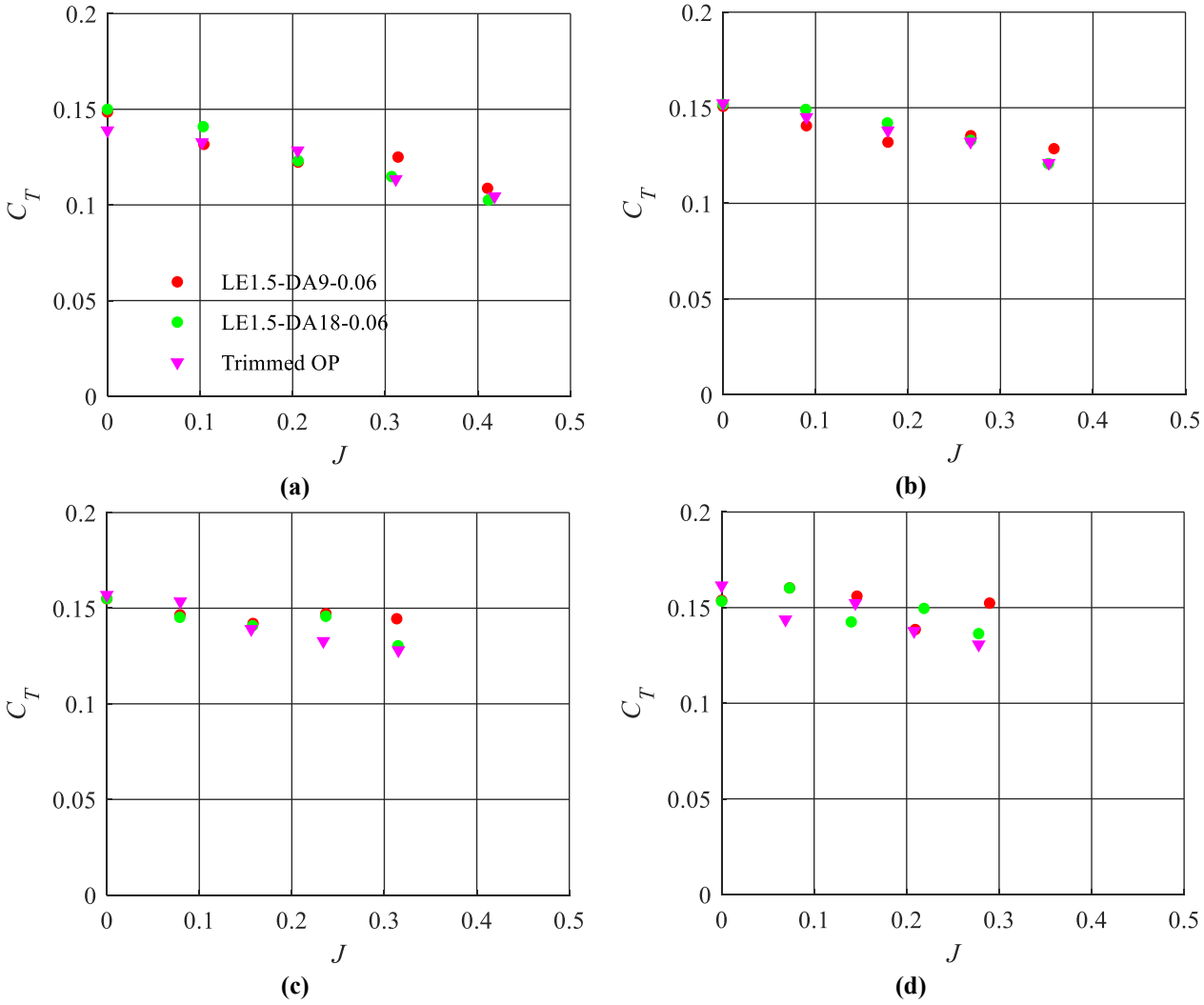

Figure 4-1: The results of C_T as a function of J of the duct models LE1.5-DA9-0.06 and LE1.5-DA18-0.06, as well as the trimmed OP, for propeller rotational speeds of n = (a) 6000 RPM (b) 7000 RPM (c) 8000 RPM and (d) 9000 RPM.

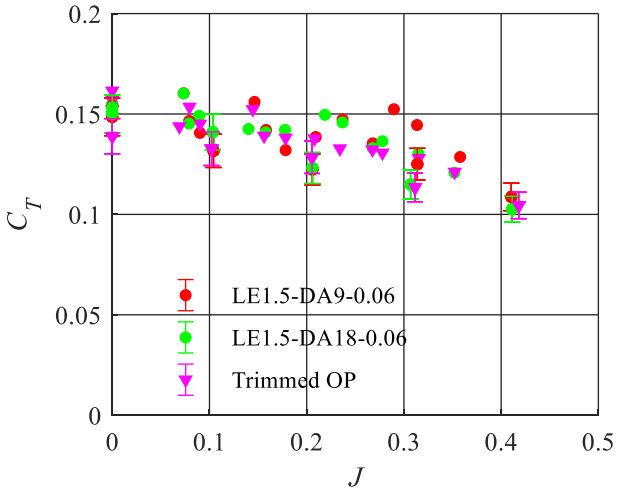

Figure 4-2: The overlapping C_T-J curves of the LE1.5-DA9-0.06, LE1.5-DA18-0.06 and trimmed OP, for 6000 RPM < n < 9000 RPM and 0 m/s < V_∞ < 10 m/s.

4.1.2 Power

The non-dimensional power consumption, C_P, of the LE1.5-DA9-0.06 and LE1.5-DA18-0.06 ducted propeller systems as well as the trimmed OP for propeller rotational speeds of n = 6000 RPM, 7000 RPM, 8000 RPM and 9000 RPM is presented as a function of the advance ratio J in Figure 4-3(a) to (d), respectively, for 0 m/s < V_∞ < 10 m/s. The results shown in Figure 4-3 (a) to (d) demonstrate that for a fixed n and increasing J the power consumption from all three systems remains approximately unchanged; however, it must be noted that the results presented in Figure 4-3 (a) to (d) are not for constant C_T. Examination of the power consumption results at the hover condition (J = 0) shows that both ducted propeller models performed at a higher power consumption than the trimmed OP for all n values tested. The maximum C_P increments with respect to the trimmed OP by the LE1.5-DA9-0.06 and LE1.5-DA18-0.06 ducted propeller systems in hover were 7.52% (n = 8000 RPM) and 6.91% (n =7000 RPM), respectively. Similar to the thrust generation results, the difference between the LE1.5-DA9-0.06 and LE1.5-DA18-0.06 ducted propeller systems is marginal, and shows no significant changes in power consumption with the applied change in θ_D.

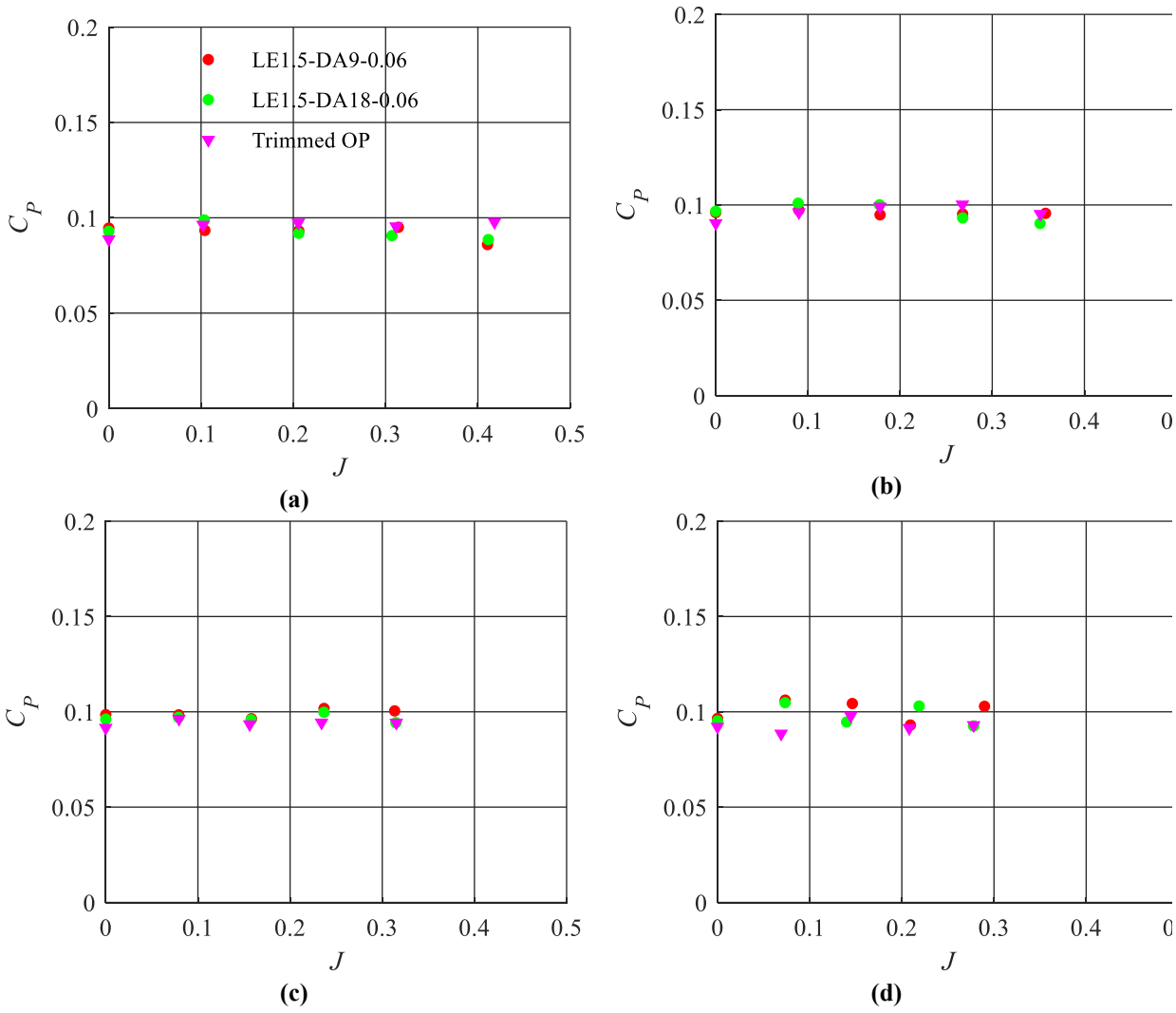

Figure 4-3: The results of C_P as a function of J of the duct models LE1.5-DA9-0.06 and LE1.5-DA18-0.06, as well as the trimmed OP, for propeller rotational speeds of n = (a) 6000 RPM (b) 7000 RPM (c) 8000 RPM and (d) 9000 RPM.

The data at all four n values has been conglomerated to generate overlapping C_P-J curves for the LE1.5-DA9-0.06, LE1.5-DA18-0.06 and trimmed OP systems, and are shown in Figure 4-4. The results from Figure 4-4 confirm that the three systems operate at approximately equal power consumption, regardless of the propeller's rotational speed.

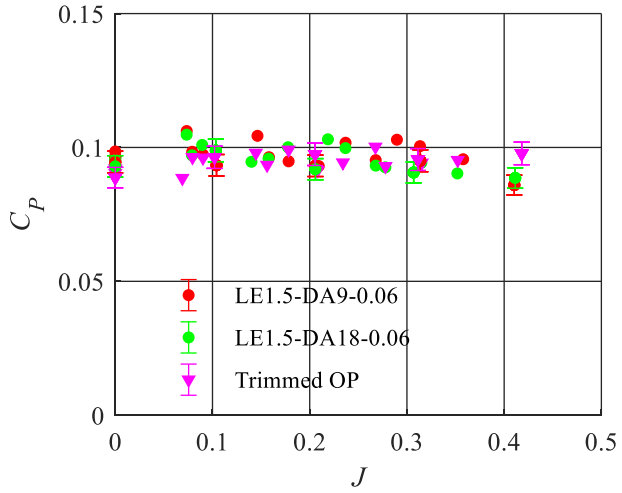

Figure 4-4: The overlapping C_P-J curves of the LE1.5-DA9-0.06, LE1.5-DA18-0.06 and trimmed OP, for 6000 RPM < n < 9000 RPM and 0 m/s < V_∞ < 10 m/s.

4.1.3 Propulsive Efficiency

The propulsive efficiency, η, of the LE1.5-DA9-0.06 and LE1.5-DA18-0.06 ducted propeller models as well as the trimmed OP are shown in Figure 4-5 (a) to (d), for n = 6000 RPM, 7000 RPM, 8000 RPM and 9000 RPM, respectively. The trends observed in Figure 4-5 (a) to (d) for all three cases is the same: the propulsive efficiency increases with increasing advance ratio. It must be noted that if higher advance ratios were tested, the trends would eventually achieve a maximum η value and begin to descend at further values of J. The first data point of each set in Figure 4-5 (a) to (d) corresponds to the hovering (static) efficiency, and is theoretically 0% since V_∞ = 0 m/s and consequentially J = 0. For the results at n = 6000 RPM and n = 7000 RPM shown in Figure 4-5 (a) and (b) it can be observed that both ducted propeller systems perform at a higher η than the trimmed OP. The LE1.5-DA9-0.06 ducted propeller system exhibits a significant improvement in η with respect to the LE1.5-DA18-0.06 ducted propeller and the trimmed OP for n = 6000 RPM and J > 0.3. This result is not as evident for n = 8000 RPM and n = 9000 RPM. For all four n values investigated, results from Figure 4-5 (a) to (d) suggest that for J < 0.2 the propulsive efficiency of the LE1.5-DA9-0.06, LE1.5-DA18-0.06 and trimmed OP systems have negligible differences with respect to each other. The maximum η achieved by the LE1.5-DA9-0.06, LE1.5-DA18-0.06 and trimmed OP systems in the J range investigated is shown in Table 4-1.

Table 4-1: The maximum propulsive efficiency achieved by the LE1.5-DA9-0.06, LE1.5-DA18-0.06 and trimmed OP systems in for 6000 RPM < n < 9000 RPM and 0 m/s < V_∞ < 10 m/s.

n (RPM)	Maximum η achieved		
	LE1.5-DA9-0.06	LE1.5-DA18-0.06	Trimmed OP
6000	52%	48%	45%
7000	48%	47%	45%
8000	45%	44%	43%
9000	43%	41%	39%

To better visualize the gain/loss in propulsive efficiency from the ducted propellers relative to the trimmed OP, the difference in the propulsive efficiency, $\Delta\eta$, with respect to the trimmed OP is presented in Figure 4-6 (a) to (d) for n = 6000 RPM, 7000 RPM, 8000 RPM and 9000 RPM, respectively. The results from Figure 4-6 (a) to (d) show that the maximum $\Delta\eta$ achieved, with respect to the trimmed OP, by the LE1.5-DA9-0.06 and LE1.5-DA18-0.06 systems are 7.24% (n = 6000 RPM, J = 0.41) and 2.96% (n = 6000 RPM, J = 0.41), respectively. The general behaviour of both ducted propeller systems shows a slight tendency of increment in $\Delta\eta$ with increasing J, for the n range investigated. It can be observed from these results that both the LE1.5-DA9-0.06 and the LE1.5-DA18-0.06 ducted propeller systems provide an increment of η with respect the trimmed OP, for 56% and 75% of the operating conditions investigated, respectively, not considering the static (J = 0) operating condition.

The overlapping η-J curves for 6000 RPM < n < 9000 RPM for the LE1.5-DA9-0.06, LE1.5-DA18-0.06 and the trimmed OP are plotted in Figure 4-7, where it can be observed that the η response at various n values follow a single trend for J < 0.25, and for the higher advance ratios both the LE1.5-DA9-0.06 and the LE1.5-DA18-0.06 ducted propellers demonstrate a higher η than the trimmed OP.

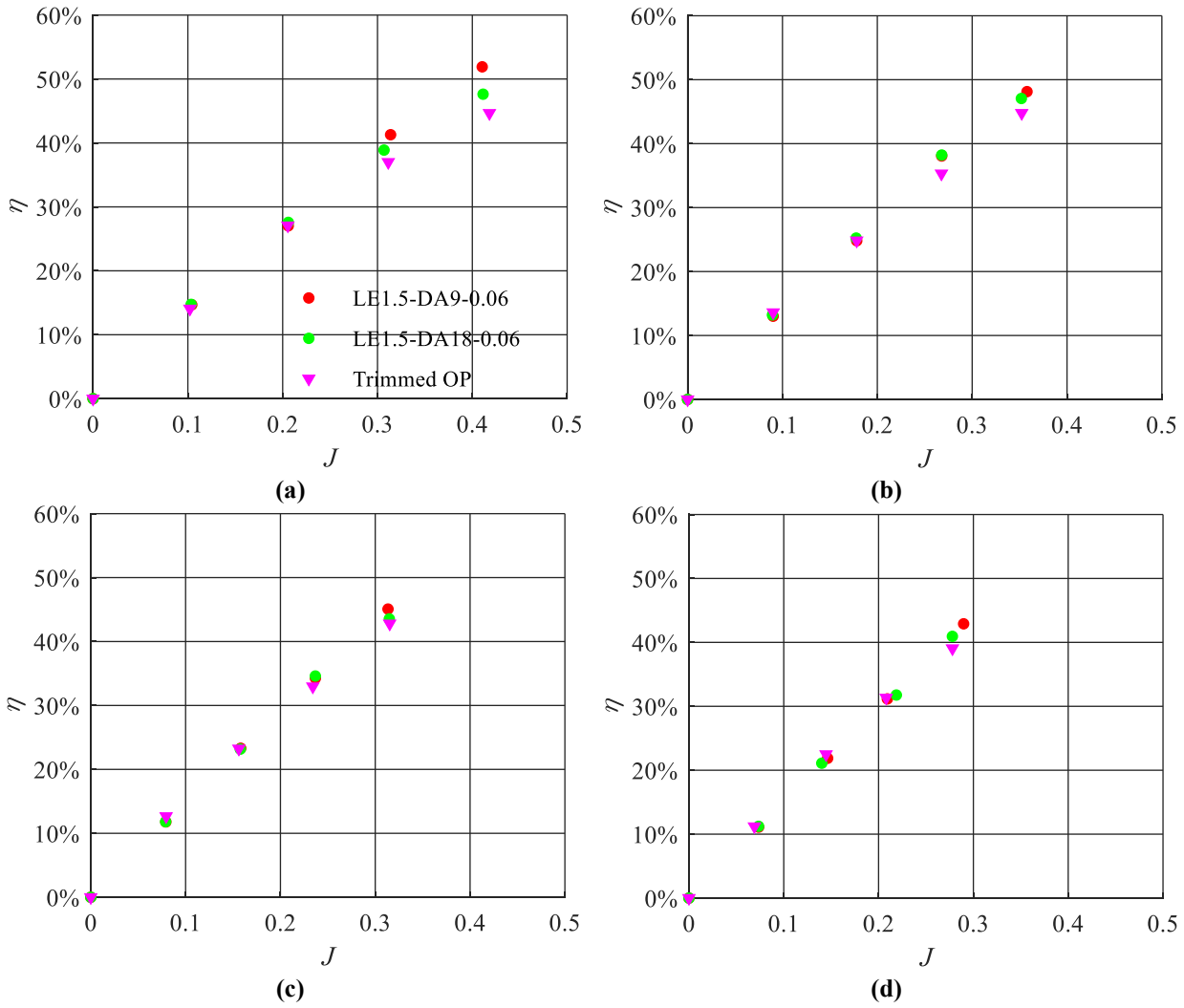

Figure 4-5: The propulsive efficiency, η, results of the ducted propeller models LE1.5-DA9-0.06 and LE1.5-DA18-0.06 as well as the trimmed OP, for propeller rotational speeds of n = (a) 6000 RPM (b) 7000 RPM (c) 8000 RPM and (d) 9000 RPM.

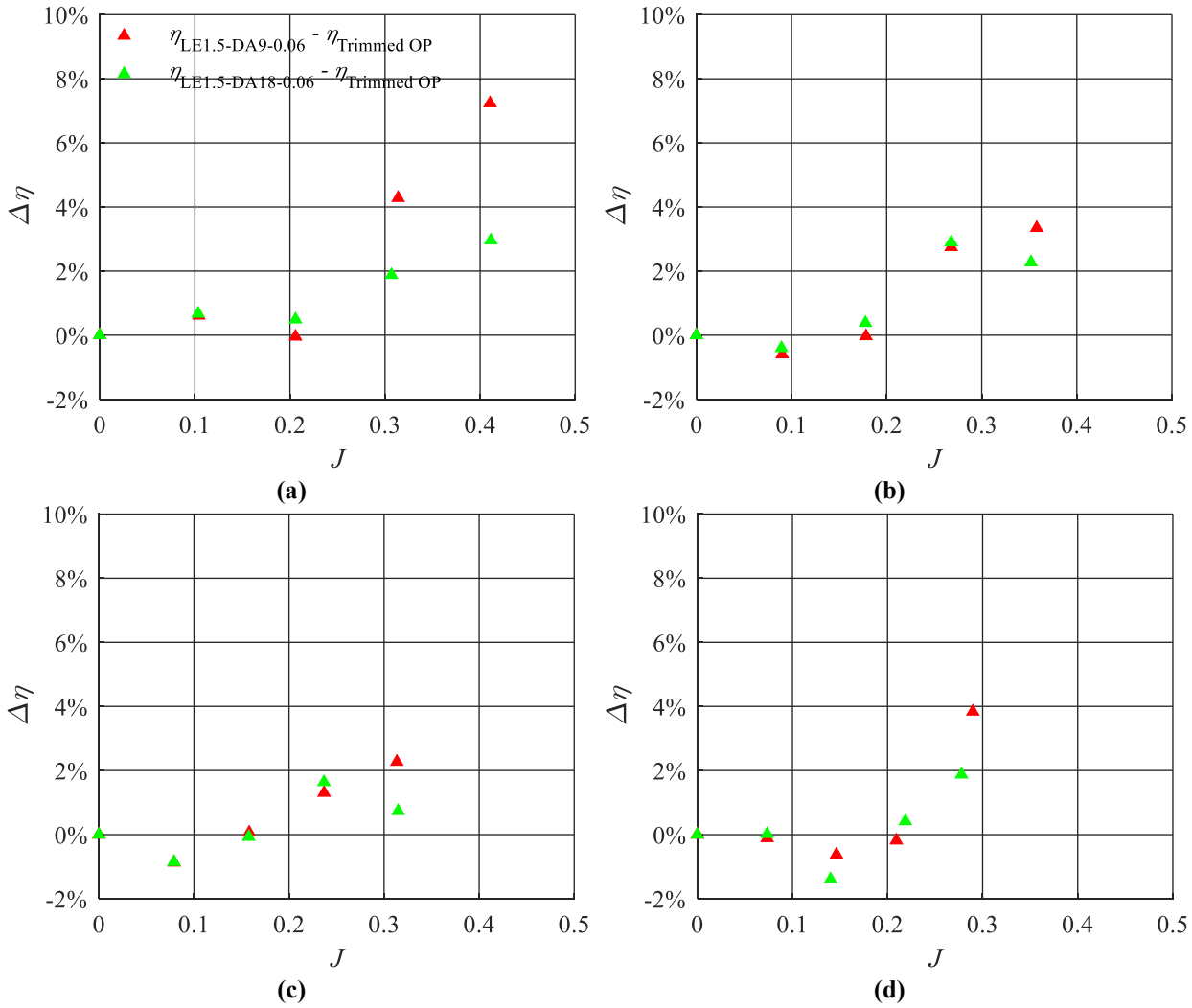

Figure 4-6: The propulsive efficiency difference between the ducted propeller models (LE1.5-DA9-0.06 and LE1.5-DA18-0.06) and the trimmed OP as a function of *J*, for *n* = (a) 6000 RPM (b) 7000 RPM (c) 8000 RPM and (d) 9000 RPM.

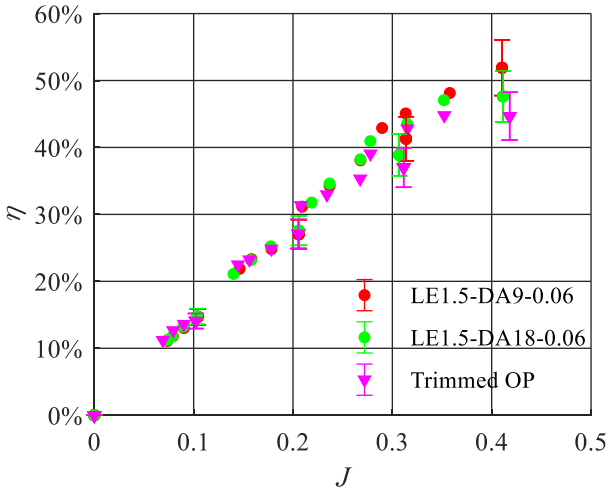

Figure 4-7: The overlapping η -J curves of the LE1.5-DA9-0.06, LE1.5-DA18-0.06 and trimmed OP, for 6000 RPM < n < 9000 RPM and 0 m/s < V_∞ < 10 m/s.

The results shown in Figure 4-1 to Figure 4-6 compared the aerodynamic performance of the LE1.5-DA9-0.06 and LE1.5-DA18-0.06 ducted propellers, as well as the trimmed OP. The thrust and power consumption results demonstrated that increasing θ_D from 9° to 18° resulted in no significant difference in performance. The propulsive efficiency results showed that η increased with increasing J for the three systems tested. An interesting find was that the ducted systems demonstrated a higher propulsive efficiency at the highest J value tested in the experiment. In comparison to the trimmed OP, the ducted propeller with $\theta_D = 9°$ demonstrated a larger increment of η than the ducted propeller with $\theta_D = 18°$, but the LE1.5-DA18-0.06 provided an increment of η at more operating conditions than the LE1.5-DA9-0.06. The data also shows that the range of J investigated was not sufficient to achieve a thrust coefficient of $C_T = 0$ for the n values tested.

4.2 Effect of Duct Thickness

4.2.1 Thrust

The non-dimensional thrust coefficient response, C_T, of the LE1.5-DA18-0.06, LE1.5-DA18-0.14 and the trimmed OP is presented as a function of J in Figure 4-8 (a) to (d) for n = 6000 RPM, 7000 RPM, 8000 RPM and 9000 RPM, respectively, for 0 < V_∞ < 12 m/s. As expected, the general trend of all three systems shows a decrease in C_T with increasing J, for all n values tested. The response

from each system shows no significant change in C_T with change in n. In the hover condition ($J = 0$) the data shows that the LE1.5-DA18-0.14 ducted propeller provides the largest thrust generation, followed by the LE1.5-DA18-0.06 ducted propeller, and lastly by the trimmed OP. With respect to the trimmed OP, the LE1.5-DA18-0.06 and LE1.5-DA18-0.14 systems provided a maximum static C_T increment of 10.4% ($n = 8000$ RPM) and 22.3% ($n = 7000$ RPM), respectively.

The axial flow results ($J > 0$) of all four n values show that the trends for the LE1.5-DA18-0.06, LE1.5-DA18-0.14 and the trimmed OP intersect at an advance ratio of approximately $J = 0.25$~0.35. At advance ratios of $J < 0.25$~0.35 the LE1.5-DA18-0.14 system exhibits a greater C_T generation than the LE1.5-DA18-0.06 and the trimmed OP. Also for $J < 0.25$~0.35 the trimmed OP shows the lowest C_T generation of the three systems tested. For $J > 0.25$~0.35, the C_T of the LE1.5-DA18-0.14 drops below that of the LE1.5-DA18-0.06 ducted propeller for all four n values investigated. For the tests at $n = 6000$ RPM and 7000 RPM where data beyond $J = 0.35$ is available it can be observed in Figure 4-8 (a) and (b) that the C_T performance of the LE1.5-DA18-0.14 even drops below that of the trimmed OP.

The existence of such threshold J range is better appreciated in Figure 4-9, where the overlapping C_T-J curves at 6000 RPM $< n <$ 9000 RPM have been plotted for the LE1.5-DA18-0.06, LE1.5-DA18-14 and trimmed OP. For the reader's convenience, the threshold range $0.25 < J < 0.35$ has been enclosed by to vertical red dotted lines in Figure 4-9. The plot in Figure 4-9 also confirms that there is insignificant variation to the C_T-J response from the systems due to changes in the propellers rotational velocity. Comparing the results from Figure 4-9 and Figure 4-2 it can be observed that the LE1.5-DA18-0.06 and the LE1.5-DA18-0.14 demonstrate less scatter in the data with respect to the LE1.5-DA9-0.06. This may suggest that the LE1.5-DA9-0.06 model experienced higher vibrations which may have influenced the data during tests. Evidently, it is observed from Figure 4-9 that both the LE1.5-DA18-0.06 and the LE1.5-DA18-0.14 ducted propellers provide a higher C_T than the trimmed OP at the lower advance ratio range of approximately $J < 0.25$. More specifically, for the same J range of $J < 0.25$, the thicker ducted propeller (LE1.5-DA18-0.14) performs at a higher C_T than the thinner ducted propeller (LE1.5-DA18-0.06).

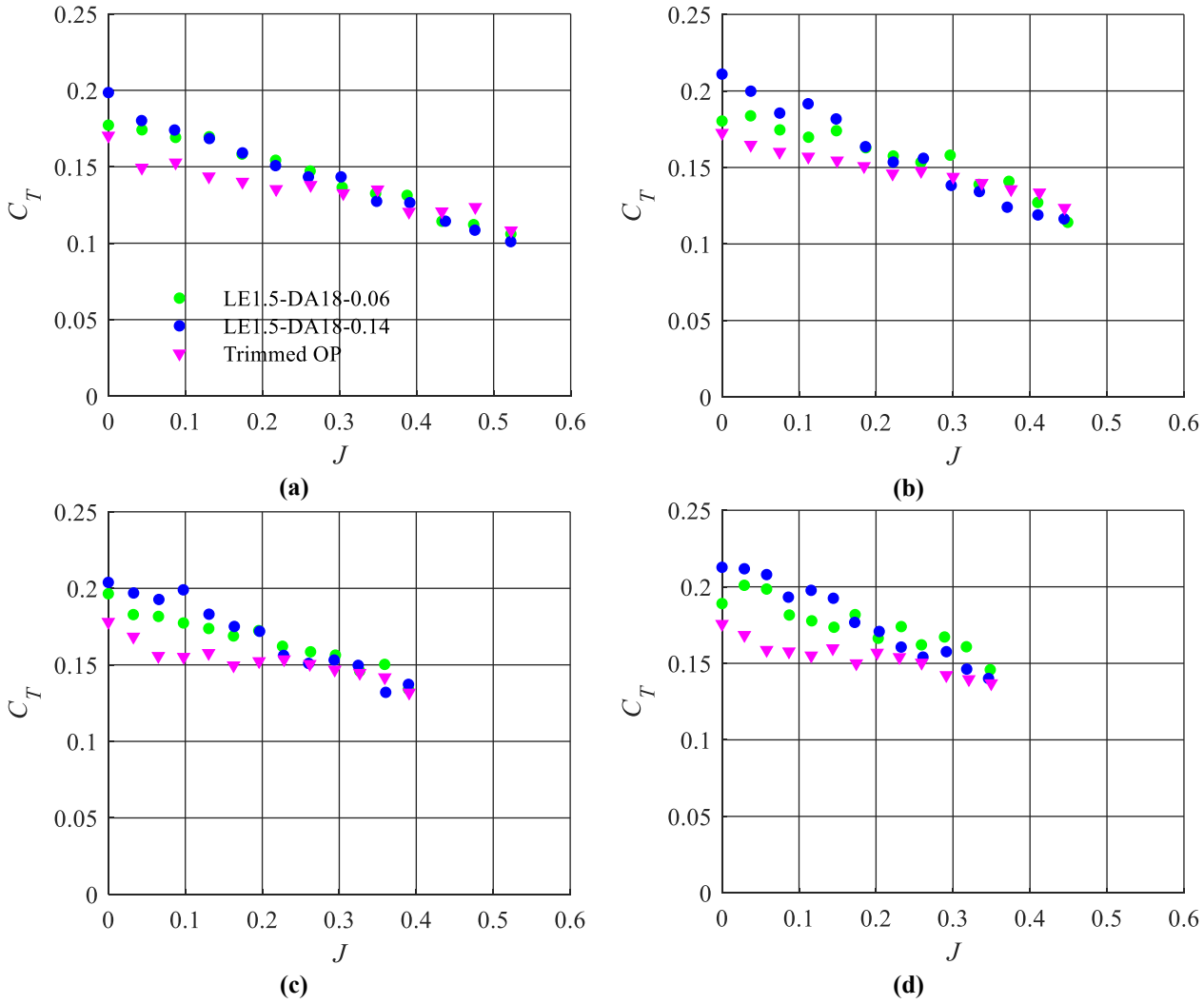

Figure 4-8: The results of C_T as a function of J of the duct models LE1.5-DA18-0.06 and LE1.5-DA18-0.14, as well as the trimmed OP, for propeller rotational speeds of n = (a) 6000 RPM (b) 7000 RPM (c) 8000 RPM (d) 9000 RPM.

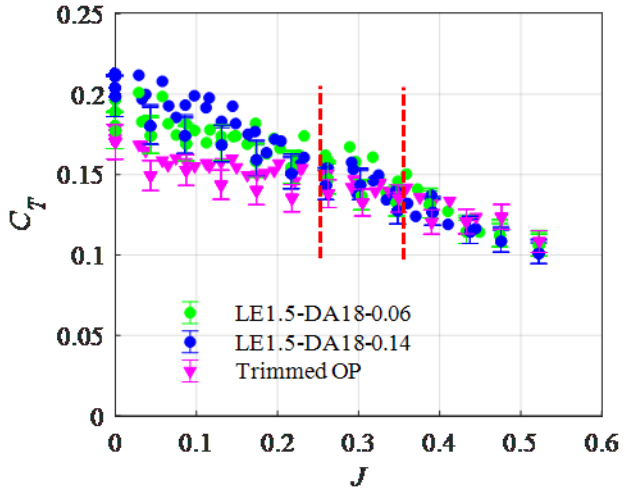

Figure 4-9: The overlapping C_T-J curves of the LE1.5-DA18-0.06, LE1.5-DA18-0.14 and trimmed OP, for 6000 RPM < n < 9000 RPM and 0 m/s < V_∞ < 12 m/s.

4.2.2 Power

The results of the non-dimensional power consumption, C_p, of the LE1.5-DA18-0.06, LE1.5-DA18-0.14 and trimmed OP systems are presented as a function of J in Figure 4-10 (a) to (d). These results are shown for the free-stream range of 0 m/s < V_∞ < 12 m/s, and for n = 6000 RPM, 7000 RPM, 8000 RPM and 9000 RPM, respectively. For the ducted propellers, the results at all n values display a C_P behaviour that is approximately decreasing with increasing J; and for the trimmed OP it is approximately unresponsive to changes in J. The LE1.5-DA18-0.14 ducted propeller shows in Figure 4-10 (a) and (b) a slight decreasing trend with increasing J. Upon visual evaluation of the results in Figure 4-10 (a) to (d) it can be observed that the LE1.5-DA18-0.06 system operates at a higher C_P than the LE1.5-DA18-0.14 system for all the operating points (J values) investigated. The C_P-J curves for all three systems intercept at approximately J = 0.25~0.35. For J < 0.25, both the LE1.5-DA18-0.06 and the LE1.5-DA18-0.14 ducted propellers operate at a higher C_P than the trimmed OP. For J > 0.35 the data presented shows that the C_P response surpasses that of both ducted propeller systems.

The results from Figure 4-10 (a) and (d) have been conglomerated into overlapping C_P-J curves that includes the data from 6000 RPM < n < 9000 RPM, and are plotted in Figure 4-11. The plot in Figure 4-11 provides corroboration of the previously discussed intersection J range, and clearly shows that the C_P-J curve for the LE1.5-DA18-0.06 and LE1.5-DA18-0.14 systems decrease with

increasing *J*. As previously done in the thrust generation plots, the advance ratio threshold range is shown between two vertical red dotted lines, for the reader's convenience.

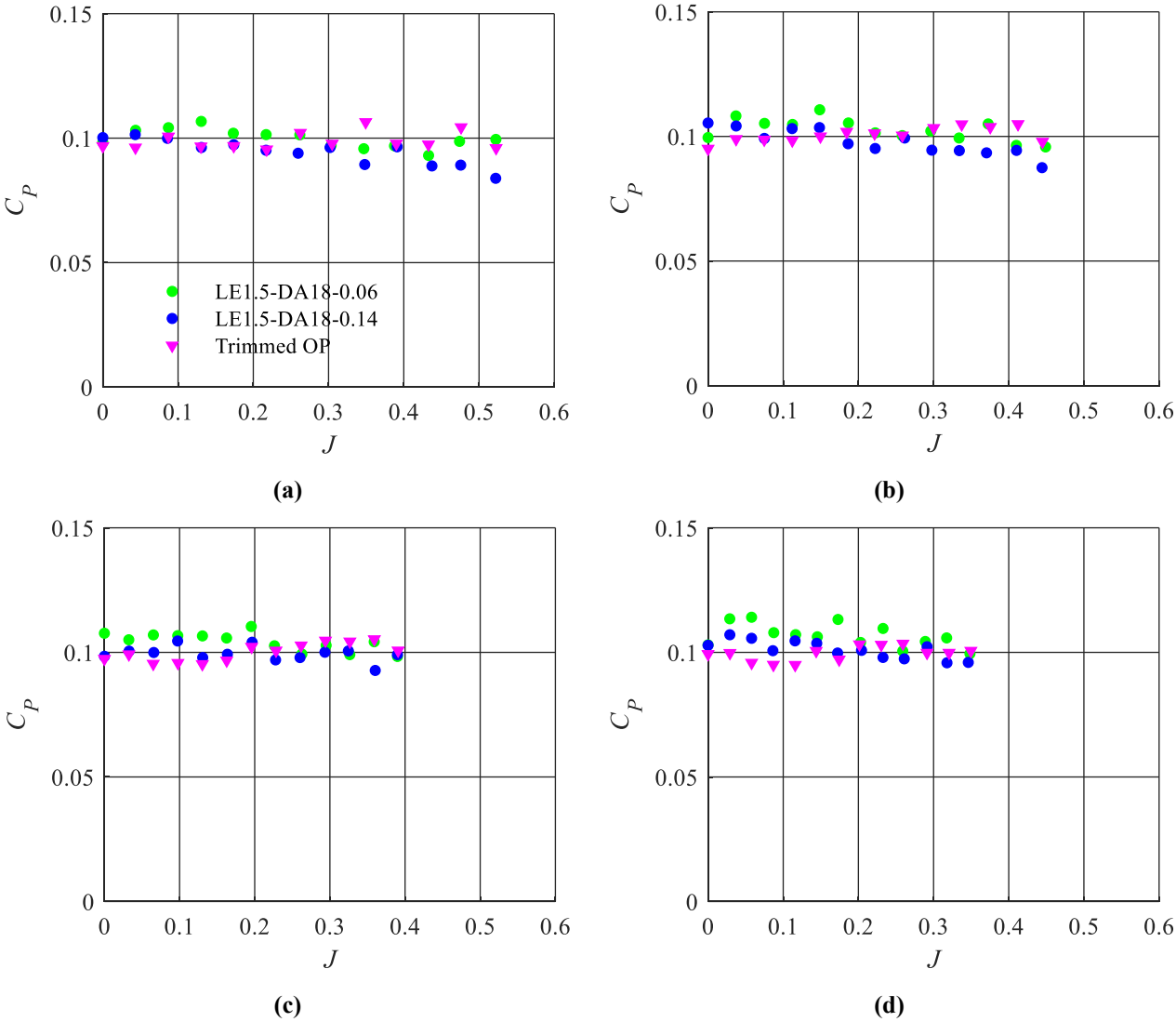

Figure 4-10: The results of C_P as a function of J of the duct models LE1.5-DA18-0.06 and LE1.5-DA18-0.14, as well as the trimmed OP, for propeller rotational speeds of n = (a) 6000 RPM (b) 7000 RPM (c) 8000 RPM (d) 9000 RPM.

In Figure 4-11 it can be clearly seen that regardless of the angular rotation used in the tests, both the LE1.5-DA18-0.06 and LE1.5-DA18-0.14 ducted propellers operated at a higher power consumption than the trimmed OP for $J < 0.25$~0.3. Beyond this approximate advance ratio range, the trimmed OP operates at higher C_P than the ducted propeller systems. The result in Figure 4-11

also shows that for the range of advance ratios tested, the thinner duct (LE1.5-DA18-0.06) performed at higher C_P values than the thicker duct (LE1.5-DA18-0.14).

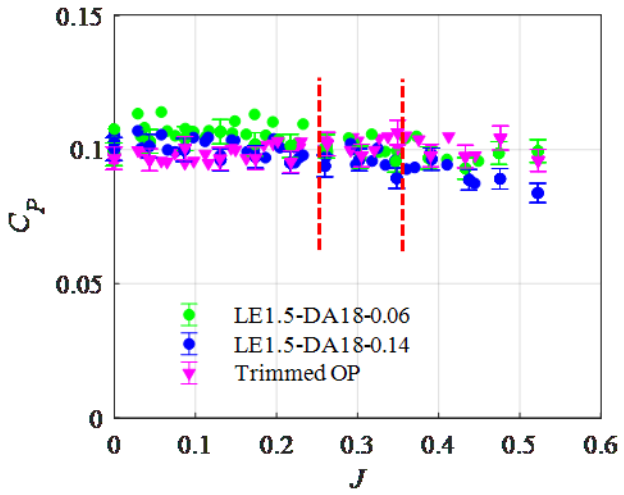

Figure 4-11: The overlapping C_P-J curves of the LE1.5-DA18-0.06, LE1.5-DA18-0.14 and trimmed OP, for 6000 RPM < n < 9000 RPM and 0 m/s < V_∞ < 10 m/s.

4.2.3 Propulsive Efficiency

The propulsive efficiency results, η, of the LE1.5-DA18-0.06 and LE1.5-DA18-0.14 ducted propellers as well as the trimmed OP are presented as a function of J in Figure 4-12 (a) to (d) for n = 6000 RPM, 7000 RPM, 8000 RPM and 9000 RPM, respectively. The general trend of all three systems presented in Figure 4-12 (a) to (d) displays a parabolic response of η with respect to J. For the range of J investigated, the propulsive efficiency from the LE1.5-DA18-0.06, LE1.5-DA18-0.14 ducted propellers and the trimmed OP show an increase of η with respect to J. The maximum η values achieved by each of the systems presented in Figure 4-12 (a) to (d) are summarized in Table 4-2 for each n tested. The LE1.5-DA18-0.14 ducted propeller achieved the highest propulsive efficiency of η = 62.91% at n = 6000 RPM and J = 0.52. It can be observed in Figure 4-12 (a) to (d) that for the entirety of the J range investigated, both the LE1.5-DA18-0.06 and the LE1.5-DA8-0.14 ducted propellers performed at a higher propulsive efficiency than the trimmed OP.

The results in Figure 4-12 (a) to (d) have been superimposed and plotted in Figure 4-13 to show overlapping η-J plots for the LE1.5-DA18-0.06, LE1.5-DA18-0.14 and the trimmed OP at

6000 RPM < n < 9000 RPM. The purpose of this figure is to show that the efficiency output of the three systems does not depend on variations in the angular speed of the propeller.

As it was done is section 4.1.3, the propulsive efficiency difference, $\Delta\eta$, between the ducted propellers LE1.5-DA18-0.06 and LE1.5-DA18-0.14 and the trimmed OP has been plotted as a function of J in Figure 4-14 (a) to (d), for n = 6000 RPM, 7000 RPM, 8000 RPM and 9000 RPM, respectively. The $\Delta\eta$ results of both the LE1.5-DA18-0.06 and LE1.5-DA18-0.14 show that the ducted propellers provide larger propulsive efficiency with respect to the trimmed OP for the majority of the advance ratio range investigated. The efficiency gain from both ducted propeller models increases with increasing J for the approximate range of J < 0.25~0.35. This operating point coincides with the C_T results, in which a threshold of J = 0.25~0.35 marked the operating condition at which the thrust generation behavior of the ducted propellers dropped below the trimmed OP.

Table 4-2: The maximum propulsive efficiency achieved by the LE1.5-DA18-0.06, LE1.5-DA18-0.14 and trimmed OP systems in for 6000 RPM < n < 9000 RPM and 0 m/s < V_∞ < 12 m/s.

n (RPM)	Maximum η achieved		
	LE1.5-DA18-0.06	LE1.5-DA18-0.14	Trimmed OP
6000	56%	63%	59%
7000	54%	59%	56%
8000	53%	54%	51%
9000	51%	51%	48%

For J < 0.25 the LE1.5-DA18-0.14 system exhibits a higher $\Delta\eta$ with respect to the trimmed OP than the LE1.5-DA18-0.06 system. Beyond this J value, the difference in $\Delta\eta$ between the two ducted propellers becomes less discernible. The maximum $\Delta\eta$ achieved by the LE1.5-DA18-0.06 and LE1.5-DA18-0.14 ducted propellers are 4.80% (n = 9000 RPM, J = 0.29) and 5.26% (n = 6000 RPM, J = 0.35), respectively.

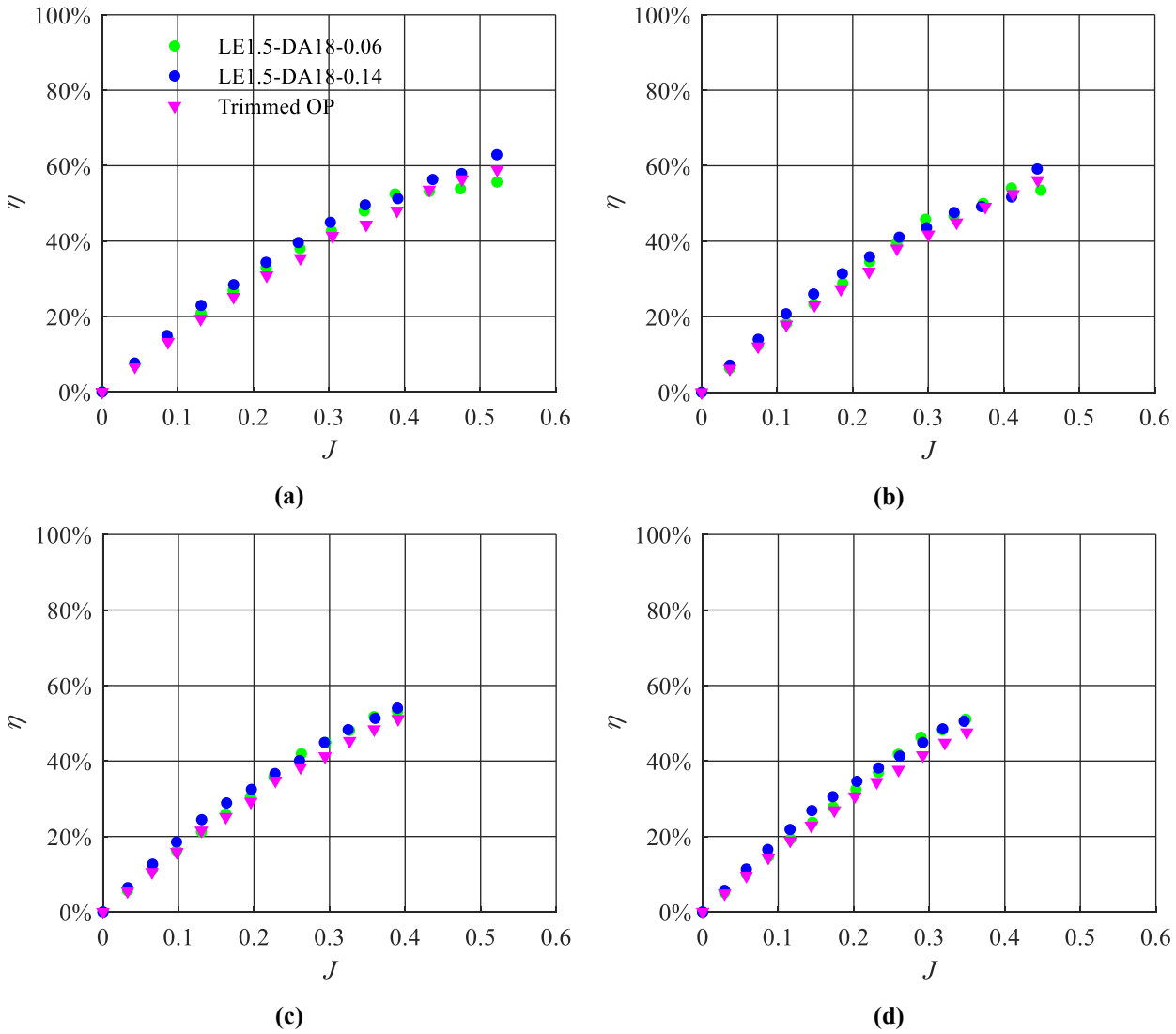

Figure 4-12: The propulsive efficiency, η, results of the ducted propeller models LE1.5-DA18-0.06 and LE1.5-DA18-0.14 as well as the trimmed OP, for propeller rotational speeds of n = (a) 6000 RPM (b) 7000 RPM (c) 8000 RPM (d) 9000 RPM.

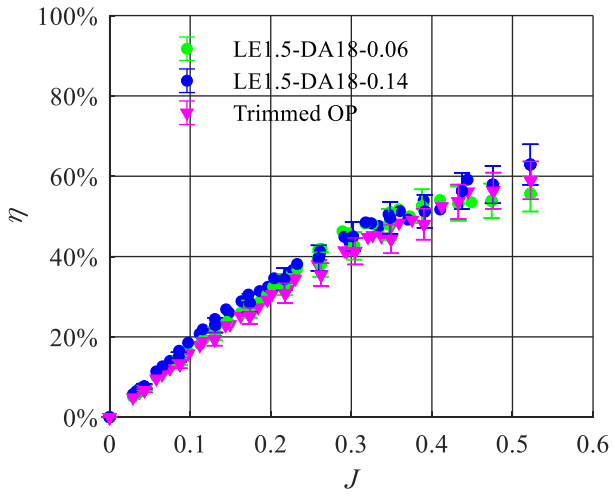

Figure 4-13: The overlapping η-J curves of the LE1.5-DA18-0.06, LE1.5-DA18-0.14 and trimmed OP, for 6000 RPM < n < 9000 RPM and 0 m/s < V_∞ < 10 m/s.

The propulsive efficiency difference plots shown in Figure 4-14 (a) to (d) have been superimposed and plotted in the same graph, and the result is shown in Figure 4-15. As previously done in the thrust generation and power consumption results, the threshold advance ratio range previously described has been noted by the region between two vertical red dotted lines in the figure. The results from this image suggest that this threshold range of $0.25 < J < 0.35$ holds for various rotational speeds of the propeller.

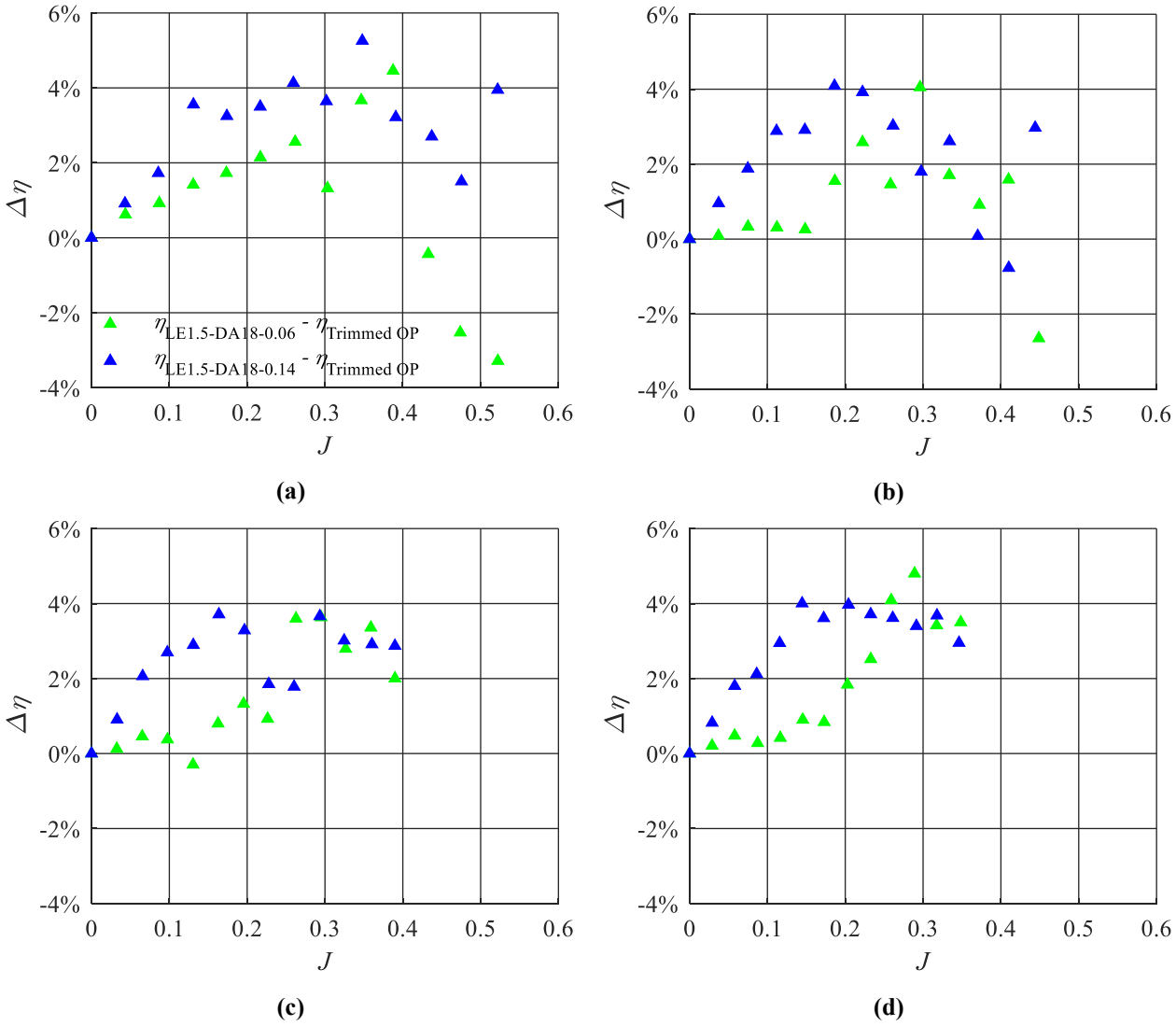

Figure 4-14: The propulsive efficiency difference between the ducted propeller models (LE1.5-DA18-0.06 and LE1.5-DA18-0.14) and the trimmed OP as a function of *J*, for *n* = (a) 6000 RPM (b) 7000 RPM (c) 8000 RPM (d) 9000 RPM.

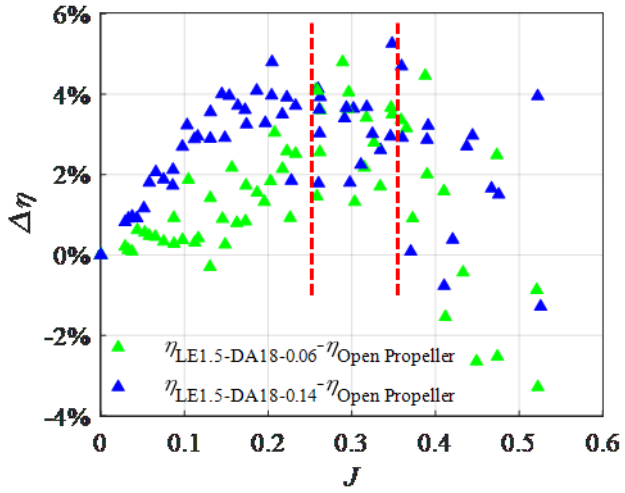

Figure 4-15: The overlapping curves of the propulsive efficiency difference between the ducted propeller models (LE1.5-DA18-0.06 and LE1.5-DA18-0.14) and the trimmed OP as a function of J for 6000 RPM < n < 9000 RPM and 0 m/s < V_∞ < 10 m/s.

The C_T-J and C_P-J results presented in Figure 4-8 and Figure 4-10, respectively, showed a clear drop in performance from the ducted propellers at $J > 0.25$. This provides evidence of a free-stream advance ratio threshold that marks the operating point beyond which the ducted propellers cease to provide thrust benefits with respect to the open propeller. This result may be explained by an increment of the total drag from the ducts themselves, either through increased skin friction from the external surface of the ducts, of by the pressure drag created by the projected area of the ducts in the axial direction. This behaviour is also exhibited through the propulsive efficiency results as well, where the $\Delta\eta$ with respect to the trimmed OP ceases to increase at approximately $J = 0.25$. However, beyond $J = 0.25$, both the LE1.5-DA18-0.06 and the LE1.5-DA18-0.14 ducted propellers still operated at higher propulsive efficiencies than the trimmed OP. The duct with a $t/c_D = 0.14$ demonstrated a higher efficiency increment with respect to the trimmed OP than the duct with $t/c_D = 0.06$ for $J < 0.3$. Additionally, the duct with $t/c_D = 0.14$ demonstrated a higher C_T generation than the duct with $t/c_D = 0.06$ for the range $J < 0.25$. From these results, it is suggested that the duct with the higher t/c_D ratio, in this case the LE1.5-DA18-0.14 model performed better than the LE1.5-DA18-0.06 model. It is notable how an increase of 133% in t/c_D did not generate significant amounts of additional drag in comparison to the duct with a lower t/c_D ratio, rather,

beyond the threshold operating point found, both ducts operated at approximately the same propulsive efficiency, power consumption and thrust generation.

4.3 Effect of Rotor Disk Area

In this section, performance comparisons of thrust, power and propulsive efficiency between the LE1-DA18-0.14 ducted propeller, the trimmed OP and untrimmed OP are presented as a function of the advance ratio *J*. The performance of the LE1-DA18-0.14 is investigated in this section because due to spatial requirements of the stereoscopic PIV experiment described in section 3.6.2, the aspect ratio of the leading edge had to be decreased to make way for the laser sheet. The value of *J*, as defined in equation 2-43, is a function of the blade tip speed, which depends on the propeller diameter. Since the diameter of the untrimmed OP is 21.1% larger than the diameter of the LE1-DA18-0.14 propeller and the trimmed OP, a different *J* value was obtained. The trimmed OP data displayed in this section correspond to the data presented in sections 4.1 and 4.2 for $n = 6000$ RPM.

4.3.1 Thrust

The non-dimensional thrust generation, C_T, of the LE1-DA18-0.14 ducted propeller, the trimmed OP and untrimmed OP is shown as a function of *J* in Figure 4-16(a), for $n = 6000$ RPM and $0 \text{ m/s} < V_\infty < 15 \text{ m/s}$. The C_T-*J* plots in Figure 4-16(a) show that due to untrimmed OP being normalized by the full propeller diameter of 269.5 mm, both the LE1-DA18-0.14 and the trimmed OP operate at a higher C_T than the untrimmed OP for the entirety of the *J* range investigated. However, in Figure 4-16(b) the C_T for all three systems are normalized by the trimmed propeller diameter, 230.7 mm, and it demonstrates that the untrimmed OP generates a higher thrust force than the trimmed OP and the LE1-DA18-0.14 systems, when compared under the same basis of normalization.

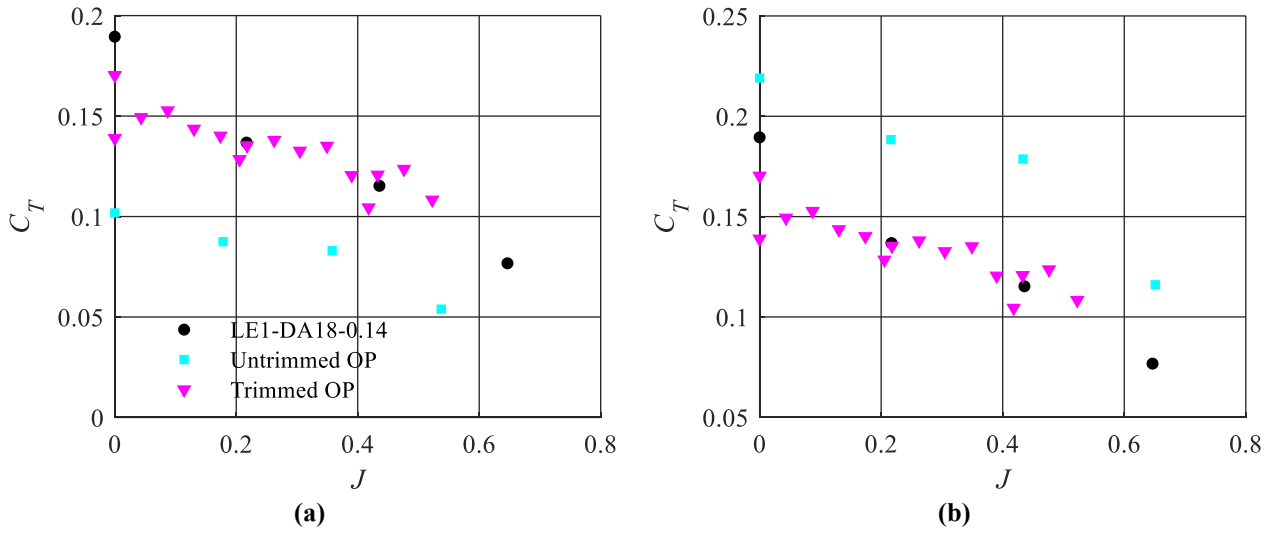

Figure 4-16: (a) The results of C_T as a function of J of the LE1-DA18-0.14 ducted propeller, the trimmed OP and the untrimmed OP. The C_T for the untrimmed OP is normalized with respect to the full propeller diameter (269.5 mm) for n = 6000 RPM. The figure in (b) shows the same results, but the C_T for all three systems are normalized with the trimmed propeller diameter (230.7 mm).

Although the J range investigated in this section was increased with respect to the range tested in sections 4.1 and 4.2, the highest advance ratio achieved, $J = 0.65$, was not sufficient to achieve zero thrust production, $C_T = 0$ from either the LE1-DA18-0.14 or the untrimmed OP systems.

4.3.2 Power

Non-dimensional power consumption, C_P, for the LE1-DA18-0.14, trimmed and untrimmed OP systems is shown as a function of J in Figure 4-17, for n = 6000 RPM. The results show that both the LE1-DA18-0.14 and the trimmed OP systems operate at a higher C_P than the untrimmed OP, for the J range investigated. The plots in Figure 4-17 demonstrates that testing at higher J values provides evidence of a parabolic behaviour not observed in the results of section 4.1.2 and 4.2.2. The C_P-J curve for the LE1-DA18-0.14 system shows that a maximum C_P value is achieved at an advance ratio of approximately J=0.2~0.3. The parabolic shape of the C_P response observed for the LE1-DA18-0.14 system is not evident for the trimmed and untrimmed OP results. The C_P results of the trimmed and untrimmed OP systems show an approximately invariant response with changes in J.

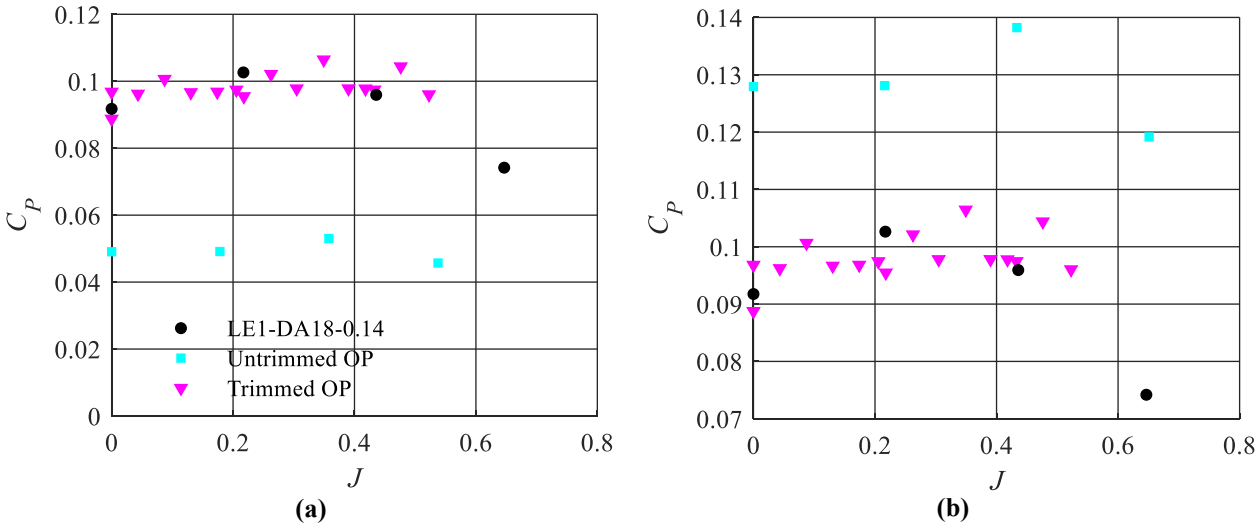

Figure 4-17: (a) The results of C_P as a function of J of the LE1-DA18-0.14 ducted propeller, the trimmed OP and the untrimmed OP for n = 6000 RPM. The value of C_P for the untrimmed case has been computed using the full nominal diameter of the propeller (269.5 mm) The figure in (b) shows the same C_P-J trends, where C_P has been computed using the same diameter (230.7 mm) for all three systems.

4.3.3 Propulsive Efficiency

The propulsive efficiency, η, of the LE1-DA18-0.14, trimmed OP and untrimmed OP systems is presented as a function of J in Figure 4-18, for n = 6000 RPM. The propulsive efficiency presented in this figure has been calculated for all three systems by non-dimensionalizing the data with respect to a common propeller diameter of D = 230.7 mm. The results in Figure 4-18 show that the untrimmed OP operates at a higher η than the LE1-DA18-0.14 and trimmed OP systems until approximately J = 0.55. Comparing the η response between the trimmed OP and the LE1-DA18-0.14 ducted propeller shows that the trimmed OP operates at a marginally higher η than the ducted propeller, for the J range investigated. The maximum propulsive efficiency achieved by the untrimmed OP and the LE1-DA18-0.14 are 63.40% and 66.88%.

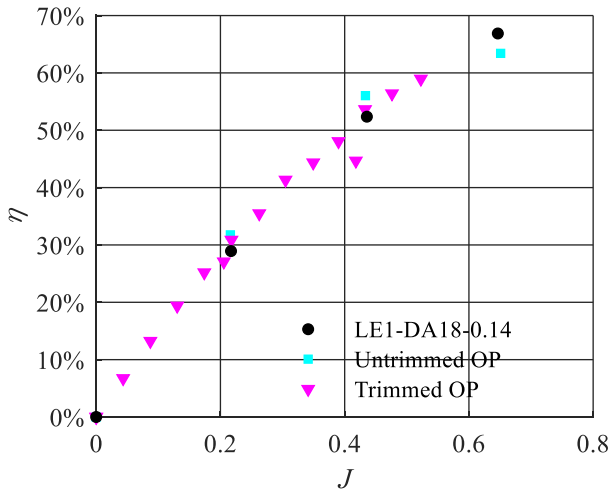

Figure 4-18: The propulsive efficiency, η, results of the LE1-DA18-0.14 ducted propeller, the trimmed OP and the untrimmed OP, for n = 6000 RPM.

Due to the definition of CT and CP from equations 2-41 and 2-42, and the fact that the untrimmed OP has a propeller diameter 21.1% larger than the LE1-DA18-0.14 and trimmed OP systems, the CT-J and CP-J plots presented in Figure 4-16 and Figure 4-17, respectively, demonstrate that the untrimmed OP performed at a lower CT and CP than the LE1-DA18-0.14 and trimmed OP systems for the range $0 < J < 0.65$ and n = 6000 RPM. The propulsive efficiency results shown in Figure 4-18 exhibited that the untrimmed OP operated at higher η than both the LE1-DA18-0.14 and trimmed OP systems until an approximate advance ratio of $J = 0.55$, where the η-J plots of the three systems appear to intercept.

4.4 Inlet Flow Structure Comparison

One of the main benefits of using a duct with a curved leading edge around the propeller blades is its potential to accelerate the flow towards the rotor disk. As discussed in section 2.4, the acceleration of the flow increases the mass flow rate through the rotor disk plane, and its effects are twofold: first it allows the propeller blades to be loaded in regions closer to the tip of the blade, where flow tends to leak, reducing the generation of tip vortices; and second it decreases the α_b of the blade elements, offloading the propeller. In this section the ability of the duct to accelerate the flow is investigated by presenting the velocity fields upstream of the rotor disk, as well as the

changes to the inlet mass flow rate. This section presents the results from the Stereoscopic PIV experiment described in section 3.6.2, performed at the inlet of the LE1-DA18-0.14 and untrimmed OP. The results from the correlation are shown in Figure 4-19 to Figure 4-22, for n = 6000 RPM and V_∞ = 0 m/s, 5 m/s, 10 m/s and 15 m/s, respectively. The operating conditions selected for these tests are chosen based on the load measurements previously presented in section 4.3. In parts (a) and (b) of Figure 4-19 to Figure 4-22, the velocity vector fields of the inlet flow's axial and radial velocities, w and v, respectively, are superimposed over a contour plot of the axial velocity, w, normalised by the blade tip speed of the trimmed propeller, ΩR_T. As a means of reference, the values of $V_\infty/\Omega R_T$ corresponding to V_∞ = 0 m/s, 5 m/s, 10 m/s and 15 m/s are 0, 0.07, 0.14 and 0.21, respectively. The number of vectors shown in the ducted propeller's inlet velocity fields has been reduced by a factor of 33 in the case of V_∞ = 0 m/s and 5 m/s, and by a factor of 30 in the case of V_∞ = 10 m/s and 15 m/s to enhance visualization. For the open propeller results, the number of vectors has been reduced by a factor of 33 in all four free-streams investigated. The vertical axis of the figures is the y direction, which coincides with the radial direction, and is non-dimensionalized by the internal diameter of the duct, D. The horizontal axis of the figures is the z direction or axial direction, also non-dimensionalized by D. In these figures, a vertical white dotted line has been plotted to indicate the location of the rotor disk plane, or z/D = 0.

In part (c) of Figure 4-19 to Figure 4-22 the axial velocity profiles of the LE1-DA18-0.14 and untrimmed OP systems have been plotted for the location z/D = 0, which corresponds to the rotor disk plane location. The vertical axis of these figures is once again the non-dimensional radial direction y/D, and the horizontal axis is the magnitude of the non-dimensional axial velocity $w/\Omega R_T$.

Comparing the results presented in parts (a) and (b) of Figure 4-19 to Figure 4-22 it can be observed that the LE1-DA18-0.14 ducted propeller achieved a higher maximum axial free-stream velocity than the untrimmed OP, for all four free-streams investigated. This observation is characterized by the larger values of $w/\Omega R_T$ achieved by the ducted propeller at the z/D = 0 location, which is also visualized on the axial velocity profiles plotted in part (c) of Figure 4-19 to Figure 4-22.

These results provide evidence of a higher loading of the propeller when it is accompanied by the LE1-DA18-0.14 duct. However, evaluation of Figure 4-19 to Figure 4-22 demonstrates that even with the use of the LE1-DA18-0.14 duct, the ducted propeller experiences a small drop in mass

flow rate in the region near the tip of the propeller blade, located at $y/D = 0.48$ (a region not included in the domain of the FOV). It can be observed in the results of the LE1-DA18-0.14 ducted propeller that the magnitude of $w/\Omega R_T$ achieves its maximum value in the radial position range of approximately $0.2 < y/D < 0.35$. This is best observed through the axial velocity profiles shown in part (c) of Figure 4-19 to Figure 4-22. This result suggests that the ducted propeller did not mitigate tip leakage flow to its entirety, which is attributed mainly to the δ_{tip} used in the configuration. Another possible conclusion that may be drawn from these results is the existence of a stagnation point at the location where the flow is incident on the leading edge of the duct.

The axial velocity results (V_∞ = 5 m/s, 10 m/s and 15 m/s) of the LE1-DA18-0.14 ducted propeller shown in Figure 4-20(a), Figure 4-21(a) and Figure 4-22(a) exhibit a momentum defect at the rotor disk plane for the approximate range $0.12 < y/D < 0.2$. Due to its location, this does not correspond to the presence of a propeller hub and is attributed to excessive glare reflected from the experimental setup during the image acquisition process, previously mentioned in section 3.6.4. This momentum deficiency is reflected in part (c) of Figure 4-20 to Figure 4-22 as a significant drop of $w/\Omega R$ in the location defined by the same y/D range. Image pre-processing steps were taken as attempts to minimize the effect of glare on these images as discussed in section 3.6.4; however, it was not possible to eliminate the effect.

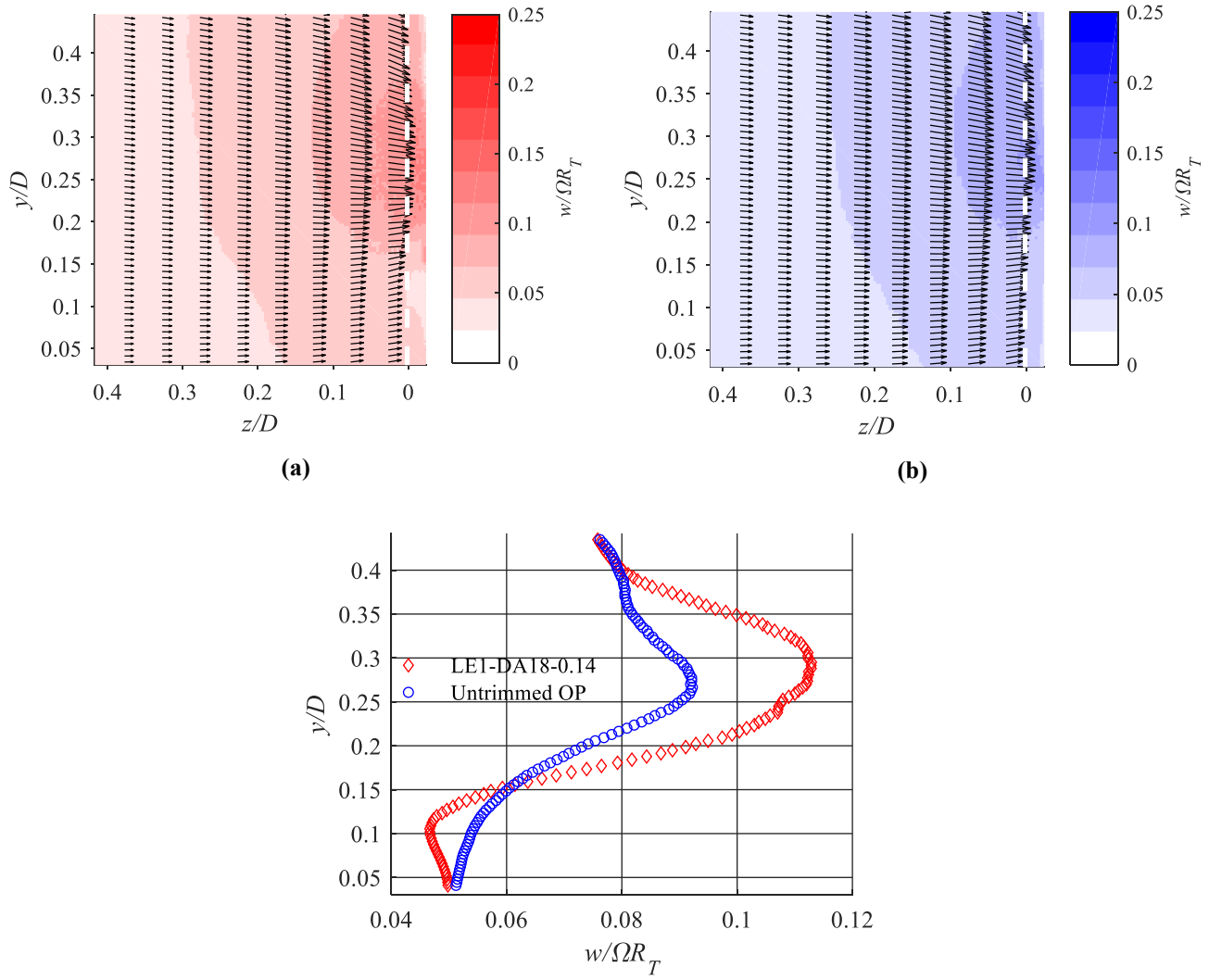

Figure 4-19: The stereoscopic PIV results of the inlet flow for the (a) LE1-DA18-0.14 and the (b) untrimmed OP, operating at V_∞ = 0 m/s and n = 6000 RPM (J = 0). For the same operating condition, the plot in (c) shows a comparison of the axial velocity profile normalized by the blade tip speed, $w/\Omega R$, at the z/D = 0 location (rotor disk plane).

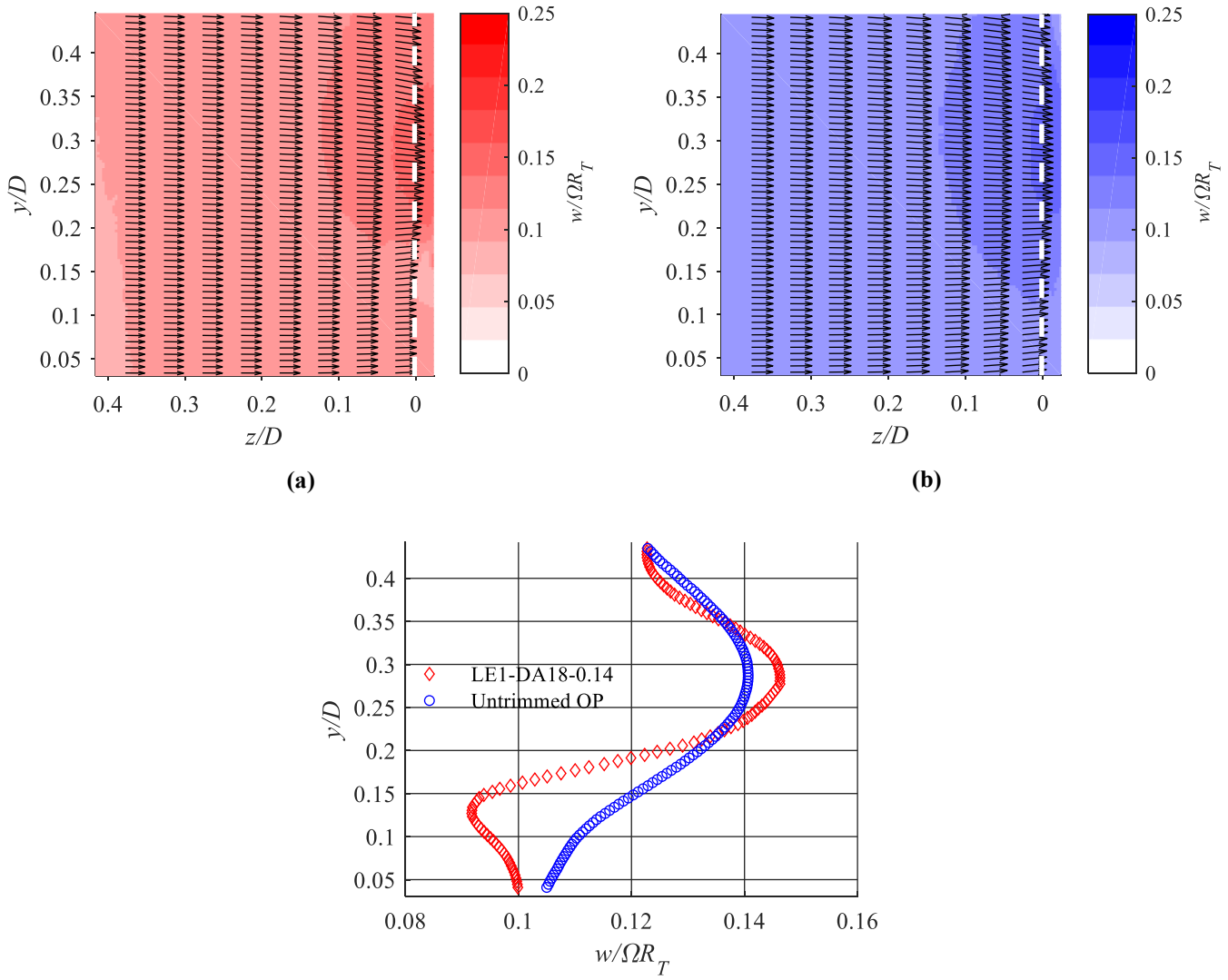

Figure 4-20: The stereoscopic PIV results of the inlet flow for the (a) LE1-DA18-0.14 and the (b) untrimmed OP, operating at V_∞ = 5 m/s and n = 6000 RPM (J = 0.22 and J = 0.18 for the LE1-DA18-0.14 and untrimmed OP systems, respectively). For the same operating condition, the plot in (c) shows a comparison of the axial velocity profile normalized by the blade tip speed, $w/\Omega R$, at the z/D = 0 location (rotor disk plane).

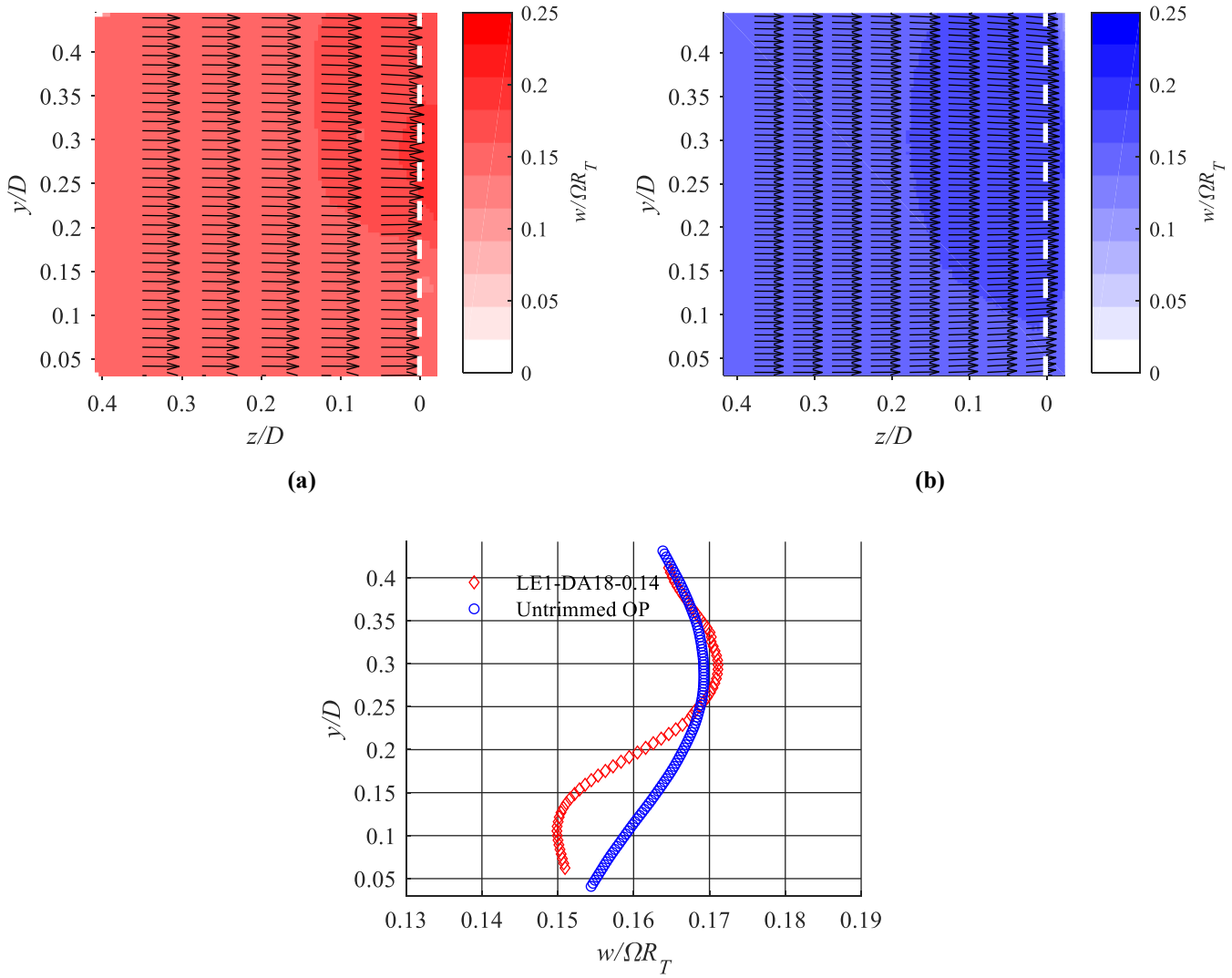

Figure 4-21: The stereoscopic PIV results of the inlet flow for the (a) LE1-DA18-0.14 and the (b) untrimmed OP, operating at V_∞ = 10 m/s and n = 6000 RPM (J = 0.44 and J = 0.36 for the LE1-DA18-0.14 and untrimmed OP systems, respectively). For the same operating condition, the plot in (c) shows a comparison of the axial velocity profile normalized by the blade tip speed, $w/\Omega R$, at the z/D = 0 location (rotor disk plane).

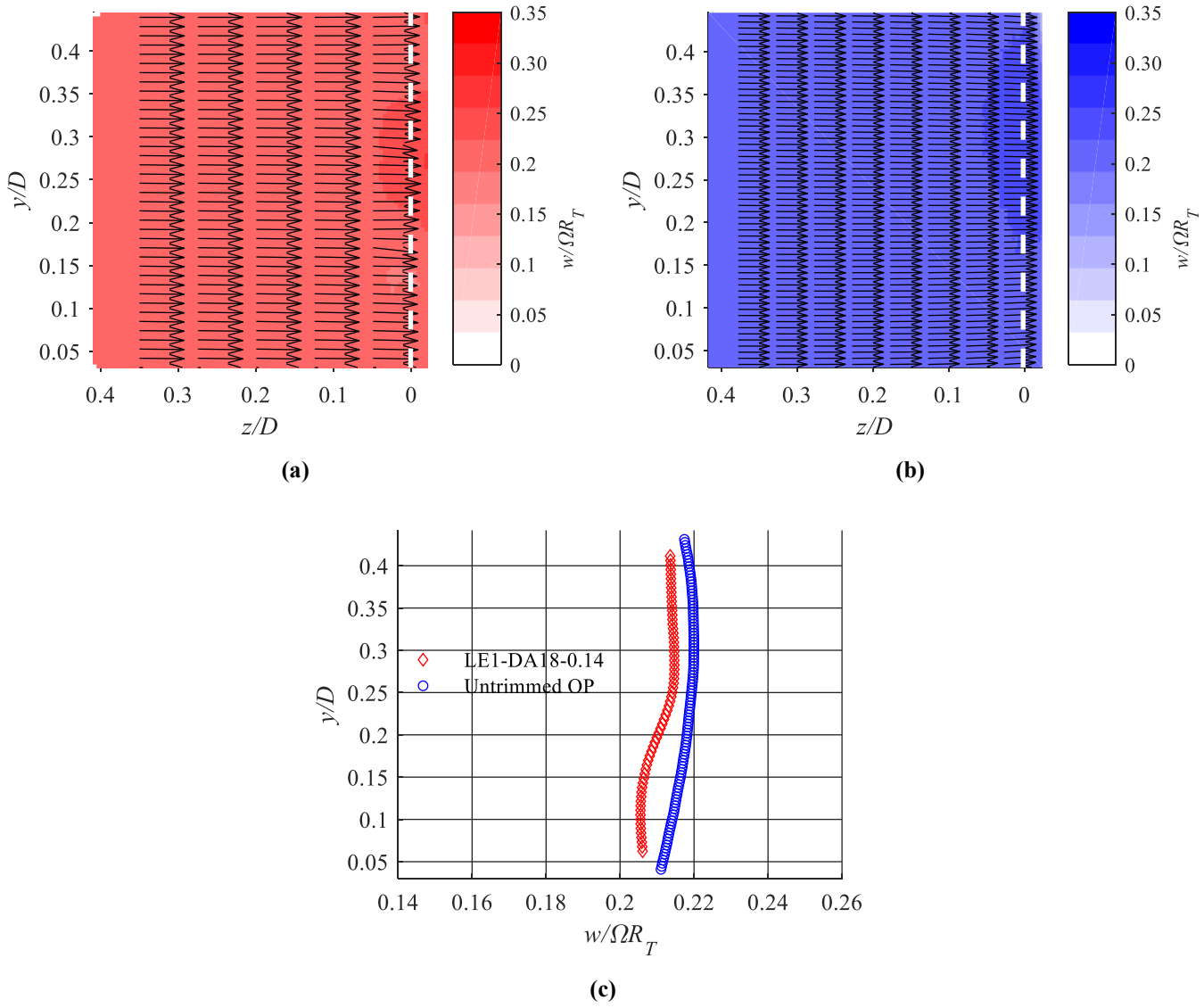

Figure 4-22: The stereoscopic PIV results of the inlet flow for the (a) LE1-DA18-0.14 and the (b) open propeller, operating at V_∞ = 15 m/s and n = 6000 RPM (J = 0.65 and J = 0.54 for the LE1-DA18-0.14 and untrimmed OP systems, respectively). For the same operating condition, the plot in (c) shows a comparison of the axial velocity profile normalized by the blade tip speed, $w/\Omega R$, at the z/D = 0 location (rotor disk plane).

Comparing the axial velocity profile plots in part (c) of Figure 4-19 and Figure 4-22 it is observed how with increasing V_∞, the $w/\Omega R$ gap between the red circles trend representing the untrimmed

OP and the blue circles trend representing the LE1-DA18-0.14 system decreases. In other words, the difference in axial velocity along the radial direction y decreases between the untrimmed OP and the ducted propeller with increasing free-stream velocity. The axial velocity profiles also reveal how the untrimmed OP achieves a stronger uniformity in the distribution of w along the radial direction y. This is attributed to two influential factors: first, the momentum deficiency observed for the LE1-DA18-0.14 system in the range $0.12 < y/D < 0.2$ previously discussed, and second, the momentum deficiency observed for the LE1-DA18-0.14 system near the blade tip location. The latter mentioned evidences the ineffectiveness of the δ_{tip} on the ducted configuration.

4.4.1 Inlet Mass Flow Rate

The thrust output of a propeller is directly proportional to the mass flow rate through the rotor disk plane as shown in equation 2-13. Assuming incompressible flow, the mass flow rate through the rotor disk is calculated as

$$\dot{m} = \rho A w \tag{4-1}$$

where

$$A = \pi R^2$$

and

$$w = \Omega R \cdot w(y)$$

To approximate the total mass flow rate through the rotor disk using the discretized data obtained through the PIV experiments, the disk is divided into differential ring elements as shown in Figure 4-23. The area inside each ring element is calculated using the internal and external diameters of the element, namely r_i and r_o, as:

$$dA = \pi(r_o^2 - r_i^2)$$

The mass flow rate through each ring element is then calculated as:

$$d\dot{m} = \rho \cdot w(y) \cdot \pi(r_o^2 - r_i^2)$$

Therefore, the total mass flow rate through the rotor disk plane is equal to the sum of the mass flow rates from all the ring elements. This approximation is shown in the expression below:

$$\dot{m} \approx \sum_{r_o=R_h+dr,\ r_i=R_h}^{r_o=R,\ r_i=R-dr} \rho w \pi(r_o^2 - r_i^2) \tag{4-2}$$

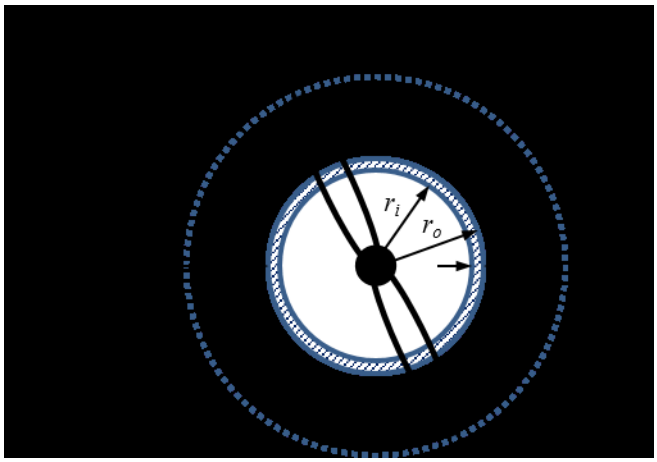

Figure 4-23: Diagram showing the differential ring elements used in the approximation of the mass flow rate calculation through the rotor disk plane.

The axial velocity w for each ring element is obtained from the axial velocity profiles presented in Figure 4-19 to Figure 4-22. Since the number of axial velocity data points for the LE1-DA18-0.14 case are less than the ones available for the untrimmed OP results at V_∞ = 10 m/s and 15 m/s (due to an increment in the IW size when processing the PIV images for the ducted case at V_∞ = 10 m/s and 15 m/s), the length of dr is different in these two cases. In other words, the ring elements used for the mass flow rate approximation of the ducted case at V_∞ = 10 m/s and 15 m/s are thicker (higher dr) than the ring elements used for the remaining cases. Therefore the mass flow rates through each ring element have been normalized by the corresponding dr used, and the results are shown in Figure 4-24 (a) to (d) for V_∞ = 0 m/s, 5 m/s, 10 m/s and 15 m/s, respectively. It must be noted that since the axial velocity profiles were obtained for the range $0.05 < y/D < 0.4$, the mass flow rate obtained through this analysis corresponds to the circumferential area defined by the same range. In the current analysis it is assumed that the axial velocity profile described by the data acquired is the same at all azimuthal locations of the rotor disk. This analysis also assumes incompressible flow ($d\rho/dt = \partial\rho/\partial x = \partial\rho/\partial y = \partial\rho/\partial z = 0$). The results in Figure 4-24 show that the mass flow rate per ring element increases the further its location from the center of the disk, and this is mainly due to the increase in area dA as y increases, since, as it was observed in Figure 4-19 to Figure 4-22, the axial velocity decreases in regions near the tip of the blade.

As a result of the assumptions discussed above, alongside the experimental setbacks discussed in section 4.4, the mass flow rate approximation discussed in the following paragraphs possesses low reliability. In addition to the fact that data was not collected for an inlet region that covered the entire radius of the propeller, the results shown in Figure 4-24 suggest that there is still a significant reading of mass flow at regions near the tip of the blades ($y/D = 0.45$). In the case of the ducted system, the mass flow rate should diminish quickly to 0 kg/s, as the radial location increases, as it approaches the physical barrier imposed by the internal duct wall.

The results for $V_\infty = 0$ m/s shown in Figure 4-24(a) demonstrate that the ducted propeller achieved higher mass flow rates through the ring elements than the untrimmed OP, particularly in the region defined by $0.16 < y/D < 0.36$. As the free-stream velocity is increased, the results of Figure 4-24 (b)-(d) reveal that the mass flow rate through each ring element increases, and the difference in $d\dot{m}/dr$ between the LE1-DA18-0.14 and untrimmed OP systems decreases. The latter mentioned result is evidence of the decrement in performance enhancement effects of the duct at the higher advance ratio regime.

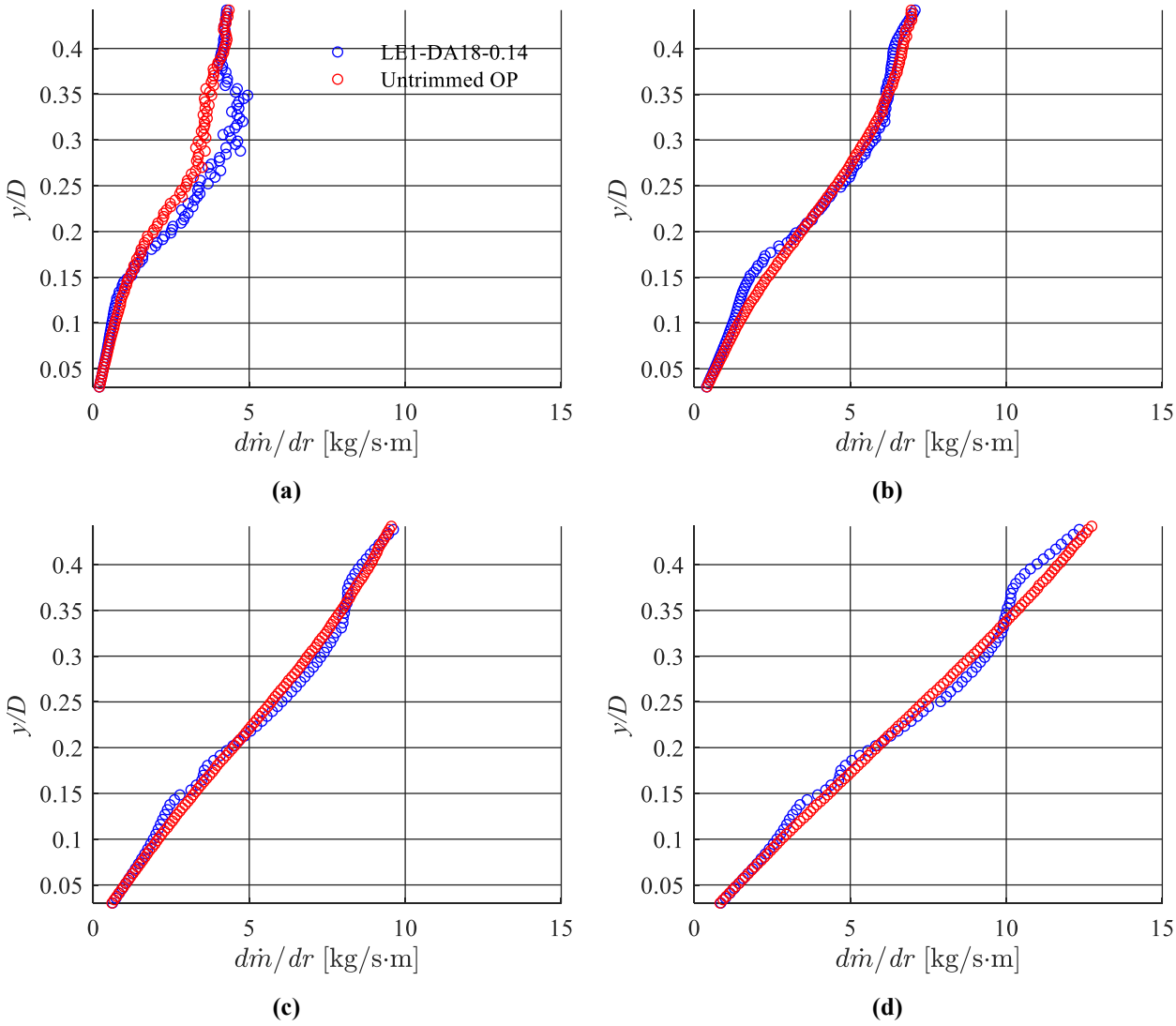

Figure 4-24: The plots show the mass flow rate per radial thickness of the ring elements, *dr*, for each differential ring element within the rotor disk, for the LE1-DA18-0.14 and untrimmed OP systems. The plots in (a) – (d) correspond to V_∞ = 0 m/s, 5 m/s, 10 m/s and 15 m/s, respectively. The vertical axis of the plots indicates the non-dimensional distance *y*/*D* from the center of the rotor disk.

The data in Figure 4-24 (a) to (d) was integrated in MATLAB using trapezoidal integration, in order to obtain an approximation of the total mass flow rate through the rotor disk. The results of this approximation are shown in Figure 4-25(a). These results demonstrate that regarding the mass flow rate, the ducted propeller system outperformed the open propeller only in hovering.

The percentage difference in mass flow rate with respect to the untrimmed OP case is shown in Figure 4-25(b), where the results demonstrate that for the static test the LE1-DA18-0.14 system

achieved an increment in the calculated $\dot{m}$ of 13% over the untrimmed OP, and for tests conducted at V_∞ = 5 m/s, 10 m/s, 15 m/s the calculated $\dot{m}$ for the untrimmed OP was higher than that of the LE1-DA18-0.14 system by an average of 1.83%.

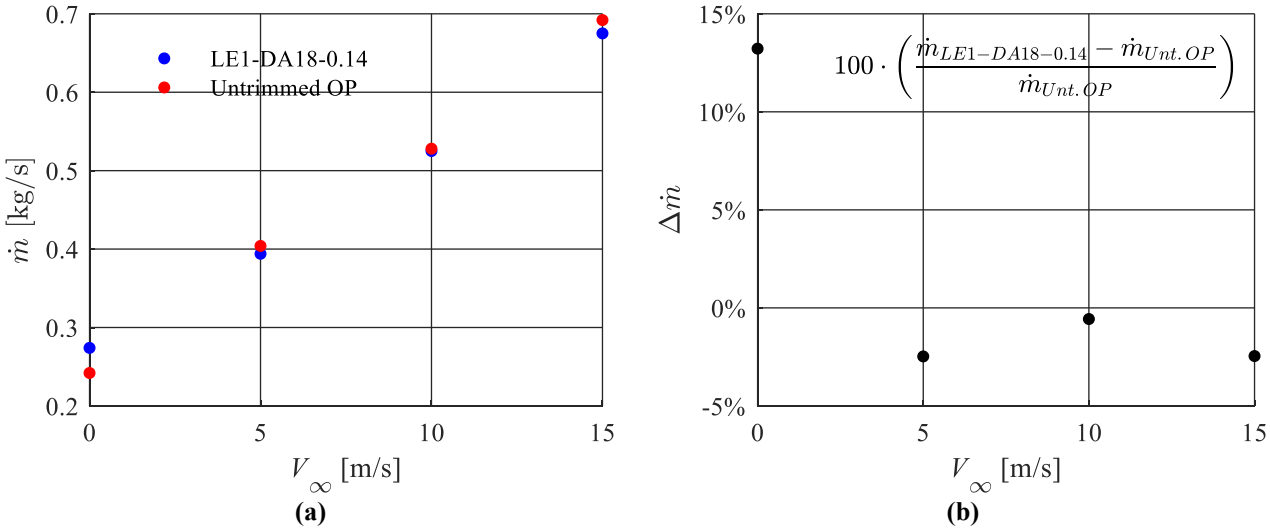

Figure 4-25: The resultant inlet mass flow rate, $\dot{m}$ as a function of J, calculated by integrating the measured axial velocity distribution $w(y)$ over the radial coordinate y, for the LE1-DA18-0.14 and untrimmed OP. The data corresponds to n = 6000 RPM.

The structure of the flow field in the region -0.01 < y/D < 0.47 and -0.05 < z/D < 0.43 (upstream of the rotor disk plane) has been studied using the velocity vector fields and axial velocity contours presented in Figure 4-19 to Figure 4-22; obtained through the stereoscopic PIV investigation described in section 3.6.2. It was determined that errors in the image acquisition procedure, associated with extraneous glare from the duct's internal surface hindered the quality of the velocity vector fields obtained for the LE1-DA18-0.14 ducted propeller. These errors manifested as a momentum deficiency region near the root of the propeller blade. The results revealed that the LE1-DA18-0.14 achieved greater acceleration of the free-stream towards the rotor disk plane than the untrimmed OP, and higher axial velocities towards the tip of the propeller blades (higher loading), for equal V_∞ and n.

Using the axial velocity data obtained at the rotor disk location, an approximation of the mass flow rate was calculated for the region 0.05 < y/D < 0.4, and the results showed the ducted propeller provided a higher mass flow rate than the untrimmed OP only at the static condition test by 13%,

but underperformed the untrimmed OP at the axial flow tests by an average of 1.83%. This drop in mass flow rate by the ducted propeller corresponds to the loss in thrust generation found in sections 4.1 to 4.3.

4.5 Wake Structure Comparison

The structure of the flow field in the wake region of the ducted and open propeller systems is of interest because it provides information regarding the degree of contraction of the slipstream. As previously discussed in Chapter 2, a reduction of the slipstream contraction by a ducted propeller results in an increase of propulsive efficiency. Similarly, a reduction in the generation of tip vortices also signifies an improvement to the efficiency of the system. This will also be investigated by looking into the vorticity of the flow structure in the wake region.

In this section the results from the planar PIV experiment described in section 3.6.3, performed on the wake region of the LE1-DA18-0.14 ducted propeller, the trimmed OP and the untrimmed OP, are shown in Figure 4-26 to Figure 4-29, for n = 6000 RPM and V_∞ = 0 m/s, 5 m/s, 10 m/s and 15 m/s, respectively. Parts (a), (b) and (c) of these figures show the average velocity vector fields of the resultant vector between the axial and radial velocities, w and v, respectively, superimposed over a contour of the non-dimensional axial velocity normalized by the blade tip speed of the trimmed propeller, ΩR_T. The region of the flow shown in these images is defined by the ranges $0.27 < y/D < 0.67$ and $0.58 < -z/D < 1.11$. The left edge of the figures is immediately downstream of the duct's trailing edge. The location of the duct's external diameter, D_E, is indicated in parts (a) and (d) of the figures on the vertical axis, and the location of the internal diameter corresponds to the value $y/D = 0.5$. The number of vector grid displayed in the images has been reduced to 15×20 to enhance visualisation.

To characterize the slipstream contraction of the wake achieved by each system, the location of the shear layer between the exit jet and the surrounding free-stream was approximated. The velocity data obtained for the hovering condition (V_∞ = 0 m/s) through stereoscopic PIV did not exhibit values close to 0 m/s in the entire grid of data points, therefore part (d) of Figure 4-26 shows a plot of the iso-contour lines of the exit jet velocity corresponding to w = 1 m/s, which when normalized by the blade tip speed translates to $w/\Omega R_T = 0.014$.

To characterize the location of the shear layer in the axial flow tests, iso-contour lines of locations where the exit jet velocity was within a 20% increment of the free-stream velocity were generated, and the results are shown in part (d) of Figure 4-27 to Figure 4-29. The plots show the iso-contour lines of the exit jet velocity corresponding to $w/V_\infty = 1$, which translates to the ranges $w/\Omega R_T = 0.07$, $w/\Omega R_T < 0.14$ and $w/\Omega R_T < 0.21$, for $V_\infty = 5$ m/s, 10 m/s and 15 m/s, respectively.

The relative size and orientation of the velocity vector arrows shown in Figure 4-26 to Figure 4-29 indicate the magnitude of the average velocity v is significantly lower than the axial velocity w. Comparing the axial velocity contours of the exit jet results shown in parts (a), (b) and (c) of Figure 4-26 to Figure 4-29, it can be observed that the LE1-DA18-0.14 ducted propeller produced an exit jet velocity lower than that of the trimmed and untrimmed OP systems. This result is congruent with the findings from Yilmaz *et. al.* [25], in which the axial velocity at the wake region was reduced by the use of a duct. The axial velocity contour plots of the LE1-DA18-0.14 ducted propeller show a region of momentum deficit that covers the approximate radial location $0.53 < y/D < 0.6$ for the results at $V_\infty = 5$ m/s and 10 m/s, and $0.55 < y/D < 0.6$ for the test at $V_\infty = 15$ m/s. This momentum deficit is a result of the blockage from the duct.

The results shown in part (d) of Figure 4-27 to Figure 4-29 demonstrate that the system with the largest absolute exit jet stream tube cross-section was achieved by the untrimmed OP, followed by the LE1-DA18-0.14 ducted propeller, and lastly by the trimmed OP, based on the threshold velocity immediately downstream of the duct's trailing edge. The radius of exit jet area used to calculate σ_e is the y location of the data point at $z/D = 0.58D$, and the value of σ_e is calculated through the equation

$$\sigma_e = \frac{\pi y^2}{\pi R^2} = \left(\frac{y}{R}\right)^2 \qquad \textbf{4-3}$$

For the hover condition, an effective area ratio was not computed, since the threshold of $w = 1$ m/s is not representative of the shear layer that separates the exit jet flow and the free-stream. The value of σ_e calculated for each system has been summarized in Table 4-3.

Table 4-3: The calculated effective slipstream contraction, σ_e, of the LE1-DA18-0.14, untrimmed OP and trimmed OP systems, at 5 m/s < V_∞ < 15 m/s and n = 6000 RPM.

V_∞ (m/s)	Effective Area Ratio, σ_e		
	LE1-DA18-0.14	Trimmed OP	Untrimmed OP
5	1.00	0.88	0.78
10	1.04	0.91	0.80
15	1.04	0.90	0.77

The results in Table 4-3 suggest that although the untrimmed OP achieved a larger exit jet stream tube, the LE1-DA18-0.14 ducted propeller was the only system out of the three to achieve an effective exit area-to-rotor area ratio greater than 1, meaning that not only was it successful in reducing the slipstream contraction, but that it expanded the exit area. Ideally the value of the expansion ratio would be σ_i = 1.40, which corresponds to the flow fully expanding to the exit area of the duct. The results provide evidence that the exit jet flow from the LE1-DA18-0.14 system did not adhere completely to the internal surface of the diffuser section.

Comparing the shear layer results for the free-stream velocities V_∞ =5 m/s, 10 m/s and 15 m/s, the trimmed OP and untrimmed OP systems demonstrate a straight shear layer in the stream-wise direction. In contrast, the shear layer exhibited by the LE1-DA18-0.14 ducted propeller appears to shift from an expansion to a contraction with increasing free-stream velocity. This indicates that the ducted propeller generates a lower acceleration of the flow with respect to the free-stream velocity, thus, the exit jet stream expands at a faster rate to the atmospheric pressure.

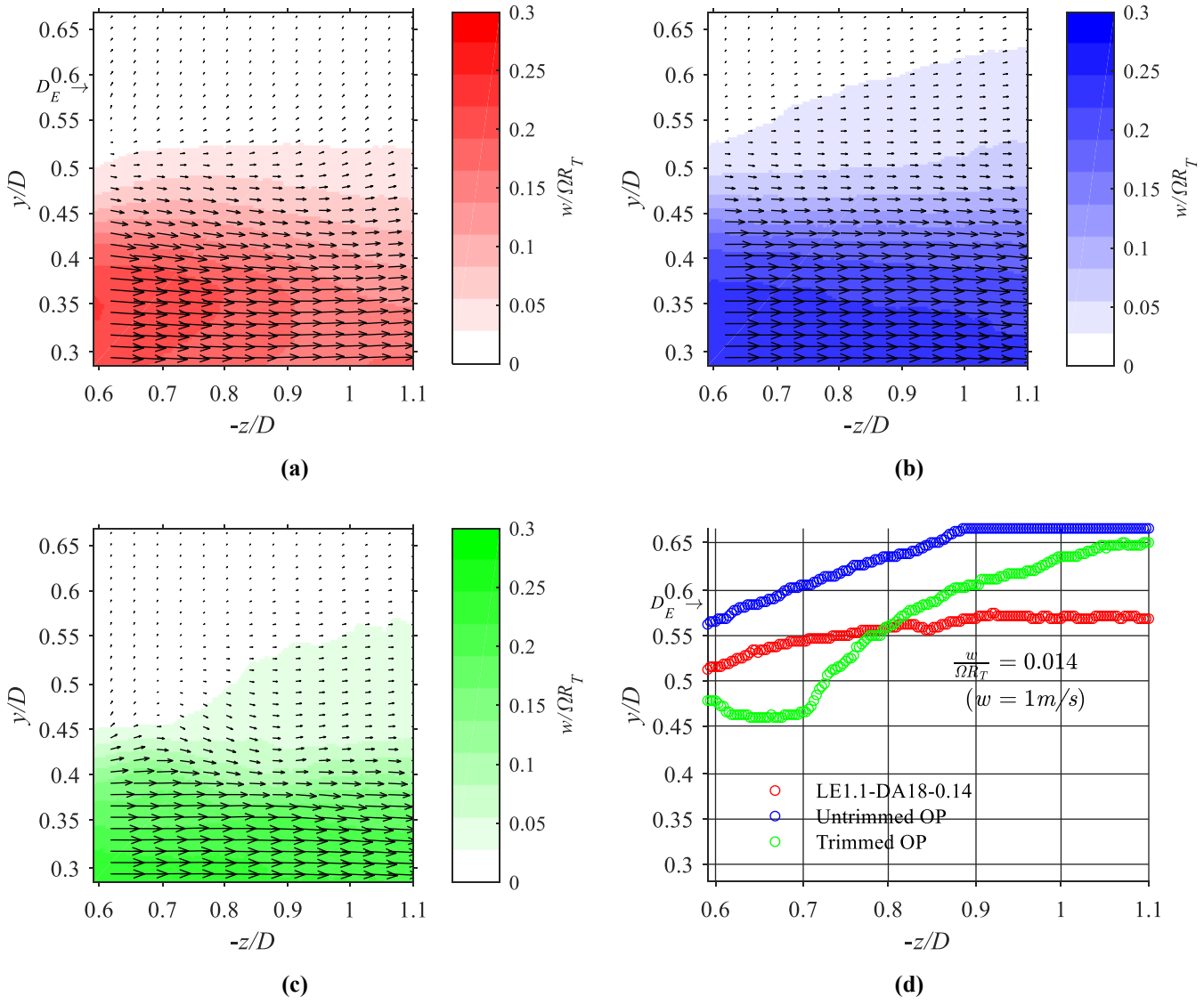

Figure 4-26: Planar PIV results of the exit jet flow for the (a) LE1-DA18-0.14, (b) untrimmed OP and (c) trimmed OP; operating at V_∞ = 0 m/s and 6000 RPM (J = 0). The plot in (d) shows a comparison of the velocity region characterized by the threshold velocity w = 1 m/s, at the wake region 0.57D < z < 1.1D.

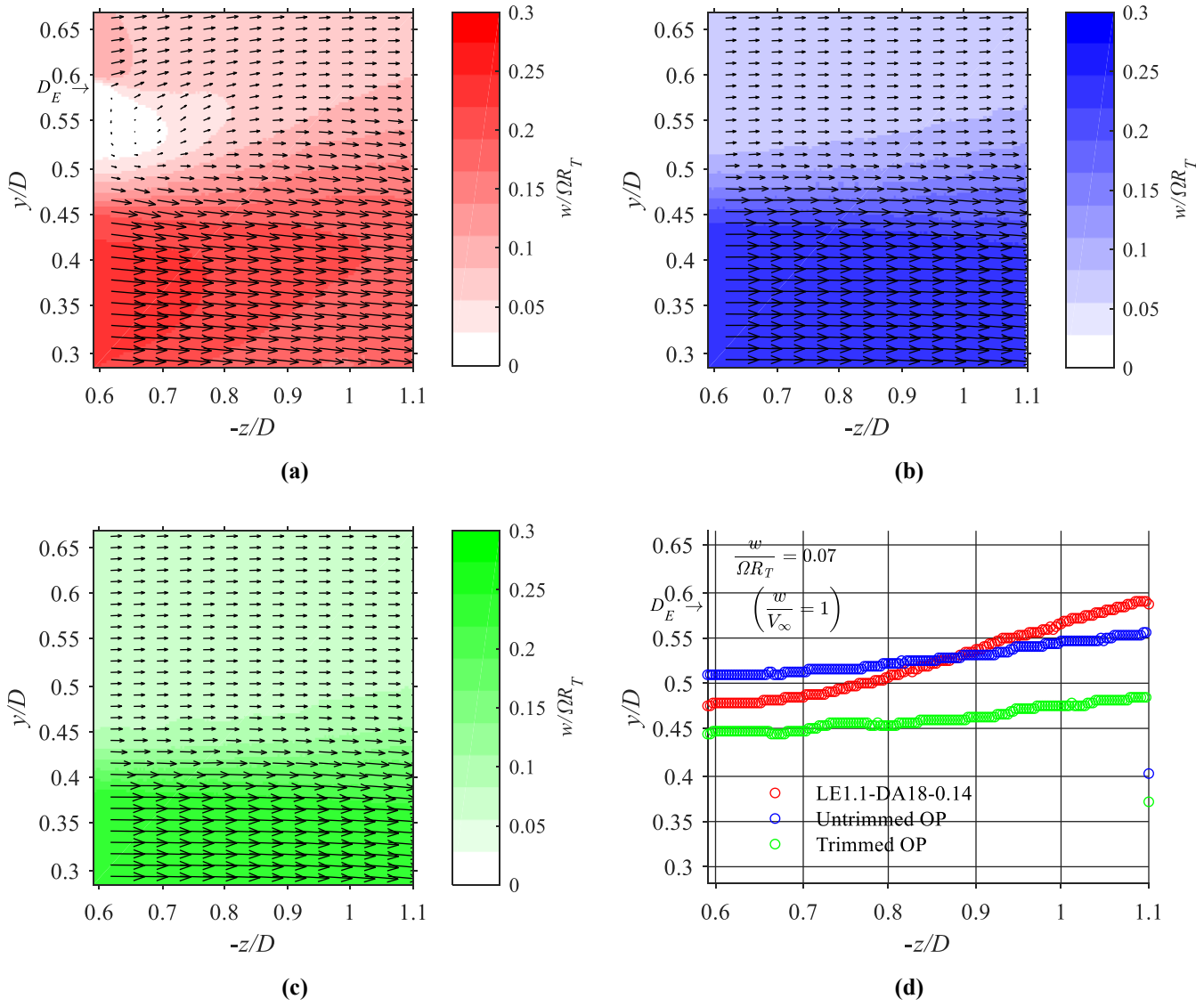

Figure 4-27: Planar PIV results of the exit jet flow for the (a) LE1-DA18-0.14, (b) untrimmed OP and (c) trimmed OP; operating at V_∞ = 5 m/s and 6000 RPM (J = 0.22 for the LE1-DA18-0.14 and trimmed OP systems, and J = 0.18 for untrimmed OP system). The plot in (d) shows a comparison of the shear layer characterized by the threshold velocity range $1 < w/V_\infty < 1.2$, at the wake region $0.57D < z < 1.1D$.

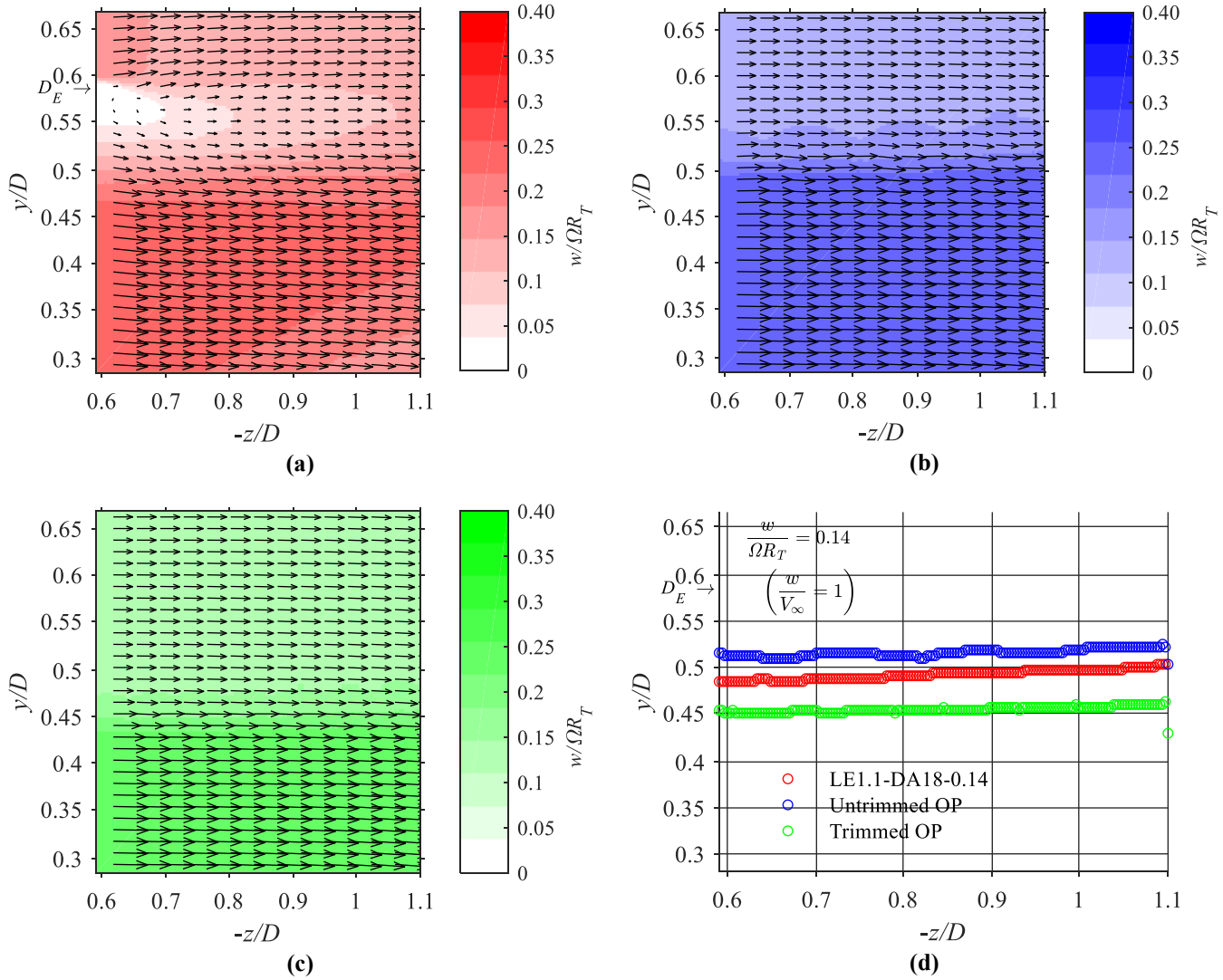

Figure 4-28: Planar PIV results of the exit jet flow for the (a) LE1-DA18-0.14, (b) untrimmed OP and (c) trimmed OP; operating at $V_\infty = 10$ m/s and 6000 RPM ($J = 0.44$ for the LE1-DA18-0.14 and trimmed OP systems, and $J = 0.36$ for untrimmed OP system). The plot in (d) shows a comparison of the shear layer characterized by the threshold velocity range $1 < w/V_\infty < 1.2$, at the wake region $0.57D < z < 1.1D$.

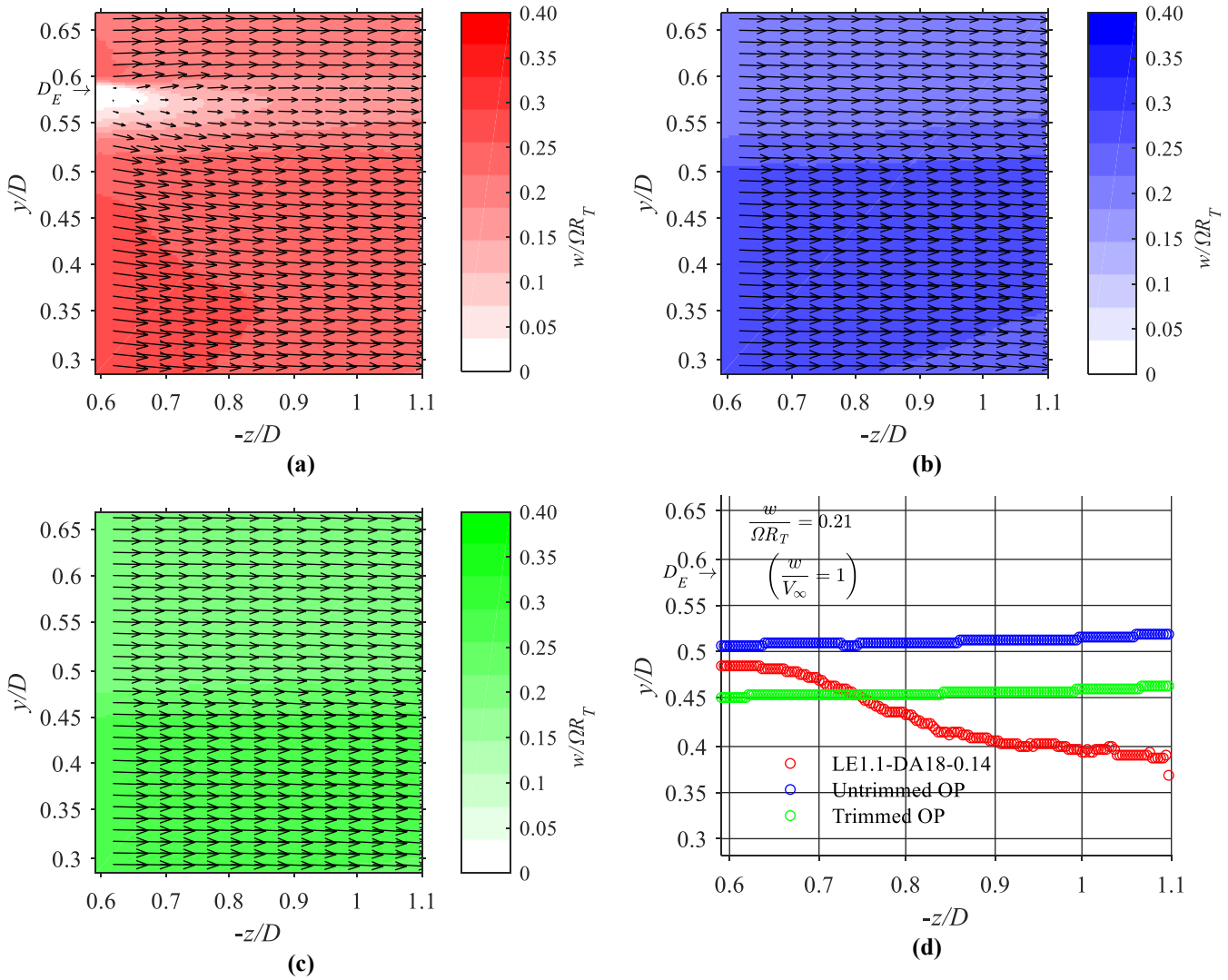

Figure 4-29: Planar PIV results of the exit jet flow for the (a) LE1-DA18-0.14, (b) untrimmed OP and (c) trimmed OP; operating at $V_\infty = 15$ m/s and 6000 RPM ($J = 0.65$ for the LE1-DA18-0.14 and trimmed OP systems, and $J = 0.54$ for untrimmed OP system). The plot in (d) shows a comparison of the shear layer characterized by the threshold velocity range $1 < w/V_\infty < 1.2$, at the wake region $0.57D < z < 1.1D$.

4.5.1 Characterization of Trailing Vortices through Instantaneous Vorticity

The presence of tip-vortices in the exit jet flow of the LE1-DA18-0.14, trimmed OP and untrimmed OP systems has been characterized by plotting contours of the *x*-vorticity component, ζ_x, of instantaneous snapshots of the wake region for all three systems. The results are shown in Figure 4-31 to Figure 4-34, for n = 6000 RPM and V_∞ = 0 m/s, 5 m/s, 10 m/s and 15 m/s, respectively. In the figures, parts (a), (b) and (c) corresponds to the results of the LE1-DA18-0.14, trimmed OP and untrimmed OP systems, respectively. The vorticity vector is defined as

$$\zeta = \left(\frac{\partial V}{\partial z} - \frac{\partial W}{\partial y}\right)\vec{\imath} + \left(\frac{\partial U}{\partial z} - \frac{\partial W}{\partial x}\right)\vec{\jmath} + \left(\frac{\partial U}{\partial y} - \frac{\partial V}{\partial x}\right)\vec{k} \qquad \textbf{4-4}$$

but since the available planar PIV data provided only the *v* and *w* velocities, only the *x* component of vorticity was considered, and thus equation 4-4 is reduced to

$$\zeta_x = \left(\frac{\partial v}{\partial z} - \frac{\partial w}{\partial y}\right)\vec{\imath} \qquad \textbf{4-5}$$

The highly rotational motion of the flow inside the helical vortex creates a centrifugal effect on the tracer particles used for seeding, and 'pushes' them out of the vortex core. Due to this effect, it is not able to capture particles at the vortex core itself with the applied PIV experiment, and this can be observed in the sample raw images presented in Figure 4-30, where snapshots of the flow at three different instances during the data acquisition period are presented, for the exemplary case of the trimmed OP at V_∞ = 5 m/s. Sample raw image snapshots of the flow such as the ones showed in Figure 4-30 are shown in Appendix C for the remaining tests configurations and operating conditions.

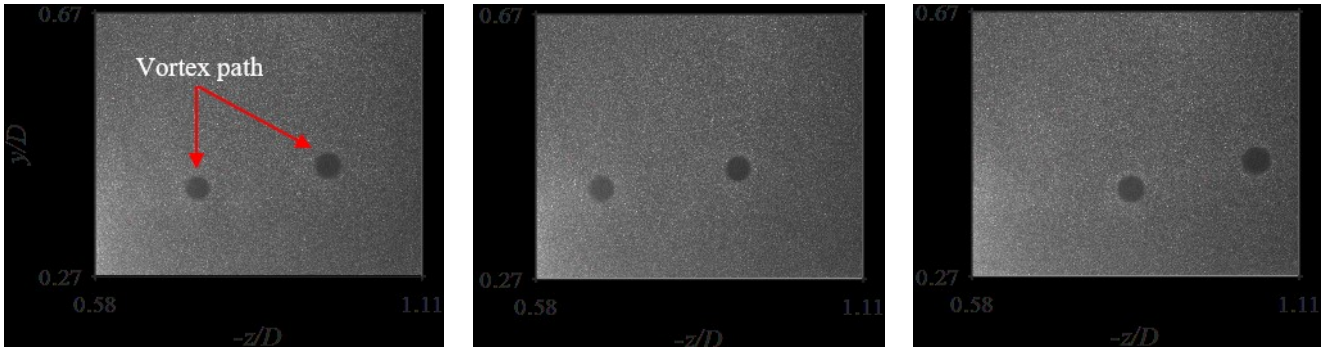

t = 20 s t = 40 s t = 60 s

Figure 4-30: Three sample instantaneous snapshots of the wake region from the trimmed OP system at V_∞ = 5 m/s. The top row shows raw data images, where the core of the helical tip vortex system is identified by the black circle shapes indicating a lack of tracer particles.

The correlation results are presented in Figure 4-31 to Figure 4-34, where velocity vector fields have been superimposed over the vorticity contours. In the velocity vector fields shown, the free-stream velocity has been subtracted from the axial component (z-component) of velocity, in order to display the rotation of the flow at the regions of vorticity. In the images, the tip vortices manifest as regions of high vorticity, with vortex cores displaying $\zeta_x > 2000$. The vortices shown in Figure 4-31 to Figure 4-34 are traces of the location where the core of the trailing helical vortex intersects the F.O.V. Comparing the wake structures in hover (Figure 4-31) to those in axial flow (Figure 4-32 to Figure 4-34), it is seen that for the hovering case there are numerous traces of vorticity towards the hub of the propeller. This is evidence that in hover, vortex shedding from the propeller blades begins at a closer location to the center of the rotor disk (lower y/D), contrasting the axial flow results, where the vorticity is shed mainly near the tip of the blades (higher y/D). From the figures, it can be observed that as the free-stream velocity is increased the diameter of the tip vortex cores decreases. However, due to the lack of information of the flow inside the vortices themselves, it is not possible to approximate the energy of such vortices, and thus, a reduction in the size of the vortices is not necessarily a reduction in the energy dedicated to the generation of tip vortices. In addition to the contour indicating a region of high vorticity by its color, the presence of the tip vortices is also observed through the velocity vectors, as recirculation appears around the circular shapes of high vorticity in the contour plots. The ducted propeller case shows traces of vorticity in the low y/D region than the OP cases, this may be due to two reasons: first, the canalization and acceleration of the flow towards the rotor disk plane may result in higher vortex shedding from the motor and stinger support apparatuses; and second, early tip vortex formation at low y/D locations within the propeller blades.

It can also be observed from Figure 4-31 to Figure 4-34 that the radial location at which the core of the vortex is emanated from the propeller blades increases as J is increased. For example, the results in Figure 4-32(c) for the untrimmed OP at $V_\infty = 5$ m/s show that the vortex cores are located approximately in the range of $0.41 < y/D < 0.44$, and the results in Figure 4-34(c) show the vortex cores at approximately $y/D = 0.47$.

The results for the LE1-DA18-0.14 in part (a) of Figure 4-31 to Figure 4-34 show that a region of vorticity is present at the location corresponding to the trailing edge of the duct. As the free-stream is increased, the presence of counter-rotating vortices at the trailing edge of the duct becomes

clearer. This is observed through the coinciding regions of negative (blue contours) and positive (red contours) regions of vorticity in part (a) of Figure 4-31 to Figure 4-34. Another factor that may influence the shedding of vortices downstream of the rotor disk in the LE1-DA18-0.14 system may be the presence of the two sets of duct support rods.

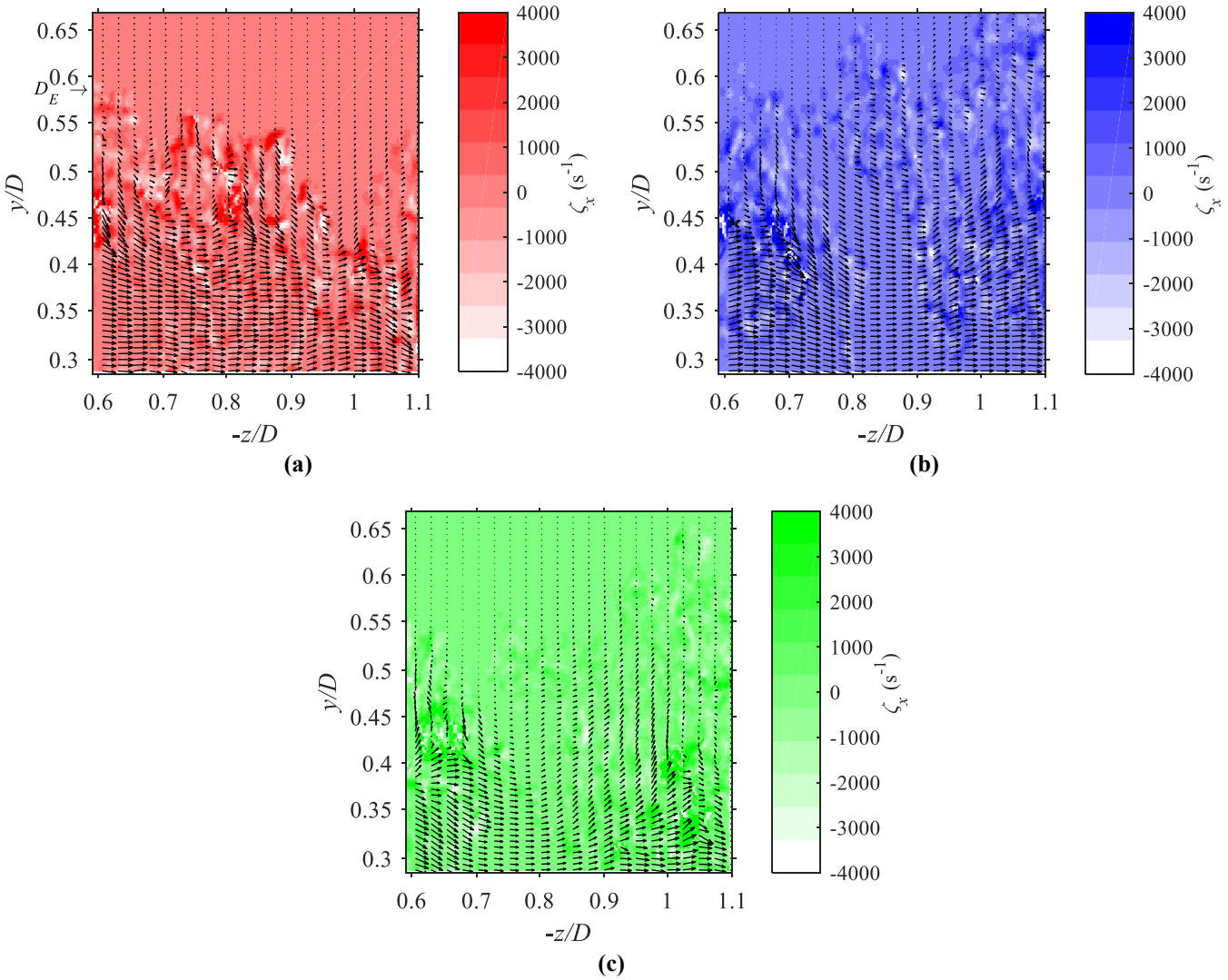

Figure 4-31: A contour of the *x*-component of vorticity, ζ_x, in the wake region of the (a) LE1-DA18-0.14, (b) untrimmed OP and (c) trimmed OP; operating at $V_\infty = 0$ m/s and 6000 RPM ($J = 0$).

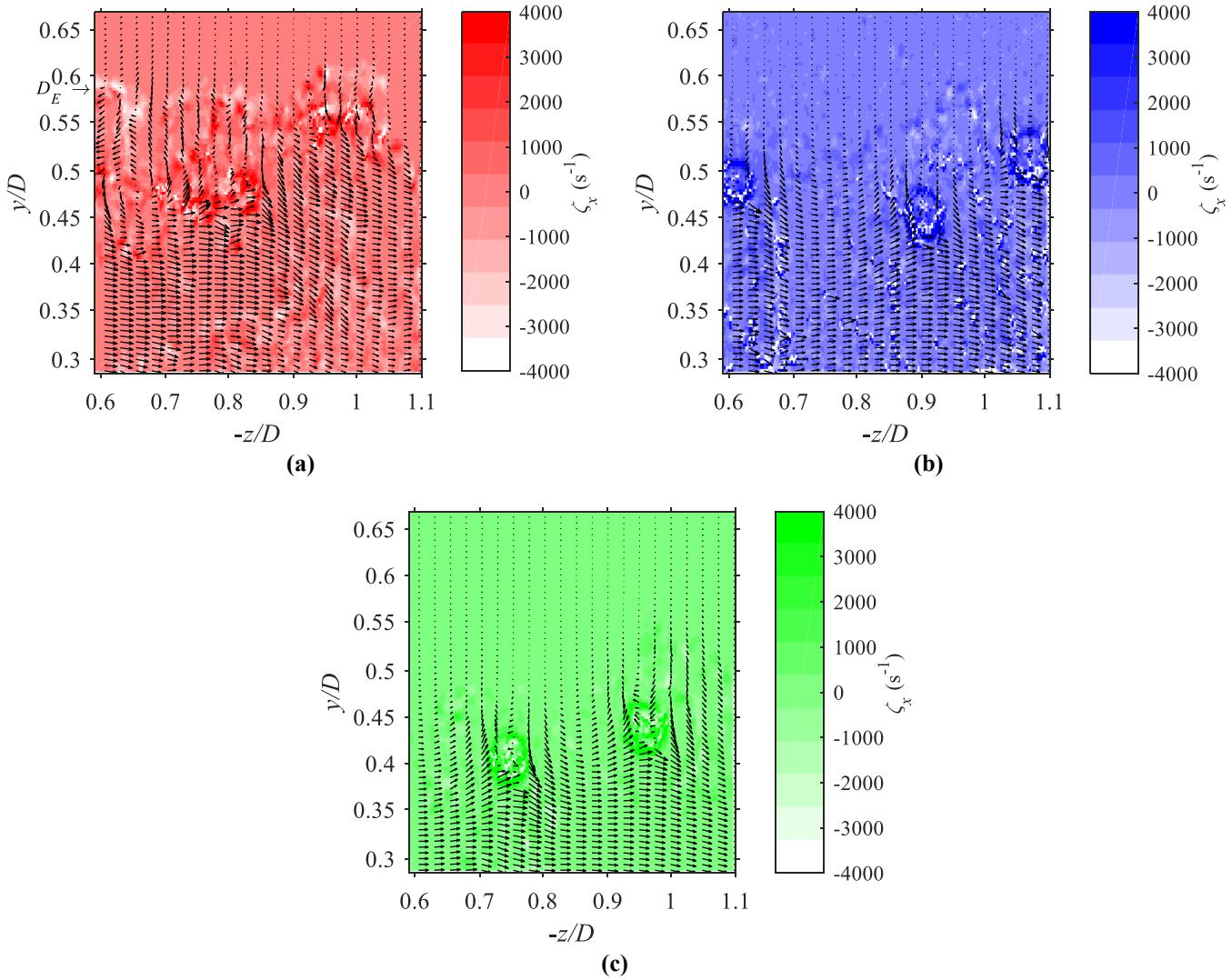

Figure 4-32: A contour of the *x*-component of vorticity, ζ_x, in the wake region of the (a) LE1-DA18-0.14, (b) untrimmed OP and (c) trimmed OP; operating at V_∞ = 5 m/s and 6000 RPM (J = 0.22 for the LE1-DA18-0.14 and trimmed OP systems, and J = 0.18 for untrimmed OP system).

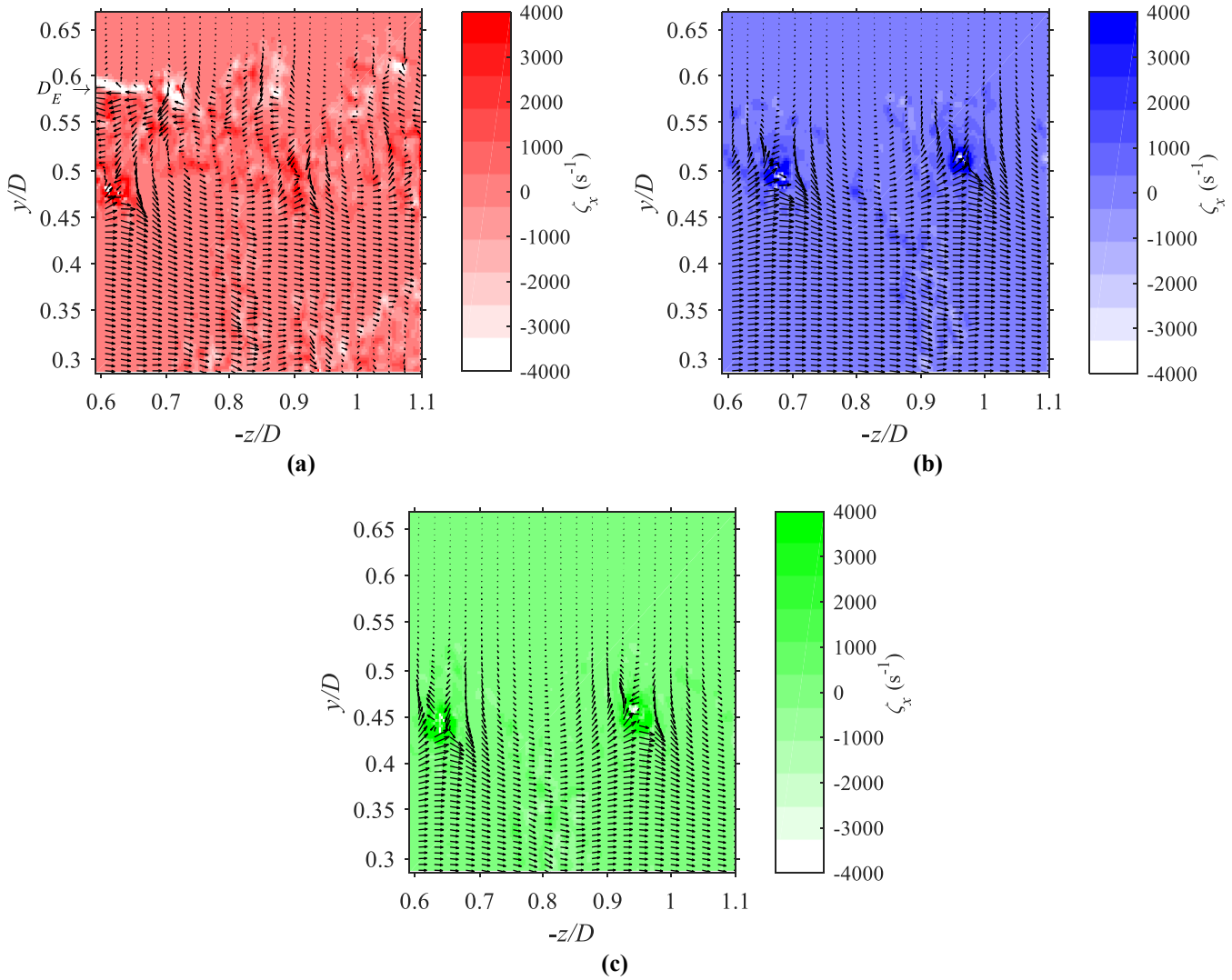

Figure 4-33: A contour of the *x*-component of vorticity, ζ_x, in the wake region of the (a) LE1-DA18-0.14, (b) untrimmed OP and (c) trimmed OP; operating at V_∞ = 10 m/s and 6000 RPM (J = 0.44 for the LE1-DA18-0.14 and trimmed OP systems, and J = 0.36 for untrimmed OP system).

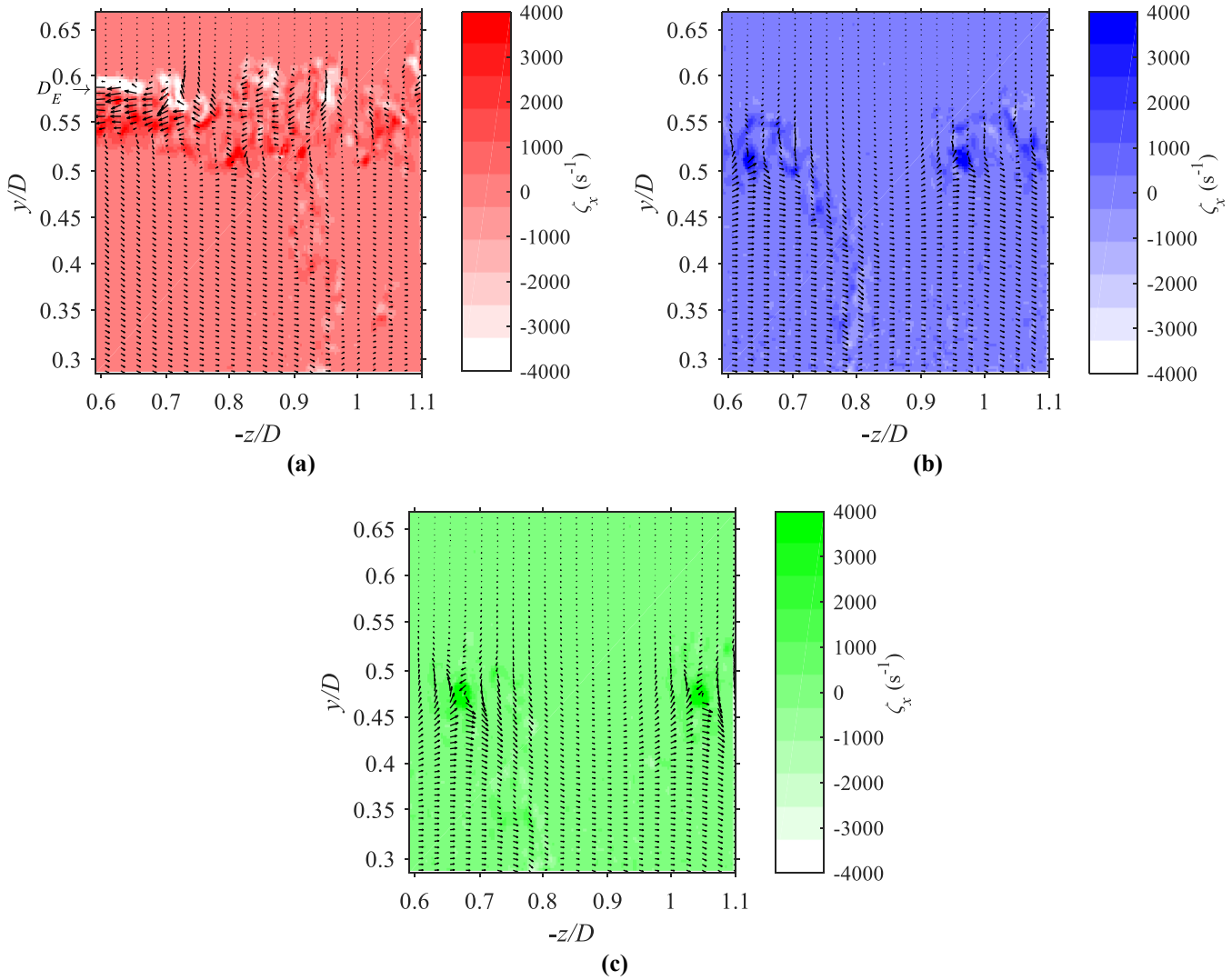

Figure 4-34: A contour of the *x*-component of vorticity, ζ_x, in the wake region of the (a) LE1-DA18-0.14, (b) untrimmed OP and (c) trimmed OP; operating at V_∞ = 15 m/s and 6000 RPM (J = 0.65 for the LE1-DA18-0.14 and trimmed OP systems, and J = 0.54 for untrimmed OP system).

The exit jet flow in the wake region of the LE1-DA18-0.14, trimmed OP and untrimmed OP systems, defined by $0.27 < y/D < 0.67$ and $0.58 < -z/D < 1.11$, was studied using velocity vector fields, contour plots of the axial velocity and contour plots of the *x*-component of vorticity. The results were obtained through the experiment defined in section 3.6.3. The velocity vector plots shown in Figure 4-26 to Figure 4-29 revealed that relative to the trimmed OP and untrimmed OP systems, the LE1-DA18-0.14 ducted propeller reduced the magnitude of the exit jet velocity. Plots of the shear layer were generated and the results demonstrated that for the axial flow tests at

V_∞ = 5 m/s, 10 m/s and 15 m/s, the trace of the shear layer for the trimmed OP and untrimmed OP systems displayed marginal expansion in the radial direction, with increasing z (downstream) location. For the LE1-DA18-0.14 ducted propeller, the shear layer displayed a contracting behaviour with increasing V_∞ in the stream-wise (z) direction. Using the location of the shear layer immediately downstream of the duct's trailing edge the effective exit area-to-rotor area ratios were computed for each system, and it was found that the duct achieved the highest value of σ_e = 1.04. Unexpectedly, the calculated value of σ_e increased with increasing free-stream velocity.

The presence of trailing vortices was investigated through contour plots of the x-component of instantaneous vorticity, ζ_x, shown in Figure 4-31 to Figure 4-34 in the same wake region previously defined. The results showed the trail of the tip vortex translation manifested as regions of high vorticity, and revealed that with increasing V_∞, the strength of the trailing vortices increased and the diameter of their cores decreased. The results also showed evidence of vortex shedding near the root of the blade (closer to the center of the rotor disk). The results for the LE1-DA18-0.15 ducted propeller showed vorticity traces emanated from the duct's trailing edge. It was observed that as the free-stream velocity was increased, the trail of the high vorticity region was shifted outwards in the radial direction.

4.6 Conclusions from the Investigation

The performance of a ducted propeller with an internal diameter of 240 mm was investigated through aerodynamic load measurements and flow visualization using particle image velocimetry (PIV). Two design parameters of the duct were tested, namely the duct diffuser angle, varied from 9° to 18° and the thickness-to-chord ratio, varied from 0.06 to 0.14, for a total of three ducted propeller configurations. The ducts were equipped with a propeller that was trimmed down to a diameter of 230.7 mm to fit inside the duct. The performance of the ducted propellers was compared to the performance of an open propeller of the same diameter (230.7 mm) and an untrimmed propeller (279.4 mm). Load cell measurements were obtained for free-stream advance ratios ranging from 0 to 0.65 (free-stream velocities ranging from 0 m/s to 15 m/s, and propeller rotational speeds ranging from 6000 RPM to 9000 RPM).

The load measurements in static condition confirmed that the three ducted propellers provided thrust increments over the open propellers, with a maximum increment of 22.3%, achieved by the duct with a diffuser angle of 18° and a thickness-to-chord ratio of 0.14. The wind tunnel tests

showed no significant differences in performance between the ducted propellers with different diffuser angles, but the duct with a thickness-to-chord ratio of 0.14 generated greater thrust results than the 0.06 model. The free-stream tests revealed that at an advance ratio of approximately 0.25~0.35 the ducted propellers ceased to provide thrust improvements over the trimmed and untrimmed open propellers. The propulsive of the systems were improved by the use of the ducts, but it was observed that beyond the advance ratio previously mentioned the percentage increment in efficiency ceased to increase. The reasons for this drop in performance were attributed to skin friction drag effects from the duct itself. The highest propulsive efficiencies achieved by the ducted propeller models, the trimmed open propeller and the untrimmed open propeller were 66.88%, 63.4% and 58.96%, respectively. The results evidenced that the performance benefits of the ducted propeller systems decay sharply as the advance ratio increases.

Flow visualization of the inlet and wake regions was performed through stereoscopic and planar PIV, respectively. The PIV experiments were carried out with a duct that had a thickness-to-chord ratio of 0.14 and a diffuser angle of 18°. Resultant velocity fields demonstrated that the ducted propeller producer greater acceleration of the free-stream flow towards the rotor disk with respect to the untrimmed open propeller. Profiles of the axial velocity along the radial direction, at the rotor disk plane location, were extracted from the inlet PIV results. Using these velocity profiles, the mass flow rate through the region defined by the radial range $0.05 < y/D < 0.4$ was calculated. At the static conditions, the mass flow rate through the rotor disk of the ducted propeller is higher by 13%, but as the advance ratio is increased, it falls below that of the untrimmed open propeller by an average of 1.83%.

The exit jet visualization results revealed that the ducted propeller successfully decreased the axial velocity in the wake region when compared to the wake of the open propellers. Plotting the shear layer demonstrated that at the location immediately downstream of the duct, the ducted propeller achieved a lower slipstream contraction that the trimmed open propeller. The maximum exit area-to-rotor disk area ratio achieved by the ducted propeller was 1.04, which demonstrated that the duct did not achieve the ideal expansion ratio set by the duct geometry.

Chapter 5. Propeller Performance at Non-Zero Angles-of-Attack

The increased capability of UAVs to engage in a variety of flight operations during a single flight mission forces the operation of rotor disks at angles-of-attack, α_P, with respect to the free-stream, or travelling velocity vector, that ranges from 0° to 90°. In contrast, the rotor disks of a helicopter during forward flight usually remains at angles-of-attack ranging from 90° to 80°. On the opposite end of the spectrum, propeller powered airplanes operate at rotor disk angles-of-attack that vary between 0° to 15°. Consequently, the majority of the research work done on propellers have been on large scale propellers operating in small α_P values, and of rotor disk sizes that correspond to full scale aircrafts. For example, McLemore and Cannon [42] investigated the performance of a 5.33 ft diameter rotor in an α_P range of $0° < \alpha_P < 180°$. In the investigation McLemore and Cannon [42] showed that C_T and C_P increased with increasing J_a. The emergence of VTOL created a special interest on the study of propellers at non-zero α_P. Yaggy and Rogallo [43] investigated the performance of three propellers ranging in diameters from 9.5 ft to 12 ft, and noted that increasing α_P increased the rate of change of the performance coefficients (C_T, C_P, C_{Mx}, C_{My}) with respect to the J_a. Other experimenters have implicitly tested the performance of rotors at non-zero α_P by performing tests on an assembly, such as the experiments by Kuhn and Draper [41], where multiple propellers models of 2 ft diameter rotor disks where tested in a wing-propeller combination. Kuhn and Draper [41] were also investigating the performance of such systems for VTOL aircrafts, and tested the assemblies at the range of $0° < \alpha_P < 90°$. Similar to the findings of McLemore and Cannon [42], Kuhn and Draper demonstrated that C_T increased with increasing J_a.

Due to the majority of scenarios where rotors are operated at non-zero α_P involve a small range of angles (helicopter flight being the most popular case, $90° < \alpha_P < 80°$), the attempts to develop performance prediction models have focalised on these ranges as well. In the determination of aerodynamic forces on a propeller blade, one of the biggest challenges is the determination of an appropriate induced velocity, v_i, onto the rotor disk plane. For a rotor in hover or axial flow ($\alpha_P = 0°$) v_i is uniformly distributed along the azimuthal direction Ψ, meaning all blade elements located at the same radial distance from the hub will be subject to the same value of v_i. On the other hand, for rotors operating at non-zero angle-of-attack the value of v_i varies with both the azimuthal and radial locations. Therefore models based on the blade element theory have been

developed to account for this distribution of v_i over the rotor disk area during forward flight. One of the first inflow models was developed by Glauert [10], where a linear distribution of the predicted value of v_i through momentum theory is suggested along the longitudinal direction (perpendicular to the direction of travelling velocity) of the rotor disk. Other models such as the ones developed by Drees [12], Pitt and Peters [13] and Coleman *et. al.* [11] make use of the wake skew angle, χ, to determine the distribution of v_i over the rotor disk area. These models are considered as fist-harmonic approximations of the induced velocity, and as of today are still used across the industry. However, they have been developed exclusively for large scale propellers, and their accuracy has not been tested in ranges outside of the common operational angle-of-attack ranges of helicopter rotors.

The work done on small scale propellers is increasing due to its expanding market, nonetheless, the performance of small scale rotors at non-zero angle-of-attack has not been extensively covered in the literature. A significant data base regarding the performance of small scale rotors in axial flow was conducted by Brandt and Selig [40], where 79 propellers ranging in diameter from 9 to 11 inches were tested, and their C_T, C_P and η was determined for various free-stream velocities and rotational speeds. Carrol [45] studied the performance of a 18 in rotor at an angle-of-attack range of $-30° \leq \alpha_P \leq 90°$, and obtained similar results to those investigations performed on large scale rotors. Carrol [45] determined that for increasing α_P and J, the thrust generation of the propeller increased. In addition to the performance measurements, Carrol [45] also developed an analytical performance prediction model based on the blade element momentum theory, where a wake-interaction model based on vortex theory was implemented to determine the inflow distribution over the rotor disk.

In lieu of the scarcity of information of small scale rotors operating at non-zero angle-of-attack, even the development of a database such as the one consolidated by Brandt and Selig [40] would be helpful to UAV users and designers. A deeper understanding of the behaviour of small scale rotors when operating at non-zero angles-of-attack is of aid to the development of the instrumentation systems dedicated towards the stability and control of UAVs.

The following section entails the results of the investigation on the aerodynamic performance of four 12 inch diameter propellers tested at non-zero angle-of-attack. The performance of the propellers has been characterized through measurements of thrust, power consumption, pitch and

yaw moments, as well as propulsive efficiency. For this purpose, force and torque measurements have been obtained for the four different propellers using a six-axis load cell in a wind tunnel. Additionally, the applicability of already existing inflow models is tested at the angle-of-attack range of $0° \leq \alpha_P \leq 90°$, and a method to solve for a more appropriate model is suggested, using the Genetic Algorithm optimization tool from MATLAB.

5.1 Thrust Generation

The coefficient of thrust is presented for the two SF propellers models with 4.7 in/rev and 6 in/rev pitch, and the SP model with 5 in/rev and 6 in/rev pitch in Figure 5-1 (a), (b), (c), and (d) as a function of J and J_a, respectively. The angle-of-attack of the propeller disk is varied within $0° \leq \alpha_P \leq 90°$. The C_T-J data shows a common trend that increase of α_P results in a higher coefficients of thrust, for any particular value of J. The results of the SF propellers show that for the tests conducted at $\alpha_P < 60°$, the value of C_T reduces with increase in J. At $\alpha_P > 60°$, C_T increases with increasing J for the SF12×4.7 and SF12×6 propellers. The small increase of C_T with J at $\alpha_P = 90°$ was also observed by Carrol [45] in his experiments. The behavior of the SP model propellers demonstrates similarities in the C_T-J data with the results obtained for the SF models. Both SP12×5 and SP12×6 propellers exhibit reduction of C_T with increase of J for $\alpha_P < 50°$. It is also observed that for small free-stream advance ratio of $J < 0.2$, the C_T-J curves for different α_P approximately overlap, suggesting that the influence of α_P on the thrust generation of the SP propellers is not significant in this regime. The results of all four propellers shown suggest that for advance ratio values smaller than $J = 0.4$, thrust generation is approximately independent of α_P.

One difference that appears when comparing the results between the SF models and the SP models is the behavior of the propellers at the $J > 0.4$ and $\alpha_P > 70°$ regime. On this domain, it can be seen that for the SF models, the value of C_T exhibits a near exponential increment for increasing values of J; whereas for the SP models, the value of C_T increases at a lower rate, and reaches an approximately plateau state. The behavior of C_T with respect to changes in α_P exhibited in Figure 5-1 (a) to (d) agrees with the findings from Kuhn and Draper [41] and McLemore and Cannon [42], in which the value of C_T increases with increasing α_P; however, Kuhn and Draper [41] demonstrated this to be true for a constant disk loading, rather than for a constant J. The results obtained by Carrol [45] demonstrated a more prominent increase in rate of change of C_T (at a constant J) when α_P was increased, in comparison to the trends exhibited in Figure 5-1 (a) to (d).

The use of the inflow advance ratio J_a results in the overlap of C_T data for different values of α_P into one common trend for each propeller. For a constant Ω, higher values of α_P translate to lower values of J_a; therefore, in Figure 5-1 (a) to (d) the C_T data points contract into a smaller range of J_a with increase of α_P. This is true for all values of α_P except for two cases: the first when $\alpha_P = 0°$ for which the C_T-J_a curves are identical to the C_T-J plots, since for $\alpha_P = 0°$ $J = J_a$; and second, for the case $\alpha_P = 90°$ which represents complete edgewise flow, and hence no portion of the free stream flows in the direction of the thrust vector, resulting in a constant value of $J_a = 0$ for all tests performed at this α_P. In addition to the experimental data, the plots in Figure 5-1 include a second-order fit of C_T-J_a data and the corresponding equation. This second-order fits can be used to estimate the thrust of the four propellers at a variety of α_P and free-stream condition.

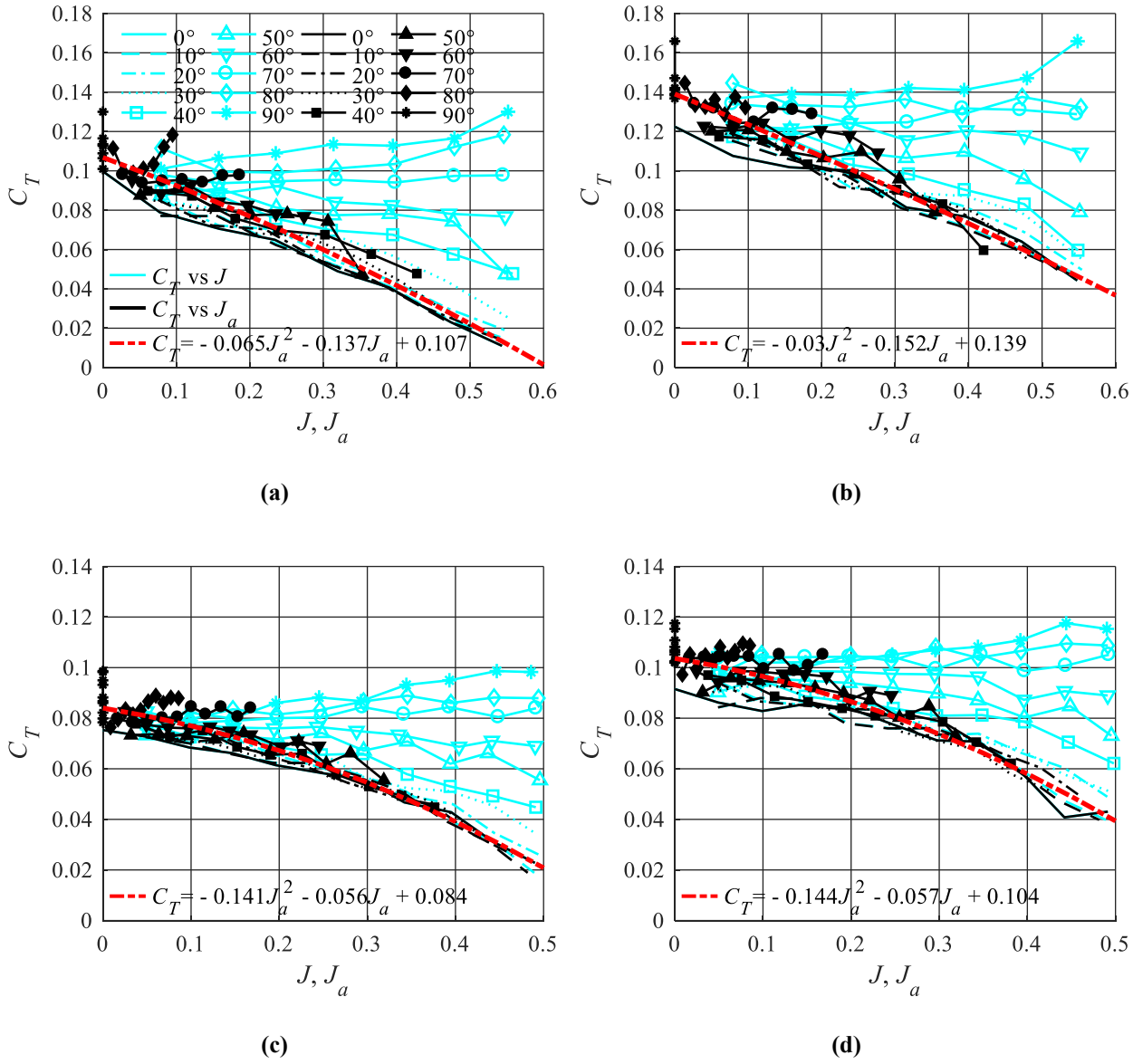

Figure 5-1: C_T as a function of J and J_a for multiple values of α_P, for (a) SF12×4.7, (b) SF12×6, (c) SP12×5, and (d) SP12×6 propellers.

The C_T-J_a curves in Figure 5-1 (a) to (d) demonstrate no increment in C_T with respect to changes in α_P, which is analogous of the $\alpha_P = 0°$ curve with a constant decrease of C_T with increasing J_a. The only exception to this trend is observed in the C_T-J_a results of the SF12×4.7 propeller, at $\alpha_P \geq 70°$. For both the SF and SP models an increase in the propeller pitch results in larger C_T. The absolute thrust variation by increasing the propeller pitch from 4.7 to 5 in/rad and from 5 to 6 in/rad for the SF and the SP propellers versus J_a is estimated using the second-order fits of Figure

5-1 and plotted in Figure 5-2. For both propeller models, the thrust gain increases exponentially with increasing J_a.

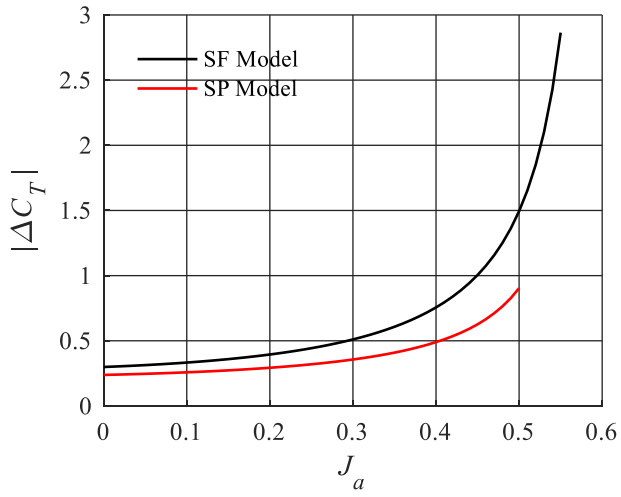

Figure 5-2: Variation in C_T as a result of increase in the nominal pitch of the propeller versus the inflow advance ratio J_a, for the SF and SP models. The ΔC_T of the SF and the SP are calculated as $C_{T,\ SF12\times4.7} - C_{T,\ SF12\times6}$ and $C_{T,\ SP12\times5} - C_{T,\ SP12\times6}$, respectively.

5.2 Power Consumption

The plots in Figure 5-3 (a) to (d) show the variation of C_P as a function of J and J_a for $0° \leq \alpha_P \leq 90°$ for the four investigated propellers. For $J < 0.3$, there are marginal differences in the power consumption of the two SF propellers for various values of α_P, as C_P appears to be independent of α_P in Figure 5-3 (a) and (b). However, for $J > 0.3$, the tests at different α_P start to depart from each other, and an evident difference is visible. In the range of $J > 0.3$, for both SF propellers, C_P demonstrates a decreasing trend for $\alpha_P < 50°$, and for $\alpha_P > 50°$ an increasing trend with increase of J. This response was also observed by Carroll [45], where a decreasing trend was seen for $\alpha_P < 50°$ and $J < 0.4$. The plot in Figure 5-3(b) shows that for the SF12×6 propeller tests at $\alpha_P = 90°$, the rate of increase of the power consumption increases with increase of J. The variation of C_P for the SP12×5 and SP12×6 propellers in Figure 5-3 (c) and (d) between the tests conducted at different α_P is marginal. For both SP models, the C_P-J lines for multiple α_P overlap for the range of $J < 0.4$. The most evident difference between the results for the SF and SP propeller models is the

sensitivity to changes in α_P. A wider separation between the C_P-J curves for different α_P is seen in the case of the SF model propellers. For the SP propellers, the curves are closer together, and demonstrate that α_P has a smaller influence on C_P. Similar to the results for thrust, the plots of C_P-J_a for different α_P overlap. Figure 5-3 also includes a second order polynomial fit over the C_P-J_a data for power prediction of these propellers. The decrease of C_P with respect to J observed for the C_P-J curves at $\alpha_P = 0°$ is in agreement with the findings by Brandt and Selig [40] for a 11 in diameter propeller (APC, Thin Electric) tested at the same J range.

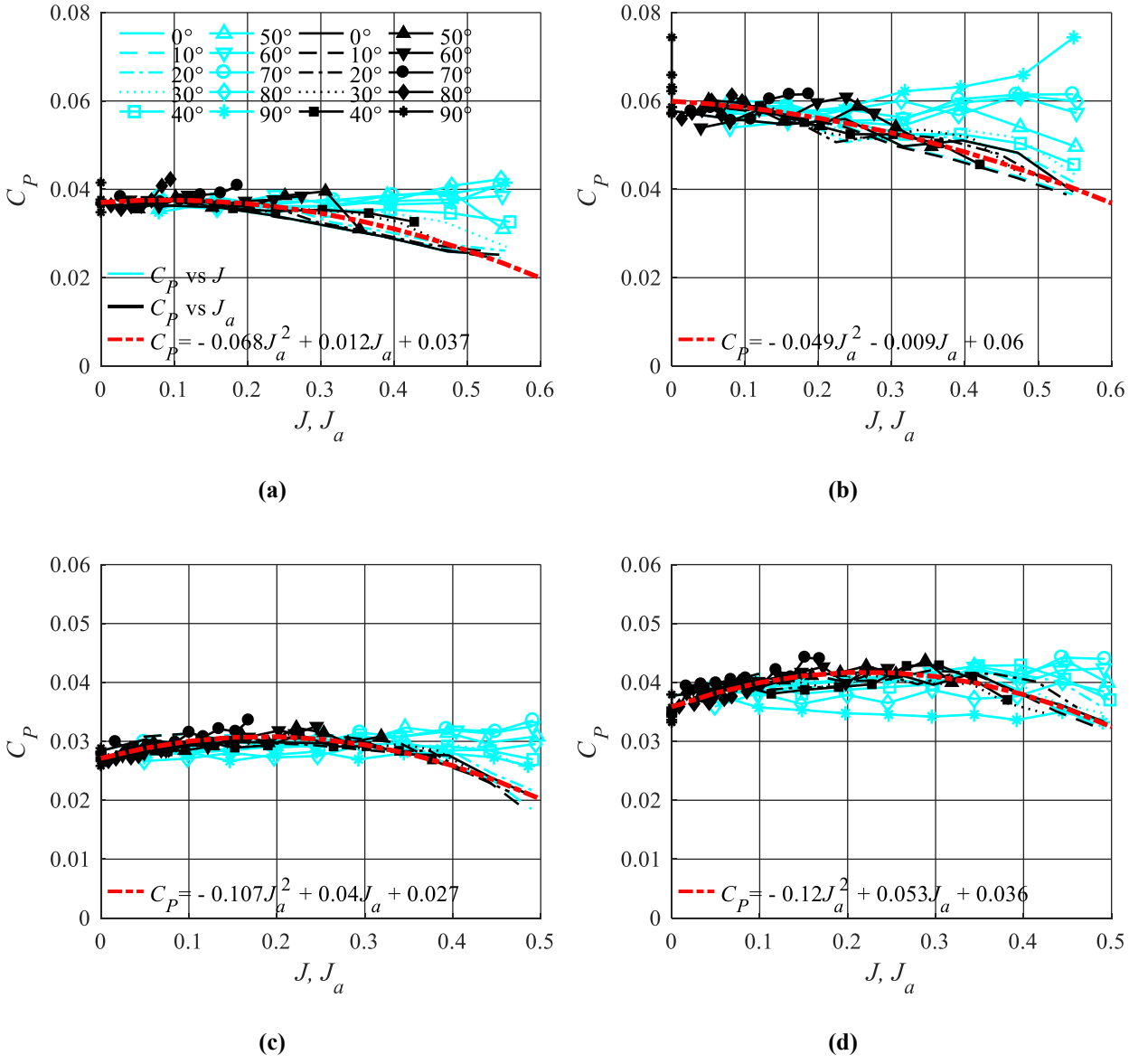

Figure 5-3: C_P as a function of J and J_a for multiple values of α_P, for (a) SF12×4.7, (b) SF12×6, (c) SP12×5, and (d) SP12×6 propellers.

The C_P-J_a curves in Figure 5-3 (a) to (d) demonstrate a parabolic variation of C_P with respect to J_a for all the propellers tested. The parabolic response of the C_P-J_a curves was also observed by McLemore and Cannon [42]. The maximum C_P values obtained were 0.042, 0.074, 0.034 and 0.044 at J_a = 0.095, 0, 0.17 and 0.15 for the SF12×4.7, SF12×6, SP12×5 and SP12×6 propellers, respectively. It is also evident that an increase in C_P is obtained by increasing the nominal pitch of the propellers. The percentage increment in C_P obtained form an increase in nominal pitch from 4.7 to 6 inches/rev for the SF propellers, and from 5 to 6 inches/rev for the SP propellers is shown in Figure 5-4. It can be seen that the increment is parabolic with respect to J_a with the minimum value at J_a=0.25 and J_a = 0 for the SF and SP models, respectively.

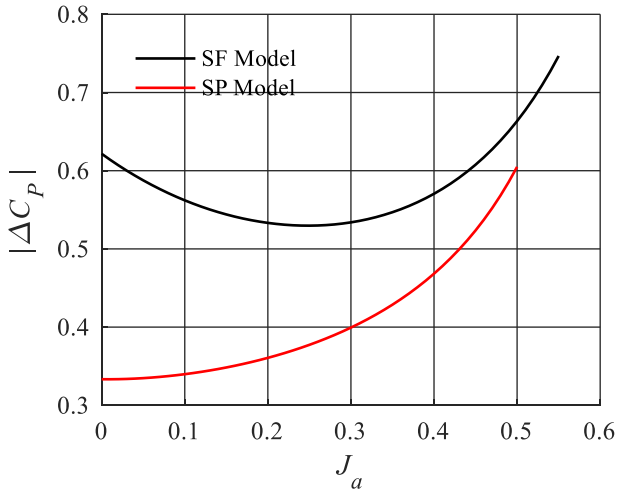

Figure 5-4: Variation in C_P as a result of increase in the nominal pitch of the propeller versus the inflow advance ratio J_a, for the SF and SP models. The ΔC_P of the SF and the SP are calculated as $C_{P,\ SF12\times4.7}$ - $C_{P,\ SF12\times6}$ and $C_{P,\ SP12\times5}$ - $C_{P,\ SP12\times6}$, respectively.

5.3 Pitch and Yaw Moments

The plots presented in Figure 5-5 (a) to (d) show variation of the pitch moment C_{My} as a function of J for the four propellers tested within $0 \leq \alpha_P \leq 90°$. The results for both the SF and SP propellers in Figure 5-5 (a) and (b) demonstrate that the value of C_{My} increases with increase of J and α_P. Yaggy and Rogallo [43] also obtained the same relationship between C_{My} and α_P in their experiments. It is observed in Figure 5-5(a) for the SF12×4.7 propeller that there is a negligible

variations of C_{My} with respect to J at $\alpha_P < 30°$, while for $\alpha_P > 30°$ the rate of change of C_{My} with respect to J is larger. A similar variation is also observed for the other propeller as the variation of C_{My} with J increases at larger α_P. The comparison of Figure 5-5 (a) and (b) shows that for the C_{My}-J curves of the SF12×4.7 propeller are closer together than the curves for the SF12×6 propeller. This suggests that a propeller with larger pitch (and larger C_T) is more susceptible to variations in C_{My} due to changes in α_P. The results for the SP propeller models in Figure 5-5 (c) and (d) show that the moment significantly increases when α_P increases from 40° to 50°. This suggests two regimes for C_{My} response: a region where C_{My} is invariant with respect to J, which occurs at the approximate range of $\alpha_P < 40°$; and a region of increasing C_{My} with respect to J, which occurs at the approximate range of $\alpha_P > 50°$.

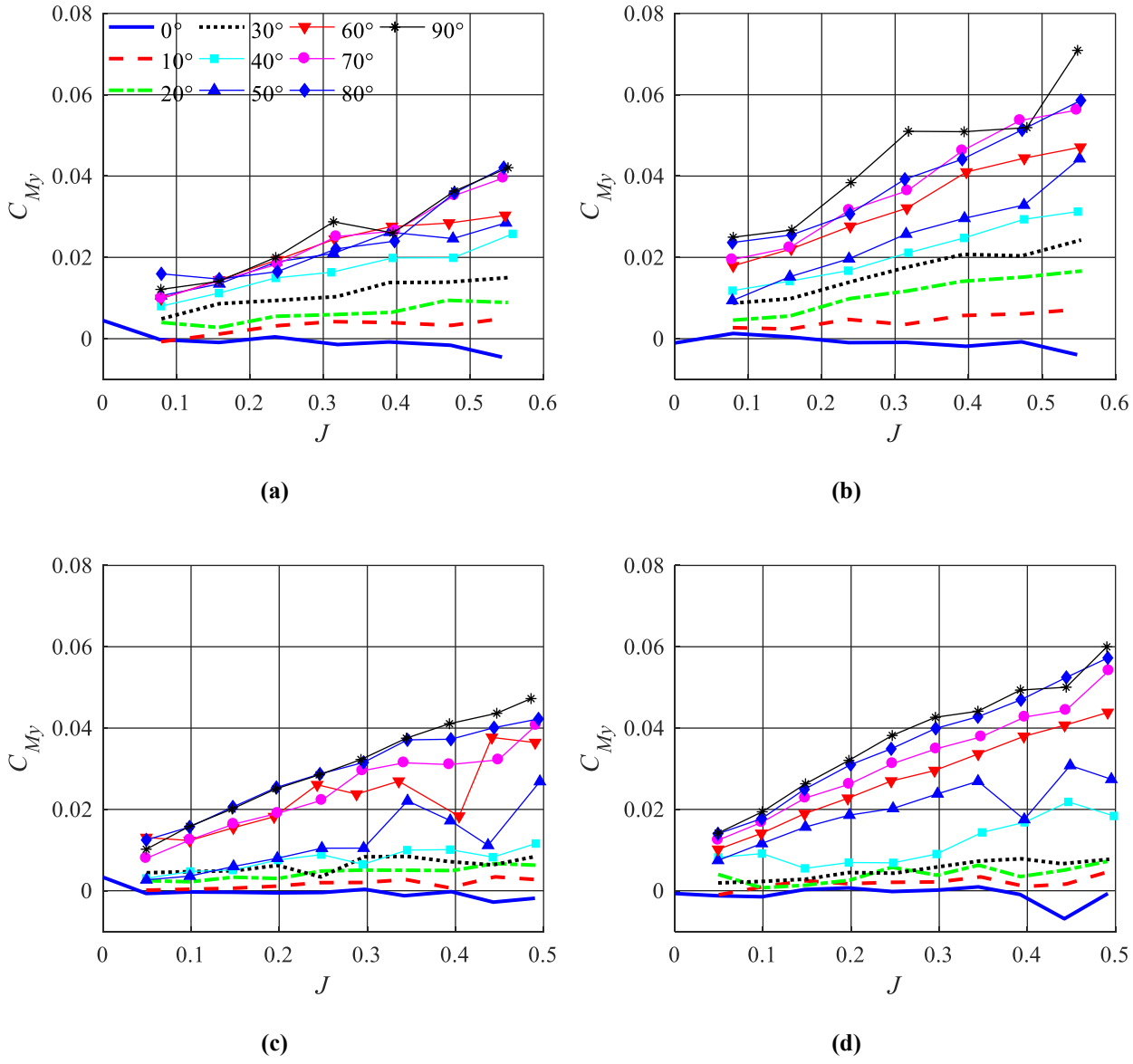

Figure 5-5: The variation of C_{My} as a function of J for multiple values of α_P for (a) SF12X4.7, (b) SF12X6, (c) SP12X5, and (d) SP12X6 propellers.

The coefficient of yaw moment about the x-axis, C_{Mx} is shown in Figure 5-6 (a) to (d) as a function of J, for the SF12×4.7, SF12×6, SP12×5 and SP12×6 propellers, respectively. It must be noted that in the results presented in Figure 5-6 (a) to (d), the value of C_{Mx} includes the moment generated by the drag force of the motor and motor casing acting at a distance from the load cell. The operation of the propeller results in a negative x moment which increases with increase of J and α_P. A larger increase of C_{My} for the SP12×6 propeller is observed at $\alpha_P = 40°$ to $50°$ in Figure

5-6(d). The results from Figure 5-5 and Figure 5-6 suggests that increasing the angle-of-attack of the rotor disk while maintaining a constant J (or vice versa) increases the differential thrust produced at the quadrant of the rotor disk corresponding to $90° < \psi < 180°$.

5.4 Propulsive Efficiency

The propulsive efficiency of propellers is evaluated using equation 3-8 and equation 3-11 and is shown in Figure 5-7 (a) to (d) as η versus J and J_a for $0 \leq \alpha_P \leq 90°$. Figure 5-7 (a) and (b) show the results for the SF12×4.7 and SF12×6 propellers, respectively. In Figure 5-7(a), the η-J curves at $\alpha_P < 40°$ reach a maximum value, which increases with increasing α_P. The tests conducted at $\alpha_P > 40°$ show a steady increase of η with J. A comparison between the results for the SF12×4.7 and SF12×6 propellers shows that for $\alpha_P > 60°$, the SF12×6 has smaller η with respect to the SF12×4.7 model. The graphs show that for tests conducted at $\alpha_P > 50°$, η increases approximately linearly with respect to J. Figure 5-7 (a) to (b) also demonstrate that the value of η increase with increasing α_P for all J values.

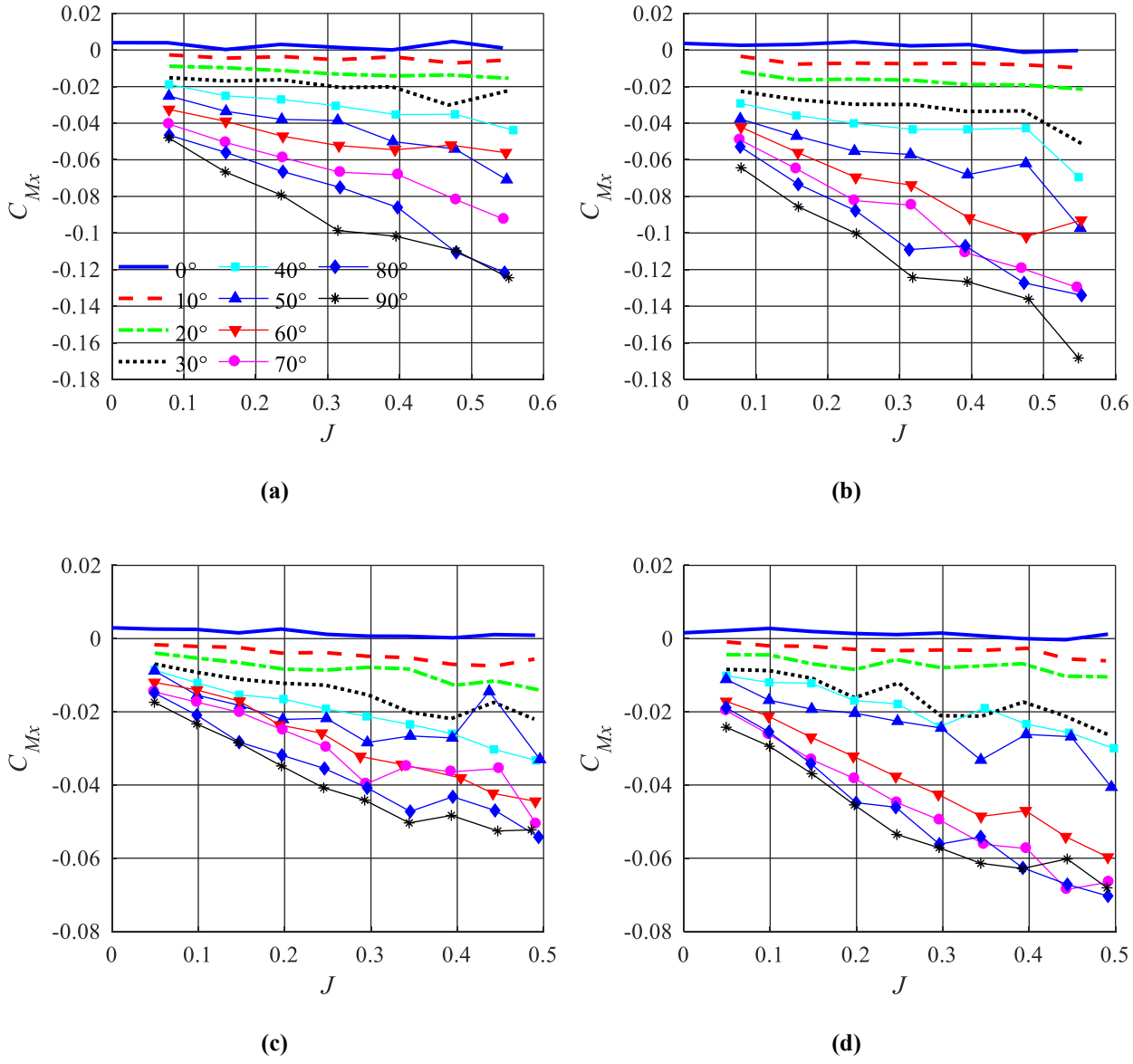

Figure 5-6: The variation of C_{Mx} as a function of J, for multiple values of α_P, for propellers (a) SF12X4.7 (b) SF12X6 (c) SP12X5 (d) SP12X6

The results for the SP propellers show that the value of η increases with increasing α_P, for any particular value of J. For the results of the SP model propellers, only the tests for the SP12×5 propeller at $\alpha_P < 20°$ provide evidence of a maximum value of η. The difference in η between the SP12×5 and SP12×6 propellers, at all values of α_P investigated is not significant.

At high J and high α_P, all four propellers exhibit an η value greater than 100%, which shows that presenting η as a function of J is misleading. For a propeller in a multi-rotor vehicle, in which the

rotor disk plane is tilted with respect to the free-stream, the definition of propulsive efficiency not be measured only with regards to the forward advancing speed of the vehicle; rather, it should be measured using the velocity component that is collinear with the direction of the thrust vector. Therefore, η'-J_a curves have been presented as well in this paper.

The η'-J_a curves in Figure 5-7 (a) to (d) for all four propellers demonstrate significant overlap between for all α_P values. For both the SF and SP model propellers, the higher pitch propeller (SF12×6 and SP12×6) achieves its maximum value of η' at a higher value of J_a than the low pitch model. Second-order polynomial fits are developed over the η'-J_a efficiency curves for each propeller and shown in Figure 5-7 (a) to (d). The percent difference in η' due to a change in the nominal pitch of the propellers was calculated using the polynomial fits, and the results are shown in Figure 5-8. It can be observed from Figure 5-8 that an increase in the nominal pitch of the propeller does not always translate into an increase in efficiency; rather, it shows that this depends on J_a. It is also noted from Figure 5-8 that the J_a value at which the higher pitch propeller begins to provide and increment in η' occurs at approximately J_a=0.3, for both propeller models.

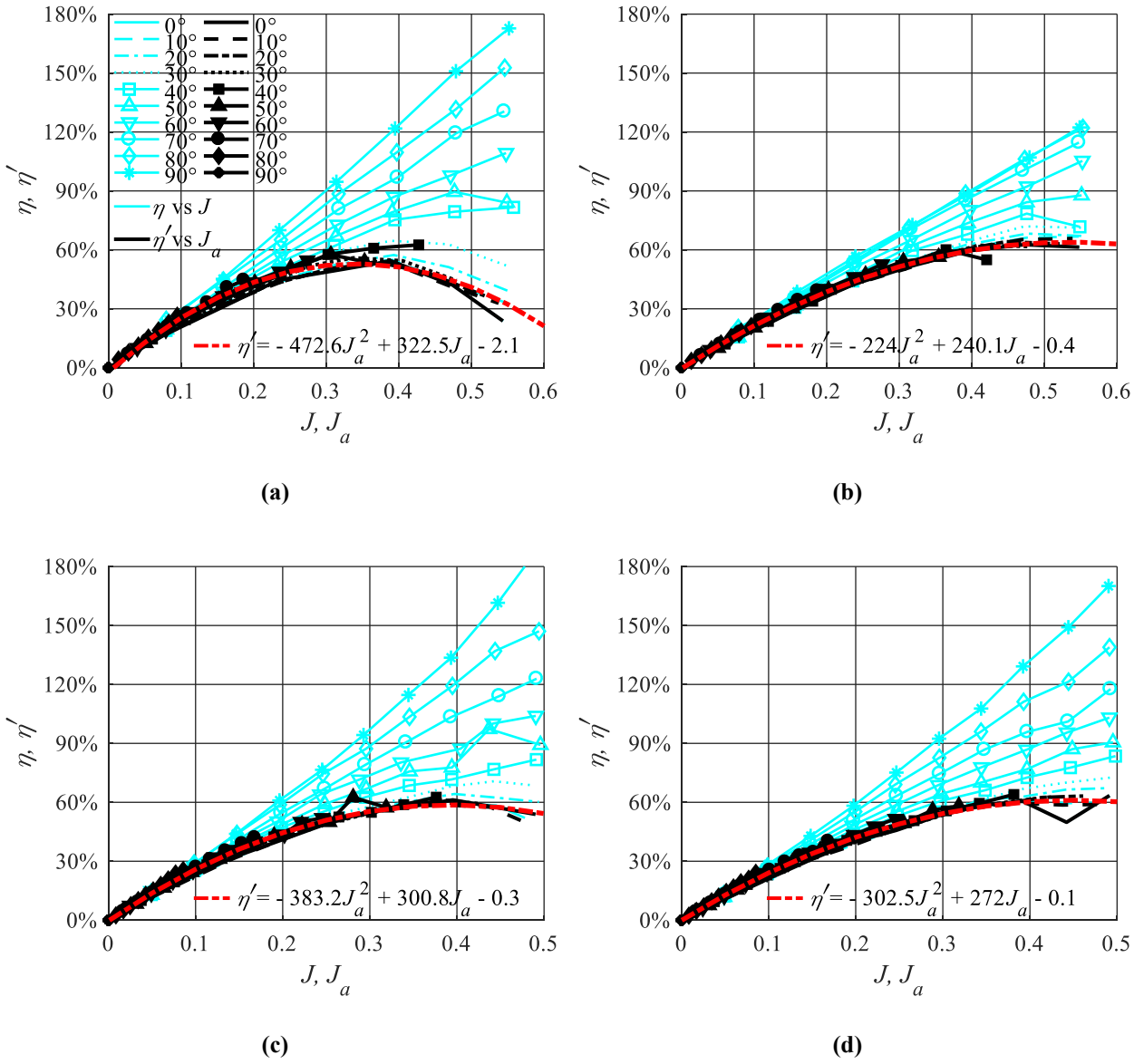

Figure 5-7: Modified propulsive efficiency as a function of the modified advance ratio, for multiple values of α_P, for propellers (a) SF12X4.7 (b) SF12X6 (c) SP12X5 (d) SP12X6

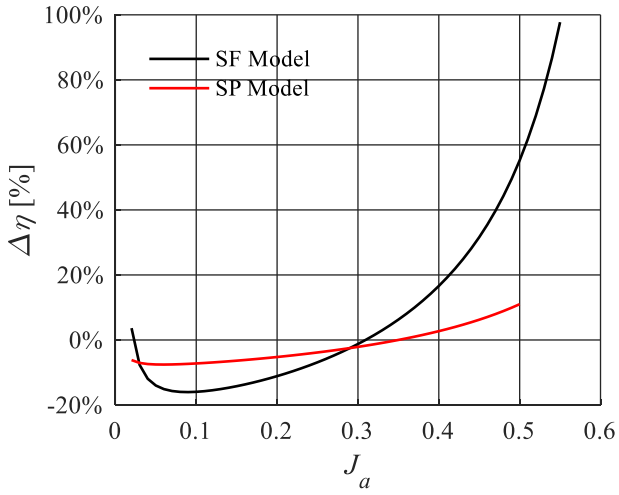

Figure 5-8: Variation in η' as a result of increase in the nominal pitch of the propeller versus the inflow advance ratio J_a, for the SF and SP models. The $\Delta\eta'$ of the SF and the SP are calculated as $\eta'_{SF12\times4.7} - \eta'_{SF12\times6}$ and $\eta'_{SP12\times5} - \eta'_{SP12\times6}$, respectively.

5.5 Analytical Performance Prediction

5.5.1 Sectional Lift and Drag Coefficients

The sectional lift and drag coefficients used in equations 2-48 and 2-49, for the NACA 4412 and Eppler 63 airfoils, were obtained from the open source web-site Airfoil Tools [64]. The *Re* distribution over the rotor disk is shown in Figure 5-9 for $\alpha_P = 90°$, approximated using the geometrical information from Figure 3-8(b), the rotational speed of the experiments, and the maximum free-stream velocity for the SF and SP models as

$$Re = \frac{\rho V_R c}{\mu} \qquad \textbf{5-1}$$

where μ is the dynamic viscosity of air. The $\alpha_P = 90°$ condition is displayed because it is the condition where the propeller's cross-section experiences a maximum *Re* of 160,000 and 180,000 for the SF and SP propellers, respectively. Airfoil Tools [64] provides C_l-C_d data for *Re* =50,000, 100,000 and 200,000; therefore, for sections in the rotor disk where the local *Re* fell within these values, the corresponding C_l and C_d were interpolated using the three available data sets. The C_l and C_d data was fitted with a fourth order polynomial, in order to calculate the coefficients at the various values of α_b. The C_l-α_b and C_d-α_b data provided by Airfoil Tools [64] does not include C_l-

C_d data in the range -10° > α_b > 18°; therefore, for the rotor regions in which α_b exceeded the range of data points provided, a value of $C_l = 0$, was prescribed. In regards to C_d, the extrema values of C_d in the C_d-α_b curves were prescribed to these rotor areas. A study such as the one performed by Critzos [65] where the aerodynamic performance of a NACA 0012 airfoil was studied within $0° < \alpha_b < 180°$ is necessary on the airfoils used in the propeller blades to complete the C_l and C_d data range.

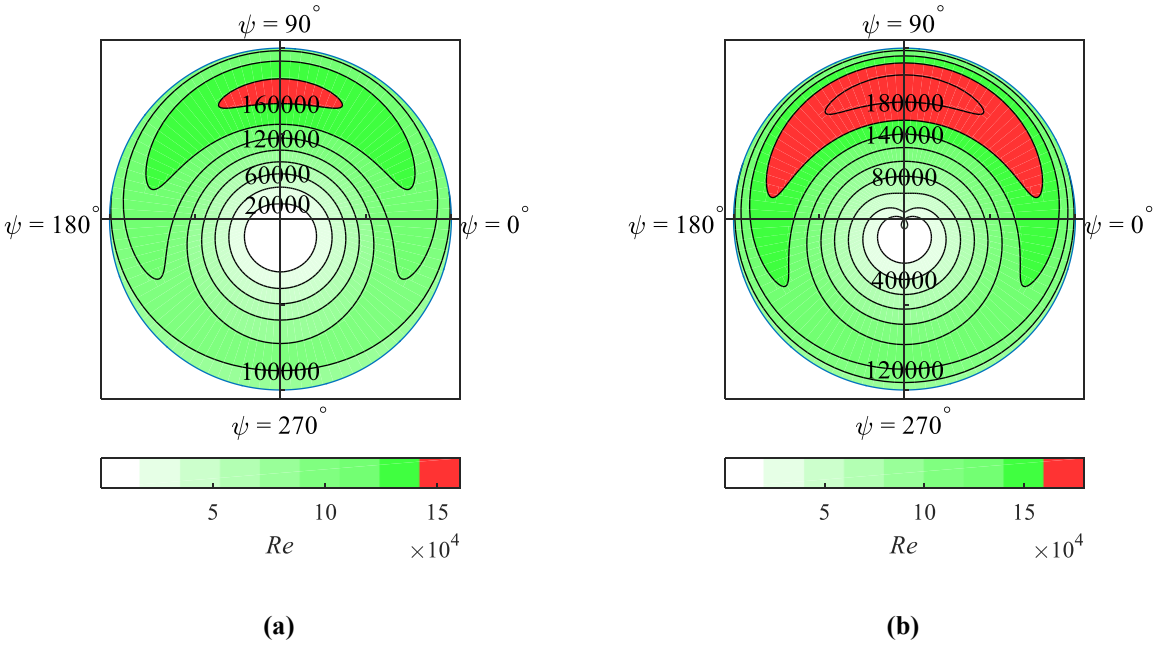

Figure 5-9: Distribution of *Re* over the rotor disk, for the (a) SF12X6 and (b) SP12X6 propellers at α_P = 90° and V_∞=14 m/s and 20 m/s, respectively.

The rotor disk was discretized using 100 radial elements, over 100 azimuthal locations (angularly separated by 2π/100 rad). The location of any blade element in the rotor disk may be described using the Cartesian coordinate system as defined in Figure 3-10(c), with coordinates x and y being the lateral and longitudinal directions, respectively, and where the origin is located at the propeller hub; or a polar coordinate system, where the radial coordinate r represents the distance from the hub, and the azimuthal angle ψ is the angular location in degrees. The area in the rotor disk occupied by the hub has been treated as a flat disk.

5.5.2 Analytical Model Results

The analytical models described in the previous sections were implemented to the SP12X6 propeller and are graphically compared with the experiments at V_∞= 8, 10, 12 and 14 m/s (J = 0.197, 0.246, 0.295, and 0.344) in Figure 5-10 (a) to (d), respectively.

Comparison of Existing Inflow Models and Formulation of Suggested Model

Despite the clear discrepancies between the prediction models and the experimental results, the models form Dress [12], Coleman *et. al.* [11] and Pitt and Peters [13] overlap over the investigated range of α_P, and demonstrate to have the capacity to predict the overall trend of thrust generation as a function of α_P correctly. The results shown in Figure 5-10 (a) to (b) exhibit discrepancies between the inflow models presented and the experimental data even at the range $75° \leq \alpha_P \leq 90°$, where they are most commonly applied for forward flight of a helicopter. Therefore, a variation to Pitt and Peter's model is suggested, where the definition of the weighing coefficient k_x is maintained the same, but is multiplied by a correction factor f_1 that is a linear function of α_P as

$$f_1 = a_1 \cdot \alpha_P + a_2 \qquad \textbf{5-2}$$

The coefficients a_1 and a_2 are estimated here based on the experimental data. A lateral variation of the induced velocity is also introduced by replacing k_y with new function f_2, which is defined as

$$f_2 = a_3 \cdot \alpha_P + a_4 \qquad \textbf{5-3}$$

where a_3 and a_4 are again coefficients to be determined from experimental data. Thus, the suggested model is

$$\lambda_i = \lambda_0 \left(1 + k_x \cdot f_1 \frac{(-x)}{R} + f_2 \frac{y}{R}\right) \qquad \textbf{5-4}$$

In equations 5-2 and 5-3 the value of α_P is computed in radians. Similar to the work of Drees [12], the value of f_2 was fixed to $f_2 = 0$ at $\alpha_P = 0°$ to preserve the symmetry of α_b over the rotor disk. Using the experimental data obtained in this investigation as a reference, the values of a_1, a_2, a_3 and a_4 were optimized using the inbuilt Genetic Algorithm (GA) solver in MATLAB, which obtains the optimal solution to constrained and unconstrained problems. The GA generates a random population of values of the variables (in this case the variables a_1, a_2, a_3 and a_4) that constitute the function that is being optimized. It repeatedly modifies the values in a population by

performing a series of operations on the 'parents' of a generation, to create 'children' values that will constitute the following generation. Through this mechanism the GA solves for the variable values that will provide the minimum from a target function. In the current investigation, the GA has been used to the values of the coefficients a_1 to a_4 that would yield the lowest least-mean square of the difference between the thrust predicted by the model described in equation 5-4 and the experimental data. Through the use of the GA, the random variables in equations 5-2 and 5-3 were determined for the example cases of V_∞ = 8, 10, 12 and 14 m/s (J = 0.197, 0.246, 0.295 and 0.344), and can be found in Table 5-1. Several runs of the GA were performed in order to refine the bounds of the free variables. All of the variables were obtained by reaching convergence prior to 100 generations. The results of the GA have been included in Figure 5-10 (a) to (b), where it can be observed that the suggested model provides an improved overlap with the reference experimental data, when compared to the previously existing models by Glauert [10], Drees [12], Coleman *et al.* [11], Pitt and Peters [13] as well as the BEMT model with uniform inflow.

Table 5-1: Weighting factors determined through the Genetic Algorithm for the suggested non-linear inflow model.

J	a_1	a_2	a_3	a_4
0.197	0.4018	0.72567	-3.9691	1.236
0.246	0.3364	0.052097	-4.0305	0.99547
0.295	0.4641	0.070415	-4.7882	1.4304
0.345	0.11733	0.14509	-4.9527	1.3511

All of the models, including the suggested formulation, coincide at the same value of T for the axial flow condition, since at this operating point, a condition of uniform distribution of the induced velocity over the rotor disk area is imposed to all models. This leads to an increasing underestimation of the value of T at α_P = 0° that can be observed in the results of Figure 5-10 (a) to (d), where a maximum discrepancy of 66% is obtained in the results of V_∞ = 14 m/s. The results show that the models suggested by Glauert [10], Drees [12], Coleman *et al.* [11], Pitt and Peters [13] as well as the BEMT model with uniform inflow provide an over-estimation of the thrust force generated at all values of α_P, with the exception of the axial flow (α_P=0°). In an investigation

on the induced velocity produced by a 0675 m rotor operating at $J_a = 0.067$ and 0.1, Cheeseman and Haddow [15] used hot wire anemometry data to experimentally determine χ and calculate k_x using Coleman's method, and compared the results with the option of determining χ from equation 2-59. By this evaluation, Cheeseman and Haddow [15] showed that the deviation in these results was between 45% and 56%.

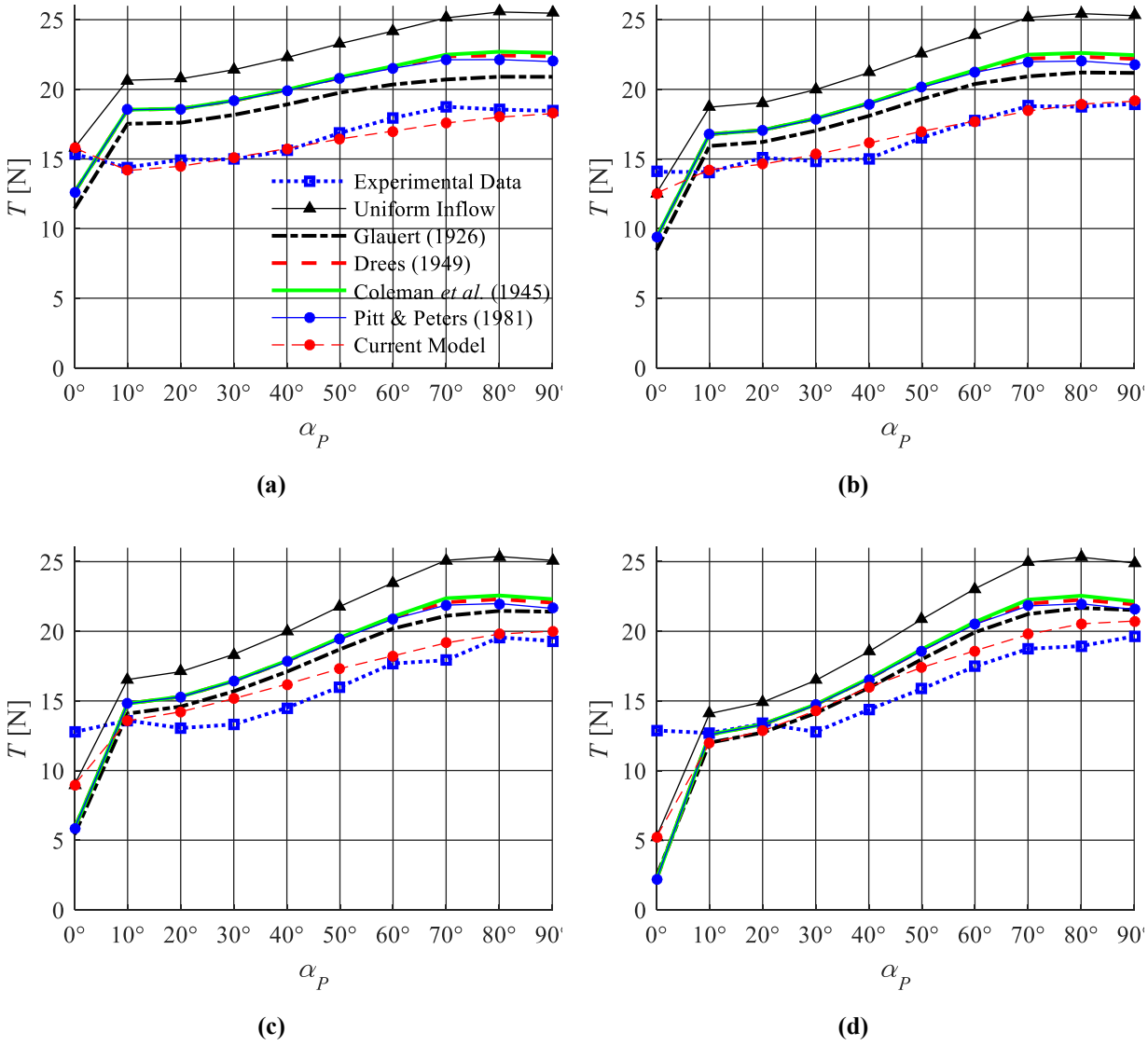

Figure 5-10: Comparison between analytical and experimental thrust data, for *J* values of (a) 0.197 (b) 0.246 (c) 0.295 and (d) 0.345.

Distribution of Local Effective Angle-of-Attack and Differential Thrust

The distributions of α_b and dT over the rotor disk area were obtained by applying the model developed in the previous section and are shown in Figure 5-11. The contours presented in the left column of Figure 5-11 correspond to α_b while the right column shows the thrust distribution over the rotor disk, for the SP12X6 propeller operating at V_∞=10 m/s and α_P = 0°, 30°, 60° and 90°, respectively. The axial flow condition shown in Figure 5-11 (a) and (b) exhibit a symmetric distribution of α_b and dT with respect to the y axis (passing through ψ=90° and 270°) over the rotor disk area, as expected.

As the rotor disk angle (α_p) is increased, α_b increases over the majority of the rotor disk area. The largest α_b is generated by the advancing blades located in the azimuthal coordinates of 0°<ψ<180°. The value of α_b inside this region increases in magnitude with increase of α_p achieving a maximum value of α_b = 20°, and the region itself expands with increase of α_p. The increase of α_p also results in a region of recirculating flow, located below the origin of the graphs, in the region of retreating blades, which increases in size with increasing α_p. This region has a high α_b gradient with respect to the radial direction. Evaluation of Figure 5-11 (c), (e) and (g) reveals that sections of the rotor disk at 270°<ψ<90° operates at α_b values lower than the $\alpha_{L=0}$ of the NACA 4412 airfoil, therefore producing negative lift. In the region of maximum α_b, the blade elements achieve α_b values higher than the stall angle; therefore, as can be seen from Figure 5-11 (d), (f) and (h) this region of the rotor disk performs at dT = 0 N since a value of C_l = 0 is prescribed for this range of α_b.

For increasing values of α_p, the thrust results in Figure 5-11 show that the magnitude of dT increases over the advancing and retreating blade regions. The dT distributions shown in Figure 5-11 show that the maximum dT contribution is achieved in a region closer to the tip of the advancing blades located at 90°<ψ<180°, at the edgewise flow condition (α_p = 90°). Comparison between the left and right columns of Figure 5-11 demonstrates that the regions of maximum α_b do not translate into regions of maximum dT. This may be due to variations in the magnitude of V_R along the radial direction, and the influence it has in the production of lift of the blade elements in the region.

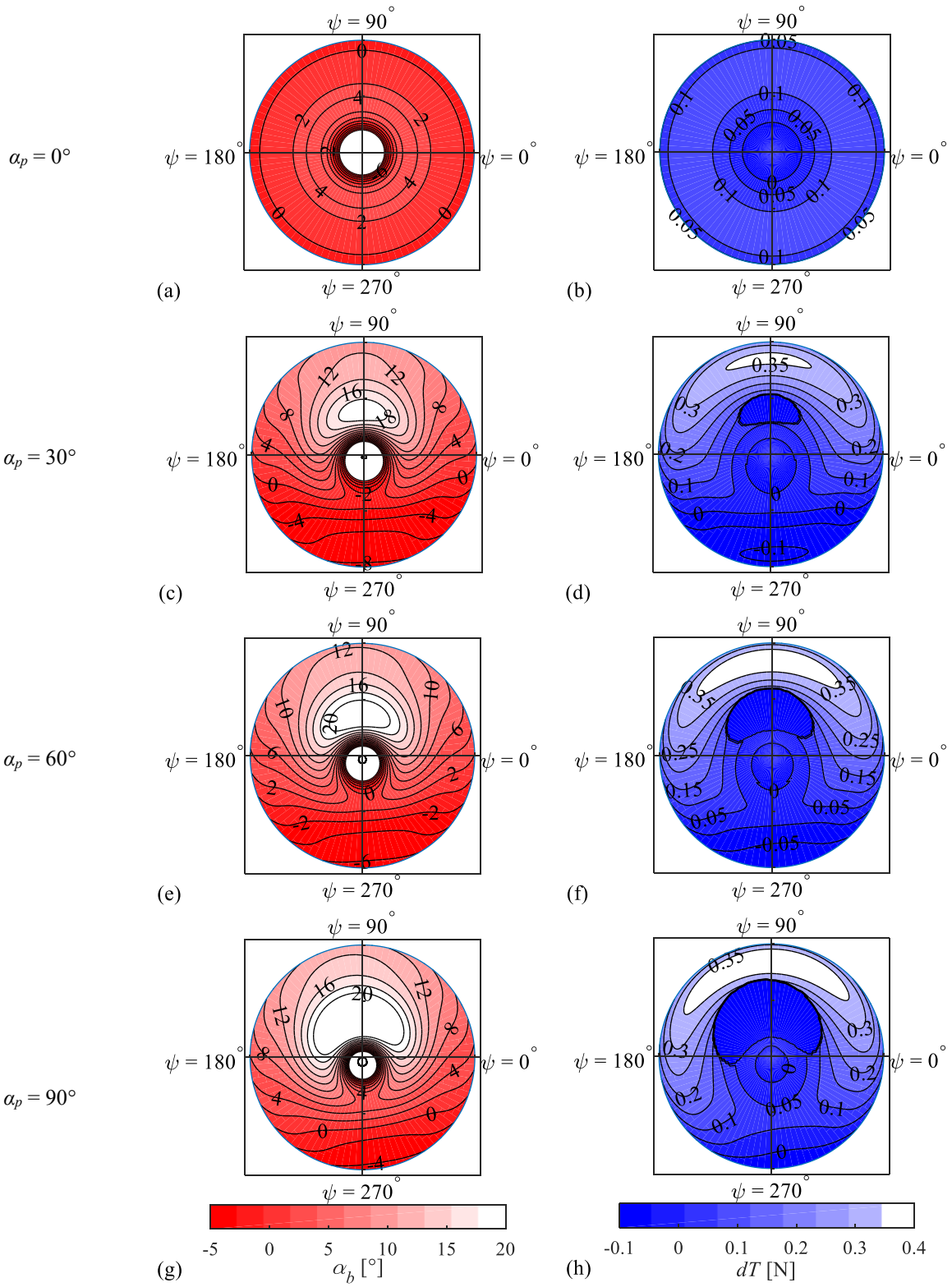

Figure 5-11: Analytical results for V_∞ = 10 m/s (a), (c), (g) and (h): Distribution of α_b over the rotor disk area for α_P=0°, 30°, 60° and 90°, respectively.(b), (d), (f) and (h): Distribution of dT over the rotor disk area for α_P=0°, 30°, 60° and 90°, respectively.

Comparing Figure 5-11 (d), (f) and (h) it can be observed that the model predicts a significant decrease in the *dT* contribution from the rotor disk sections located at within the advancing blade region; which signifies that both the advancing and retreating blades have detrimental effects on the thrust generation in this range of azimuthal locations. The results in Figure 5-11 shows a strong tendency of the region of high thrust generation to shift from being symmetric about the *y*-axis of the rotor disk, to having the majority of its area located within the azimuthal locations $90° < \psi < 180°$. Thus, the results suggest that moments about the longitudinal and lateral axes of the rotor disk are expected, which would translate as pitch and yaw moments on the aircraft equipped with the rotor.

5.5.3 Conclusions from the Investigation

The aerodynamic performance of four 12 in diameter propellers from APC propellers was investigated at propeller angles-of-attack ranging from 0° to 90°. The propeller models tested were the Slow Flyer (SF) with pitches 4.7 in/rev and 6 in/rev, and the remaining two were the Sport (SP) model with pitches 5 in/rev and 6 in/rev. Wind tunnel tests were executed to a maximum free stream advance ratio of 0.55 and 0.5 for the SF and SP model propellers, respectively. The wind tunnel data showed that for all four propellers, the thrust generated increased with increasing propeller angle-of-attack, for all the free stream advance ratios tested. Power consumption results demonstrated a lower sensitivity to changes in the propeller angle-of-attack; however, for the SF model, power consumption increased with increasing propeller angle-of-attack, for the tests performed at free stream advance ratios higher than 0.3. As expected, the resulting moments generated by the difference in performance between the advancing and retreating blades increases with increasing propeller angle-of-attack. The results demonstrated that both a pitching and yawing moment act upon the rotor disk when it is subject to a non-zero angle-of-attack. Evaluation of the propulsive efficiency demonstrated that there is no significant enhancement in the propulsive efficiency of the propellers with changes in the propeller angle-of-attack.

A first harmonic inflow model was suggested, based on the previous model by Pitt and Peters [13], for the approximation of the performance of rotors operating at angles-of-attack ranging from 0° to 90°. The model was developed using MATLAB's Genetic Algorithm solver, where the parameters of the model were refined for the example case of the SP12X6 propeller operating at free stream advance ratios of 0.197, 0.246, 0.295 and 0.344, for angles-of-attack ranging from 0° to 90°. A comparison between the existing inflow models and the suggested model showed that

greater representation of the experimental results was achieved through the suggested model. Distributions of the local effective angle-of-attack and differential thrust distribution over the rotor disk showed that the suggested model provided coherent distributions of these two parameters by indicating the correct advancing and retreating regions, a region of recirculation, and the correct distribution of forces which comply with the result obtained from the experimental campaign.

Chapter 6. Conclusion

Potential improvements to the performance and analysis of UAVs were investigated by studying the aerodynamic performance of a small scale ducted propeller system (240 mm internal diameter), and the aerodynamic performance of open propellers at high angle-of-attack ($0° < \alpha_P < 90°$). An investigation on a small scale ducted propeller system was conducted, and it was focused on the performance of the system during axial flight conditions ($V_\infty > 0$ m/s), covering a free-stream advance ratio range of $0 < J < 0.65$. Two geometric design parameters of the duct model were investigated, namely the diffuser angle and the thickness to chord ratio. Load measurements revealed that changes to the diffuser angle from 9° to 18° produced no significant changes in performance, but an increase in the thickness-to-chord ratio from 0.06 to 0.14 provided the benefit of higher thrust production as well as higher propulsive efficiency. When compared to the open propeller system, the ducted propellers offered significant improvements in thrust in the static tests ($V_\infty = 0$ m/s), achieving a maximum thrust increment of 22.3%. However, the ducted propellers were only superior in performance (thrust generation, power consumption and propulsive efficiency) for an advance ratio range $0 < J < 0.25$~0.35. Beyond this point the performance of the ducted propellers fell below that of the open propellers, and this was attributed to the increased drag of the duct at higher free-stream velocities. Inlet flow visualization performed through stereoscopic PIV provided evidence that as the advance ratio was increased (by increment of V_∞), the mass flow rate through the rotor disk plane of the open propeller system surpassed that of the ducted propeller. The results suggested that the ducted propeller achieved higher loading of the propeller blades than the open propeller. The exit jet flow in the wake region was visualized using planar PIV, and it demonstrated that the ducted propeller system decreased the exit jet velocity, and achieved an exit area-to-rotor disk area ratio of $\sigma_e = 1.04$; whereas the open propeller of the same diameter used in the ducted system achieved a maximum area ratio of $\sigma_e = 0.90$, based on the stream tube defined by the shear layer between the exit jet and the free-stream flow. The benefits of the ducted propeller over an open propeller system are evident for the static condition and the low advance ratio regime; however, these performance enhancements decay rapidly as the free-stream (and hence advance ratio) is increased.

The wide range of propeller powered UAV flight missions imply that the rotor disk be subject of high propeller angles-of-attack, α_P. The performance of four 12 in diameter propellers was

investigated in an angle-of-attack range of $0° < \alpha_P < 90°$. Two of the propellers tested were the Slow Flyer (SF) model and two other were the Sport (SP) model, both from APC Propellers. For each model, two different propeller nominal pitches were tested (4.7 and 6 for the SF model and 5 and 6 inches/revolution for the SP). Load cell measurements were acquired for the advance ratios $0 < J < 0.55$ for the SF model and $0 < J < 0.5$ for the SP model. Load cell measurements acquired during the wind tunnel tests revealed that the inflow condition generated by the increment of α_P resulted in an increment of the thrust generation, for a constant free-stream advance ratio. The thrust, power and propulsive efficiency results were graphically presented as a function of the free-stream advance ratio, J, and the inflow advance ratio, J', and it was shown that the change to with respect to J' the data for multiple α_P overlap showing a single performance curve (for each propeller). The data also showed evidence of the existence of both a pitching and yawing moment acting upon the rotor disk when subject to $\alpha_P > 0°$. An analytical performance prediction model was developed using the blade element momentum theory alongside a first harmonic inflow model of the induced velocity, v_i. The model was fine-tuned using the experimental data of the SP propeller (6 inches/rev) and the Genetic Algorithm from MATLAB. The results were compared to predictions of already existing first harmonic models. The suggested model in this investigation showed greater adherence to the experimental data than the existing models. The model was used to generate contours of the effective angle-of-attack of the blade elements, σ_e, as well as the differentia thrust, dT, and it successfully modelled the distribution of dT over the rotor disk area which coincided with the experimental results (resultant pitch and yaw moments about the rotor hub), as well as the regions of recirculation.

Chapter 7. Suggestions for Future Research

The main challenge in the investigation presented in section Chapter 4 of this thesis was the determination of a standard design methodology or design parameters for the duct model. Although there exists numerous independent studies of duct performance and parametric studies on the duct geometry, there is no real consensus on any of the parameters. It would be of great benefit to future researchers on the topic if a consolidated effort is made to generate such documentation. Visualization of the internal surface of the diffuser would provide insightful information regarding the operational limits of the diffuser, as well as information about internal flow separation, depending on the diffuser angle setting used.

The performance data presented in section Chapter 5 of this thesis provided information for a limited advance ratio range. The reason for this issue were mainly mechanical constrains, due to structural compromises in the experimental setup. A duct manufacturing method that would allow rapid prototyping to be achieved in a singular duct piece rather than multiple pieces as was done in this thesis, would benefit the structural integrity of the experiment. This would allow testing at higher advance ratios.

One of the challenges during the investigation elaborated in Chapter 5 of this thesis had to do with the selection of a tip-loss factor for the propeller operation at non-zero angles-of-attack. The already existing models have been, in their majority, developed in helicopter research, and are intended to be use for small angle-of-attack. The necessity for an updated tip-loss model for propeller blades operating at high angle-of-attack, is of importance for further propeller and UAV research.

References

[1] Gent, Edd, "The Future of Drones: Uncertain, Promising and Pretty Awesome," *LiveScience*, https://www.livescience.com/52701-future-of-drones-uncertain-but-promising.html

[2] A. Frank, J. McGrew, M. Valenti, D. Levine and J. P. How, "Hover, Transition, and Level Flight Control Design for a Single-Propeller Indoor Airplane," AIAA Guidance, Navigation and Control Conference and Exhibit, August 2007. DOI: 10.2514/6.2007-6318.

[3] S. Siebert, J. Teizer, "Mobile 3D mapping for surveying earthwork projects using an Unmanned Aerial Vehicle (UAV) system," Automation in Construction, May 2014. DOI: 10.1016/j.autcon.2014.01.004.

[4] J. L. Pereira, "Hover and Wind-Tunnel Testing of Shrouded Rotors for Improved Micro Air Vehicle Design," Ph.D. Dissertation, Aerospace Engineering Dept., University of Maryland, College Park, 2008.

[5] L. Kort, "Combined Device of a Ship's Propeller Enclosed by a Nozzle," 1936.

[6] L. Stipa, "Experiments With Intubed Propellers," L'Aerotecnica, 1931.

[7] E. Ahci-Ezgi, U. Denecke, S. Emmerling, G. Kuntze-Fechner, and P. Rauch, "Evolution of FenestronTM Development in terms of Safety, Design and Substantiation Characteristics," American Helicopter Society 71st Annual Forum, Vol. 71, May 2015.

[8] H. Glauert, The Elements of Aerofoil and Airscrew Theory, 2nd ed., The Syndics of the Cambridge University Press, London, 1959, Chap. 15.

[9] J. G. Leishman, Principles of Helicopter Aerodynamics, 2nd ed., Cambridg University Press, New York, 2006, Chaps. 2-3.

[10] H. Glauert, "A General Theory of the Autogyro," R&M No. 1111, British A.R.C., November 1926.

[11] R. P. Coleman, A. M. Feingold, and C. W. Stempin, "Evaluation of the Induced-Velocity Field of an Idealized Helicopter Rotor," NACA-WR-L-126, June 1945.

[12] J. M. Drees, “A Theory of Airfoil Through Rotors and Its Application to Some Helicopter problems,” Journal of the Helicopter Association of Great Britain, Vol. 3, No. 2, 1949, pp. 79-104.

[13] D. M. Pitt and D. A. Peters, ‘Theoretical Prediction of Dynamic-Inflow Derivatives,” Sixth European Rotorcraft and Powered Lift Aircraft Forum, Paper No. 47, September 1980.

[14] R. T. N. Chen, “A Survey of Nonuniform Inflow Models for Rotorcraft Flight Dynamics and Control Applications,” NASA-TM-102219, November 1989.

[15] I. C. Cheeseman and C. Haddow, “An Experimental Investigation of the Downwash Beneath a Lifting Rotor and Low Advance Ratios,” Fourteenth European Rotorcraft Forum, Paper No. 8, September 1988.

[16] B. B. McCormick, *Aerodynamics, aeronautics, and flight mechanics*, New York: Wiley, 1979.

[17] R. I. Lewis, Turbomachinery Performance Analysis, Arnold, London, 1996.

[18] L. Prandtl, “Applications of Modern Hydrodynamics to Aeronautics,” NACA-TR-116, January 1923.

[19] W. Khan, R. Caverly, M. Nahon, “Propeller Slipstream Model for Unmanned Aerial Vehicles,” AIAA Modeling and Simulation Technologies (MST) Conference, Boston, August 2013. DOI: 10.2514/6.2013-4907.

[20] D. Stewart, G. Hamill, H. Johnston, “Velocities in a ship’s propeller wasah,” International Symposium on Environmental Hydraulics, Rotterdam, 1991.

[21] J. F. Mcmahon, “Characteristics of Ducted Propellers,” Propellers/Shafting ’94 Symposium, 1994.

[22] D. M. Black, H. S. Wainauski, and C. Rohrbach, “Shrouded Propellers - A Comprehensive Performance Study,” AIAA 5th Annual Meeting and Technical Display, no. 68–994, 1968.

[23] R. J. Platt Jr, “Static Tests of a Shrouded anf Unshrouded Propeller,” NACA RM-L7H25, February 1948.

[24] J. D. Van Manen and M. W. C. Oosterveld, “Analysis of Ducted-Propeller Design,” Annual Meeting of the Society of Naval Architects and marine Engineers, Vol. 288, New York, pp. 522–562, 1966.

[25] S. Yilmaz, D. Erdem, and M. S. Kavsaoglu, “Performance of a ducted propeller designed for UAV applications at zero angle of attack flight: An experimental study,” Aerospace Science and Technology, Vol. 45, pp. 376–386, June 2015. DOI: 10.1016/j.ast.2015.06.005.

[26] A. Akturk and C. Camci, “Tip Clearance Investigation of a Ducted Fan Used in VTOL UAVs Part I: Baseline Experiments and Computational Validation,” Proceedings of ASME 2011 Turbo Expo: Turbined Technical Conference and Exposition, Vol. 7, pp. 331-344, June 2011. DOI: 10.1115/GT2011-46356.

[27] A. Akturk and C. Camci, “Tip Clearance Investigation of a Ducted Fan Used in VTOL UAVs Part 2 : Novel Treatments Via Computational Design,” Proceedings of ASME 2011 Turbo Expo: Turbined Technical Conference and Exposition, Vol. 7, pp. 3345-357, Vancouver, June 2011. DOI: 10.1115/GT2011-46359.

[28] M. Lazareff, “The Aerodynamics of V/STOL Aircraft,” Advisory Group for Aerospace Research and Development, Rhode-Saint Genèse, pp 237-290, May 1968.

[29] J. D. Van Manen and M. W. C. Oosterveld, “Series of model Tests on Ducted Propellers,” Netherlands Ship Model Basin, 1953.

[30] W. Kruger, “On Wind Tunnel Tests and Computations Concerning The Problem of Shrouded Propellers,” NACA TM-1202, February 1949.

[31] B. Gamse and K. W. Mort, “A wind-tunnel investigation of a 7-foot- diameter ducted propeller,” NASA TN-D-4142, August 1967.

[32] L. P. Parlett, “Aerodynamic characteristics of a small-scale shrouded propeller at angles of attack from 0° to 90°,” NACA TN-3547, November 1955.

[33] H. S. Fletcher, “Experimental Investigation of Lift, Drag, and Pitching Moment of Five Annular Airfoils,” NACA TN-4117, October 1957.

[34] R. T. Taylor, “Experimental Investigation of the Effects of Some Shroud Design Variables on a Shrouded Propeller Submerged in a Wing,” NACA TN-4126, January 1958.

[35] Hiller Aircraft Corporation, “Comparative Performance Charts For Ducted Propellers,” Palo Alto, California, 1960.

[36] A. Abrego and R. Bulaga, “Performance Study of a Ducted Fan System,” American Helicopter Society Aerodynamics, Acoustics, and Test and Evaluation Technical Specialists Meeting, San Fracisco, pp. 1–6, January 2002.

[37] W. Graf, J. Fleming, and W. Ng, “Improving Ducted Fan UAV Aerodynamics in Forward Flight,” AIAA, 46th AIAA Aerospace Science Meet and Exhibit, pp. 1–11, January 2008. DOI: 10.2514/6.2008-430.

[38] P. Martin and C. Tung, “Performance and Flowfield Measurements on a 10-inch Ducted Rotor VTOL UAV,” NASA Ames Research Center, p. 21, January 2004.

[39] A. Akturk and C. Camci, “Experimental and Computational Assessment of a Ducted-Fan,” Journal of Aricraft, Vol. 49, No. 3, pp. 885–898, 2012. DOI: 10.2514/1.C031562.

[40] J. B. Brandt and M. S. Selig, “Propeller Performance Data at Low Reynolds Numbers,” AIAA Paper 2011-1255, January 2011.

[41] R. E. Kuhn and J. W. Draper, “Investigation of the Aerodynamic Characteristics of a Model Wing-Propeller Combination and of the Wing and Propeller Separately at Angles of Attack up to 90°,” NACA TR-1263, January 1956.

[42] H. C. McLemore and M. D. Cannon, “Aerodynamic investigation of a four-bladed propeller operating through an angle-of-attack range from 0 to 180 degrees,” NACA TN-3228, June 1954.

[43] P. Yaggy and V. Rogallo, “A Wind-Tunnel Investigation of Three Propellers Through an Angle of Attack from 0 to 85 deg,” NACA TN-D-318, May 1960.

[44] C. E. Hughes and J. A. Gazzaniga, “Low-Speed Wind Tunnel Performance of High-Speed Counterrotation Propellers at Angle-of-Attack,” AIAA Paper 89-2583, January 1989.

[45] T. B. Carroll, “A Design Methodology for Rotors of Small Multirotor Vehicles,” M.Sc. Disseration, Aerospace Engineering Dept., Ryerson University, Toronto, 2017.

[46] Drela, M, “QPROP Formulation,” MIT Aero & Astro, June 2006.

[47] Goldstein, S, “On the Vortex Theory of Screw Propellers,” Proceedings of the Royal Society of London. Series A, Containing Papers of a Mathematical and Physical Character, Royal Society, Vol. 123, London, April 1929, pp 440-465.

[48] G. Kostiuk, L. W., Johnson, M. R. & Thomas, “University of Alberta Flare Research Project Final Report,” Independent Report, Edmonton, 2004.

[49] M. S. Selig, “Eppler 63 low Reynolds number airfoil,” UIUC Airfoil Coordinates Database, http://m-selig.ae.illinois.edu/ads/coord_database.html [retrieved 1 September 2017].

[50] A. Melling, “Tracer particles and seeding for particle image velocimetry,” Measurement Science and Technology, Vol. 8, No. 12, pp. 1406–1416, 1997.

[51] M. Raffel, C. E. Willert, S. T. Wereley, and J. Kompenhans, Particle Image Velocimetry, Springer Berlin Heidelb, pp. I–XX, 2007.

[52] R. J. Adrian, “Twenty years of particle image velocimetry,” Experiments in Fluids, Vol. 39, No. 2, pp. 159–169, 2005.

[53] D. B. Barker and M. E. Fourney, “Measuring fluid velocities with speckle patterns,” Optic Letters, Vol. 1, No. 4, p. 135-137, 1977. DOI: 10.1364/OL.1.000135.

[54] T. D. Dudderar and P. G. Simpkins, “Laser speckle photography in a fluid medium,” International Journal of Science, Vol. 270, No. 5632, pp. 45–47, 1977. DOI: 10.1038/270045a0.

[55] R. Grousson and S. Mallick, “Study of flow pattern in a fluid by scattered laser light,” Applied Optics, Vol. 16, No. 9, pp. 2334–2336, 1977. DOI: 10.1364/AO.16.002334.

[56] C. J. D. Pickering and N. a. Halliwell, “Laser speckle photography and particle image velocimetry: photographic film noise,” Applied Optics, Vol. 23, No. 17, p. 2961, March 1984. DOI: 10.1364/AO.23.002961.

[57] R. J. Adrian, “Scattering particle characteristics and their effect on pulsed laser measurements of fluid flow: speckle velocimetry vs particle image velocimetry,” Applied Optics, Vol. 23, No. 11, pp. 10–11, June 1984. DOI: 10.1364/AO.23.001690.

[58] A. H. Sacks and J. A. Burnell, “Ducted propellers – A critical review of the state of the art,” Hiller Aircraft Corporation, 1959.

[59] E. M. Sparrow, J. P. Abraham and W. J. Minkowycz, “Flow separation in a diverging conical duct: Effect of Reynolds number and divergence angle,” International Journal of Heat and Mass Transfer, Vol. 52, No. 13, pp. 3079-3083, 2009. DOI: 10.1016/j.ijheatmasstransfer.2009.02.010

[60] V. Chandavari and S. Pelekar, “Diffuser angle control to avoid flow separation,” International Journal of Technical Research and Applications, Vol. 2, No. 5, pp. 16-21, 2014.

[61] R. Bontempo and M. Manna, “Effects of Duct Cross Section Camber and Thickness on the Performance of Ducted Propulsion Systems for Aeronautical Applications,” International Journal of Aerospace Engineering, 2016. DOI: 10.1155/2016/8913901

[62] W. B. Morgan, “A theory of the ducted propeller with a finite number of blades,” University of California, No. 19, 1961.

[63] “Airfoil Tools.” [Online]. Available: http://airfoiltools.com.

[64] C. C. Critzos et. al, “Aerodynamic Characteristics of NACA 0012 Airfoil Section at Angles of Attack from 0 degrees to 180 degrees,” NACA-TN-3361, January 1955.

[65] J. D. Anderson Jr, Fundamentals of Aerodynamics, 5th ed., McGraw Hill Education, New York, 2005.

[66] E. L. Houghton and N. B. Carruthers, Aerodynamics for Engineering Students, 3rd ed., Routledge, Chapman and Hall, Inc, London, New York, 1982.

[67] B. W. McCormick, Aerodynamics, Aeronautics, and Flight Mechanics, The Pennsilvania State University, 1979.

Appendices

Appendix A: Support Structure Interference Test Results

The influence of the support structure on the load cell measurements was tested by conducting tests with the untrimmed SP11×7 propeller with and without the duct support rods described in section 3.4, at a propeller rotational speed of n = 6000 RPM and free-stream speeds ranging from 0 m/s to 15 m/s. The results of this test are shown in Figure A. 1 (a) to (d).

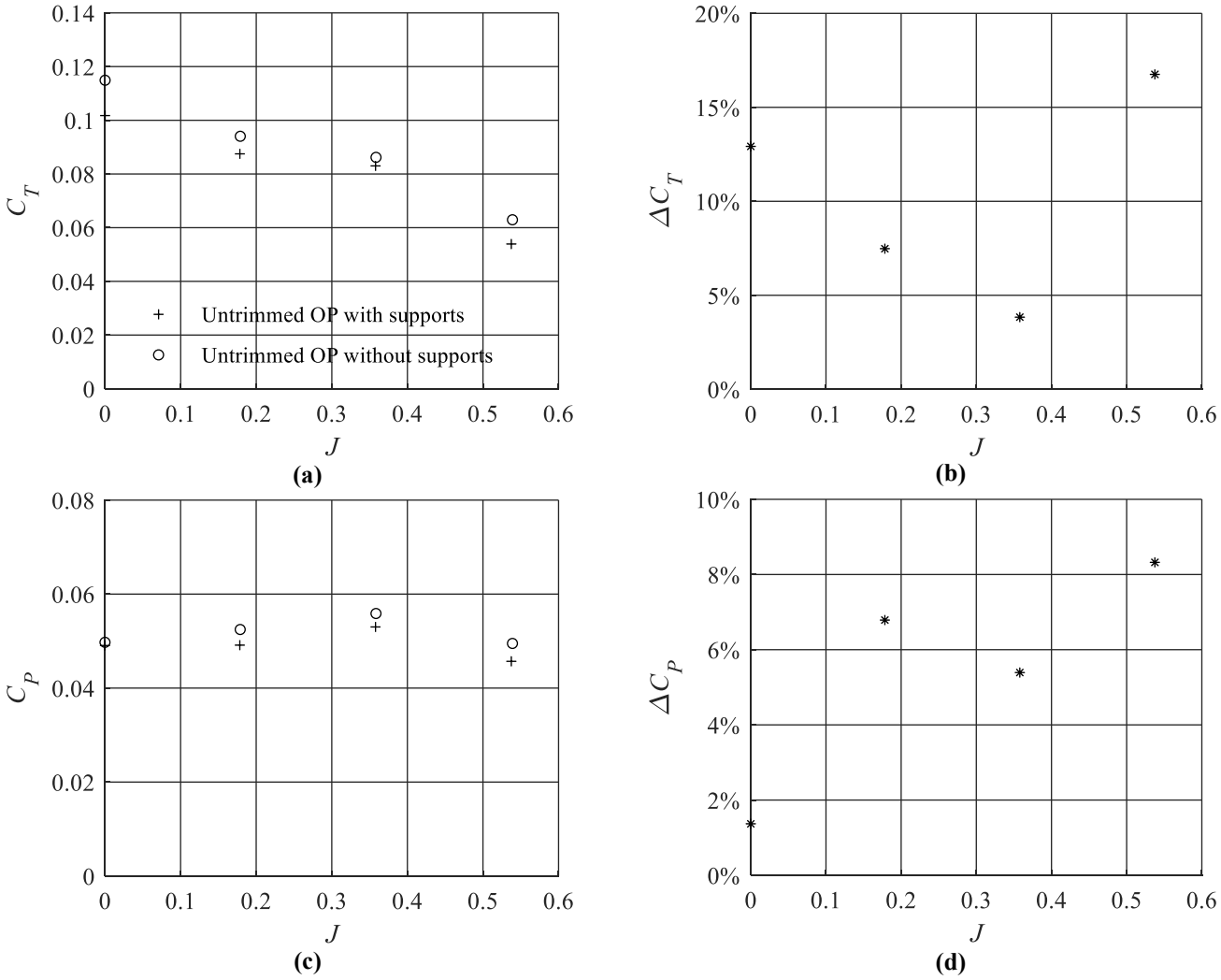

Figure A. 1: The results from testing the influence of the duct support rods on the load measurements using the untrimmed SP11×7 propeller. The C_T-J response is shown in (a), and the percent difference between the two cases is shown in (b). Similarly, the C_P-J response is shown in (c), and the percent difference between the two cases is shown in (d).

In Figure A. 1(b) it is shown that the maximum C_T deviation between the case including the duct supports and the case excluding the supports is 16.75%. The percent deviation in C_P is shown in Figure A. 1(d), and the maximum deviation is 8.32%.

Appendix B: Photographs of the Stereoscopic PIV Setup

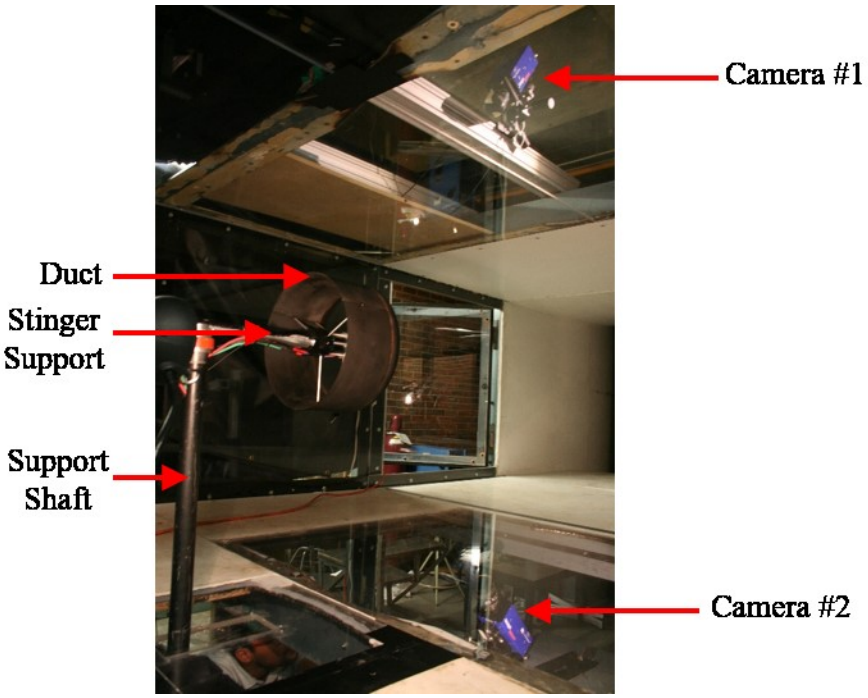

Figure A. 2: Photograph of the cameras configuration in the Stereoscopic PIV experiment discussed in section 3.6.2 showing the cameras, ducted propeller and support system.

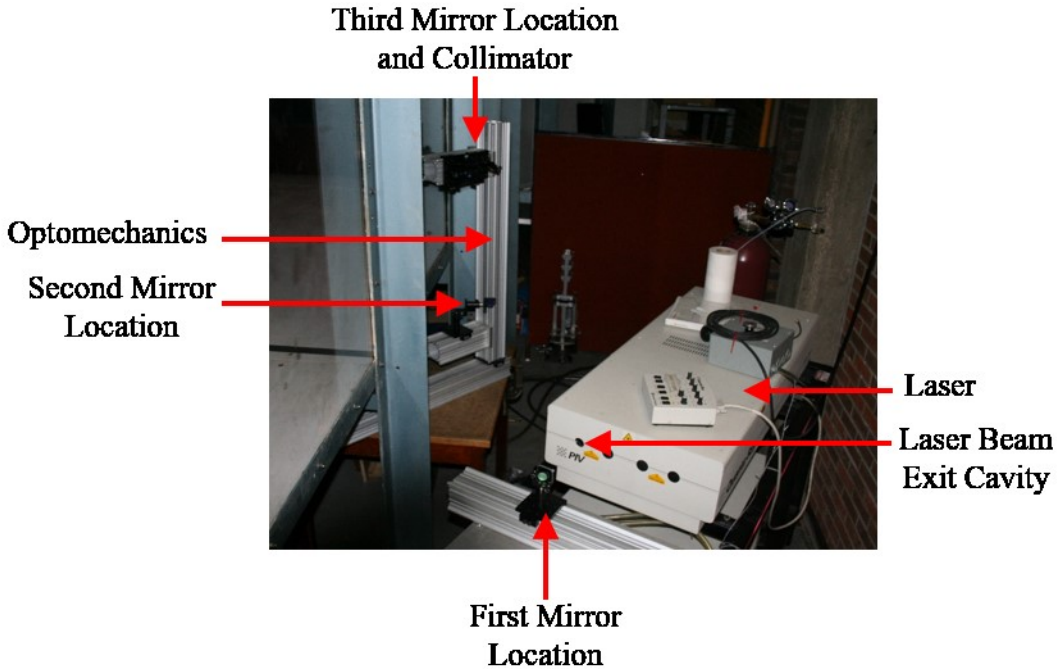

Figure A. 3: Photograph of the Quanta-Ray PIV 400, Spectra Physics Laser used in the Stereoscopic PIV experiment. The image shows the optomechanics used to redirection the laser beam.

Appendix C: Instantaneous Images of the Wake Flow for the LE1-DA18-0.14, trimmed OP and untrimmed OP Systems

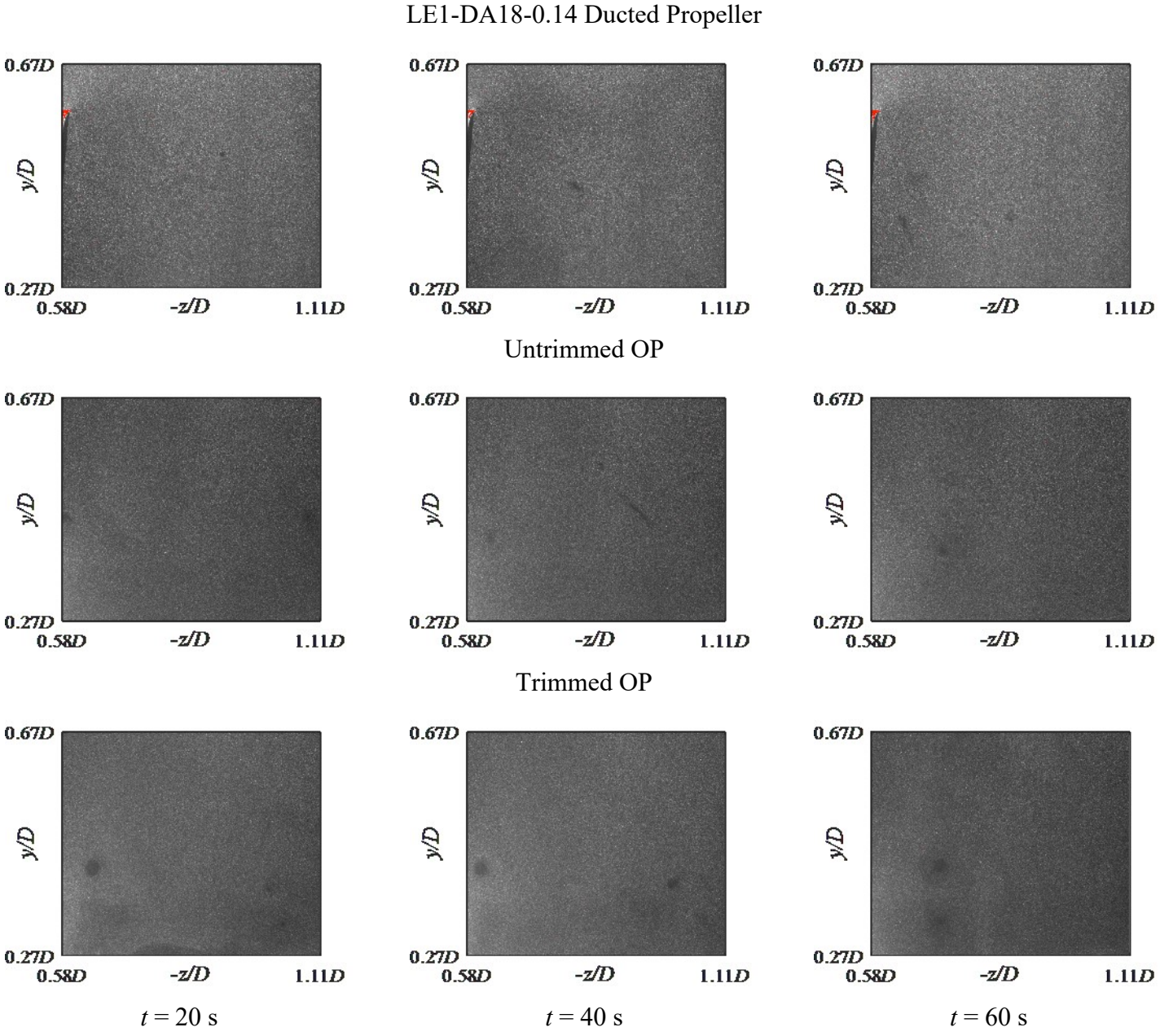

Figure A. 4: Snapshots of the flow in the wake region of the LE1-DA18-0.14 ducted propeller, trimmed OP and untrimmed OP at V_∞ = 0 m/s and n = 6000 RPM.

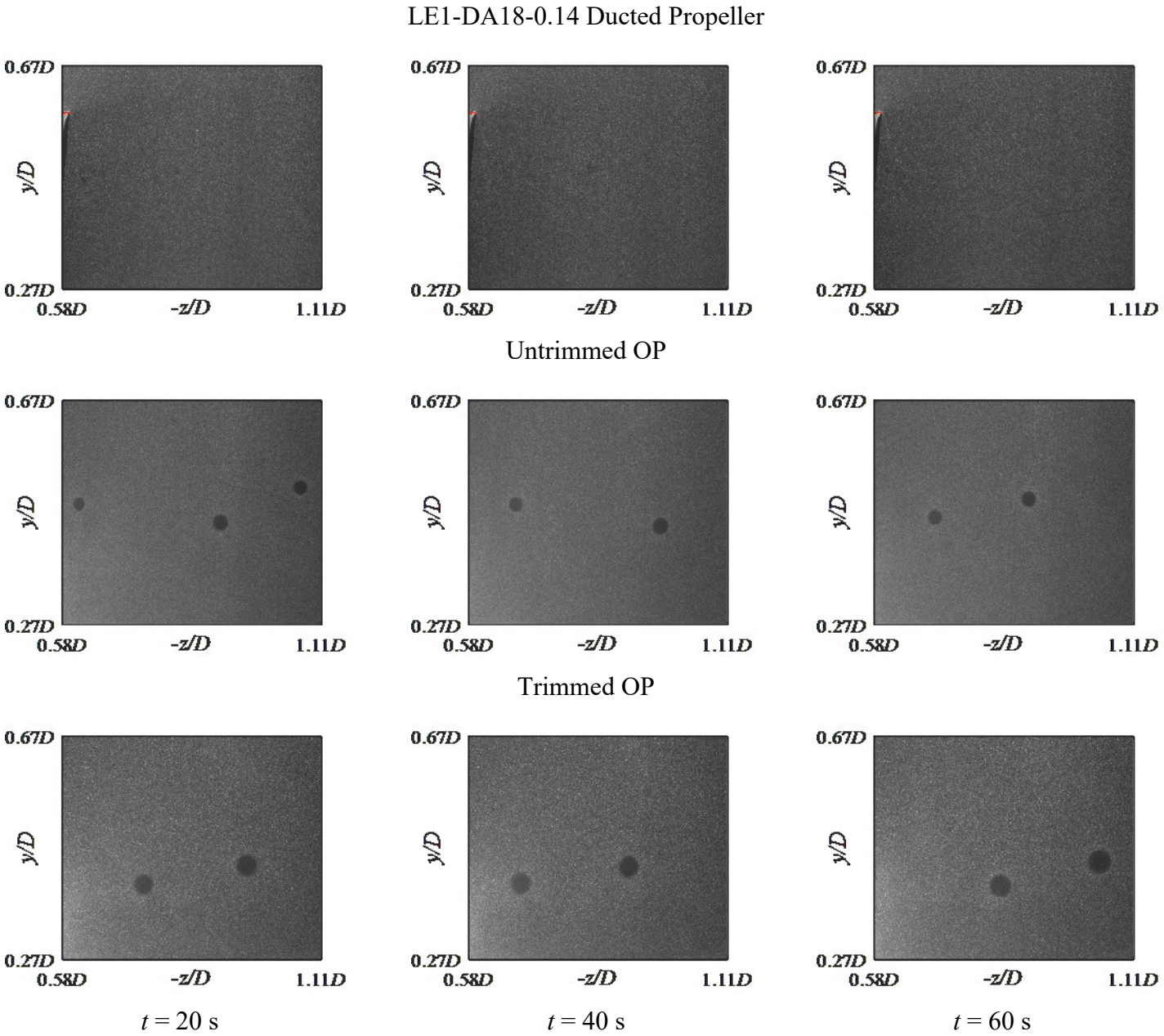

Figure A. 5: Snapshots of the flow in the wake region of the LE1-DA18-0.14 ducted propeller, trimmed OP and untrimmed OP at V_∞ = 5 m/s and n = 6000 RPM.

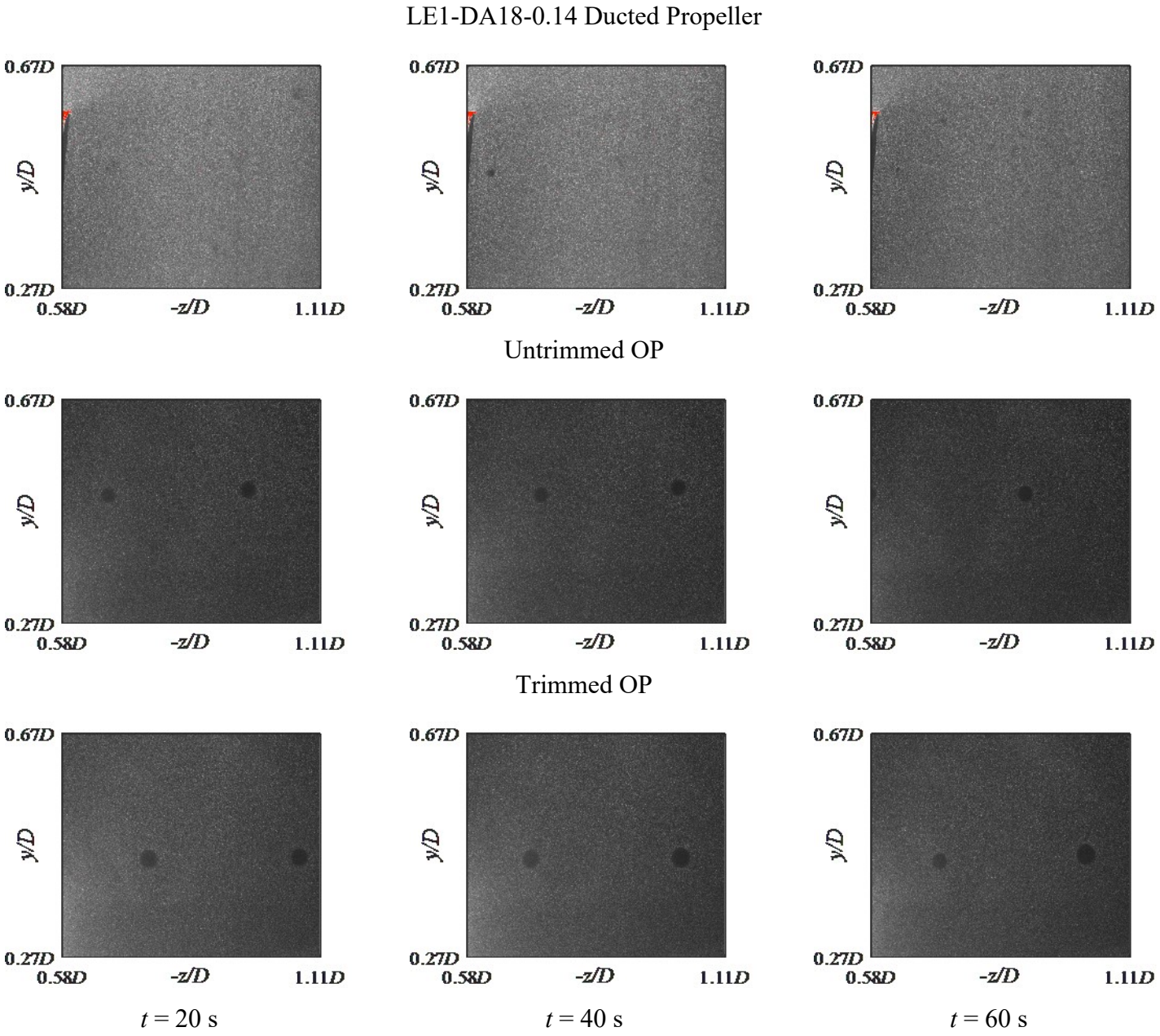

Figure A. 6: Snapshots of the flow in the wake region of the LE1-DA18-0.14 ducted propeller, trimmed OP and untrimmed OP at V_∞ = 10 m/s and n = 6000 RPM.

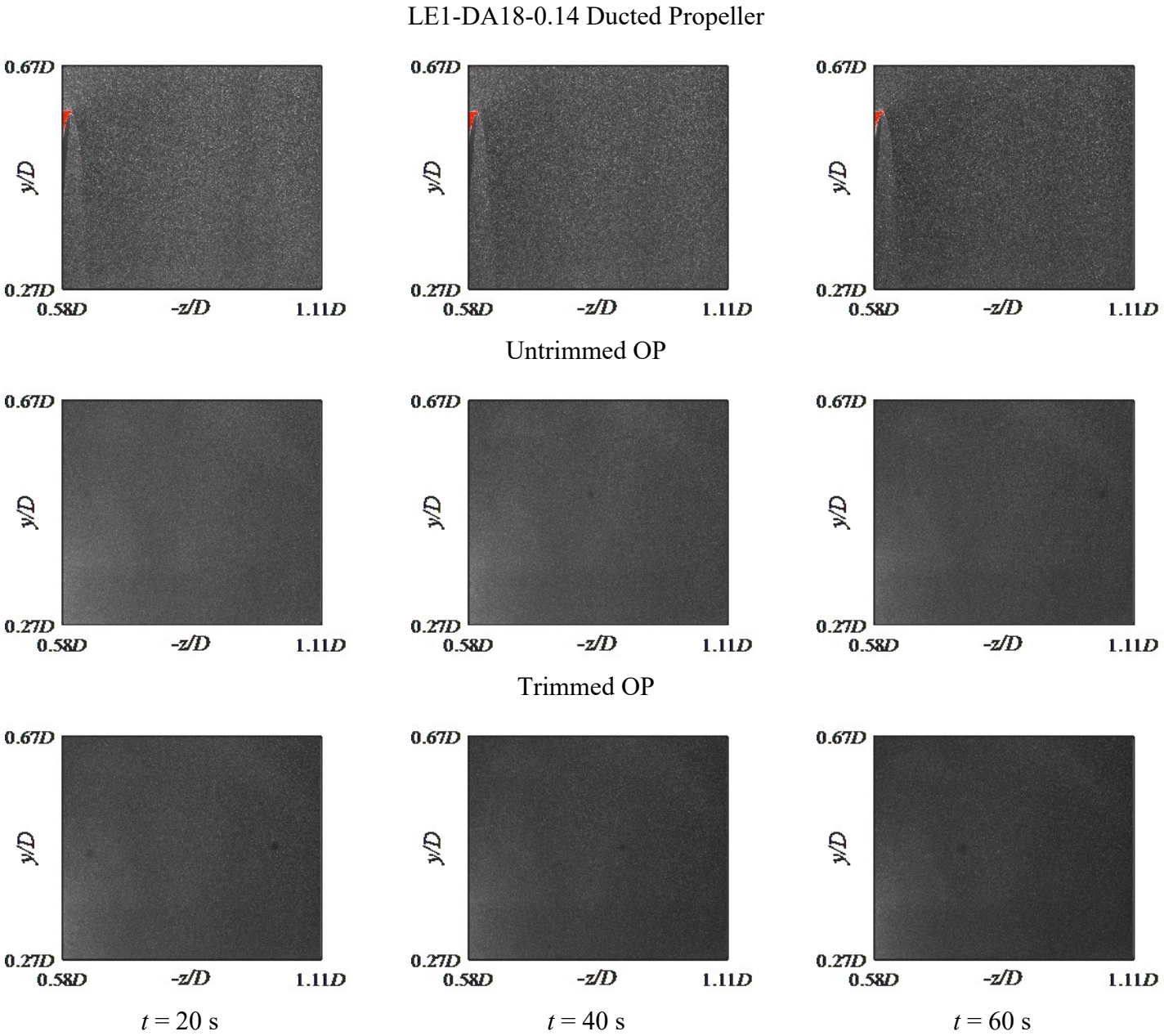

Figure A. 7: Snapshots of the flow in the wake region of the LE1-DA18-0.14 ducted propeller, trimmed OP and untrimmed OP at V_∞ = 15 m/s and n = 6000 RPM.

Appendix D: Requests for Image Usage and other Permissions

In this appendix, email communications between the author of this thesis and several image owners is displayed as evidence of efforts to comply with copyright and authorization requirements.

Permission requested for figures acquired from the NASA Research Center.

UNIVERSITY OF ALBERTA

David Serrano <dserrano@ualberta.ca>

RE: NASA STI Information Desk - General Contact

HQ-STI-INFODESK <hq-sti-infodesk@mail.nasa.gov> 20 July 2018 at 07:28
To: "dserrano@ualberta.ca" <dserrano@ualberta.ca>

Re: your request: "...I was wondering if I need to request permissions to use the figures from NACA reports found in your website for my thesis; and if so, where and how can I ask for these permissions."

Dear David Serrano:

Thank you for contacting the NASA STI Information Desk. NACA reports available from NTRS (https://ntrs.nasa.gov) are in the public domain, and if the requested figures constitute a small portion of the number of figures and report, NASA has no problem with you using the figure as long as you:

- Make an effort to get permission from the authors *
- Do not alter the figure in any way.
- Cite that it has been taken from the paper [ex. "This figure is taken from NASA/CP-1998-207654, [add Title, list authors] and used with permission of NASA"]
- Do not indicate that NASA endorses your paper or work in any way.

*Note that, since NACA papers were published a long time ago now, it's very unlikely you would find authors to contact, but the other conditions would still apply…

Please be sure to see our complete copyright notice here: (https://www.sti.nasa.gov/disclaimers/).

I hope this helps answer your question. Please let us know if we can be of additional assistance.

Best regards,

Richard Anderson

NASA STI Information Desk

Connect with NASA STI on:

www.sti.nasa.gov Twitter Facebook YouTube

UNIVERSITY OF ALBERTA

David Serrano <dserrano@ualberta.ca>

Thesis Figure Permissions

NASA-ResearchAccess <nasa-researchaccess@mail.nasa.gov> 24 July 2018 at 14:52
To: David Serrano <dserrano@ualberta.ca>

Dear David,

Thank you for contacting the NASA Research Access Help Desk. In regard to your question of whether you can use research/data found in NTRS, please note that many documents are in the public domain and can be referenced as research resources. Please be sure to see our complete copyright notice: https://www.sti.nasa.gov/disclaimers/. If you plan to re-use specific figures or other content, NASA asks that you:

- Make an effort to get permissions from the authors.
- Do not alter figures (etc.) in any way.
- Cite the figures (etc.) accordingly (e.g., "This figure is taken from NASA-MEMO-5-19-59E, [add title, list authors] and used with permission of NASA")
- Do not indicate that NASA endorses your work in any way.

I recommend reviewing our NTRS Search Tips: https://www.sti.nasa.gov/ntrs-search-tips/#.WaXFomdvkek. You may find the Thesaurus helpful, too: https://www.sti.nasa.gov/nasa-thesaurus/#.WaXF1mdvkek. These pages provide starting points for clarifying research questions.

I hope this information is helpful in your research. Please let me know if we can be of additional assistance.

Best regards,

Melissa Kennedy
NASA Research Access Help Desk
nasa-researchaccess@mail.nasa.gov
(757) 864-6736

Connect with NASA STI on:
www.sti.nasa.gov Twitter Facebook YouTube

Sincerely,

[Name]

[Signature]

Permission requested for figures from the U.S.A Navy website:

UNIVERSITY OF ALBERTA

David Serrano <dserrano@ualberta.ca>

RE: Feedback from Navy.mil website (CAPTCHA verified)

navymedia <navymedia@navy.mil> 23 July 2018 at 08:09
To: "dserrano@ualberta.ca" <dserrano@ualberta.ca>, "Sharpe, John F CDR CHINFO, DMA Liaison" <john.f.sharpe2.mil@mail.mil>

Mr. Serrano,
Most of the imagery on Navy.mil is in the public domain. Photos marked as "courtesy of..." may have limitations from the imagery provider. Anything that says U.S. Navy photo by.../Released is public domain.

For more information, please visit:
http://www.dimoc.mil/resources/limitations/

Thank you,
Damon

Damon J. Moritz
Office of Information
1200 Navy Pentagon RM 4B463
Washington, DC 20350-1200
(703) 614-9154 (office)
224-9154 (DSN)
Damon.moritz@navy.mil
Damon.moritz@imagery.navy.mil

-----Original Message-----
From: dserrano@ualberta.ca <dserrano@ualberta.ca>
Sent: Monday, July 23, 2018 12:46 AM
To: navymedia <navymedia@navy.mil>; Sharpe, John F CDR CHINFO, DMA Liaison <john.f.sharpe2.mil@mail.mil>
Subject: Feedback from Navy.mil website (CAPTCHA verified)

Hello, My name is David Serrano, I am an MSc student from the University of Alberta in Edmonton, Canada. I would like to use a photo in your website of the MQ-8B Fire Scout UAV for my Thesis. I would like to request the appropriate permissions to do this. Thank your very much, David Serrano.

Permission requested from Draganfly Innovations Inc.:

UNIVERSITY OF ALBERTA

David Serrano <dserrano@ualberta.ca>

Photograph Permission for Thesis

Garry Reusch <gbr677@yahoo.ca> 20 July 2018 at 08:37
To: David Serrano <dserrano@ualberta.ca>

This from Zenon

On Jul 20, 2018, at 7:32 AM, Zenon Dragan <zenon.dragan@draganfly.com> wrote:

No problem,
but that's not a Draganflyer x6 it's an x4p, can contact me directly. I also high-quality images if he would like,

Regards,

Zenon Dragan

On Jul 19, 2018, at 9:33 PM, Garry Reusch <gbr677@yahoo.ca> wrote:

Sent from my iPhone

Begin forwarded message:

From: David Serrano <dserrano@ualberta.ca>
Date: July 19, 2018 at 20:28:56 PDT
To: gbr677@yahoo.ca, mterkeurs@gmail.com
Subject: Photograph Permission for Thesis

Hi Garry,

It's been a long time since we last made contact! I'm now finished my Masters degree, and I'm just in the process of submitting my thesis to the faculty. However I need permission to use some of the figures in my thesis. I was would like to request permission from Draganfly Innovations Inc. to use one photograph of the Dragnflyer X6, shown below. If there is a formal way on doing this, I was hoping you could point me in the right direction.

Thank you for your help!!

<image.png>

David Serrano - E.I.T
BSc. Mechanical Engineering
MSc. Mechanical Engineering Student
University of Alberta
Edmonton

<image.png>

Permission requested for figures from V-Bat website

UNIVERSITY OF ALBERTA

David Serrano <dserrano@ualberta.ca>

V BAT Photograph Permission Request

Info <Info@martinuav.com> 19 July 2018 at 05:52
To: David Serrano <dserrano@ualberta.ca>

Yes it is no problem to use.

Thanks

Phil Jones

COO

Martin UAV LLC

Cell: + 1 702 465 3540

Web: www.martinuav.com

From: David Serrano <dserrano@ualberta.ca>
Date: Thursday, July 19, 2018 at 12:31 AM
To: Info <Info@martinuav.com>
Subject: V BAT Photograph Permission Request

Hello,

My name is David Serrano, I am an MSc student from the University of Alberta and I would like to request permission to use one photograph of the V BAT in my MSc thesis. I found the photograph on Google, it is the one below, however I am having trouble confirming that this image is indeed yours. If so, would you be able to point me in the right direction regarding where and how may I ask for permission?

Permission requested to use figures from Jason L. Pereira's Doctoral Thesis:

UNIVERSITY OF ALBERTA

David Serrano <dserrano@ualberta.ca>

Re: FW: Website Form Submission

Aileen Hentz <anhentz@umd.edu> 25 July 2018 at 09:02
To: dserrano@ualberta.ca, "Matthew J. Sinclair" <mjsinc13@umd.edu>
Cc: "Dr. Jewel Barlow" <barlow@glmwt.umd.edu>

Hello David,

Dr. Pereira graduated many years ago, so we are unable to provide you with current contact information. If the figures you are requesting to use are available via a published source, such as a thesis or dissertation that is published, then you should properly cite the thesis or dissertation when using the material.

Warm Regards,

Aileen

On Fri, Jul 20, 2018 at 8:09 PM, Aileen Hentz <anhentz@gmail.com> wrote:

---------- Forwarded message ---------
From: **Dr. Jewel Barlow** <barlow@glmwt.umd.edu>
Date: Fri, Jul 20, 2018, 6:44 PM
Subject: FW: Website Form Submission

Aileen,

Can you respond to this inquiry about permission for use of figures from a thesis?

Dr. Jewel B. Barlow
Director, Glenn L. Martin Wind Tunnel
www.glmwt.umd.edu
Phone: (240) 464 3871
Rm 2102, bldg. #081
8167 Paint Branch Drive
College Park, MD 20742

From: eng-webmaster@umd.edu <eng-webmaster@umd.edu> on behalf of David Serrano <dserrano@ualberta.ca>
Sent: Friday, July 20, 2018 12:10:47 AM
To: GLMWT - Engineers
Subject: Website Form Submission

Submitted on Friday, July 20, 2018 - 00:10
Submitted by anonymous user: [184.70.166.90]
Submitted values are:

Your Name: David Serrano
Your Company: University of Alberta
Your Email: dserrano@ualberta.ca
Your Message: Hello, my name is David Serrano and I am an MSc student from the University of Alberta. I would like to use some figures from Jason L.

> Pereira's PhD Thesis: "Hover and wind-tunnel testing of shrouded rotors for improved micro air vehicle design". I am wondering where could I request for permission on using these figures? Thank you for your help,
>
> The results of this submission may be viewed at:
> https://windtunnel.umd.edu/node/1240/submission/68
>
> ---
>
> You're receiving this message because you're a member of the GLMWT – Engineers group.

--

Attention Students: Please include your name and UID # in all email communications.

Aileen N. Hentz
Program Director, Undergraduate Studies
Department of Aerospace Engineering
3179G Glenn L. Martin Hall Bldg #088
University of Maryland
College Park, MD 20742
pronouns: she/her/hers
P: 301-405-1980
F: 301-314-9001
E: anhentz@umd.edu
http://www.aero.umd.edu/
http://www.aero.umd.edu/staff/hentz

Permission requested to use figures from Akturk and Camci's works:

UNIVERSITY OF ALBERTA

David Serrano <dserrano@ualberta.ca>

Request to Use Figures from Publications

Cengiz Camci <C-CAMCI@engr.psu.edu> 24 July 2018 at 01:18
To: David Serrano <dserrano@ualberta.ca>

David

Yes, you could use them in your thesis, as long as you clearly reference them in the manuscript and under the figures.

Please send me a copy of your thesis for scholarly exchange. I am very much interested in what you are researching.

All the best,

Cengiz

Cengiz Camci,
Professor of Aerospace Engineering

ASME Fellow
Associate Editor, Journal of Turbomachinery
Associate Editor, International Journal of Turbomachinery, Propulsion and Power, IJTPP

The Pennsylvania State University

Turbomachinery Aero-Heat Transfer Laboratory
223 Hammond Building, University Park, PA, 16802
Ph: (814) 404 2060, Fax: (814) 865-7092, E-mail: cxc11@psu.edu

From: David Serrano <dserrano@ualberta.ca>
Sent: Monday, July 23, 2018 1:31 AM
To: aua162@psu.edu; Cengiz Camci
Subject: Request to Use Figures from Publications

[Quoted text hidden]

Appendix E: Mechanical Drawings of the Duct Models and Stinger Support System

This appendix include the following drawings:

Drawing 1: Stinger Support Exploded View

Drawing 2: Main Shaft to Connecting Beam adapter

Drawing 3: Connecting Beam

Drawing 4: Connecting Beam to Load Cell Adapter

Drawing 5: Mini40 to Mini45 Adapter

Drawing 6: Motor Adapter Mount

Drawing 7: Rigidity Base

Drawing 8: Duct Support Shaft

Drawing 9: Rigidity Strut

NOTE:

All of the connections were fastened with M3×0.5 6 mm long bolts, except the interface between the Motor Adapter Mount and the Load Cell where M3×0.5 4 mm long bolts were used.